京都大学化学研究所
国際共同利用・共同研究拠点

令和７年度
成果報告書

化学関連分野の深化・連携を基軸とする
先端・学際グローバル研究拠点

京都大学化学研究所
国際共同利用・共同研究拠点

化学関連分野の深化・連携を基軸とする
先端・学際グローバル研究拠点

令和 7 年度
成果報告書

まえがき

京都大学化学研究所は、平成２２年度から「化学関連分野の深化・連携を基軸とする先端・学際研究拠点」（平成２８年度から第二期）として国内外の共同利用・共同研究を推し進め、それを新たな糧としてより多様でグローバルな化学研究の展開と若手研究者の育成・輩出を図って参りました。特にこの拠点活動では、化学関連コミュニティの研究者の皆様からの要請を踏まえながら、化学研究所の研究分野の広がりと深さに加えて、これまでの様々な連携実績を活かし、国内外の研究機関の相互協力を担保するハブ環境も提供してきました。先端・学際的分野深耕にあたっては、関連コミュニティの研究者の皆様と化学研究所の教員が推進する分野選択型、課題提案型、施設・機器利用型、連携・融合促進型等の多彩な共同研究と、拠点として主催・共催する各種国際会議、シンポジウム、研究会等を通じて、多様性と先進性を担保し、さらに、国際的視点に基づいて次代の化学関連分野を担う若手研究者の育成にも注力しました。また、拠点運営では、所外、学外の関連分野有識者と化学研究所の教員を委員とする共同研究委員会および運営評議会を核として、共同研究課題の公募・採択などを戦略的に遂行してきました。

このようなグローバルな拠点活動が評価され、化学研究所は、平成３０年１１月１３日文部科学大臣から国際共同利用・共同研究拠点に認定され、「化学関連分野の深化・連携を基軸とする先端・学際グローバル研究拠点」として発展的な活動を強化しています。国際共同利用・共同研究拠点活動第二期４年目にあたる令和７年度には、化学研究所教員が一丸となって、２３７件の応募の中から採択された１４１件の共同研究を遂行しました。そのうち、グローバルな化学研究の展開と人材育成のため、国際共同研究枠を採択数の５３％に当たる７５件（若手国際枠１６件を含む）を遂行しました。新型コロナウイルス感染症拡大による災禍を機に整備したリモート実験環境やハイブリッド会議システムなども、拠点活動の新しい形態としてしっかりと定着してきました。今後とも、国際的ハブ機能を活用し、国際共同利用・共同研究の一層の促進、国際学術ネットワークの充実、国際的・先進的視野をもつ若手研究者の育成に取り組むことで、化学を中心とする研究分野の深化と境界学術分野の新規開拓を一層推進して参ります。皆様にはさらなるご支援・ご協力のほどよろしくお願い申し上げます。

本報告書は、令和７年度の本拠点における研究成果をとりまとめたものです。本報告書をご一読頂き、今後の本拠点の目指すべき方向や活動の推進方法などに関する忌憚のないご意見・ご提案などをお聞かせ下されば幸甚に存じます。

化学研究所
所長 島川 祐一

令和7年度 共同利用・共同研究報告書 目次

１．共同研究成果報告

分野選択型共同研究

ビーム科学分野

2025-1※ Development of high sensitive x-ray spectrometer using microcapillary
Ecole Polytechnique Michel Koenig 1

2025-2※ Development of energy sensitive muon spin rotation (muSR) spectrometer III
RIKEN Ma, Yue 2

2025-3※ Multi-particle Imager for Next-Generation Exotic Atom Spectroscopy
KEK Sohtaro KANDA 3

2025-4※ Clarification of the mechanism of dose rate dependence on the enhancement of biological effectiveness by gold nanoparticles
QST Tamon KUSUMOTO 4

2025-5 Development of real-time dosimeter for ultra-high dose-rate irradiation (FLASH)
Masayori Ishikawa Hokkaido University 5

2025-6 水ベース液体シンチレータの開発と電子ビームを用いた性能評価
京都大学 木河 達也 6

2025-7 Biochemical Phenomena of FLASH Irradiation of Three-Dimensional Oral Cancer Models
Okayama University Kazuyo Igawa 7

元素科学分野

2025-8※ On the mechanism of the C-H bond activation of hydrocarbons catalyzed by a $[Ni_4H_4(P^tBu_3)_4]$ cluster
Chalmers University of Technology W. M. C. Sameera 8

2025-9※ Mechanistic investigations into CO_2 to CH_4 conversion catalyzed by a $[Mo_3S_4Fe]$ clusters
Yilin Hu University of California, Irvine 9

2025-10※ Half-sandwich Rh Complexes Having Bulky Cp Ligand toward Borylation Catalyst of Inert Hydrocarbons
Universiti Teknologi Malaysia Mohamad Shazwan Shah Jamil 10

2025-11※ High-performance Fe-perovskites as oxygen electrodes for solid oxide fuel cells (SOFCs)
Complutense University of Madrid Susana García-Martín 11

2025-12※ Synthesis and physical properties research of new transition metal compounds with mixed-anions
Chinese Academy of Sciences Haichuan Guo 12

2025-13※ Photocatalytic C-H Silylation under visible-light enabled Fe-catalysis
VISVA-BHARATI UNIVERSITY ALAKANANDA HAJRA 13

2025-14※ Computational Study on Lignin Degradation Reaction in Woody Plant Cell Walls
Chalmers University of Technology W. M. C. Sameera 14

2025-15※ Development of Efficient Mixed Sn and Pb-based Perovskite Photovoltaics
University of Valencia Silver-Hamill Turren-Cruz 15

2025-16※ Functionalization of liver organoids from human pluripotent stem cells by using THz waves
New York University Abu Dhabi Kenichiro Kamei 16

2025-17※ Spin-wave excitation of van der Waals magnetic semiconductors by intense terahertz magnetic field pulses
Columbia University Taketo Handa 17

※ 国際共同利用・共同研究

2025-18　電子移動制御を利用したナノ金属クラスター触媒の高活性化
東京科学大学　近藤 美欧　18
2025-19　Development of Novel Planar-Chiral Ferrocenylphosphine Ligands Based on the Restricted Cp-Fe-Cp Rotation: phase 2
Masamichi Ogasawara　Tokushima University　19
2025-20　六方晶フェライトの磁気異方性を制御による広帯域ミリ波用電波吸収体の開発
岡山大学　藤井 達生　20
2025-21　Development of nickel cluster catalysts for highly selective functionalization
Yokohama National University　Ayako Taketoshi　21
2025-22　Spin control by high-power THz pulse in orthoferrite
Osaka University　Hiroshi Watanabe　22
2025-23　Investigation on microscopic mechanism of light-induced anomalous Hall effects
Tohoku University　Shunsuke Sato　23
2025-24　High-harmonic generation in magnonic systems with topological edge states
Hokkaido University　Hideaki Obuse　24
バイオ情報学分野
2025-25※　Integrating omics data and module-based network with deep learning to develop cancer type predictive models
National Yang Ming Chiao Tung University　Jinn-Moon Yang　25
2025-26※　Developing machine learning approaches for prediction of protein stability changes upon missense mutations
Monash University　Jiangning Song　26
2025-27※　Marine giant viruses functional profiling
CEA/Genoscope　Eric Pelletier　27
2025-28※　Dynamics of marine plankton cell lysis as revealed by field observation and mathematical modeling
CNRS　David Demory　28
2025-29※　A Study on Optimal Transport for Learning with Graph Structured Data
Hokkaido University　DAI HAI NGUYEN　29
2025-30　遺伝子破壊株における発現量データとシミュレーション結果の比較解析
山口大学　高坂 智之　30
2025-31　Control and Analysis of Complex Networks via Probabilistic Minimum Dominating Sets
Toho University　Jose Nacher　31
2025-32　環境ウイルス情報を統合した次世代ウイルス分類ツールの開発
海洋研究開発機構　西村 陽介　32
2025-33　Elucidation of host-giant virus interaction using transcriptomics of giant virus-infected acanthamoeba cells
Tokyo University of Science　Masaharu Takemura　33
2025-34　海産原生生物ラビリンチュラゲノムに潜む新奇ウイルス「ミルスウイルス」の探索
福井県立大学　高尾 祥丈　34
2025-35　機械学習による作物根の微生物叢の比較解析
帯広畜産大学　大西 一光　35

※ 国際共同利用・共同研究

物質合成分野
2025-36※ Fabrication of cellulose nanofiber/polymer monolith composite materials with 3D cell structures
University of Bristol Steve Eichhorn 36
2025-37※ Synthesis of Wide-Surface Molecular Nanocarbons
Inner Mongolia University CHAOLUMEN 37
2025-38※ Exploration of aromatic-ring homologue of benzo[c]furan with guanidine functionality
Rudjer Boskovic Institute MARGETIC, Davor 38
2025-39※ Advancing Molecular-Surgery Method for Expansion of Endohedral Fullerenes towards Novel Applications
Sungkyunkwan University IL JEON 39
2025-40※ Elucidation of the mechanism of troponoid-mediated controlled radical polymerization
National Taiwan University Chi-How Peng 40
2025-41※ Exploration of perovskite solar cell composition: Correlating device performance and fundamental property
Sungkyunkwan University Hyunjung Shin 41
2025-42※ Perovskite Device Engineering with Cross-linkable Hole Transport Materials
CSIR-NIIST JOSHY JOSEPH 42
2025-43 Synthesis of borane-functionalized azulene derivative, and the relationship between the aggregation state and color
Suzuka University of Medical Science Shigeharu Wakabayashi 43
2025-44 酸素吸蔵材料の開発
京都工芸繊維大学 細川 三郎 44
2025-45 Development of novel chiral silica based on controlling of hierarchical structure
Osaka Institute of Technology Tomoyasu Hirai 45
2025-46 有機高分子材料の重水素化技術の確立と中性子散乱による高次構造の解明
東北大学 岡 弘樹 46
2025-47 液体界面におけるセルロースナノファイバー膜の粘弾性測定
九州大学 横田 慎吾 47
2025-48 ナノ粒子超構造体における量子協同過程の超高速光電流計測
横浜国立大学 田原 弘量 48
2025-49 塗布重合による2次元共有結合性有機構造体の精密成膜
大阪大学 鈴木 充朗 49
2025-50 高い電気伝導率を指向したn型有機金属半導体の開発
大阪工業大学 村田 理尚 50
現象解析分野
2025-51※ Resolving Pre-GOE Oxygen Whiffs and Post-GOE Redox State of Paleoproterozoic Oceans through Mo and W isotope Analyses of Sedimentary Rocks of the Dharwar Craton
Birbal Sahni Institute of Palaeosciences Gurumurthy GP 51
2025-52※ Trace metal elemental and isotopic composition in the North Pacific Ocean: the roles of aerosol deposition
Academia Sinica HO, Tung-Yuan 52
2025-53※ Chain orientation in single electrospun fibers: diameter dependence and correlation with mechanical properties
National Cheng Kung University Chi Wang 53

※ 国際共同利用・共同研究

2025-54※ Imaging of block copolymer morphology with small angle x-ray scattering
Argonne National Laboratory Byeongdu Lee 54
2025-55※ Elucidation of anti-stokes shifted photoluminescence from lead-based halide perovskite
RMIT University Yasuhiro Tachibana 55
2025-56※ Investigation of molecule arrangements in artificially abrupted self-assembled monolayers with surface specific spectroscopy techniques
National Taiwan University Wei-Ssu Liao 56
2025-57※ Nonlinear Rheology of Dynamically Associative Ionomers
Chinese Academy of Sciences Quan Chen 57
2025-58 Stoichiometry of biologically active trace metals in Osaka Bay and its inflowing rivers (3)
Kindai University Yuzuru Nakaguchi 58
2025-59 Separation and concentration of rare metals by a liquid membrane transport method using ionic liquid
Kyoto University of Education Hiroshi Mukai 59
2025-60 時分割超小角・小角・広角X線散乱法によるゴム中フィラーの分散に関する研究
山形大学 西辻 祥太郎 60
2025-61 プラズモニック合金ナノ粒子を設計するための理論的指針の構築
北海道大学 飯田 健二 61
2025-62 Structure analysis of liquid crystalline organic thin films
Tohoku University Shingo Maruyama 62
2025-63 Study on crystalline structure and transistor characteristics of liquid crystalline organic semiconductors
Institute of Science Tokyo Hiroaki Iino 63
2025-64 Relationship between primary structure of partially fluorinated phospholipids and membrane properties
Gunma University Takafumi Shimoaka 64
2025-65 Identification of bioactive gibberellins in the liverwort Marchantia polymorpha
Kyoto University Yoshihiro Yoshitake 65
2025-66 実験およびシミュレーションによる非絡み合い高分子のダイナミクスの統一的解析
金沢大学 佐藤 健 66

量子情報・スピントロニクス分野

2025-67※ Exploring Spin Wave Dynamics: From Doppler Effects to Magnonic Black-Hole Analogues
Korea Advanced Institute of Science and Technology Kab-Jin Kim 67
2025-68※ Possible Quantum Origin of Unusual Magnetoresistance in Thin-Film Magnetic Metals
Virginia Tech Satoru Emori 68
2025-69※ Research on Magnetic Octupoles in Non-Collinear Antiferromagnets
University of Ulsan Sanghoon Kim 69
2025-70※ Research on high-sensitive quantum sensor with high quality diamond
Stuttgart University Jörg Wrachtrup 70
2025-71 Visualization of magnetization vector using magneto-thermo and magneto-optical effects
Institute of Science Tokyo Kihiro Yamada 71

※ 国際共同利用・共同研究

2025-72 Study on generation of spin-polarized current using insulating ferrite films
Nagoya Institute of Technology Masaaki Tanaka 72
2025-73 Research on heat transport mechanism of MgO | Co-Fe-B structure
Tokyo University of Science Minori Goto 73
2025-74 量子スピントロニクスのためのダイヤモンド半導体材料研究
金沢大学 徳田 規夫 74
2025-75 量子センサの高感度化のためのリンドープダイヤモンド合成研究
産業技術総合研究所 牧野 俊晴 75
スピン生命フロンティア分野
2025-76※ Research on the efficient color centers creation in nanodiamond for bio-application
ETH Zürich Takuya F. Segawa 76
2025-77※ Synthesis of Pyrene-based Materials with Diradical Character
Memorial University of Newfoundland Graham J. Bodwell 77
2025-78※ Investigation of geometric magnetic frustrated materials with structure design and high-pressure synthesis
National Taiwan University Wei-Tin Chen 78
2025-79※ Development of solution-processable multi-resonant TADF emitters
University of St Andrews Eli Zysman-Colman 79
2025-80※ Design of novel organic emitters for highly efficient OLED: Theory meets Synthesis
University of Parma Francesco Di Maiolo 80
2025-81※ Synthesis of higher acene derivatives and the evaluation of their singlet-fission properties
CRPP-CNRS Andrej Jancarik 81
2025-82※ Modelling, design and synthesis of chiral dyes for CISS and CPL
University of Parma Dang Khoa Andrea Phan Huu 82
2025-83※ High-Performance Solution-State Light-Emitting Devices through Excimer-Formation
University of Cologne Malte Gather 83
2025-84 生命科学分野への応用に向けたナノダイヤモンド高感度化研究
量子科学技術研究開発機構 五十嵐 龍治 84
2025-85 Elucidation of electronic state for bis-homo in-plane aromatic molecules
Hiroshima University Eiichi Kayahara 85
2025-86 熱変換型π電子系有機材料の合成と半導体素子の作製
愛媛大学 奥島 鉄雄 86
2025-87 固体NMRとEDMR・ODMRの連携による電子・正孔対の挙動解析
東北大学 森下 弘樹 87
2025-88 Visualization and Analysis of Cellular Phase-Separating Proteins
Osaka University Kazuya Kikuchi 88
2025-89 HR-MAS法を用いた悪性腫瘍の代謝プロファイリング
京都大学 服部 鮎奈 89
課題提案型共同研究
2025-90※ Chemical Genetics of XZA-1
Fudan University Lu Zhou 90
2025-91※ Exploration and Analysis of Fluorescent Probes for Biomolecular Condensates
POSTECH Young-Tae Chang 91
2025-92※ Synthetic and Functional Investigation of Arvenin I
Peking University Xiaoguang Lei 92

※ 国際共同利用・共同研究

2025-93※ Biogenesis, functions, and application of bacterial extracellular membrane vesicles
Kunming University of Science and Technology Wei Yunlin 93
2025-94※ Structural and functional analysis of the surface polysaccharides of outer membrane vesicles released by bacteria
University of Naples Federico II Maria Michela Corsaro 94
2025-95※ Exploration of useful bacteria for nanobiotechnology
UC San Diego Douglas Bartlett 95
2025-96※ Recycling of polymer-matrix composites by subcritical/supercritical water II
Stony Brook University Maya Endoh 96
2025-97※ Synthesis and Tribological Applications of Polyether-Brush-Coated Particles
Osaka Metropolitan University Kohji Ohno 97
2025-98※ Real-time observation of self-assembly and phase transformation of nanocrystals
Ulsan National Institute of Science and Technology Oh-Hoon Kwon 98
2025-99※ Ultrafast measurement of relativistic laser-generated plasma
National Institute for Fusion Science Masato Ota 99
2025-100※ Search for four-wave-mixing in the vacuum - Unveiling dark components in the Universe -
Hiroshima University Kensuke Homma 100
2025-101※ Flow Chemistry for the investigation of sustainable cyclisation conditions
Cardiff University Thomas Wirth 101
2025-102※ Synthesis and characterization of raw and polymerized Asian lacquer samples: towards the development of a comprehensive collection of lacquer reference samples for materials science and conservations studies
University of Pisa Ilaria BONADUCE 102
2025-103※ DNA-binding properties of chemically modified homeoproteins
Sorbonne University Fabienne Burlina 103
2025-104※ Analysis of intracellular delivery mechanism of nanomedicine
Institute for Advanced Chemistry of Catalonia Sílvia PUJALS 104
2025-105※ Visualizing RNA Editing in Action: Developing Single-Molecule Resolution Techniques for Live Cells
Colorado State University Tim Stasevich 105
2025-106※ Molecular mechanisms for the inactivation of a growth hormone in rice
Chinese Academy of Sciences Zuhua He 106
2025-107※ Identification of biosynthetic genes for a novel signaling molecule that modulates plant development
University of California, Riverside David C. Nelson 107
2025-108※ Analysis of novel transporters for strigolactones or their biosynthetic intermediates
University of California San Diego Yunde Zhao 108
2025-109※ Cycloparaphenylene/Fullerenes Supramolecular Complexes in Chiroptical Applications
Univeristy of Oxford Matthew J. Fuchter 109
2025-110※ Synthesis and Electrocatalysis of Hetero-Metal Porphyrin(2.1.2.1) Arrays
Jiangsu University Songlin Xue 110
2025-111※ Vacuum-deposited Perovskite Optoelectronic Devices with Advanced Hole-selection Materials
National Tsing Hua University Hao-Wu Lin 111
2025-112※ Elucidating molecular functions of plant hormones in light-responsive morphological plasticity in *Arabidopsis* thaliana
University of Toronto NAMBARA, Eiji 112

※ 国際共同利用・共同研究

2025-113※ Imaging analysis of zinc transporter and lipid kinase-associated pollen vesicle transport
Georg-August-Universität Göttingen　KAWACHI-REUSCHER, Miki 113
2025-114※ Crossroads of proteostasis and RNA processing in Arabidopsis photomorphogenesis
National Center of Biotechnolog　RUBIO, Vicente 114
2025-115 Development of Covalent Small Molecules That Potentiates Antitumor Immunity
Fukushima Medical School　Misao Takemoto 115
2025-116 Machine-Learning Prediction of Self-Assembly Compounds
Kyoto University　Daniel Packwood 116
2025-117 Analysis and application of the physiological functions of extracellular vesicles secreted by intestinal bacteria
Kansai University　Shino Yamasaki 117
2025-118 Analysis of membrane lipid-dependent fermentation stress response in acetic acid bacteria
Ritsumeikan University　Yosuke Toyotake 118
2025-119 溶媒含浸樹脂を用いた連続的分離法による希土類元素分離の最適化
大阪公立大学工業高等専門学校　倉橋 健介 119
2025-120 3Dプリンティング技術を用いた3次元構造化モノリス造形
共立女子大学　村瀬 浩貴 120
2025-121 カチオン交換非平衡単一半導体ナノプレートのエネルギー準位の解明
東京科学大学　真島 豊 121
2025-122 大型レーザー装置を利用した電荷交換反応の地上再現実験と天体放射モデルの構築
京都大学　内田 裕之 122
2025-123 高強度レーザーと構造性ターゲットとの相互作用による水素・ホウ素核融合等価プラズマ生成と緩和・閉込め過程の検証
京都大学　岸本 泰明 123
2025-124 On demand design of peptides targeting RNA structures
Konan University　Tamaki Endoh 124
2025-125 インクジェットプリンターによる細胞内への機能性ペプチド送達研究
大阪公立大学　中瀬 生彦 125
2025-126 Identification of novel strigolactone biosynthetic inhibitors
Meiji University　Yoshiya Seto 126
2025-127 揮発性植物ホルモン様分子による生長制御機構の解析
広島大学　深澤 壽太郎 127
2025-128 高分子複合材料における多分岐高分子の挙動
福井大学　田上 秀一 128
2025-129 超分岐構造高分子の滑剤作用の解明と最適化
東北大学　髙橋 裕 129
2025-130 Regulatory mechanisms of vegetative reproduction in response to environmental cues
Yamato University　Shiori S Aki 130
2025-131 Biochemical characterization of aldehyde dehydrogenases involved in the biosynthesis of plant volatile benzenoids
Yamaguchi University　Takao Koeduka 131

連携・融合促進型共同研究

2025-132※ The 18th International Workshop for East Asian Young Rheologists
University of Osaka　Tadashi Inoue 132

※ 国際共同利用・共同研究

施設・機器利用型共同研究

2025-133※ High pressure synthesis of new Rh based quantum materials
University of Edinburgh　Sean Dusan Alexander Injac 134

2025-134※ Atomic Structure Investigation by Advanced Transmission Electron Microscopy of AlxCrFeNiCu Alloys
Burapha University　Natthaphol CHOMSAENG 135

2025-135※ Tackling Plasmon Dispersions in Quantum Matters by Momentum-Resolved Electron-Energy Loss Spectroscopy
National Taiwan University　Ming-Wen Chu 136

2025-136※ Nano-structural and Atomic-resolution Characterization on the Local Structure of Novel Functional Energy Materials by Advanced Transmission Electron Microscopy
Chiang Mai University　Thapanee SARAKONSRI 137

2025-137 レーザー駆動イオン加速機構による高品質なイオンビーム生成のためのレーザー照射条件の最適化
量子科学技術研究開発機構　小島 完興 138

2025-138 スギ木質組織構造の効率的化学分解過程から先端化学物質生産をめざした質量分析解析
奈良県立医科大学　秦野 修 139

2025-139 Theoretical design of low-dimensional silicon material embedded in a flat two-dimensional sheet and exploration for operating principles
Tohoku University　Masae Takahashi 140

2025-140 13族元素水素化物の合成と分子構造の解明
近畿大学　松尾 司 141

2025-141 Cs_4PbBr_6薄膜への電子線照射による$CsPbBr_3$ナノ光源生成
九州大学　斉藤 光 142

※ 国際共同利用・共同研究

２．国際学会、シンポジウム・研究報告会

・赤外ラマンセミナー「振動分光学の研究最前線」 143

・NIMS AWARD Post Symposium 145

・International Symposium on Atomic Level Characterizations for New Materials and Devices in Winter 2026(ALC-W’26) 146

３．成果発表論文

147

（令和 8 年 3 月までに刊行された論文で、平成22－令和 6 年度の成果報告書に掲載されていないもの）

紙数の都合により、*を付けた論文のみについて、別刷りを本報告書に記載する。

1)* Direct observation of cation-dependent polarisation switching dynamics in fluorite ferroelectrics, *Nat. Commun.*, 17, 2660 (2026).

2)* A giant virus forms a specialized subcellular environment within its amoeba host for efficient translation, *Nat. Microbiol.*, 11, 584–596 (2026).

3) Catalytic Photooxygenation Demonstrates Therapeutic Efficacy in Transthyretin Amyloidosis, *J. Am. Chem. Soc.*, 147, 28860–28874 (2025).

4) Time resolution of terahertz scanning tunneling microscopy measurements inside a superconducting magnet using a hollow waveguide, *Rev. Sci. Instrum.*, 96, 043004 (2025).

5) Synthesis of wave-shaped Cu(ii) porphyrin arrays and their electrocatalytic hydrogen evolution activity, *Chem. Sci.*, 16, 22498-22503 (2025).

6) Synthesis of an Oxo-Bridged Fe(III) Porphyrin(2.1.2.1) Dimer and Its Enhanced Electrocatalytic Oxygen Evolution, *Inorg. Chem.*, 64, 22262–22268 (2025).

7) Synthesis of C62N Containing a Heptagon, *Org. Lett.*, 27, 8685–8689 (2025).

8) Spin-Dependent Exciton Transport and Effective Negative Diffusion in Thermally Activated Delayed Fluorescence Crystals, *J. Phys. Chem. Lett.*, 16, 11074–11080 (2025).

9) Live-Cell Monitoring and Omics Analysis of Liquid-Solid Transitions of Biomolecular Condensates, *J. Am. Chem. Soc.*, 147, 37056–37064 (2025).

10) Light-Induced SO Extrusion from Tribenzothiepine S-oxides: A Precursor Approach to the Triphenylene Core, *Chem. Eur. J.*, 31, e02655 (2025).

11) Hyperbranched Poly(octadecyl Acrylate)s as Lubricant Additive Studied by Resonance Shear Measurement, *Langmuir*, 42,509−516 (2026).

12) Discovery of a self-assembling small molecule that sequesters RNA-binding proteins, *Chin. Chem. Lett.*, 36, 110135 (2025).

13) A 2 nm Molecular Ladder with a Twisted Backbone, *Org. Lett.*, 27, 8365–8369 (2025).

14) π -Extended 1,1′ -Binaphthyl with Fused Pentagons, *Org. Lett.*, 27, 8969–8973 (2025).

15) 1,6-Disila[4.4.4]propellane revisited part 1: improved synthesis by a mechanistically logical fluorosilane route and its structural aspects including linear stacking along the Si-Si bond in the crystalline state, *Bull. Chem. Soc. Japan*, 99, uoaf119 (2026).

16) Face-to-Face Helical Columns with Permanent Polarity Consisting of Homochiral End-Functionalized Helicenes, *J. Am. Chem. Soc.*, 147, 25978–25989 (2025).

17) Controlling CsPbCl3 Nanocuboid Size and Photoluminescence Quantum Yield with Hot-Injection Reaction Conditions, *J. Photopolym. Sci. Technol.*, 38, 369-375 (2025).

18) Air-Stable 2,2′ -Azobispyridine Radical-Boron Complexes and Their Near-Infrared Absorption Properties, *Chem. - Eur. J.*, 32, e03525 (2026).

19) A multi-resonant thermally activated delayed fluorescence emitter with a twisted second-generation carbazole dendron showing suppressed concentration quenching and its use in solution-processed organic light-emitting diodes, *Org. Chem. Front.*, 12, 3279-3287 (2025).

20) Organophotoredox-Catalyzed Postfunctionalization of Poly(methacrylate) Derivatives via Radical-Polar Crossover Phosphonylation, *Angew. Chem., Int. Ed.*, 64, e202507572 (2025).

21) Homogenized Optoelectronic Properties in Perovskites: Achieving High-Efficiency Solar Cells with Common Chloride Additives, *J. Am. Chem. Soc.*, 148, 6229–6237 (2026).

22) Accessing Metal-Containing Species in Tin-Lead Perovskite Precursor Solutions via Molecular Strategies Guided by the Hard-Soft Acid-Base Principle, *Angew. Chem., Int. Ed.*, 137, e202514010 (2025).

23) Carbenes Embedded in Cyclic Paraphenylenes: Detection, Ground-State Spin Multiplicity, and Mobius Aromaticity, *J. Am. Chem. Soc.*, 148, 6544–6550 (2026).

24) Kinetic resolution of racemic planar-chiral vinylcymantrenes by molybdenum-catalyzed asymmetric metathesis dimerization, *Beilstein J. Org. Chem.*, 22, 568–574 (2026).

25) Direct observation of cation-dependent polarisation switching dynamics in fluorite ferroelectrics, *Nat. Commun.*, 17, 2660 (2026).

25) π-Truncation of a Parent Nanographene: Chirally Twisted Green Fluorophores, *Org. Lett.*, 27, 7009-7013 (2025).

26) Molecular orientation analysis of perfluoroalkyl groups in the solid surface by backscattering Raman spectrometry, *Anal. Sci.*, 41, 1355–1364 (2025).

27) Substrate-Independent and Antisolvent-Free Fabrication Method for Tin Perovskite Films via Imidazole-Complexed Intermediates, *ACS Energy Lett.*, 10, 5047-5056 (2025).

28) Humidity-driven modulation of ferroelectricity in hafnia-zirconia membranes, *Mater. Horiz.*, 12, 5762-5770 (2025).

29) Full Spin-Orbit Torque Switching of the Magnetic Cluster Octupole in Mn3Sn/W Bilayer via Interface Engineering, *ACS Nano*, 19, 39747–39756 (2025).

30) Photoelectron holography characterization of protonated brownmillerite SrCoO2.5 epitaxial films, *J. Ceram. Soc. Jpn.*, 133, 503-507 (2025).

31) Insights into the giant magnetocaloric effect in $BiCu_3Cr_4O_{12}$ with charge-spin-lattice coupling, *J. Mater. Chem. A*, 13, 34286-34296 (2025).

32) Asymmetric perinone-based electron-collecting monolayer materials for n-i-p perovskite solar cells, *J. Mater. Chem. C*, 13, 14991-15001 (2025).

33) Counteranion Engineering of Ethylenediammonium Salts for Reproducible Surface Modification in p-i-n Perovskite Solar Cells, *Sol. RRL*, 10, e202500950 (2026).

34) Mercapto-functionalized scaffold improves perovskite buried interfaces for tandem photovoltaics, *Nat. Commun.*, 16, 4917 (2025).

35) Thickness dependence of the electro-optic properties in epitaxial $Hf_{0.5}Zr_{0.5}O_2$ thin films: Evident response down to 3 nm, *Appl. Phys. Lett.*, 126, 242901 (2025).

36) Search for sub-eV axion-like particles in a quasi-parallel stimulated resonant photon-photon collider with coronagraphy, *J. High Energy Phys.*, 2025, 138 (2025).

37) Correlation between structural properties and electrochemical proton insertion in (001) VO2 epitaxial films, *Appl. Phys. Express*, 18, 045501 (2025).

38) Ultrafast modulation of the anomalous Hall conductivity by coherent magnetization precession in Co-Pt thin films, *Phys. Rev. Applied*, 24, 044079 (2025).

39) Towards high performance lithium storage anodes: Design strategy for carbon coated SnS-SnO2/rGO nanocomposites, *Radiat. Phys. Chem.*, 235, 112821 (2025).

40) Spatial mapping of an effective magnetic field at the NiFe/NiO interface, *Jpn. J. Appl. Phys.*, 64, 120905 (2025).

41) Reaching the Nonlinear Spin-Dynamics Regime in Antiferromagnets Using Terahertz Pulses, *J. Phys. Soc. Jpn.*, 94, 111006 (2025).

42) Néel vector rotation driven by spin-orbit torque in amorphous ferrimagnetic GdCo, *Appl. Phys. Lett.*, 126, 232406 (2025).

43) First-principles study of structural stability and magnetic properties in Fe-Pd-In alloys, *J. Magn. Magn. Mater.*, 636, 173649 (2025).

44) Ferroelectric $ZrO_2/Hf_{0.5}Zr_{0.5}O_2$ epitaxial Moiré heterostructures, *Appl. Phys. Lett.*, 127, 112901 (2025).

45) Data-Writing and Shifting Processes Toward a Vertical Domain Wall Motion Memory, *IEEE Trans. Magn.*, 61, 3401004 (2025).

46) Anomalous Nernst effect in Co thin films under laser irradiation, *Phys. Rev. Applied*, 24, 044101 (2025).

47) All-optical helicity-dependent switching in $NiCo_2O_4$ thin films, *Appl. Phys. Lett.*, 126, 212405 (2025).

48) First principles study of flat silicon rich 2D alloys SixBey, *Discov. Nano.*, 21, 50 (2026).

49) Earth-Lens Telescope for Distant Axion-like Particle Sources with Stimulated Backward Reflection, *Universe*, 11, 287 (2025).

50) Characteristics of passive dosimeters for ultra-high dose rate protons and electrons, *Radiat. Meas.*, 192, 107629 (2026).

51) Charge carrier dynamics controlling performance of lead-based halide perovskite solar cells, *Jpn. J. Appl. Phys.*, 64, 050806 (2025).

52) Acid-leachability of metals from suspended particles in the Pacific Ocean, *Mar. Chem.*, 273, 104571 (2025).

53) Exposing binding-favourable facets of perovskites for tandem solar cells, *Energy Environ. Sci.*, 18, 7680-7694 (2025).

54) Ecophysiology and global dispersal of the freshwater SAR11-IIIb genus *Fontibacterium*, *Nat. Microbiol.*, 10, pages2194–2206 (2025).

55) Biochemical characterization of benzaldehyde dehydrogenases from petunia, *Plant Mol. Biol.*, 115, 70 (2025).

56) The plant Cleavage Factor I complex is essential for precise cleavage and polyadenylation site determination, *Plant Physiol.*, 199, kiaf483 (2025).

57) Simple Cytosolic and Nuclear Introduction of Boron Compounds Using Cationic Lipids to Enhance Cancer Cell-Killing Activity in Boron Neutron Capture Therapy, *Biol. Pharm. Bull.*, 48, 344-354 (2025).

58) Giant viruses specific to deep oceans show persistent presence and activity, *mSystems*, 10, e00932-25 (2025).

59) A novel prohibitin inhibitor acts as a dual inhibitor of angiogenesis and fibrosis, *Biochem. Biophys. Res. Commun.*, 805, 153386 (2026).

60) Ultrafast modulation of the anomalous Hall conductivity by coherent magnetization precession in Co-Pt thin films, *Phys. Rev. Applied*, 24, 044079 (2025).

61) Reaching the nonlinear spin-dynamics regime in antiferromagnets using terahertz pulses, *J. Phys. Soc. Jpn.*, 94, 111006 (2025).

62) Time resolution of terahertz scanning tunneling microscopy measurements inside a superconducting magnet using a hollow waveguide, *Rev. Sci. Instrum.*, 96, 043004 (2025).

63) Synthesis of a twisted azananographene featuring a diquinoxaline-fused pyrene, *Chem. Commun.*, 61, 11401-11404 (2025).

４．参考資料

4-1.令和 7 年度公募要領 187
4-2.令和 7 年度採択課題一覧 192

1. 共同研究成果報告

Development of high sensitive x-ray spectrometer using microcapillary

Michel Koenig　Ecole Polytechnique

Objectives

The primary objective of this joint research project was the development and implementation of a high-sensitivity X-ray spectrometer utilizing polycapillary optics. The specific goals for the facility time at the Institute for Chemical Research included establishing alignment methods for the polycapillary using the T6 laser's plasma X-ray source, evaluating far-field image quality, and assessing temporal pulse broadening.

Spectrometer Design and Experimental Methods

Due to logistical constraints preventing the arrival of the polycapillary optics, the methodology pivoted to the theoretical design of the spectrometer and critical baseline diagnostic characterization. For the T6 environment, a spatial characterization layout was designed to measure the capillary output directly, establishing a fixed 200 mm source-to-optic distance and a variable optic-to-detector translation axis to empirically map X-ray divergence and intensity scaling.



Figure 1: (a) Schematic of the T6 target chamber layout for spatial characterization, illustrating the fixed 200 mm source distance and the variable detector axis to evaluate polycapillary divergence. (b) Baseline experimental data: Pinhole image captured via X-ray streak camera, characterizing the bare plasma source emission

In December 2025, the research team established the required baseline environment at the T6 facility. Consumable funding was utilized to procure copper and aluminum foils for target testing. The target chamber was configured, requiring physical adaptations to utilize the alignment device within spatial constraints. An X-ray CCD camera coupled with a pinhole was installed, and data acquisition was established. Subsequently, a CCD-coupled spectrometer utilizing a Beryllium window and an RbAP crystal was mounted to observe the bare target spectrum and evaluate ambient background noise. Physical measurements of the chamber ports were conducted to finalize the integration geometry for the delayed polycapillary device.

Outcomes and Analysis

The deployment of the secondary diagnostics yielded the required baseline data. The XSC and pinhole setup successfully detected signals and established proper spot size characterization of the bare plasma source, verifying the diagnostic timing and spatial alignment.

The CCD spectrometer encountered operational issues; despite rigorous troubleshooting, realignment of the RbAP crystal geometry, and comparison with historical data, the setup failed to yield a resolvable image. Documenting this zero-signal failure provides a necessary baseline, indicating that the baseline X-ray flux or the specific interaction geometry in the T6 chamber requires the high-efficiency throughput and focused spatial profile of the proposed polycapillary optic to achieve a viable signal-to-noise ratio. The theoretical design framework confirms that the extremely low divergence of the transmitted X-rays will overcome these flux limitations in future experimental runs.

Publications

No publications or presentations have resulted from this preparatory phase of the project.

Acknowledgements

This work was supported by the International Collaborative Research Program of Institute for Chemical Research, Kyoto University (Grant No. 2025-1).

Development of energy sensitive muon spin rotation (muSR) spectrometer III

Yue MA　RIKEN

Research Purpose

Muon spin rotation (muSR) is a powerful technique to probe local magnetic fields in materials using the spin precession of implanted muons. The measurement relies on the correlation between the muon spin direction and the emission angle of decay positrons; higher-energy positrons provide a stronger correlation and thus a cleaner asymmetry signal. Conventional muSR spectrometers typically lack positron energy information, limiting the achievable resolution. Our project develops an energy-sensitive muSR spectrometer based on PbG Cherenkov calorimetry to measure positron energy and to improve the muSR time-spectrum (A(t)) resolution via energy selection.

Progress in FY2025

Our J-PARC MLF General Use proposal for an energy-sensitive muSR validation experiment was accepted with high priority (experiment number: 2025B0007), and the beamtime is scheduled for late February 2026. Owning to the support from KAKEN budget, manufacturing of the PbG calorimeter crystals has been completed. The detector modules are ready for integration (mechanics, PMT coupling, and DAQ) toward the February 2026 beamtime. In addition, we completed a detailed end-to-end simulation and obtained results consistent with the detector concept, indicating an expected ~20% improvement in muSR resolution with positron energy selection.

Outlook and Summary

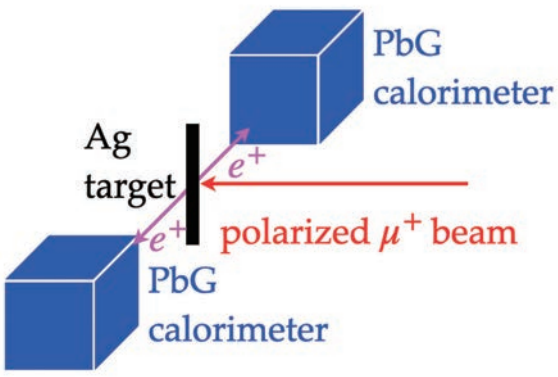


Figure 1, Schematic setup for energy sensitive muSR at J-PARC MLF.

We will perform the world first energy sensitive muSR experiment at the J-PARC MLF S1 muon beamline during Feb. 25th~26th. Polarized surface muons will be implanted into a standard Ag sample with 50 Gaus external magnetic field, and decay positrons will be detected by two PbG Cherenkov calorimeter sectors as illustrated in Fig. 1. A reference measurement using a conventional plastic scintillator with the same readout chain will be conducted to benchmark the gain from energy selection. Full PMT waveforms will be digitized (500 MS/s) and analyzed offline to reconstruct positron energy and timing (including CFD), select high-energy positrons (E > 30 MeV), and quantify the improvement in A(t) resolution relative to the baseline.

Multi-particle Imager for Next-Generation Exotic Atom Spectroscopy

Sohtaro Kanda　KEK

Objectives Precision measurements of exotic atoms, such as muonium and antihydrogen, provide stringent tests of the Standard Model and fundamental symmetries. However, the statistical precision of these experiments is often limited by the low detection efficiency of signal particles, typically vacuum ultraviolet (VUV) photons or low-energy charged particles. The objective of this project is to develop and characterize a new multi-particle imager that simultaneously achieves high detection efficiency and position sensitivity for both VUV photons and charged particles. This device combines a tapered microchannel plate (T-MCP) with a resistive anode encoder (RAE).

Experimental Methods To validate the imaging capability, we constructed a prototype detector using a MCP stack coupled with an RAE. A beam test was conducted using the Kyoto Electron Linac (KEL) at the Institute for Chemical Research (ICR), with the operational support of our ICR partner researcher, Prof. Kyo Tsukada. The prototype was installed inside a vacuum chamber, and a pulsed electron beam was irradiated (Fig. 1).

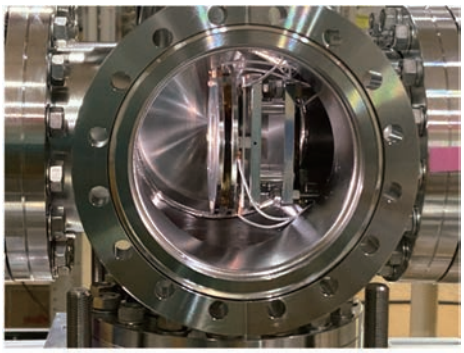


Figure 1: Experimental setup.

Outcomes The electron beam was successfully imaged using the prototype detector at the KEL beamline (Fig. 2). The 2D position of the incident electrons was reconstructed via the charge centroid method using the integrated charge from the four corners of the RAE.

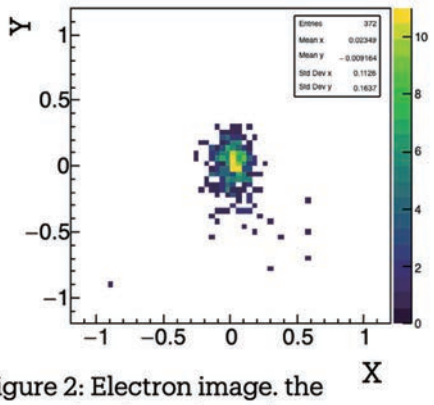


Figure 2: Electron image. the conversion factor from the normalized coordinate to the physical position is 38.2 mm

Analysis The full width at half maximum (FWHM) of the reconstructed position distribution was approximately 7.4 mm. This beam spread is consistent with our expectations when accounting for the 5 mm aperture size of the collimator and the multiple Coulomb scattering occurring at the beam window. These results were presented at the international conference SSP2025.

Publications S. Kanda, A. Powell, K. Tsukada, Y. Ma, and S. Matoba, "Development of a Multi-particle Imager for Exotic Atom Spectroscopy and Interferometry," to be published in JPS Conf. Proc.

Clarification of the mechanism of dose rate dependence on the enhancement of biological effectiveness by gold nanoparticles

Tamon Kusumoto　QST

FLASH radiotherapy has been attracted a great attention due to its advantages that healthy tissues are spared, while effectiveness to tumors is maintained. Also, gold nanoparticles (GNPs) have been recognized as a radiosensitizer. The mechanisms of both methods (FLASH and GNPs) could be related to changes in yields of water radiolysis products. To holistically clarify their mechanisms, we in this project tackle to evaluate changes in water radiolysis species using a linac equipped to Kyoto Univ., which enables to provide high-intensity short pulse electron beams (14 MeV). Last year, we have successfully done dosimetry using FTR-125 film. This achievement has been published in Radiation Measurements (see: Kodaira et al., *Radiat. Meas*. **192** (2026) 107629). Based on the dosimetry results, we will address to evaluate changes in yields of water radiolysis species.

In this year, we have evaluated changes in yields of typical water radiolysis species (i.e., OH radicals, hydrogen peroxide, and hydrated electrons) under electrons (250 kGy/s as instantaneous dose rate). As a reference of FLASH irradiation, gamma rays from Cs-137 source with dose rate of 0.1 Gy/s are employed as a conventional dose rate exposure.

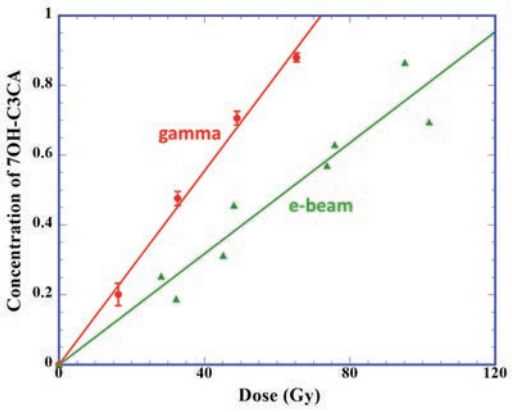


Fig. 1 The concentration of 7OH-C3CA formed under electrons (FLASH) and gamma rays (conventional).

By irradiation of electrons and gamma rays, the concentration of 7OH-C3CA formed increases with dose. The slope of fitting line using linear function (y = ax) is gentle under FLASH irradiation (i.e., electrons), compared to conventional exposures to gamma rays (Figure 1). The relative yield change is -43 ± 8%. This value is consistent with previously obtained one by another group. A similar trend is seen in the case of hydrated electrons. The relative yield change is -44 ± 9.8%. This value is almost equivalent to that of OH radicals. This finding implies that yields of OH radicals decrease due to the reaction with hydrated electrons. This finding would demonstrate that dense track distribution is formed by high-dose rate irradiation. Therefore, reactions between water radiolysis species formed by neighboring tracks significantly occur under high-dose rate irradiation, resulting in the suppression of the biological effectiveness. This would be one of the mechanisms of sparing effects seen in FLASH radiotherapy.

Development of a real-time dosimeter for ultra-high dose-rate irradiation (FLASH)

Masayori Ishikawa　Hokkaido University

1. Purpose

FLASH irradiation, which delivers radiation at ultra-high dose rates exceeding 40 Gy/sec, has recently attracted attention as a novel radiotherapy technique. However, real-time dose measurement under such conditions remains difficult. In this study, we investigated the feasibility of dose measurement in a FLASH electron beam irradiation field using a SOF dosimeter (Scintillator with Optical Fiber dosimeter) developed in our laboratory, which combines a plastic scintillator and an optical fiber.

2. Methods

Preliminary experiments conducted in 2024 using the electron linear accelerator at Kyoto University indicated that the SOF dosimeter operating in pulse measurement mode could accurately measure dose independent of beam intensity (nC/pulse). Based on these results, the SOF dosimeter was calibrated using radiochromic film (EBT3), and dose distributions were measured. The dose distribution obtained with EBT3 was compared with that measured using the SOF dosimeter with a scanning system.

3. Results and Discussion

In current measurement mode (conventional method), the detector response ranged from 0.500 to 1.578 (SD: 0.446) at dose rates of 0.91–3.39 Gy/sec, and decreased as the dose rate increased, indicating significant dose rate dependence. In contrast, in pulse measurement mode, the response ranged from 0.937 to 1.165 (SD: 0.0843), showing substantially reduced dose rate dependence and improved measurement stability.

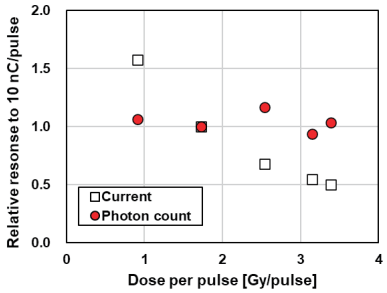
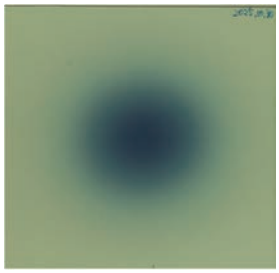
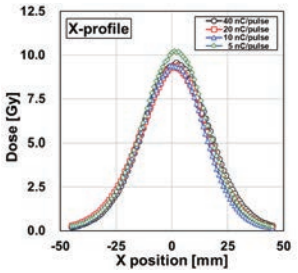


Fig. 1 Relationship between dose rate and detector response

Figure 2 shows the 2D dose distributions measured using EBT3 film. 1D dose profile along the X-axis was extracted from the 2D distribution, and compared with measured data using SOF dosimeter with a scanning system (Fig. 3). Since the dose per pulse was too high, both measurements were normalized for comparison. A slight discrepancy was observed at 5 nC/pulse, while good agreement was confirmed at 10–40 nC/pulse.

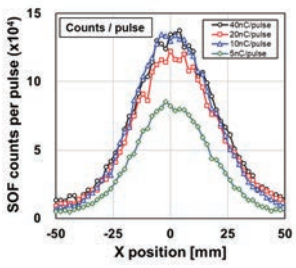


(a) After irradiation

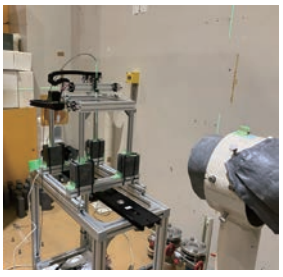


(b) X-axis dose profile

Fig. 2　Dose distribution measured by EBT3



(a) Scanned SOF profile



(b) Experiment geometry

Fig. 3　1D dose profile measured by SOF dosimeter with scanning system

水ベース液体シンチレータの開発と電子ビームを用いた性能評価

木河達也　京都大学

本研究の目的は 2028 年に開始予定のハイパーカミオカンデ実験に向け、水ベース液体シンチレータ(WbLS)検出器の開発と性能測定を行うことである。ハイパーカミオカンデ実験では J-PARC で生成されたニュートリノビームを直後に設置された前置検出器と 295km 離れたハイパーカミオカンデ検出器で測定することにより、ニュートリノ振動の精密測定を行う。ハイパーカミオカンデ検出器と同じ水を主成分とする WbLS を前置検出器に導入することにより、ニュートリノと水との相互作用を精密に測定することが可能になり、ハイパーカミオカンデ実験におけるニュートリノ振動の測定精度が飛躍的に向上する。我々は図 1 のように WbLS をグリッド状の反射材により多数のセルに光学的に分離し、それぞれのセルに波長変換ファイバーを通して、ファイバーの先端に設置した SiPM により光を検出するという全く新しい飛跡検出器を考案し、波長変換ファイバーでの読み出しに適した WbLS を開発した。この WbLS を用いて試作機を製作し、2025 年 10 月 8-10 日に京都大学化学研究所電子線形加速器の単電子ビームライン（90°ビームライン）において WbLS 試作機の性能評価試験を行った。図 2 のように電子ビームに対して串刺し状に WbLS 試作機とビームの位置測定用のホドスコープを設置する。ビーム試験に適したエネルギー・広がり・レートの電子ビームが照射されるように、化学研究所の若杉氏、塚田氏のもとで加速器の調整を行った。ホドスコープを用いて電子ビームが試作機に確実に当たるイベントを選択したときの試作機の 1 つのチャンネルにおける典型的な光量分布が図 3 の通りである。平均で 5.63 ± 0.45 光電子であり、これはファイバーの端面加工やより光子検出効率が高い SiPM を用いることで 27.2 ± 2.7 光電子まで向上できる。またセル間での光学的クロストーク率は 4%未満と十分に小さいことが確認された。いずれも飛跡検出器としては十分な水準であり、WbLS を用いた新型検出器の実用可能性を示す結果となった。

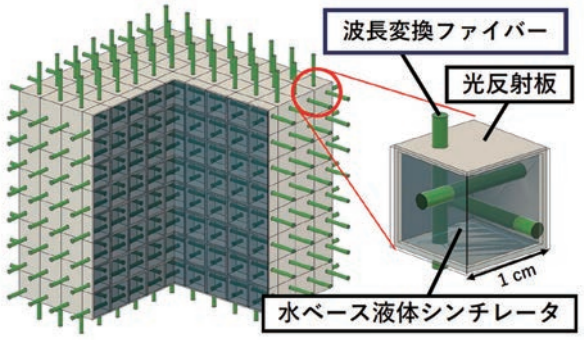


図 1: WbLS を用いた新型飛跡検出器の概念図

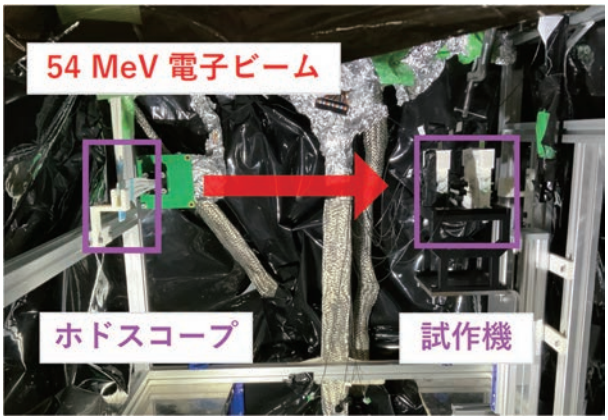


図 2: 電子ビーム試験のセットアップ

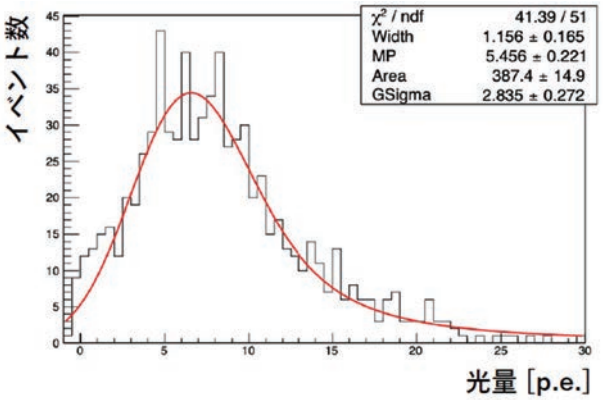


図 3: 典型的なチャンネルあたりの光量分布

Biochemical Phenomena of FLASH Irradiation of Three-Dimensional Oral Cancer Models

Kazuyo Igawa　Okayama University

【Objective】In recent years, FLASH irradiation, known as ultra-high dose rate irradiation, has been anticipated for clinical application in radiation therapy as a next-generation innovative irradiation technique and method. However, the mechanism behind the FLASH effect−which maintains high antitumor efficacy while suppressing damage to normal tissues−remains unclear. Development of a linear accelerator at the Institute for Chemical Research, Kyoto University, has progressed, enabling FLASH irradiation with a 20 MeV electron beam. This study evaluates the biochemical effects of FLASH irradiation on a three-dimensional culture model replicating the human tumor microenvironment, using the electron beam FLASH irradiation system at the Institute for Chemical Research, Kyoto University（KFL）.

【Methods】After evaluating the FLASH irradiation field using a cellulose triacetate film dosimeter (FTR-125, Fujifilm), four types of human-derived cells (oral cancer cells HSC, oral cancer-associated fibroblasts CAF, oral fibroblasts NOF, and skin fibroblasts NHDF) are cultured in three dimensions and subjected to electron beam FLASH irradiation. Three days after FLASH irradiation, the biological effects on the three-dimensional cell cultures are evaluated by assessing cell survival using the Trepan Blue staining counting method and by histological analysis using HE staining.

【Result and discussion】To establish an electron beam FLASH irradiation protocol for 3D cell culture, we measured the KFL beam profile (Figure 1). The irradiation field for 3D cell culture was defined as the range (ϕ 30 mm) where the intensity reaches 90% of the pixel value peak. Therefore, we prepared four types of human-derived cells in 4-well plates for each dose (Figure 2). Electron beam FLASH irradiation of 3D cultured cancer cells and normal cells is performed in February and March 2026. The biochemical effects of FLASH irradiation on cancer cells and normal cells in both 2D and 3D cell cultures are evaluated. Physical dose measurements will be performed by Co-Investigator Ogawara (RIKEN) and Co-Investigator Kusumoto (QST). FLASH irradiation will be conducted by Co-Investigator Wakasugi (Kyoto University). Cell culture and cell viability assessment will be carried out by Principal Investigator Igawa (Okayama University).

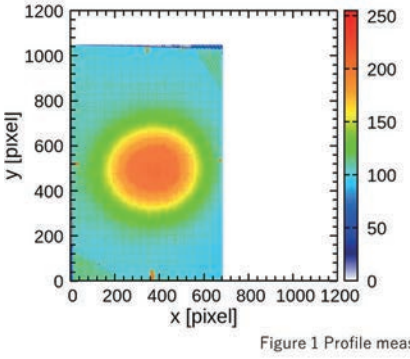
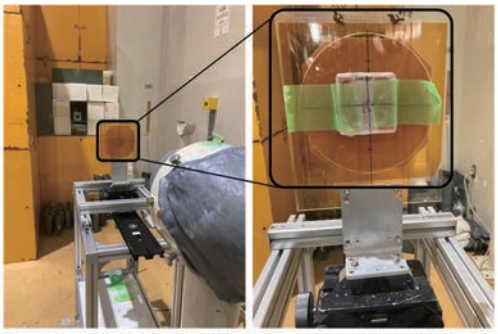


Figure 1 Profile measurement


Figure 2　Electron Beam FLASH Irradiation of 3D Cultured Cells

【Outcome】We plan to publish a paper summarizing the results of FLASH irradiation on 2D cell cultures in fiscal year 2024 and on 3D cell cultures in fiscal year 2025.

On the mechanism of the C-H bond activation of hydrocarbons catalysed by a $[Ni_4H_4(P^tBu_3)_4]$ cluster

W. M. C. Sameera　Chalmers University of Technology

Objectives. We have synthesised a tetranuclear Ni-hydride-phosphine cluster, $[Ni_4H_4(P^tBu_3)_4]$ (**1**). Computational methods were used to determine its ground-state structure and to rationalise the intramolecular C–H bond activation of P^tBu_3 and intermolecular C–H activation of benzene.

Methods. Density functional theory (DFT) computations were conducted using the BP-D3BJ functional with standard basis sets.

Outcomes. DFT calculations confirmed that the S = 0 state is the ground state of (**1**), and its geometry aligns with the X-ray structure, confirming the positions of the hydride ions. The computed free-energy barrier for the C–H bond activation of P^tBu_3 is 23.6 kcal/mol. Intermolecular C–H bond activation of benzene is initiated by the dissociation of a P^tBu_3, followed by coordination of benzene to the vacant coordination site of the Ni ion. Then, C–H bond activation of benzene occurs through a free-energy barrier of 20 kcal/mol. We concluded that both intramolecular C–H bond activation of P^tBu_3 and intermolecular C–H bond activation of benzene operate under the experimental conditions.

Publications:

[1] K. Sunami, T. Higaki, K. Tanaka, W. M. C. Sameera, R. Takahata, T. Teranishi, S. Kikkawa, S. Yamazoe, T. Shiga, M. Nihei, T. Kato, H. Izu, Y. Ohki, *A tetranuclear nickel hydride cluster capable of reversible activation of aromatic and aliphatic C-H bonds*. (*Under revision*)

[2] T. Higaki, K. Tanaka, S. Oishi, K. Kawamoto, M. Tada, W. M. C. Sameera, R. Takahata, T. Teranishi, S. Kikkawa, S. Yamazoe, T. Shiga, M. Nihei, T. Kato, R. E. Cramer, Z. Zhang, K. Meyer, Y. Ohki, 2025, 147, 4, 3215-3222.

Presentations:

[1] W. M. C. Sameera, *From Cosmic Dust to Molecules: Computational Approaches to Rationalise Interstellar Chemical Complexity*. CY Cergy Paris Université, France. (Invited Lecture)

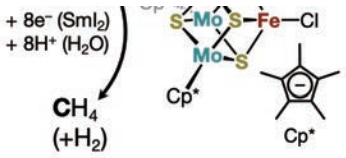
[2] W. M. C. Sameera, *Activating Inert Molecules Using Transition Metal Clusters: A Computational Study.* The 22nd International Symposium on Organometallic Chemistry Directed Towards Organic Synthesis, Kyoto, Japan. (Poster)

Mechanistic Investigations into CO_2 to CH_4 Conversion Catalyzed by a [Mo_3S_4Fe] Cluster

Yilin Hu　University of California, Irvine

[Objectives]

Our earlier work established that synthetic metal-sulfur clusters can promote the formation of short-chain hydrocarbons (HCs) from CO_2. Building on this foundation, the present project seeks to improve both the selectivity and efficiency of HC production by employing a robust Mo-Fe-S cluster developed by our collaborators, [Cp*$_3$$Mo_3S_4$FeCl] (**1**, Cp* = C_5Me_5) (Figure 1). Our last year's research revealed that cluster **1** catalyzes the CH_4 formation under a CO_2 atmosphere and identified the carbon source of the produced CH_4 as CO_2. This year's research aimed to gain more insights into the catalytic mechanism and improve the performance of the catalyst.



[Experimental Methods and Outcomes]

To isolate reaction intermediates, we first examined stoichiometric reactions with limited substrates. When cluster **1** was treated with 10 equiv. of KC_8 as a reductant under CO_2, an anionic Fe-CO complex **2** ([Cp*$_3$$Mo_3S_4$Fe(CO)]$^-$) was formed (Figure 2). The solid-state IR spectrum of **2** exhibited a band at 1692 cm^{-1} attributable to the C-O stretching vibration. When the same reaction was carried out under $^{13}CO_2$, this band shifted to lower frequency, confirming that the CO ligand in **2** originates from the reduction of CO_2. These results suggest that the reduction of CO_2 to CO occurs as an initial step in the conversion of CO_2 to CH_4 catalyzed by cluster **1**.

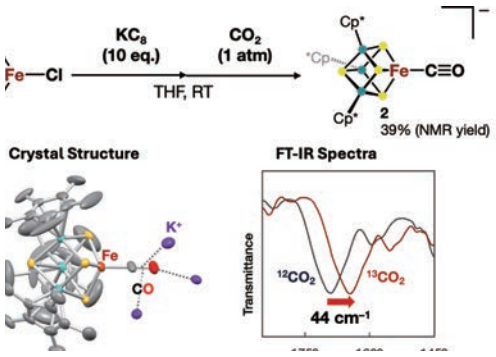


Figure 2. Reaction of **1** with CO_2 under reducing conditions. The crystal structure (bottom, left) and infra-red spectra (bottom, right) of the product are shown.

We also conducted scale-up experiments using increased amounts of reductant to improve the catalytic performance. After optimization of the reaction conditions and temperature, the catalytic activity increased dramatically, affording CH_4 with turnover numbers higher than 100,000. This value significantly exceeds the previously reported maximum for the reduction of CO_2 to CH_4 using molecular catalysts, demonstrating the exceptional stability of the cluster catalyst.

Half-Sandwich Rh complexes Having Bulky Cp Ligand toward Borylation Catalyst of Inert Hydrocarbons

Mohamad Shazwan Shah Jamil　Universiti Teknologi Malaysia

Background: The selective functionalization of hydrocarbons, which have limited utility beyond fuels and solvents, represents a highly challenging molecular transformation. Among the available approaches, C-H borylation is particularly promising, as the resulting organoboron compounds serve as highly versatile intermediates in organic synthesis.

Despite its potential, practical implementation of this transformation remains challenging. One major limitation is catalyst deactivation or decomposition under the elevated reaction temperatures (~150 ºC) typically required for C-H borylation.

Objective: In this study, we focused on half-sandwich Rh complexes bearing cyclopentadienyl ligands bulkier than Cp* as potential catalysts capable of operating under prolonged high-temperature conditions. The bulky ligands are expected to suppress catalyst aggregation, a key deactivation pathway, while simultaneously creating a hydrophobic environment around the active site that may promote substrate incorporation. As an initial step, we aimed to synthesize such Rh complexes.

Results & discussion: Half-sandwich Rh complex bearing sterically demanding Cp ligands, $Cp^{Ar}RhCl_2$ (**1**) (Cp^{Ar} = C_5Ar_5, Ar = 3,5-$Me_2C_6H_3$), were synthesized with reference to the corresponding Cp*-supported analogues. **1** was isolated as a reddish-brown solid in 66% yield. Single-crystal X-ray diffraction analysis confirmed that **1** is coordinatively unsaturated 16-electron mononuclear complexes (Figure-left). This behavior contrasts with Cp*-supported analogues, in which chloride bridging between metal centers leads to dimerization and formation of coordinatively saturated 18-electron complexes.

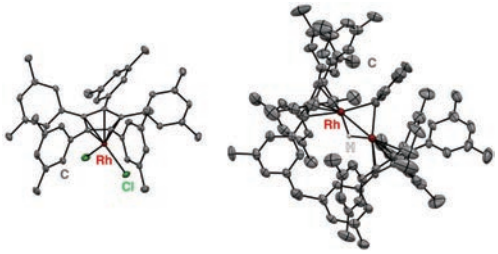


Figure. Molecular structures of complex **1** (left) and **2** (right).

To convert **1** into a catalytically relevant precursor for C-H borylation, we attempted substitution of the chloride ligands with organic groups. Treatment of **1** with KC_8 in a THF–benzene mixed solvent afforded a dinuclear complex, $[Cp^{Ar}Rh]_2(\mu\text{-}H)(\mu\text{-}C_6H_5)$ (**2**), in which a hydride and a benzene-derived phenyl group bridge two Rh centers. **2** was isolated as a green solid in 9% yield, and its molecular structure was determined by single-crystal X-ray diffraction (Figure-right).

Outcomes: We successfully synthesized Rh complexes bearing the Cp^{Ar} ligand, along with precursor complexes relevant to C-H borylation catalysis. Preliminary studies confirmed their catalytic activity toward the C-H borylation of linear saturated alkanes. Further investigations into the synthesis and catalytic performance are currently underway, and the results will be reported in due course.

High-performance Fe-perovskites as oxygen electrodes for solid oxide fuel cells (SOFCs)

Susana García-Martín　Complutense University of Madrid

Project code: 2025-11

Name of ICR partner researcher: Prof. Yuichi Shimakawa.

Objectives

The project aimed to develop novel functional materials based on Fe-oxides, with layered perovskite-related structure, that present electro-catalytical properties and potential applications as oxygen electrodes for solid oxide fuel cells (SOFCs).

Experimental Methods

Synthesis: The oxygen content of these materials, which highly impact on their properties, can be tuned by means of different methods of synthesis. The oxides have been prepared by solid state reaction at air or under argon flow. After synthesis, some oxides were heated at 473 K under flowing ozone-containing oxygen with the aim of increasing the Fe-oxidation state by increasing the oxygen content. The oxygen content of the compounds was determined by thermo-gravimetric analysis. The average oxidation state of Fe was determined by Mössbauer spectroscopy and by EELS. Nuclear and magnetic structure characterization was carried out by means of synchrotron X-ray diffraction (SXRD), Mössbauer spectroscopy, neutron diffraction (ND), electron diffraction (SAED), high resolution transmission electron microscopy (HRTEM), scan-TEM (STEM in HAADF and ABF modes) and EELS mapping. Electrochemical characterization: ORR activity of the electrode materials has been evaluated by electrochemical impedance spectroscopy (EIS) in symmetrical half-cells at different temperatures. DFT calculations of the electronic structure of some of the oxides have been carried out using the VASP program.

Results

We have studied $MM'Fe_2O_{6-\delta}$ systems with M = Pr, Gd, Tb and M' = Ba, Ca. We have found that both $TbBaFe_2O_6$ and $PrBaFe_2O_6$ present phase transitions associated to Fe charge ordering (CO) effects at different temperatures. We have also studied the crystal structure and the electrocatalytic activity of the non-stoichiometric $PrBaFe_2O_{6-\delta}$. The SAED, HRTEM, STEM and EELS results have revealed a new superstructure of the perovskite-type related to the layered ordering of the Pr and Ba atoms and location of the anion vacancies. The impedance measurements carried out in symmetrical cells with $PrBaFe_2O_{6-\delta}$ as electrodes, indicate that this oxide is a potential candidate as air electrode for SOFCs. We are currently finishing studies of the $Gd_{0.8}Ba_{0.8}Ca_{0.4}Fe_{1.8}Ni_{0.2}O_{6-\delta}$ oxide. Two articles summarizing these results are currently being drafted.

Synthesis and physical properties research of new transition metal compounds with mixed-anions

Haichuan Guo　Chinese Academy of Sciences

Introduction

A mixed-anion compound is a solid-state material containing more than one anionic species in a single phase, such as oxynitrides (oxide-nitride). Unlike oxides, which exhibit diverse chemistries and structures often known from mineralogy, the structures of most mixed-anion compounds, among other aspects, are less explored with much to learn. The different anionic characteristics, such as charge, ionic radii, electronegativity, and polarizability add new dimensions to control and tune the electronic and atomic structure of materials, which may support physical properties inaccessible to a single-anion analog. Here, a new transition metal oxynitride $NaWO_2N$ was synthesized using high-pressure and high-temperature method. The crystal structure was investigated using neutron powder diffraction (NPD) method.

Experiments and results

$NaWO_2N$ powder sample was synthesized at 9 GPa and 1100^{o}C using cubic-anvil high-pressure equipment in ICR. NPD measurement was performed on $NaWO_2N$ at Time-of-flight High Resolution Neutron Diffractometer of CSNS. The diffraction pattern of $NaWO_2N$ at room temperature is shown in Fig.1. Although the XRD pattern of $NaWO_2N$ suggests a simple cubic perovskite structure with the space group of *Pm*-3*m*, the NPD pattern indicates an *A*-site-ordered quadruple perovskite structure with a space group of *Im*-3 and a $2a\times2a\times2a$ unit cell(Fig.2), in which the same Na^+ ion at *A*-site splits into two sites. Three quarters of Na^+ ions introduced into the originally twelve-fold coordinated site form square-coordinated units that aligns perpendicular to each other. Further analysis of NPD data and physical properties measurement of $NaWO_2N$ are planned.

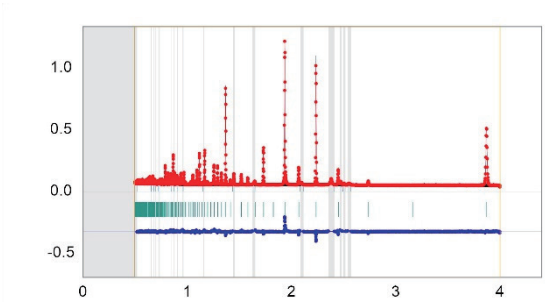


Fig.1 NPD patterns of $NaWO_2N$

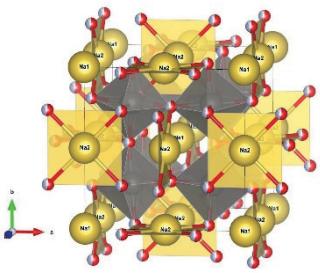


Fig.2 crystal structure of $NaWO_2N$

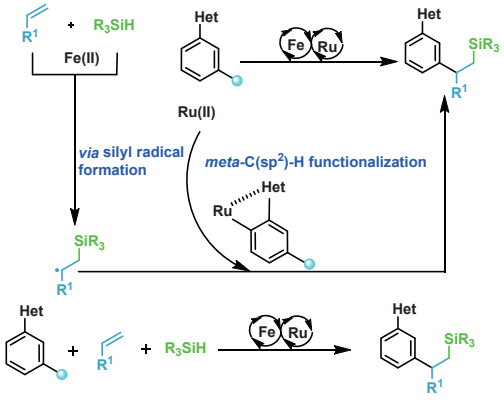
Photocatalytic C-H Silylation under visible-light enabled Fe-catalysis

Alakananda Hajra　Visva-Bharati University

ICR partner researcher’s name: Prof. Masaharu NAKAMURA

Objective: Development of C–H silylation using earth-abundant non-toxic Fe-catalysis under visible light photo-catalysis.

Visible-light photocatalysis has become an impressive tool in organic synthesis. In this realm, the merger of transition metal catalysis and visible light photoredox catalysis offers an exciting opportunity to perform the organic transformations in mild reaction conditions. Organosilicon compounds are very imporatnt due to their promising application in therapeutic agents, drug delivery, building blocks and so on. In this scenario, environment-friendly synthetic approach for silylation, such as visible-light-induced silylation is highly in demand at present days for molecule construction having C–Si bond. The accessibility of complex organosilicon derivatives by the carbosilylation of alkenes through the catalytic *meta*-C–H activation is going.



Presently we are focusing on the precise role of Fe-catalyst and visible light, and late stage modification of the compound. In addition, development of *m* C–H silylation is ongoing in our laboratory.

Outcome: Three papers are published supported by the International Collaborative Research Program of Institute for Chemical Research, Kyoto University (grant # 2025-13). Detailed mechanism studies are ongoing in our laboratories which will be published soon.

DOI: doi.org/10.1002/cptc.202500258; doi.org/10.1002/tcr.202500244 doi.org/10.1039/D5OB01878A

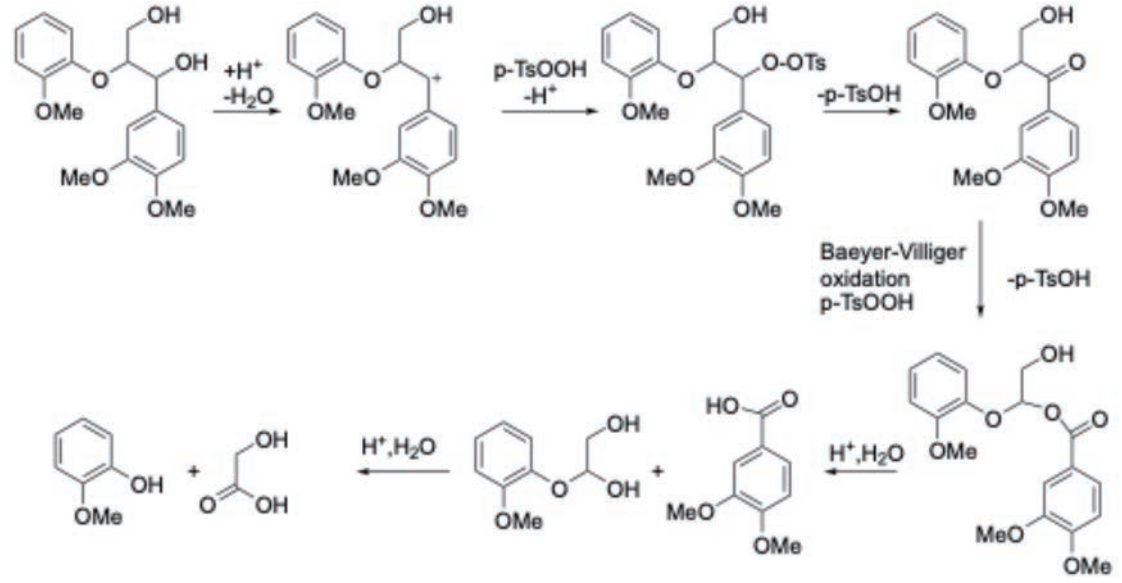
Computational Study on Lignin Degradation Reaction in Woody Plant Cell Walls

W. M. C. Sameera　Chalmers University of Technology

Objectives. We aim to investigate the mechanisms of lignin degradation in woody plant cell walls using quantum-chemical computations. Our preliminary experimental studies found that $(C_{12}H_{25})C_6H_4$-SO_2OOH can react with lignin interlinkages. Our initial attempt was to determine the quantitative mechanistic details of the reaction.

Methods. Density functional theory (DFT) computations were conducted using the ωB97X-D, def2-TZVP basis set, and implicit solvation.

Outcomes. To investigate the reaction mechanism, we employed a model system, $(CH_3)C_6H_4$–SO_2OOH, together with a representative lignin interlinkage. Various possible reaction pathways were explored, and based on the computed free-energy profiles, we identified a low-energy pathway, as shown in the diagram below. This mechanism follows a kinetically and thermodynamically favourable free-energy path for the reaction.



Publications: H. Malani, W. M. C. Sameera, M. Nakamura, et al. *Determination od of p-TsOH catalyzed β-O-4 cleavage mechanism of Lignin G-G dimer in wood biomass*. (In preparation)

Presentations: W. M. C. Sameera, *Cosmic Origins of Catalysis: Linking Molecular Evolution in Space to Sustainable Chemistry on Earth,* Institute for Chemical Research (Invited Lecture)

Development of Efficient Mixed Sn and Pb-based Perovskite Photovoltaics

Silver-Hamill Turren-Cruz　University of Valencia

Research Purpose and Achievements

This international collaborative research project successfully extended the joint study with Prof. Atsushi Wakamiya from the Institute for Chemical Research (ICR). The project addressed critical challenges related to carrier extraction and oxidation resistance in tin-based materials for high-performance tin–lead perovskite solar cells. The substitution of Sn2+ for Pb2+ in mixed perovskites, which typically leads to high defect densities due to Sn2+ oxidation to Sn4+ and accelerated crystallization, was effectively mitigated through targeted compositional and interface engineering strategies.

Through this work, we successfully improved the intrinsic quality, stability, and photovoltaic performance of mixed tin–lead perovskites, enabling their effective integration into single-junction and all-perovskite tandem photovoltaic technologies. The project built upon previous collaborative advances and demonstrated that rational cation engineering, combined with reducing agents and surface modifications, is an effective pathway toward stable, high-efficiency Sn–Pb perovskite solar cells.

The project was structured around several key research activities, with specific responsibilities assigned to collaborating groups:

Advanced bulky organic cations were successfully designed and synthesized in Prof. Turren-Cruz's group. A detailed understanding of structure–property relationships was achieved, enabling precise control over precursor solution behavior and thin-film crystallization. Dr. Pascual conducted comprehensive characterization of solution properties and crystallization dynamics, confirming their suitability for high-quality perovskite thin-film fabrication. Prof. Wakamiya's group at ICR designed and fabricated high-efficiency single-junction mixed tin–lead solar cells based on the newly developed compositions. Extensive morphological, chemical, and crystallographic analyses of the perovskite thin films were performed in collaboration with Prof. Sasamori at ICR using state-of-the-art facilities. Prof. Mora-Seró systematically evaluated device stability and photophysical properties. Finally, Dr. Hu in Prof. Snaith's group at the University of Oxford implemented the best-performing tin–lead devices in all-perovskite tandem solar cells. Tandem device fabrication and characterization confirmed performance surpassing previous benchmarks, demonstrating the successful achievement of the project objectives and advancing next-generation perovskite photovoltaic technologies.
This research advanced Sn-Pb perovskite solar cells with key achievements:

- Developed Sn-Pb single-junction cells over 18% efficiency.
- Created all-perovskite tandem cells over 23% efficiency.
- Gained insights into perovskite solution properties affecting crystallization.
- Introduced new molecular families for perovskites.
- Contributed significantly to photovoltaic science.

These results lay a foundation for future perovskite solar cell development, benefiting research groups and promoting innovations in sustainable energy.

Functionalization of Liver Organoids from Human Pluripotent Stem Cells by Using THz Waves

Kenichiro Kamei　New York University Abu Dhabi

Human pluripotent stem cell–derived liver organoids represent a promising in vitro platform for disease modeling, drug discovery, and toxicity testing. However, a major limitation of current liver organoid technologies is their insufficient functional maturation compared to adult human liver tissue. Most existing approaches to enhance organoid function rely heavily on biochemical cues such as growth factors and small molecules, which have shown limited success in fully recapitulating mature liver functions.

The objective of this joint research project was to establish a novel, non-invasive physical stimulation strategy using terahertz (THz) waves to promote the functional maturation of human ES/iPS cell–derived liver organoids. By combining advanced stem cell engineering with cutting-edge THz photonics developed at the Institute for Chemical Research (ICR), Kyoto University, this project aimed to (i) generate vascularized liver organoids, (ii) develop a THz-wave stimulation platform compatible with organoid culture, and (iii) elucidate the molecular mechanisms underlying THz-induced functional enhancement.

Experimental Methods

First, vascularized liver organoids were generated from human ES/iPS cells using recently established differentiation protocols in the Kamei laboratory. Hepatic progenitor cells, endothelial cells, and supporting mesenchymal cells were derived from a common pluripotent stem cell source and co-assembled to promote self-organized tissue architecture with integrated vascular-like networks.

Second, THz-wave stimulation conditions were optimized in collaboration with Assoc. Prof. Hideki Hirori (ICR, Nanophotonics Laboratory). Based on previously published THz pulse generation systems, stimulation parameters such as pulse energy, frequency range, and exposure duration were tuned to ensure effective cellular stimulation while avoiding thermal or phototoxic effects. Liver organoids were exposed to controlled THz pulses under sterile culture conditions.

Third, the biological effects of THz stimulation were evaluated using a combination of morphological, molecular, and functional analyses. These included immunohistochemical staining for hepatic maturation markers, transcriptomic profiling using single-cell RNA sequencing, chromatin accessibility analysis by single-cell ATAC-seq, and untargeted metabolomic analysis using mass spectrometry.

Experimental Results

Using a microfluidic organ-on-a-chip platform, we successfully generated functional vascularized liver organoids derived entirely from human ES/iPS cells. The microfluidic architecture enabled precise spatial organization of hepatic parenchymal cells and endothelial lineages, facilitating the self-assembly of perfusable vascular networks within the organoids. Continuous medium perfusion through the microchannels supported long-term culture stability and promoted endothelial maturation, which are difficult to achieve under conventional static culture conditions.

Immunohistochemical and morphological analyses confirmed the formation of interconnected endothelial networks expressing canonical vascular markers, closely associated with hepatocyte clusters exhibiting polarized tissue organization. Functionally, these vascularized liver organoids demonstrated enhanced hepatic characteristics, including improved expression of liver-specific markers and metabolic activity, indicating that microfluidic perfusion and vascular integration synergistically contribute to functional maturation.

A portion of this microfluidic vascularized liver organoid work has been peer-reviewed and published in *Cell Therapy & Engineering Connect*, validating the robustness and reproducibility of the platform. Building on this established system, the present joint research further investigated the application of THz-wave stimulation as an additional, non-invasive physical cue to enhance organoid functionality beyond what is achievable through microfluidic vascularization alone.

Following THz-wave exposure, vascularized liver organoids exhibited further improvements in functional readouts compared to non-stimulated controls, suggesting that THz stimulation acts cooperatively with microfluidic perfusion and vascular architecture. These results position microfluidic vascularized liver organoids as a highly suitable and physiologically relevant model for investigating THz-mediated functional enhancement mechanisms.

[1] K. Yoshimoto, R. Okaichi, K. Iida, S. Terada, K. Kamei* “High-Purity Production of Endothelial Cells from Human Pluripotent Stem Cells” *Cell Ther. Eng. Connect*, 1, 2025.0006 (2025); DOI: 10.69709/CTEC.2025.154455

Spin-wave excitation of van der Waals magnetic semiconductors by intense terahertz magnetic field pulses

Taketo Handa　Columbia University

The van der Waals 2D material, CrSBr, is both an A-type antiferromagnet and a direct gap semiconductor, with bandgap in the near-infrared region. The presence of both properties has led to the discovery of strong coupling of electronic properties to magnetic order, including the coupling of coherent magnons at sub-meV energies to excitons in the eV range. This has major technological implications, e.g., optical control and access to coherent magnons and quantum transduction across four orders of magnitude in energy. The novel experimental technique using strong THz magnetic field may enable unprecedented excitation and control of coherent magnons through time varying magnetic torque, while the subsequent dynamics can be conveniently probed optically in this system. With the tesla-class THz field, magnetic order transitions of CrSBr are expected to be induced, where intriguing interplay between nonequilibrium magnetic order and excitonic excitation are expected. By widely varying the strength of the driving field, we explore to establish a complete view of spin-wave dynamics from the perturbation-dominant to nonequilibrium regimes, allowing the quantitative determination of magnon nonlinearity essential to applications in wave-based computing and quantum interconnects.

In our experiment, we fabricated a spiral-shaped antenna resonator on a quartz substrate at Kyoto, using the shared facility of electron-beam lithography. Upon THz irradiation, a THz current is induced that generates a strong THz magnetic near-field at the center of the spiral [1,2,3]. We shipped the substrate to Columbia, transferred a thin flake of CrSBr onto the spiral, then sent it back to Kyoto for THz experiments. We observed that upon irradiation with the THz pulse, the visible reflection increased immediately and did not decay over hundreds of picoseconds. In contrast to the previous study, where the magnetization response is only observable around the excitonic energy [4], the reflection change in our experiment slowly varies as the photon energy of the probe pulse is tuned over this energy range. This may suggest metastable order [5]. After several measurements, we found that the antenna had burned, likely due to Joule heating. We plan to fabricate antenna resonators of various shapes to decompose the contributions of the THz magnetic and electric near-fields to the reflection signal. In the meantime, the stacking machine at Columbia has been malfunctioning. It will be recovered soon, and we will perform additional measurements on newly fabricated samples.

[1] Z. Zhang et al., Nat. Commun. 14, 1795 (2023); [2] K. Maruyama et al., APEX 17, 022004 (2024); [3] Z. Zhang et al., Nat. Mater. 24, 219‑225 (2025); [4] Y. J. Bae et al., Nature 609, 282-286 (2022); [5] B. Ilyas, et al., Nature 636, 609‑614 (2024).

電子移動制御を利用したナノ金属クラスター触媒の高活性化

近藤美欧　東京科学大学

［背景と目的］

持続可能な社会の構築に向け、温室効果ガスである二酸化炭素（CO_2）の削減と資源化を両立させた「カーボンニュートラル」な循環体系が求められている。電気化学的還元によってCO_2を炭化水素などの有用な化学種へと変換するプロセスは、その実現を支える有力な手段となる。本研究では、高い多電子移動能を持つナノ金属クラスターに対して、電荷伝達サイトを導入した電極触媒材料を創製し、電気エネルギーを介した CO_2 から炭化水素への直接変換プロセスを高度化し、高効率な物質変換を達成しようと検討を進めている（図 1）。

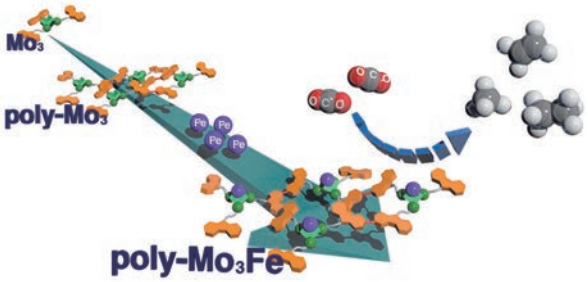


図 1. 本研究の概要図. 配位子の重合によりクラスターを集積した電極触媒材料（poly-Mo_3 ならびに poly-Mo_3Fe）を創製し, 高効率な CO_2 還元反応を目指す.

［研究成果］

昨年度までの成果を踏まえ、本年度は新たに電気化学的重合部位としてカルバゾール、クラスターへの配位部位としてテトラメチルシクロペンタジエニル基を有する配位子（HCp-Cz）を新たに設計・合成した（図 2）。

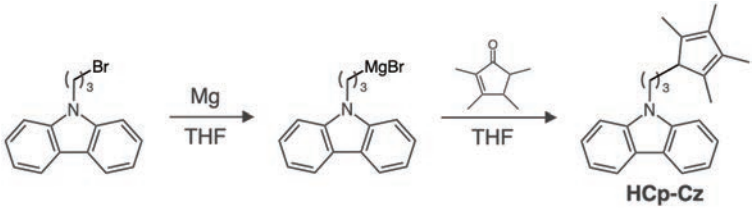


図 2. 本研究で設計した配位子の簡略化した合成スキーム.

得られた配位子を出発に、まず単核 Mo 錯体[(Cp-Cz)$MoCl_4$]（Cp-Cz: HCp-Cz の脱プロトン化体）を合成し、続くクラスター化反応により、Cp-Cz 配位子を Mo 上に有する[Mo_3S_4]クラスターへと誘導した。得られた化合物は、質量分析によりその化合物組成を確認し、^{1}H NMR スペクトルにおいても想定されるクラスター構造と矛盾しないシグナルを与えた。現在、さらに結晶化と X 線結晶構造解析による分子構造の決定を試みているところである。

得られた化合物の電気化学特性を評価するため、サイクリックボルタンメトリー測定を行ったところ、酸化側への掃引を繰り返すごとにカルバゾール部位の酸化に由来する電流値の上昇が観測され、狙い通り電極表面において重合部位間の結合形成が進行することが示唆された。また、ITO 電極を用いて同様の実験を行った場合には、複数回の掃引終了後に着色が見られ、その紫外可視吸収スペクトルは[Mo_3S_4]クラスターに特徴的な極大吸収波長を示した。以上の結果から、Cp-Cz を有する[Mo_3S_4]クラスターの電解重合による電極への担持が示唆される。今後は、得られた材料の同定を進めるとともに、電極触媒として CO_2 還元反応に対する活性評価を検討予定である。

Development of Novel Planar-Chiral Ferrocenylphosphine Ligands Based on the Restricted Cp-Fe-Cp Rotation: Phase 2

Masamichi Ogasawara　Tokushima University

During the last couple of years, we have been pursuing to "asymmetrize" DPPF (1,1'-bis(diphenylphosphino)ferrocene), a widely used anchillary achiral bidentate phosphine ligand [1], by restricting the rotation at the Cp-Fe-Cp axis. A set of DPPF derivatives **1a** and **2a** were prepared through the last year's collaboration in enantiomerically pure forms (Figure 1). Although ligands **1a** and **2a** demonstrated promising performance in the rhodium-catalyzed asymmetric hydrogenation of dehydroamino acids, there is still room for further improvement. This year, we modified **1a** and **2a** by introducing the bulky aryl groups DTBM, 3,5-di(*tert*-butyl)-4-methoxyphenyl, in place of phenyl groups in the diphenylphosphino moieties in **1a** and **2a**. The newly designed planar-chiral DPPF derivatives **1b** and **2b** were prepared as racemates. The enatiomeric resolution of the corresponding oxides was realized by the preparative chiral HPLC resolution, and following reduction provided **1b** and **2b** in enantiomerically pure forms (Scheme 1).

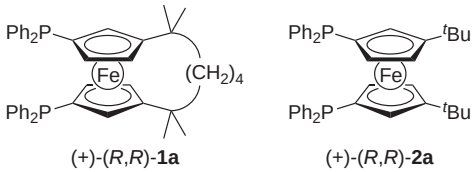
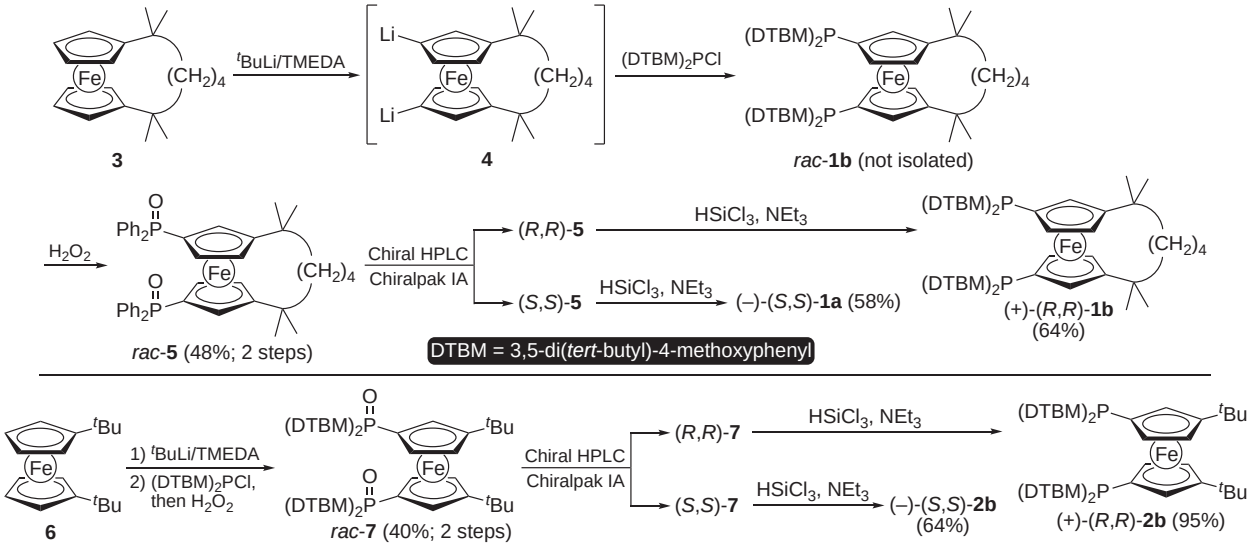


Figure 1. Chiral DPPF derivatives with -PPh_2 substituents.



Scheme 1. Preparation of chiral DPPF derivatives with -$P(DTBM)_2$ substituents.

The X-ray crystal structure analysis of PdC_2[(+)-**1b**] determined the absolute configuration of dextrorotatory **1b** to be (*R*,*R*) as depicted in Figure 2.

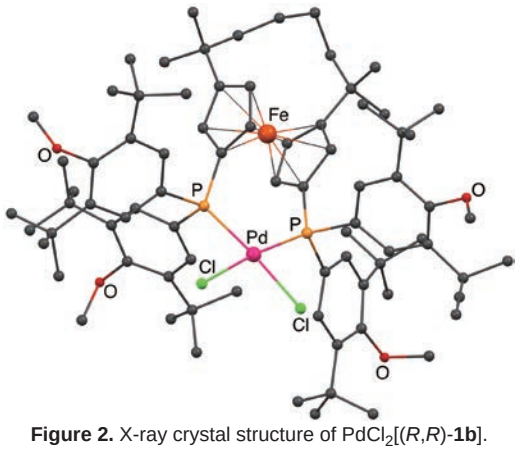
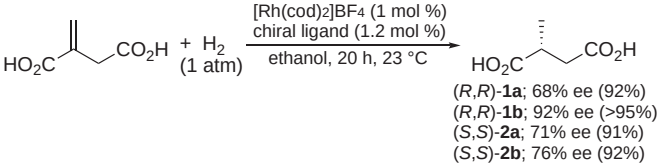


Figure 2. X-ray crystal structure of $PdCl_2$[(*R*,*R*)-**1b**].

Chiral DPPF derivatives were examined in the rhodium-catalyzed asymmetric hydrogenation of prochiral olefins. Representative results on the hydrogenation of itaconic acid are shown in Scheme 2. As we expected, introduction of DTBM substituents improved the performance of the chiral ligands. While Rh/(*R*,*R*)-**1a** afforded (*R*)-methylsuccinic acid in 68% ee and 92% yield, Rh/(*R*,*R*)-**1b** provided the hydrogenation product in 92% ee quantitatively under the identical conditions. Likewise, the enantioselectivity of 71% ee using (*S*,*S*)-**2a** was improved to 76% ee by the use of (*S*,*S*)-**2b**. Additional applications of these ligands will be studied in due course.



Scheme 2. Rh-catalyzed asymmetric hydrogenation of itaconic acid.

References.

[1] Gan, K.-S.; Hor, T. S. A. In *Ferrocenes*; Togni, A.; Hayashi, T., Eds.; VCH: Weinheim, **1995**; Chap. 1, p. 3.

六方晶フェライトの磁気異方性を制御による広帯域ミリ波用電波吸収体の開発

藤井達生　岡山大学

研究目的　近年、無線通信機器やセンシングの分野でミリ波の利用が急速に進行しており、その普及に伴い、高性能なミリ波用電波吸収体の開発が強く求められている。そこで本研究では、遷移金金属酸化物の合成や機能性探索に大きな実績がある先端無機固体化学研究室と協力し、安価で広帯域かつ無指向性のミリ波吸収体となり得る材料を設計、探索する。そのための第一歩として、安価な酸化鉄系材料に注目し、その中でも高い自然共鳴周波数を持った六方晶フェライトを活用した高性能なミリ波電波吸収体の実現を目指した。

実験方法　六方晶フェライトに巨大な磁気異方性を付与する手法として、粒子の形状異方性に注目し、針状や板状など様々な粒子形状を有する六方晶フェライト粒子を合成することを試みた。粒子形状の制御は、原料となる酸化鉄粒子の形状を制御することで行い、Na_2CO_3 塩フラックス中で $BaCO_3$ と反応させることで、目的とする形状の Ba フェライト粒子を得た。合成した粒子は、XRD による結晶相の同定や SEM による粒子形態の観察を行ったのち、SQUID 磁束計により異方性磁界を評価し、くわえて透過法によりミリ波吸収スペクトルを測定した。

結果および考察　原料となる酸化鉄粒子の形状によらず、いずれの場合も単相の Ba フェライトが生成した。しかし球状 α-Fe_2O_3粒子を出発としたフェライトの XRD パターンは、針状 α-Fe_2O_3粒子を出発としたものと比較して (00*l*) のピーク強度が大きくなっていた。そこで各試料の粒子形状を SEM 観察したところ(Fig. 1)、前者は六角板状、後者は柱状の粒子形状を保持していた。しかし柱状の Ba フェライト粒子は出発原料の α-Fe_2O_3と比較して、粒子サイズが著しく成長していた。次に、粒子形状が異方性磁界に与える影響を検証するため、両者の困難磁化方向の磁化曲線を二階微分し SPD 法により異方性磁界を算出したところ(Fig. 2)、それぞれ 16.0 kOe と 16.2 kOe となった。すなわち柱状粒子化することで、フェライトの異方性磁界をわずかではあるが変化させることができたと考えられる。くわえてミリ波吸収スペクトルから求めた共鳴周波数も 45GHz 付近から 46GHz 付近へと、高周波側へのシフトが観察された。

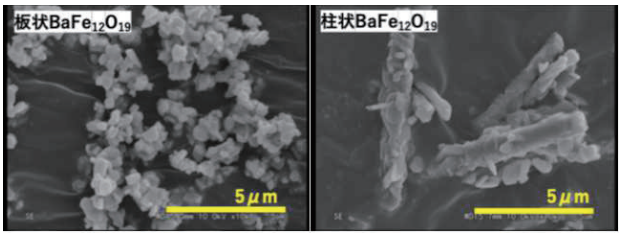


Fig.1 合成した Ba フェライト粒子の SEM 像

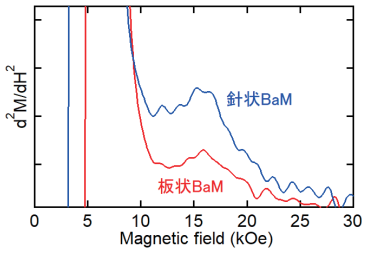


Fig.2 困難磁化方向の磁化曲線の 2 階微分

学会発表

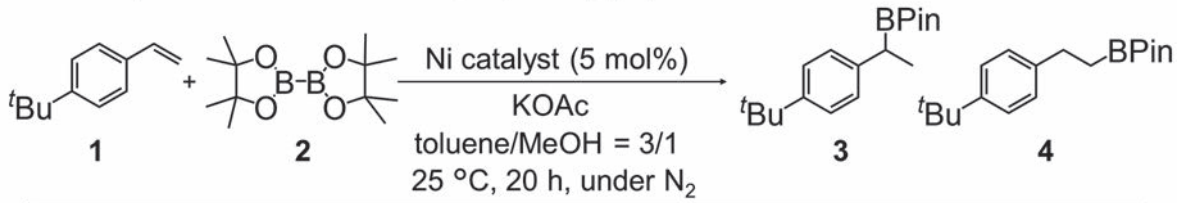
・峯川柚希，西岡栞平，狩野旬，藤井達生，柱状α-Fe_2O_3 を原料とする M 型フェライト粒子の合成，粉体粉末冶金協会 2025 年度秋季大会, 1-25A, 2025.10.28。

Development of nickel cluster catalysts for highly selective functionalization

Ayako TAKETOSHI　Yokohama National University

Hydroboration of alkenes gives useful alkylboranes as synthetic intermediates. Although numerous transition metal catalysts have been developed, Markovnikov selective hydroboration of alkenes is a more challenging reaction than the anti-Markovnikov selective one. We found that nickel(II) salts such as nickel acetate and nickel chloride efficiently catalyzed the hydroboration of 4-*tert*-butylstyrene (**1**) with a diboron reagent, bis(pinacolato)diboron (**2**), affording a Markovnikov (branched) adduct **3** with excellent selectivity (Table 1, entries 1-3). In contrast, a nickel(II) complex, $Ni(acac)_2{\cdot}nH_2O$, showed significantly lower catalytic activity, whereas a nickel(0) complex, Ni(COD)(DQ) (COD=1,5-cyclooctadiene, DQ=duroquinone), was highly active, as well as nickel(II) salts (entries 4 and 5). It is thought that nickel(0) species, such as nickel clusters, were generated from nickel(II) salts during the reaction and worked as a catalyst.

Table 1. Hydroboration of 4-*tert*-butylstyrene (**1**) by nickel salts[a]



1　**2**　**3**　**4**

Entry	Catalyst	Conv. of **1** / %[b]	Yield / %[c]	
			3	**4**
1	$Ni(OAc)_2{\cdot}4H_2O$	100	91	1
2	$NiCl_2$	100	99	0
3	$Ni(NO_3)_2{\cdot}6H_2O$	100	99	0
4	$Ni(acac)_2{\cdot}nH_2O$	26	24	0
5	Ni(COD)(DQ)	100	99	1

[a]Reaction conditions: **1** (0.5 mmol), **2** (1.0 mmol), KOAc (0.75 mmol), catalyst (0.025 mmol), toluene (3 mL), MeOH (1 mL), 25 °C, 20 h under N_2. [b]Determined by GC using undecane as an internal standard. [c]Determined by ^{1}H NMR using 1,1,2,2-tetrachloroethane as an internal standard.

Academic Meeting (domestic)

1. Poster: Markovnikov-selective hydroboration of styrenes catalyzed by commercially available nickel salts
   Yusei Kimura, Ayako Taketoshi, Yoshitaka Yamaguchi
   2025 Summer Symposium of the Japanese Society for Process Chemistry, 2P-42, Tower Hall Funabori (July, 2025)
2. Oral: Markovnikov-selective hydroboration of styrenes catalyzed by nickel salts
   Yusei Kimura, Ayako Taketoshi, Yoshitaka Yamaguchi
   88th Symposium of the Society of Synthetic Organic Chemistry, Japan (Kanto branch), B19, Kogakuin University (May, 2025)

Original Paper

1. Defective NiO Nanoparticles Supported on Nb_2O_5 for Solid-Catalyzed Markovnikov-Selective Hydroboration of Styrenes
   Ayako Taketoshi, Yusei Kimura, Eiji Hirano, Norihito Sakaguchi, Tamao Ishida, Toru Murayama, Yoshitaka Yamaguchi, *Eur. J. Org. Chem.* **2025**, e202500824. DOI: 10.1002/ejoc.202500824

Spin control by high-power THz pulse in orthoferrite

Hiroshi Watanabe　Osaka University

In this collaborative project, we investigated the control of large-amplitude spin dynamics in the orthoferrite $Sm_{0.7}Er_{0.3}FeO_3$ using intense terahertz (THz) pulses and cavity effects. Orthoferrites are canted antiferromagnets with resonance frequencies significantly higher than those of conventional ferromagnets, making them attractive materials for ultrafast spintronic applications. In addition, their spin-reorientation transitions provide a platform for enhancing magnetic responses near phase transition points. Building on previous studies demonstrating long-lived spin precession and THz-driven spin control in orthoferrites, this project focused on achieving controllable excitation of spin modes through structural and electromagnetic tuning.

Single crystals of $Sm_{0.7}Er_{0.3}FeO_3$ with thicknesses of 100 μm and 50 μm were prepared to examine thickness-dependent cavity effects. Metallic microstructures were fabricated on the crystal surfaces to enhance the local THz magnetic field via near-field effects. By irradiating the samples with intense THz pulses with peak electric fields up to 1.2 MV/cm, large-amplitude spin oscillations were excited, particularly near the spin-reorientation transition temperature where nonlinear magnetic responses are strongly enhanced.

Systematic measurements revealed that the excitation efficiency and frequency of the spin oscillations depend sensitively on sample thickness, indicating that cavity effects modify the effective resonance condition. The coupling between the intrinsic magnon modes of $Sm_{0.7}Er_{0.3}FeO_3$ and the resonant modes of the metallic microstructures plays a key role in determining the amplitude and spectral content of the excited spin dynamics. These findings demonstrate that macroscopic magnetic states can be manipulated by tailoring both sample geometry and electromagnetic boundary conditions under strong-field excitation.

The results provide important insight into nonequilibrium spin dynamics in antiferromagnets and establish a strategy for controlling ultrafast magnetic responses using intense THz fields. Such control of long-lived spin precession and nonlinear spin oscillations is expected to contribute to the development of high-speed spintronic devices and to deepen the understanding of enhanced magnetic responses near phase transitions.

Investigation on microscopic mechanism of light-induced anomalous Hall effects

Shunsuke Sato　Tohoku University

Quantum control of electronic transport using light is one of the central challenges in modern condensed matter physics. In particular, the realization and control of the light-induced anomalous Hall effect provide a promising route toward optically tunable electronic functionality. While Floquet engineering has been widely discussed since the theoretical prediction of light-induced anomalous Hall states in graphene, recent theoretical and experimental studies suggest that multiple microscopic mechanisms, such as geometric phase effects and light-carrier effects, may compete or coexist in driven systems. A comprehensive understanding of these mechanisms remains incomplete.

This project aims to clarify the microscopic origin of the light-induced anomalous Hall effect through an integrated theoretical and experimental approach. On the theoretical side, calculations were performed for driven graphene systems using a quantum master equation framework that incorporates dissipation and relaxation effects. We focused on the excitation-frequency dependence of the light-induced anomalous Hall conductivity, especially in the low-frequency regime, where scaling behavior provides crucial information about the dominant microscopic processes. These analyses extend previous theoretical proposals of the photo-carrier mechanism and provide a more realistic description of nonequilibrium steady states in driven solids.

In parallel with these theoretical studies, collaborative discussions and numerical modeling were carried out in connection with terahertz (THz) emission experiments on magnetic metamaterials. Optical generation of spin currents is of particular interest for ultrafast spintronics due to its intrinsic speed and spatial selectivity. Experiments were performed on patterned Co/Pt multilayer structures with broken spatial inversion symmetry and out-of-plane magnetization. By varying the relative angle between the incident laser polarization and the structural symmetry axis, THz emission signals were measured and analyzed. The observed angular dependence and magnetization reversal behavior indicate that both structural inversion symmetry breaking and time-reversal symmetry breaking contribute to spin-current generation.

Finite-difference time-domain (FDTD) simulations revealed that even linearly polarized incident light can induce circularly polarized near-field components around structural edges. Incorporating these near-field components into a theoretical model successfully reproduced the experimentally observed angular dependence of the photocurrent and spin current. The results suggest that linear and circular polarization components in the near field act through magneto-galvanic effects in inversion-asymmetric electronic systems, governing the light-induced spin-current generation in magnetic metamaterials.

Through this combined theoretical and experimental effort, the project advances the understanding of light-driven transport phenomena and establishes a framework for controlling charge and spin currents via optical excitation. These findings contribute to the development of next-generation optoelectronic and spintronic technologies based on nonequilibrium quantum states.

High-harmonic generation in magnonic systems with topological edge states

Hideaki Obuse　Hokkaido University

Quantum information science has advanced rapidly in recent years; however, existing qubits remain highly sensitive to environmental noise and decoherence, limiting scalability and fault-tolerant operation. Magnons—the quantized excitations of spin waves in magnetic materials—have attracted attention as potentially robust quantum states due to their relatively weak coupling to thermal environments and the possibility of room-temperature operation. Beyond quantum computation, magnons also offer prospects for low-power spintronic devices, connecting quantum and classical information technologies.

In photonic quantum technologies, nonlinear optical processes such as parametric down-conversion and four-wave mixing enable photon-pair generation and entangled states. By analogy, magnon-pair generation through nonlinear magnetic responses to a single intense external magnetic field could provide single-magnon sources and entangled magnon states for quantum information applications. Such an approach offers a conceptually simple and potentially scalable alternative to complex hybrid quantum architectures. Although hybrid magnon systems have been studied extensively, nonlinear pair generation driven directly by a strong field remains largely unexplored both theoretically and experimentally.

This project establishes a theoretical framework for magnon-pair generation and explores nonlinear magnetic responses in antiferromagnets using intense terahertz (THz) magnetic-field techniques. Theoretical analysis of one-dimensional antiferromagnetic spin chains with anisotropic exchange revealed topological edge states via the Holstein–Primakoff transformation and clarified their connection to electronic topological models known as the Su-Schrieffer-Heeger (SSH) model. The interplay between topology, symmetry, and nonlinear response functions was further examined, demonstrating enhanced higher-order effects associated with oscillating dynamics between two edge states beyond the rotation-wave approximation.

Experimentally, intense THz magnetic fields were generated using spiral resonators with antennas, and magneto-optical sampling on terbium–gallium–garnet confirmed pulsed magnetic fields up to 0.96 T. These experimentally validated strong-field conditions provide a quantitative basis for accessing nonlinear magnetic regimes relevant to magnon-pair generation. Together, the theoretical insights and experimental capabilities open new directions toward magnon-based quantum information science, ultrafast coherent spin control, and future functional quantum and spintronic device applications.

Integrating Omics Data and Module-based Network with Deep Learning to Develop Cancer Type Predictive Models

Jinn-Moon Yang　National Yang Ming Chiao Tung University

Objective. In biomedicine and bioinformatics, classification and prediction of cancer subtypes have been an important research topic. Indeed, various machine learning methods have been developed for that purpose. However, many existing studies focus on specific cancer types, and thus it is needed to explore mechanisms across multiple cancer types. To this end, it is crucial to analyze the topology of biological networks, biochemical progress in cells, interactions among cells, and structural information of relevant proteins. Therefore, it is important to develop integrated analysis methods for omics data and multiple types of biological networks. Although various studies have been done, currently available approaches are not yet satisfactory.

In this project, we will continue our collaboration to extend our previous approach (Lin et al.: J. Bioinform. Comput. Biol.,17:1940005, 2019) to include other kinds of omics data, such as genetic and metabolic networks as well as PPIs (protein-protein interactions) and protein structures. To this end, we plan to extend and combine our deep learning-based methods (Wang et al.:Scientific Reports, 12:229, 2022) and our dense subgraph-based methods (Li et al.: BMC Bioinformatics, 23:431, 2022). Furthermore, we plan to apply matrix factorization framework to integrate multiple types of omics data and to use large language models (LLMs) to obtain feature vectors from protein sequence and structure data.

Results. To capture an overview of LLM methods for analyzing protein sequence and structure data, one graduate student in ICR performed a survey on these LLMs. Another graduate student in ICR also examined the possibility of application of matrix factorization to analysis of omics data. However, it is found that we need much more time and effort to make effective use of such technologies.

To closely discuss extension of our previous approaches with introducing recent AI technologies including generative adversarial networks, LLMs, and autoencoders, one Ph.D student and one research assistant of Prof. Yang’s Laboratory will visit Prof. Akutsu’s Laboratory for about two weeks in February-March, 2026. We hope that this visit will lead to fruitful discussions and contribute greatly to the progress of research.

Developing machine learning approaches for prediction of protein stability changes upon missense mutations

Jiangning Song　Monash University

Objective. It is significantly important to predict the stability of a protein against mutations because it is known that even a single missense mutation of an amino acid can change its structure and stability, and missense mutations can be harmful to the health and disease-related by causing changes in the stability of a protein. Accordingly, accurate estimation of protein stability change (ΔΔG) measured as Gibb's free energy change is critically important, and thus many methods have been developed to date. However, the resulting accuracy of such methods is not yet satisfactory. Therefore, we have been developing novel machine learning methods to address this problem, by combining state-of-the-art machine learning techniques and various types of informative protein sequence and structural features. Our team has successfully developed various methods/tools for analyzing protein sequence data, which include PROSPER, iLearn, iProt-Sub, Cascleave, and PROSPERous. The main purpose of this project is to continue and extend our development for prediction of protein stability change.

Results. We developed SFMNet, a powerful deep learning model for prediction of protein stability change, constructed with graph neural networks-based multiway feature extractors and a new context-aware selective fusion module that jointly leverages the sequence, structural, and evolutionary information [1]. This novel neural network architecture enables SFM-Net to effectively and selectively use features from different sources to facilitate binding affinity change prediction. We also conducted benchmarking experiments and targeted ablation studies. The results illustrate the effectiveness and robustness of our method for improving the binding affinity change prediction. Furthermore, we have made the code publicly available via: https://github.com/LIU-CT/SFM-Net.

Publication

[1] C. Liu, S. Cai, T. Pan, H. Ogata, J. Song, T. Akutsu: SFM-Net: selective fusion of multiway protein feature network for predicting binding affinity changes upon mutations. *Journal of Chemical Information and Modeling*, 65(7):3854−3865, 2025.

Marine giant viruses functional profiling

Eric Pelletier　CEA/Genoscope

In order to build from recent research from the two cooperating labs involved in this project (i.e. expertise in host-giant viruses interactions on ICR side and expertise in metabolic modelling of unicellular eukaryotes on CEA/Genoscope side), we explored the feasibility of modelling the impact of viral genes on host metabolism, and the various approaches to improve this modelling, making use of the various existing resources in each team.

The main axis is to expand the metabolic modelling system recently developed for unicellular eukaryotes [Burel et al., 2025] to achieve a good representation of giant viruses metabolic genes, and to ensure a correct modelling of their impact on the virocell. First attempt was conducted based on the *Phaeocystis globosa* model (host alone and host & 14T virus) as well as a candidate host-virus pair identified within *Tara* Ocean genomic data. In both cases, adding viral genes to the global set of genes of the virocell resulted in more reactions and more metabolites included in the model, and modifications of the predicted fluxes of metabolites within the system. The set of added reactions agrees with what is expected (modification of dNTP pools and lipids metabolisms). These encouraging preliminary results led us to set up a plan for better inclusion of giant virus biological activities in the PhotoEukStein (PES) system. We explored methods to achieve a good representation of viral metabolic genes in the PES model, based on better KO assignation and inclusion of viral genes into the reference PES protein database. A second step will require remote homology identification of viral metabolic genes candidates and addition of the corresponding reactions into PES. A working plan for these two developments have been defined and will be implemented in the next months through collaboration between the two partners.

Aside from this main axis, contact was taken between Dr Pelletier and Dr Tamura (in ICR), to develop the usage of PES-derived metabolic model for *Phaeodactylum tricornutum*, a common model microalga, to explore metabolic optimization of this host to favor specific metabolites production in a biotechnological approach. No doubt that further collaboration between the two teams will happen in the near future.

Burel, M. et al. (2024) ‘Towards an omics-based definition of unicellular eukaryote phototrophs functional traits via metabolic modelling’. bioRxiv, p. 2023.05.22.541783. Available at: https://doi.org/10.1101/2023.05.22.541783.

Dynamics of marine plankton cell lysis as revealed by field observation and mathematical modeling

David Demory　CNRS

Objectives

Protists and viruses are essential components of the microbial community and play important roles in the ecosystem and biogeochemical processes in the ocean. However, the effects of viruses on lytic cell mortality of the eukaryotic community are not well-investigated due to the lack of detection methods with sufficient sensitivity and taxonomic resolution. This study aims to combine global-scale metagenomic data and mathematical modeling to refine the dynamics of marine plankton and virus communities. We also generated a new dataset to quantify plankton cell lysis at the molecular taxonomic level.

Methods

I generated epidemiological models to predict the global distribution of marine phytoplankton *Micromonas* based on their thermal responses. Abundance profiles of marine *Micromonas* generated by Dr. Endo (ICR partner researcher) were used to test the performance of my mathematical models.

Aside from this analysis, I recently collected RNA samples from the Atlantic Ocean to evaluate taxon-specific cell lysis of microeukaryotes. For these samples, Dr. Endo performed extractions and sequencing of cellular and cell-free ribosomes derived from the microeukaryotes.

Results

The mathematical model successfully predicted the actual presence/absence patterns of *Micromonas* clades. We published these results in an international journal in 2025.

As for the Arctic Ocean sample project, I received good-quality sequencing data, and the bioinformatics analysis is ongoing. Dr. Endo and I will continue to collaborate to clarify the dynamics of marine plankton and viruses based on meta-omics and modeling approaches.

Publications

- Demory D, Endo H, Baudoux A-C, Bigeard E, Grimsley N, Simon N, Ogata H, Weitz JS. Temperature-driven biogeography of marine giant viruses infecting the picoeukaryote Micromonas. *ISME Commun*. 5(1), ycaf137 (2025)

A Study on Optimal Transport for Learning with Graph Structured Data

DAI HAI NGUYEN　Hokkaido University

Objectives

This project addresses multi-objective optimization over spaces of probability measures, motivated by applications in graph learning and chemistry, such as chemical compound generation, where multiple chemical properties must be optimized simultaneously. We aim to leverage Wasserstein geometry and tools from optimal transport theory to develop principled and scalable methods for multi-objective distributional optimization.

Theory and Method

We proposed Multi-objective Wasserstein Gradient Descent (MWGraD), a gradient-based algorithm for jointly optimizing multiple objective functionals over probability distributions. A key challenge in this setting is gradient conflict, where objectives with large gradients dominate the update direction, and hinder the progress on other objectives. MWGraD resolves this by aggregating Wasserstein gradients using dynamically adjusted weights obtained by minimizing the norm of the combined gradient, yielding a probability flow that balances all objectives.

Outcomes

We achieved both theoretical and empirical results. Theoretically, we established convergence guarantees for MWGraD under approximate gradient computation, characterizing both the ideal convergence rate and the impact of gradient approximation errors. Empirically, we evaluated MWGraD on multi-task learning problems using real-world datasets, showing that MWGraD consistently outperforms competing methods, demonstrating its effectiveness in practice.

Publications and Oral Presentation

D. H. Nguyen, A. Nakamura and H. Mamitsuka, Multiple Wasserstein Gradient Descent Algorithm for multi-objective Distributional Optimization. Proceedings of the 41st Conference on Uncertainty in Artificial Intelligence (**UAI 2025**) (Proceedings of Machine Learning Research (PLMR), 286), 3182-3199 (2025).

遺伝子破壊株における発現量データとシミュレーション結果の比較解析

高坂智之　山口大学

目的

化学量論とゲノムスケール代謝モデルを基にして行う代謝シミュレーションであるフラックスバランス解析は、微生物の定常状態における代謝予測に優れており、微生物に物質生産を行わせる上で有用な分析方法となってきている。しかし、遺伝子破壊による代謝物量調節の予測は時に実態と合致せず、任意には代謝ネットワークを改変することはできない。これは、細胞内では全ての代謝ネットワークが利用されていないこと、および、代謝経路の太さが加味されないことによるものと推察される。本研究では、遺伝子破壊により微生物細胞内で実際に利用される代謝ネットワークを予測するために、網羅的転写解析である RNA-seq による発現量データをフラックスバランス解析によるシミュレーション結果と比較検討する。これにより、遺伝子破壊株のフラックスバランス解析結果と実際の細胞による結果の差が、どのような理由で生じているか理解を深める。

実験方法

解析の材料にはモデル微生物である大腸菌を用いた。これまでの解析により、大腸菌は高温条件ではグルコースから乳酸を生成しており、この乳酸生成への乳酸脱水素酵素（Lactate dehydrogenase: LDH）の関与が明らかとなったため、この遺伝子を破壊することにした。それらの大腸菌株を最小培地である M9 培地に 1%グルコースを添加して好気的に培養し、RNA を抽出して発現遺伝子の網羅的解析を行うとともに、転写量データの分析を行なった。一方、フラックスバランス解析には大腸菌のゲノムスケール代謝モデルである iML1515 を用い、最小培地条件における定常状態での代謝予測を行った。

実験結果

大腸菌 BW25113 とその乳酸脱水素酵素破壊株（Δ*ldhA*）を培養したところ、最終到達濁度は BW25113 より Δ*ldhA* の方が高かったが、生育速度は Δ*ldhA* の方が低いことが明らかとなった。この影響を分析するために、37℃および 44℃での網羅的転写解析を行ったところ、*ldhA* の破壊によって糖の取り込みとアミノ酸であるメチオニンの生合成が低下し、べん毛の生合成が増加することが推察された。高温条件でもべん毛の生合成は増加しており、生育速度の低下に影響した可能性が示唆された。なお、生育速度は 37℃よりも 44℃の方が向上する傾向が見られたことから、*ldhA* 破壊は高温での生育に影響を与えるものではないことが示唆された。一方、*ldhA* の破壊がアミノ酸生合成に与える影響を分析するために、フラックスバランス解析に転写量データを組み合わせる解析の検討を継続している。

考察

大腸菌におけるアミノ酸生合成はタンパク質合成に直接関係しており、結果的に生育速度に影響することから、代謝におけるアミノ酸代謝の重要性を得られた転写量データより見出すことができつつある。また、代謝関連遺伝子の破壊は直接関与する経路だけでなく全体の代謝、特にアミノ酸の生合成に影響することが示唆された。そのため、アミノ酸生合成経路と中央代謝経路の関係性の分析を代謝シミュレーションによって可能にすることが今後の課題であると考えられる。

成果報告（論文、学会発表等）

2025/9/12 第 77 回 日本生物工学会（広島）「大腸菌での高温グルコース代謝に関与する転写制御因子の分析とその応用」Analysis and application of transcriptional regulators involved in high-temperature glucose metabolism in *Escherichia coli*（高坂 智之, 田中 樹里, 田村 武幸）

Control and Analysis of Complex Networks via Probabilistic Minimum Dominating Sets

Jose Nacher　Toho University

Objective. It is important for understanding the mechanism of living organisms to analyze biological networks formed by various types of molecules (e.g., proteins, chemical compounds, DNAs). To this end, we have been conducting studies on controllability of various types of biological networks. A key challenge in network control is dealing with edge failures and uncertainties in molecular interactions, especially in directed probabilistic networks. Accordingly, we proposed the concept of the probabilistic minimum dominating set (PMDS), by extending the minimum dominating set (MDS) in graph theory. We also developed a method for classifying the nodes into three categories (critical, intermittent, and redundant) based on PMDS. However, the method could not handle large-scale biological networks. To address this issue, we will develop faster methods using several heuristics.

Results. We developed a novel method for classifying the nodes into three categories based on PMDS. To efficiently identify control categories, we use a preprocessing step based on four mathematical propositions that capture a large fraction of control nodes, and then the remaining nodes are identified using an integer linear programming (ILP)-based algorithm. The method was applied to analysis of a human intracellular signal transduction network and the results suggest that critical control nodes are associated with key biological features and perturbed gene sets, including SARS-CoV-2 targets, Type 1 Diabetes Mellitus, and rare diseases like cytokine receptor deficiency [1]. In addition, we developed a preliminary version of the method for identifying critical nodes in undirected networks based on the maximum matching framework [2].

Presentations

[1] J. C. Nacher, Y. Tokuhara, J-M. Schwartz, T. Akutsu: Efficient identification of critical control nodes in probabilistic directed networks and their associations with disease genes, International School and Conference on Network Science 2025 (NetSci 2025), 2025.

[2] H. Nozaki, K. Tsuchiya, T. Akutsu, and J. C. Nacher: Network analysis of intercellular protein networks, 2025 12th Int. Conf. Biomedical and Bioinformatics Engineering (ICBBE 2025), 2025.

2025-32

環境ウイルス情報を統合した次世代ウイルス分類ツールの開発

西村陽介　海洋研究開発機構

【研究目的】ウイルスは生物にとって主要な死因の一つであるだけでなく、宿主との多様な共生関係を通じて進化や多様性の形成に深く関与し、地球規模での生命活動に重要な影響を及ぼしている。しかし、環境ウイルスの多くは分離・培養が困難であり、その大部分は未分離のまま「ウイルスダークマター」として実態が十分に解明されていない。近年、公共データベースには多様な環境に由来する膨大なメタゲノム配列データが蓄積されているものの、それらを体系的かつ効果的に活用する解析基盤は未だ発展途上にある。本研究では、メタゲノム由来のビッグデータを大規模に解析することによりウイルスゲノムを網羅的に解読し、ウイルスのゲノム情報、系統関係、生息環境、機能遺伝子情報を統合したデータベースを構築することを目的とする。これにより、生命科学および医学分野における基盤的知見の創出に貢献することを目指す。

【手法と結果】10 万件以上のメタゲノムサンプルを解析し、約 7,200 万本のウイルスゲノム配列を同定した。そのうち約 64 万本は完全長ゲノムとして復元された。これらの完全長ウイルスゲノムに対し、自作の解析パイプライン GANA を用いて、KEGG KO に基づく相同遺伝子や Pfam などの機能ドメインを体系的に探索し、ウイルスが保有する遺伝子機能情報を整備した。さらに、これまで緒方研究室で構築してきたウイルス・宿主データベース Virus-Host DB（VHDB）およびウイルスゲノム分類ツール ViPTree との統合を進めるため、融合対象となるウイルス配列の選定、配列の非冗長化手法、宿主予測手法について検討を行った。また、ウイルスに共通して存在する保存遺伝子に基づくリファレンス系統樹を構築することで、ウイルスの大分類を可能とする新たな系統分類手法の開発にも取り組んでいる。

また、本研究で得られた大規模メタゲノムデータを活用し、海洋に存在する巨大ウイルスの生態学的解析を実施した。巨大ウイルスは多様な環境に適応して進化してきたことが知られているが、その深海環境における実態は不明な点が多い。本研究では、深海に局在する巨大ウイルスゲノムを同定し、その遺伝子内容を解析した結果、深海特有の環境条件に適応するために遺伝子レパートリーが独自に進化している可能性が示された。さらに、メタトランスクリプトーム解析により遺伝子発現量を評価することで、深海に特異的で、かつ転写活性を示す巨大ウイルス群が広範に分布していることを包括的に明らかにした。

【成果報告（論文・学会発表等）】

1. Wenwen Liu, Komei Nagasaka, (7 名省略), Yosuke Nishimura, Hisashi Endo, Yusuke Okazaki, Hiroyuki Ogata. “Giant viruses specific to deep oceans show persistent presence and activity.” mSystems e00932-25 (2025)

2. 西村 陽介. 微生物進化を駆動する可動遺伝因子―メタゲノムデータと配列解析でその実像に迫る. 第 48 回日本分子生物学会年会、横浜、2025.12.4

Elucidation of host-giant virus interaction using transcriptomics of giant virus-infected acanthamoeba cells

Masaharu Takemura　Tokyo University of Science

【Introduction】Giant viruses are dsDNA viruses classified within the phylum *Nucleocytoviricota*, characterized by larger genome and particle sizes than typical viruses. They remain one of microbiology's great mysteries, with many aspects of their ecology and infection mechanisms still unknown. In 2021, Takemura isolated a novel mimivirus, *Moumouvirus lavasanguinem*, from a pond on the Gakushuin University campus. *M. lavasanguinem* exhibits an intriguing characteristic not previously observed in giant viruses: it induces resistance or persistent infection in infected acanthamoeba. Therefore, we decided to perform transcriptomics on acanthamoeba that acquired resistance (or established persistent infection) to *M. lavasanguinem* (hereinafter referred to as resistant strains). By comparing these resistant strains with normal acanthamoeba, we aimed to identify genes expressed in the resistant strains and elucidate the molecular basis of this resistance.

【Materials and methods】Acanthamoeba was cultured using PYG medium by standard methods. After infecting the cells with *M. lavasanguinem*, they were statically cultured for approximately one month to obtain resistant strains. Total RNA was extracted from these resistant strains, normal uninfected acanthamoeba, and acanthamoeba at 5 and 10 hours post-infection with *M. lavasanguinem* using the Qiagen RNeasy® Mini Kit. RNA-seq was performed on the resulting raw data. Transcriptomics was then conducted to investigate gene expression profiles specific to the resistant strains.

【Results and Discussion】The results revealed that, while many genes known from previous analyses to be specific to *M. lavasanguinem*—primarily those related to multiple types of membrane proteins—showed no characteristic changes, many genes specific to acanthamoeba genes exhibited characteristic fluctuations. Increased expression of genes likely involved in pathways centered on phagosome and lysosome responses, and decreased expression of genes likely involved in pathways related to ribosomes, DNA replication, and nuclear-cytoplasmic transport were observed. These results suggest a tendency for increased expression of genes related to the intracellular membrane system in resistant strains, though the details remain unclear at this stage. However, previous studies have obtained electron micrographs showing that in resistant strains, the maturation of the viral factory of *M. lavasanguinem* is arrested at the early to mid-stage of formation, with the rough endoplasmic reticulum surrounding it, suggesting a connection to this phenomenon. In the future, we plan to revisit our hypotheses based on these findings and explore new analytical approaches, including knockout studies of genes showing altered expression patterns.

【Achievement】

○Masaharu Takemura, Jiwan Bae. Giant viruses of the phylum Nucleocytoviricota induce unexpected behaviors in infected cells. Symposium “Artificial cell and boundary between living and non-living matters” on the 63rd Annual Meeting of the Biophysical Society of Japan, Nara, 2025.9.25.

海産原生生物ラビリンチュラゲノムに潜む新奇ウイルス「ミルスウイルス」の探索

高尾祥丈　福井県立大学

近年実施された大規模な海洋 Metagenome-Assembled Genome 解析の結果、極めて新規性の高い未分離のウイルス、「ミルスウイルス」が発見された。ミルスウイルスは、温帯から熱帯、極地周辺に至るまで世界中の有光層に広く検出され、その生態学的影響力は非常に大きいと予想されている。さらに、そのゲノムはウイルスの分類における最上位階層である 2 つの二本鎖 DNA ウイルス域(デュプロドナウイルス域とバリドナウイルス域)双方の遺伝的特徴を持つことが明らかになっており、それらの初期進化を解明する上でも重要なウイルスである。

2023 年、原生生物「ラビリンチュラ」のゲノムアッセンブルデータからこのウイルスの完全長ゲノム配列が発見され、ラビリンチュラが自然宿主の一つであることが明らかになった。ラビリンチュラは、ストラメノパイル生物群に属する従属栄養性原生生物で、沿岸域生態系において重要な分解者として認識されている。申請者はこれまでの研究から多様なラビリンチュラ株を保持している。そこで、本研究課題では、多様な「ラビリンチュラ」株のゲノム解析を実施して、新規海洋ウイルス群「ミルスウイルス」の検出・多様性解析を実施することを目的とした。

本課題では、ラビリンチュラの主要 10 属 (属レベルの系統群を含む)の 18 培養株について、ショートリード解析およびゲノムアッセンブルデータ構築を実施し、ミルスウイルス由来のシグナルの探索および多様性解析を行った。

10 属 18 株のゲノムアッセンブルを実施し、15 株のゲノムから 38 個のミルスウイルス MCP(major capsid protein)ホモログを発見した。これらの配列と既知のミルスウイルスとの系統関係を解析したところ、複数の新規系統群が含まれることが明らかになった。また、これらの系統関係とラビリンチュラの系統関係には一定の相関関係が確認された。このことは、ラビリンチュラとミルスウイルスの関係が進化的に長い期間にわたって継続し、生物群内に広く分布するに至ったことを示唆している。一方で、ミルスウイルスのシグナルが確認されなかった株が存在したことは、両者の関係性が恒久的なものではないことも示唆しており、ミルスウイルスの感染の成立・維持機構を理解する上で興味深い発見となった。

さらに、本研究に供した３株のゲノムアッセンブルデータには、ミルスウイルスと相同性の高い ORF を含み、ショートリードのマッピング率が高く長いコンティグも確認され、これらの株の細胞内に活性の高いミルスウイルスが存在していることが予想された。今後、これらの培養条件を操作し、ミルスウイルスの粒子生成条件の解明することにより、ウイルス分離株の獲得、およびシグナル非検出株への感染実験の実現を目指す。

機械学習による作物根の微生物叢の比較解析

大西一光　帯広畜産大学

近年、作物の根や根圏に存在する微生物が作物の養分吸収を促進し、生産性に重要な役割を持つことが明らかになっている。しかしながら、作物の遺伝子型や環境要因が微生物の種類や量に及ぼす効果については未解明な部分が多い。内生菌は植物体内に生息する土壌微生物の総称である。農業に有益な内生菌が報告されているが、農業利用には情報が不十分である。また、コムギの内生菌の種類や役割については不明な点が多い。本研究では、世界の重要作物であるコムギに着目し、異なる環境おや種・品種から採取した根のサンプルを用いて、内生菌叢に及ぼす遺伝的要因と環境要因の影響を調査した。

【実験１】　北海道清水町の 3 圃場で栽培された春まきコムギ品種「はるきらり」の根を用いて、環境の違いが内生菌叢を変化させるか調査した。根をサンプリング後、各圃場 40 の根の断片を表面殺菌し、培地上で菌の単離と培養を行った。得られた菌株については、シャーレ上での形態や色調から分類した。また一部のサンプルでは ITS 領域を対象とした塩基配列のシーケンス解析を行い、分類学的同定を試みた。清水町の 3 圃場における内生菌の単離率は、23.7～44.7%となり、圃場によって大きく異なっていた。 3 圃場で全 38 の内生菌が分離され、色調や形態が異なる全 22 種類に分類された。また 9 菌株の ITS 領域のシーケンス解析の結果、*Setophoma* 属や *Pleosporales* 属などの存在が確認できた。同一品種である「はるきらり」を用いているにもかかわらず圃場間で内生菌の分離率や種類に違いが認められたことから、環境条件の違いが内生菌叢に影響を及ぼしていることが示された。

【実験 2】種内および種間の比較により、遺伝的要因が内生菌叢を変化させるかを調査した。「はるきらり」、スペイン由来のスペルトコムギ系統 KU-1025、およびオオムギ品種「はるな二条」から内生菌を分離した。コロニー形態タイプから計 20 種類に分類することができた。さらに一部の菌株については、*ITS* 領域の塩基配列解析と BLAST 検索により菌群の同定を行った。非計量多次元尺度法による解析の結果、種内および種間における内生菌叢の明確な変異は認められなかった。一部の内生菌は宿主によらず高頻度で出現したことから、コムギおよびオオムギに宿主非特異的に定着する内生菌である可能性が示唆された。一方で、2018 年に十勝清水町の一般生産者圃場で栽培された「きたほなみ」から分離された内生菌とは、明確な差が認められた。

以上のことから内生菌叢は、宿主の遺伝子型、圃場環境や年次といった複数の要因が相互に作用することによって形成されていると考えられた。本研究で得られた知見は、持続可能な農業における土壌微生物の活用の実現に向け重要な基礎的知見となると考えられる。本研究は培養法により単離し内生菌叢を比較したが、今後は次世代シーケンサーを用いて多数のサンプルの内生菌叢の調査を行い、機械学習により内生菌叢と生産性の関係を解明していくことが重要と考えられる。

Fabrication of cellulose nanofiber/polymer monolith composite materials with 3D cell structures

Steve Eichhorn　University of Bristol

Polymer monoliths possessing a bicontinuous pore/skeleton structure are promising candidates for use as columns in liquid chromatography and flow reactors. From a practical viewpoint, scale-up is required; however, bulk polymerization causes shrinkage during polymerization, which often leads to cracking of the polymer monolith. In contrast, particulate monoliths can be synthesized with high uniformity via suspension polymerization, a method well suited for large-scale production. In this study, we aimed to fabricate macroscopic porous structural materials by binding monolith particles with cellulose nanofibers (CNFs).

First, a mesitylene (porogen) solution containing divinylbenzene (monomer), polydimethylsiloxane (porogen), a radical initiator, and a chain transfer agent was mixed with a 0.1 wt% CNF aqueous dispersion to form an emulsion. After emulsification, SDS aqueous solution was added as cosurfactant, then Ar bubbling was carried out. Polymerization was carried out at 65℃ for 24 h, yielding monolithic particles. FE-SEM observation of the particle cross-sections revealed the formation of a bicontinuous porous skeleton. The particle size of the monoliths depended on the concentrations of CNF and SDS, and under optimized conditions, relatively uniform particles with D_w/D_n = 1.1 were obtained. These particles could be molded into various shapes by mixing them with an aqueous CNF dispersion and acetone, followed by drying. Because poly(divinylbenzene) is inherently hard and brittle, forming it into a free-standing film is difficult. However, binding particles with CNF enabled the fabrication of composite sheet materials with high flexibility like paper (Figure 1). When these sheets were cut and subjected to dynamic mechanical analysis at 100 Hz of frequency, the storage modulus (*E*') were found to improve with increasing CNF content. In contrast, the *E*' decreased under high-humidity conditions (Figure 2), although this weakening is expected to be addressed by addition of paper-strengthening agents such as acrylamide polymers. This approach allowed the co-assembly of particles of different types (particle/pore size, chemical structure). These results suggest that the fabrication method is versatile and has potential for applications in separation materials and lightweight structural materials.

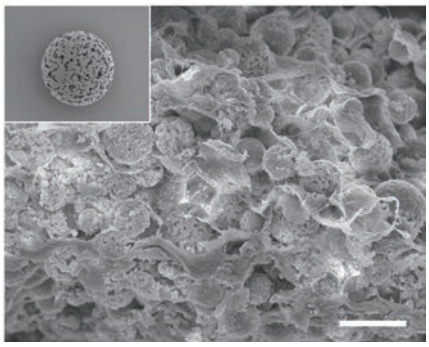


Figure 1. Cross sectional image of the monolith particle/CNF composite. Inset: single monolith particle.

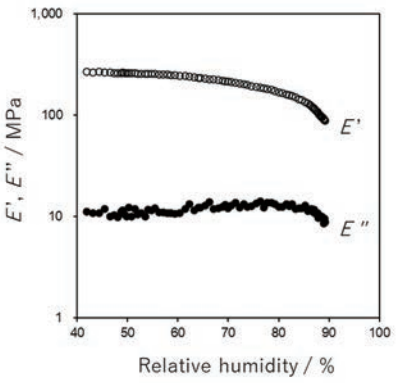


Figure 2. Relative humidity dependency of storage/loss modulus of monolith particle/CNF composite.

Synthesis of Wide-Surface Molecular Nanocarbons

Chaolumen　Inner Mongolia University

Molecular nanocarbons with extended π-surface areas have attracted increasing attention owing to their nonplanar three-dimensional frameworks, inherent chirality, and intriguing optoelectronic properties. In this research, these properties are modulated through structural design strategies such as pentagon incorporation, heteroatom insertion, and geometrical twisting, which together offer a promising platform for next-generation organic electronic materials. By these strategies, we have achieved a few research outcomes which were summarized in four publications.

(1) We reported a π-extension strategy based on a diquinoxaline-fused pyrene, leading to a red-emissive, twisted aza-nanographene that retains the intrinsic electronic characteristics of the parent scaffold, including its three-electron-accepting capability and low-lying LUMO level. (Yoshifumi Hashikawa & Chaolumen, *et al*., *Chem. Commun*., **2025**, *61*, 11401–11404. ***Selected as Outside Front Cover***)

(2) Two chirally twisted C_{64} nanographenes were designed and synthesized via π-truncation of the parent C_{76} nanographene. Notably, despite possessing the same absolute chirality, the two products exhibit opposite CPL signs. Computational analyses suggest that this inversion originates from subtle differences in the relative orientation of the electric and magnetic transition dipole moments, with the angle fluctuating around 90°. (Yoshifumi Hashikawa & Chaolumen, *et al*., *Org. Lett.* **2025**, *27*, 7009−7013.)

(3) We further reported a molecular ladder featuring four antiaromatic pentagonal rings embedded in a twisted backbone with a length of 2.000(1) nm. In the crystal, the molecules exhibit tight π–π packing with a shortest intermolecular contact of 3.210(9) Å, leading to a maximum hole mobility of μ_h = 0.035 $cm^2\ V^{-1}\ s^{-1}$ in single-crystal organic field-effect transistors. (Yoshifumi Hashikawa & Chaolumen, *et al*., *Org. Lett.* **2025**, *27*, 8365−8369.)

(4) We also reported a π-extended 1,1′-binaphthyl incorporating a nor[5]helicene skeleton, synthesized via an intermolecular S_EAr-type reaction of 5,11-di(naphthalen-2-yl)tetracene. The axially chiral 1,1′-binaphthyl unit exhibits a low flipping barrier ($\Delta G^{\ddagger}_{exp}$ = 17.3 ± 0.52 kcal mol^{-1}), resulting in rapid racemization. Accordingly, this axially chiral nanocarbon racemizes even at 0 °C, with a half-life of 6.63 ± 0.53 h. (Yoshifumi Hashikawa & Chaolumen, *et al*., *Org. Lett.* **2025**, *27*, 8969−8973.)

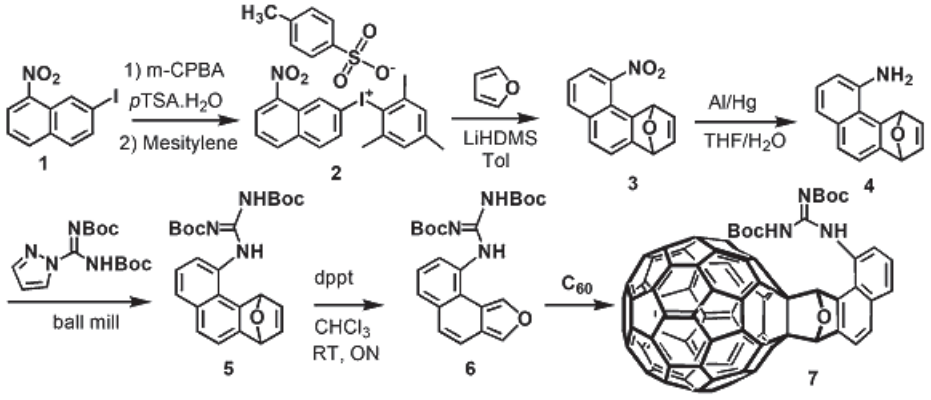
Exploration of aromatic-ring homologue of benzo[c]furan with guanidine functionality

Davor Margetic　Rudjer Boskovic Institute

Objectives

Synthesis of novel guanidine benzo[c]furan cycloaddition reagents and investigation of their reactivity for fullerene derivatisation with partner ICR researcher Professor Murata Yasujiro.

Experimental results. Several synthetic alternatives to guanidino-functionalized benzo[c]furan were explored to prepare the target molecule. The most viable preparation route was a six-step procedure starting from 2-iodo-8-nitronaphthalene **1** (Scheme 1), which itself was prepared in three synthetic steps from 2-amino-1-naphtosulphonic acid by known methods. The key precursor, a hypervalent iodonium reagent **2,** was transformed to the intermediate 8-nitro-2-naphtharyine, which was reacted with furan in situ. Chemoselective reduction of the nitro group of **3** to the amino group in **4** was followed by the guanylation of the amino group by high-speed vibrational milling. Guanylated isobenzofuran precursor **5** was treated with bis(2-pyridyl)-*s*-tetrazine (dppt), and the in situ formed benzo[c]furan **6** was engaged in Diels-Alder cycloaddition reactions with dienophiles. While the [4+2] reaction with *N*-methylmaleimide afforded a satisfactory yield of cycloadduct, the cycloaddition reactivity with fullerene was much less pronounced, and target fullerene cycloadduct **7** was obtained in minor amounts, sufficient only to spectroscopic detection (^{1}H-NMR) of its formation. In continuation, a synthetic approach to linear benzo[c]furan, starting from 2,3-dibromonaphthalene, was explored, and it was found to be unproductive. An alternative synthesis of 8-nitro 2,3-bis-TMS naphthalene as the 2,3-naphtharyine precursor was devised.



Scheme 1

Planned travel and visit to the ICR was organised in September, and a seminar lecture at the ICR was held on September 12, 2025. The results of the project were also presented as a lecture at the 35th Symposium on Physical Organic Chemistry, Nagoya, Japan, September 9-11, 2025.

Advancing Molecular-Surgery Method for Expansion of Endohedral Fullerenes towards Novel Applications

Il Jeon　Sungkyunkwan University

【Objectives】 This study proposes endohedral fullerene–based spin qubits as an alternative to the Si:P Kane model, addressing limitations in dopant control, electric-field sensitivity, and spin coherence. A DFT-based computational platform is developed to enable low-cost, high-precision screening of qubit materials and support quantum device design.

【Experimental methods】A standardized DFT framework using VASP was applied to virtually screen endohedral fullerene qubit candidates. Structurally stable systems were identified through geometry optimization, and key electronic and spin properties—such as density of states, spin polarization, magnetic moment stability, and electric-field response—were evaluated to assess coherence and controllability. Dimer models were additionally analyzed to investigate spin–spin interactions relevant to scalable multi-qubit architectures.

【Results and discussion】The simulation results demonstrate that endohedral fullerenes offer significant advantages over conventional silicon-based qubits by providing strong shielding of internal spins from external electric-field noise, resulting in enhanced spin stability and coherence (Fig. 1., Fig. 2.). Several encapsulated guest atoms exhibited robust spin polarization and minimal magnetic moment variation under applied fields, confirming the protective role of the carbon cage. The dependence of spin response on guest atom type enabled the identification of promising candidates suitable for controlled spin manipulation via ESR techniques. Furthermore, dimer structure analysis indicated that controllable inter-qubit spin interactions are achievable, supporting the feasibility of scalable qubit integration. Overall, the study validates DFT-based virtual screening as an effective strategy for designing next-generation qubit materials and provides fundamental design principles for overcoming the limitations of the Kane model in quantum device applications.

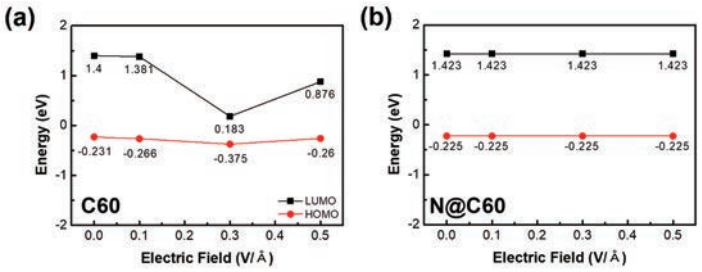


Fig. 1. LUMO and HOMO of α-molecular orbital

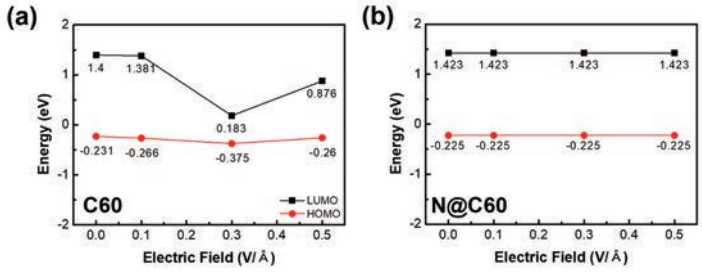


Fig. 2. LUMO and HOMO of β-molecular orbital

Elucidation of the mechanism of troponoid-mediated controlled radical polymerization

Chi-How Peng　National Taiwan University

Objectives: Reversible-deactivation radical polymerization (RDRP) serves as an effective method for synthesizing innovative polymers. Nevertheless, the presence of transition metal catalysts and residual mediators may pose contamination risks to the final polymer products, thereby restricting the range of their applications. We have developed a metal-free approach using troponoids, specifically tropone and tropolone, to control the radical polymerization. However, the control mechanism has not been fully rationalized. Therefore, we further studied the troponoid-mediated radical polymerization (TPRP) of *N*-vinylpyrrolidone (*N*VP) in aqueous phase to gain insight into the mechanism.

Experimental Methods: The mediator and VA-044 were degassed in a Schlenk flask through three freeze-pump-thaw cycles, then DI water and dried *N*VP were added under N_2. Polymerization began with stirring and heating the mixture at 40 °C.

Results and discussion: The conditions for *N*VP polymerization mediated by troponoids were optimized by adjusting the initiator equivalents. Several features of RDRP were observed during polymerization, including a linear increase in molecular weight with conversion, smooth shifts in GPC traces, and successful synthesis of block copolymers. The mechanism of troponoid-mediated radical polymerization was elucidated through chain extension studies, supporting a reversible termination mechanism. To investigate the transformation of troponoid during polymerization, we conducted a model reaction and monitored the reaction using time-dependent ^{1}H NMR spectroscopy. Notably, new signals at 1.47 and 1.52 ppm gradually appeared during the reaction and were tentatively assigned to the Tropone-VA044 adduct. Their integration exhibited a 6:1 ratio, consistent with the methyl protons of the VA-044 moiety (H_e) and the α-hydrogen of tropone (H_d). Moreover, the total integration of residual Tropone and the newly formed peaks remained constant and equal to the initial Tropone concentration, strongly supporting the formation of Tropone-VA044, as depicted in Figure 1.

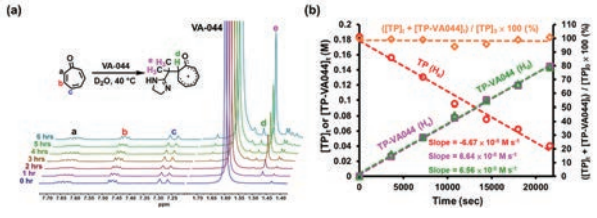


Figure 1 (a) Time-dependent ^{1}H NMR spectra of the model reaction and (b) the plots of the change in concentration of Tropone and Tropone-VA044 during the reaction

Exploration of perovskite solar cell composition: Correlating device performance and fundamental property

Hyunjung Shin　Sungkyunkwan University

Project #1: This project aims to fundamental properties of $FAPbI_3$ perovskite thin films. Circularly polarized pump–probe (CPPP) measurements were used to compare photoexcited carrier dynamics in preferentially oriented (POF) and randomly oriented (ROF) $FAPbI_3$ thin films. This approach allows direct evaluation of polarization-dependent carrier excitation and relaxation, providing insight into the effect of crystal orientation on carrier dynamics.

In [001]-oriented $FAPbI_3$ films, the transient absorption (TA) response shows a clear dependence on the helicity of the circularly polarized pump–probe configuration ($\sigma^-\sigma^-$ versus $\sigma^-\sigma^+$). This helicity-dependent asymmetry indicates the formation of an anisotropic carrier distribution in momentum space, arising from orientation-induced symmetry breaking and enhanced spin–orbit coupling. In contrast, randomly oriented films exhibit little to no polarization dependence, as helicity-selective effects are averaged out by random grain orientations.

These results demonstrate that crystal orientation control is essential for enabling polarization-selective excitation and anisotropic carrier dynamics in $FAPbI_3$, highlighting its importance for spin- and chiral-dependent optoelectronic applications.

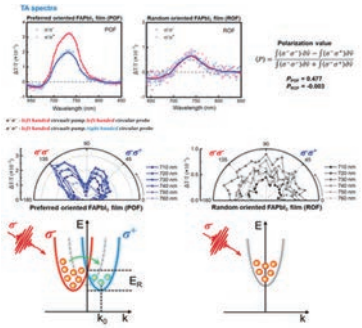


Figure 1. Spectra of circular polarization-dependent pump-probe (CPPP) and Circular polarization-dependent pump-probe (CPPP) polar plots

Project #2: This project aims to investigate the undesirable phenomenon in the interface between NiO and $FAPbI_3$. Cross-sectional transmission electron microscopy (TEM) reveals a well-defined interface between the $FAPbI_3$ perovskite layer and the underlying NiO_x layer. After annealing at 150 °C for 20 min, a thin interfacial region with contrast distinct from both layers is observed, indicating the formation of a modified interphase. Selected-area electron diffraction (SAED) from this region shows diffraction features of $FAPbI_3$ and NiO, along with partial diffraction patterns corresponding to PbI_2, providing direct evidence for localized PbI_2 formation due to partial thermal decomposition or interfacial phase segregation of $FAPbI_3$.

With extended annealing at 150 °C for 2 h, additional diffraction peaks corresponding to NH_4I (JCPDS No. 00-006-0174) appear, indicating further interfacial chemical evolution, while no NiI_2-related peaks are detected, suggesting limited iodide diffusion into the NiO_x layer at this temperature. In contrast, annealing at 200 °C for 2 h results in clear diffraction peaks of NiI_2 (JCPDS No. 00-020-0785), demonstrating that higher thermal stress promotes interfacial reactions between iodine-containing species and NiO_x. These results establish a temperature-dependent interfacial degradation pathway in $FAPbI_3/NiO_x$ heterostructures and highlight the importance of thermal budget control for maintaining interfacial stability and device performance.

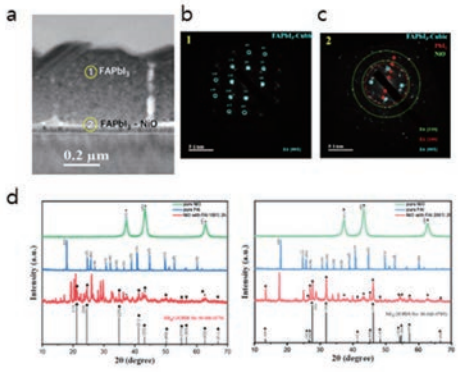


Figure 2. (a) The cross-sectional high-resolution transmission electron microscopy (HRTEM) image of the $FAPbI_3$ thin film (b) The selected area electron diffraction (SAED) pattern of position 1. (c) The SAED pattern of position 2. (d) XRD pattern of NiO/FAI samples annealed at 150 °C and 200 °C

Perovskite Device Engineering with Cross-linkable Hole Transport Materials

Joshy Joseph　CSIR-NIIST

Objectives: (i) Design and synthesis of triphenylamine-based, cross-linkable HTMs; (ii) Material characterization involving detailed photophysics and electrochemistry of newly developed HTMs; (iii) Device engineering involving p-i-n architecture and its interfacial modifications leading to devices with reproducible efficiency and stability (at Prof. Atsushi Wakamiya's Lab)

Experimental Methods:

To optimize and develop stable, high-efficiency perovskite solar cells (PSCs) using triphenylamine-based, cross-linkable HTMs and HTM monolayers, a series of target molecules (Figure 1) was designed and synthesized. These molecules were obtained in gram-scale quantities through multi-step organic synthesis at the CSIR-NIIST laboratory and were thoroughly characterized using ^{1}H and ^{13}C NMR spectroscopy and HRMS. Comprehensive photophysical and electrochemical studies were also performed, revealing favorable optoelectronic properties compared to benchmark HTMs, thereby establishing their suitability for PSC applications. Device fabrication and optimization of perovskite solar cells are being carried out at Prof. Wakamiya's laboratory. Initial PSCs with a p-i-n architecture employing cross-linkable triphenylamine-based HTMs have achieved promising PCEs of 15-18%. Further evaluation of newly synthesized HTMs, along with systematic device optimization and in-depth device-physics studies, will be conducted during the Indian PIs' visit to Prof. Wakamiya's laboratory. This collaboration is also expected to facilitate the Indian research team's redesign and development of optimized materials and device architectures.

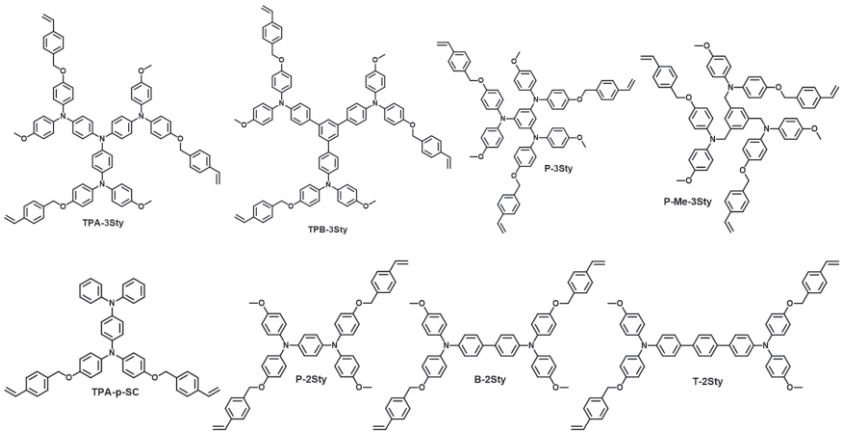


Figure 1. Structure of cross-linkable HTMs synthesized.

Outcomes: (i) Developed new HTMs with promising optoelectronic properties; (ii) PSC devices show promising PCEs (15-18%), which need to be further optimized for enhancing the performance.

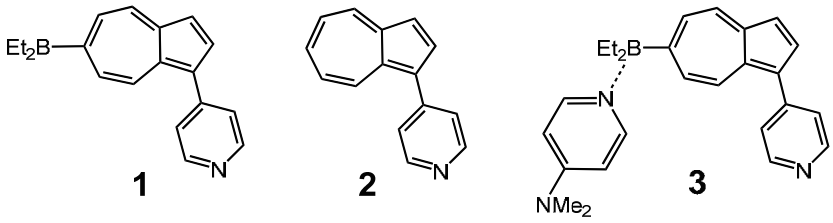
Analysis: (i) Synthesis of HTMs and preliminary PSC Device Fabrication completed. Further optimization is in progress; (ii) Visit of Indian PI and a PhD Scholar to Prof. Wakamiya's Lab is planned during Feb 03 – 14, 2026.

Publications (papers, presentations, etc.): Under preparation

Synthesis of borane-functionalized azulene derivative and the relationship between the aggregation state and color

Shigeharu Wakabayashi　Suzuka University of Medical Science

Introduction: Intermolecular boron–nitrogen coordination has emerged as a versatile interaction in supramolecular chemistry. We have previously demonstrated that borylpyridine-based molecular designs enable the formation of a variety of self-assembled architectures, highlighting their potential as modular supramolecular building blocks. Among these systems, the azulene-inserted compound **1** predominantly forms a cyclic trimer (**1**$_3$) in solution. Structural transformations occurring during self-assembly, as well as subsequent coordination with 4-dimethylaminopyridine (DMAP), were accompanied by distinct color changes. Trimerization caused a 50 nm blue shift in the absorption maximum (from 582 nm for the monomeric reference compound **2** to 532 nm for **1**$_3$), whereas DMAP-induced disassembly resulted in a red shift to 549 nm, corresponding to the DMAP adduct **3**. These spectral changes were supported by TD-DFT calculations. In this study, we investigate the dissociation constant of the DMAP-induced disassembly of **1**$_3$, and its kinetics using in-line visible absorption spectroscopy coupled with a flow microreactor.



Results and discussion: To obtain quantitative insight into this equilibrium, we analyzed the absorbance at 532 nm —characteristic of **1**$_3$— as a function of DMAP concentration. The data were fitted to the Hill equation using nonlinear regression, yielding a dissociation constant of K_d = 1.71 ± 0.26 mM (r^2 = 0.998, AIC = –78.5). We then turned to kinetic analysis, examining the time dependence of the DMAP-induced color change of **1**$_3$ by in-line visible absorption spectroscopy. The reaction progress is shown in Figure 1. Notably, the absorbance at 532 nm decreased steadily with increasing residence time, reaching near-equilibrium values within approximately 3–4 min. The decay profile was well fitted to a single-exponential model, affording a rate constant of k_{obsd} = 0.0194 ± 0.0015 s^{-1} ($t_{1/2}$ = 36 s, r^2 = 0.995).

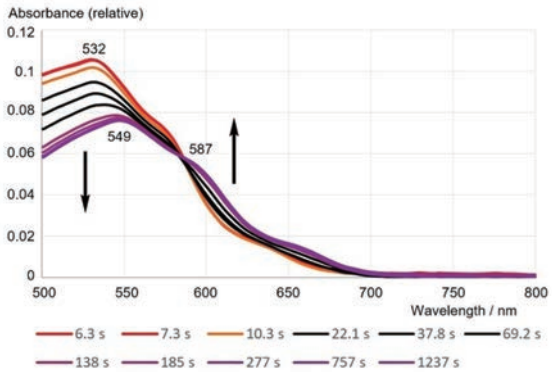


Figure 1. Spectral changes of **1** upon reaction with DMAP in $CHCl_3$ monitored by in-line analyses.

Outcome report: S. Wakabayashi, R. Kikuchi, H. Soutome, M. Takumi, M. Wakioka, T. Higaki, H. Nakanishi, Y. Ohki, A. Nagaki, *The International Chemical Congress of Pacific Basin Societies 2025 (PACIFICHEM 2025)*, Honolulu, Hawaii, USA, 2015.12.

酸素吸蔵材料の開発

細川三郎　京都工芸繊維大学

固体への酸素の脱挿入の理解は、酸化物など機能性物質の制御法の開発につながるだけでなく、電圧で酸素吸蔵量が調整可能なセラミクスなど、持続可能な社会の実現に貢献するエネルギー材料の開発につながる。一方で、どのような固体中のどのような要因によって、酸素が脱挿入可能になり、そして促進されるのかは学術的によくわかっていない。遷移金属酸化物では、その遷移金属イオンの価数に応じて酸素量が変化し、酸素の脱離・吸収が生じる。中でも、異常高原子価イオンを含む酸化物は、典型的な価数のイオンを含む酸化物と比べて非常に低い温度で酸素の脱離・吸収が起こることが期待される。そこで本研究では異常高原子価 Fe^{4+}イオンを含む $BaFeO_3$ に着目した。$BaFeO_3$ には、FeO_6 八面体が全て頂点共有で接続される 3C 型構造（単純ペロブスカイト構造）と、頂点共有と面共有を併せもつ 6H 型構造、12R 型構造（六方晶ペロブスカイト構造）の 3 種の結晶多形がある (図 1)。これらの結晶多形について、Fe の価数変化時に生じる酸素脱離・吸収挙動とそれに伴う結晶構造変化を明らかにした。

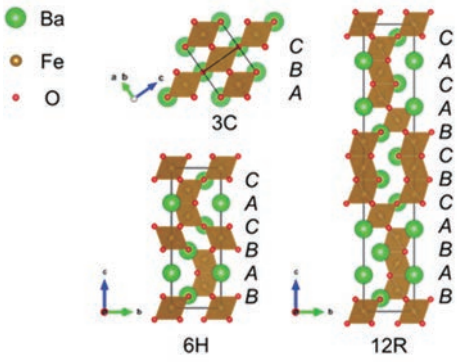


図 1. $BaFeO_3$ の結晶多形

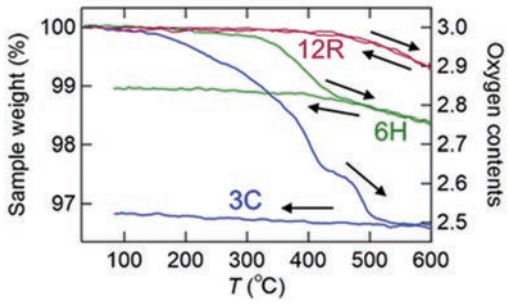


図 2. $BaFeO_3$ の熱重量分析結果

3C 型、6H 型、12R 型は、低温トポタクティック法や高圧酸化法により合成した。得られた 3 種類の結晶多形試料は、放射光 X 線回折および結晶構造解析から、いずれも不純物のない単相であり、酸素サイトの欠損も認められないことから、全て Fe^{4+}を含んだ同じ化学組成の $BaFeO_3$ となっていることを確認した。これらの試料の酸素吸収・脱離挙動を空気中での熱重量分析した。熱重量分析を行うと、加熱過程において、3C 型では酸素放出が 130 ℃程度と非常に低い温度から生じる一方で、6H 型では 320 ℃、12R 型では 460 ℃程度から生じる (図 2)。また、放射光 X 線回折からは、3C 型では頂点共有サイトの酸素がランダムに抜け始めることが明らかになった。一方で、6H 型、および 12R 型では、単位格子が c 軸方向へ異方的に伸長したことから、八面体の面共有を構成するサイトから酸素が優先的に脱離することが示唆された。さらに酸素が抜けた高温状態からの冷却過程において、3C 型は酸素を吸収しない一方で、6H 型では 600 ℃から 430 ℃の間で、12R 型では 600 ℃から 460 ℃の間で可逆的に酸素を吸収することが明らかになった。この結果は、八面体の面共有を含む六方晶ペロブスカイト構造では、空気中でも異常高原子価である Fe^{4+}を可逆的に安定化できることが明らかになった。

Development of novel chiral silica based on controlling of hierarchical structure

Tomoyasu Hirai　Osaka Institute of Technology

Controlling a polymer with a flexible main chain such that it has the preferred handed-helical structure is still difficult. Previously, the helical conformation in polyhedral oligomeric silsesquioxane (POSS)-containing polymers was controlled by mixing a small amount of chiral dopant with the polymer[1]. The helical structure thus obtained is a so-called dynamic helical structure. In contrast, the introduction of chiral molecules to a polymer via covalent bonding gives rise to a stable helical structure known as a "static helical structure." However, attempts to control the helicity of a POSS-containing polymer such that the formation of the preferred-handed static helical structure is accomplished have not yet been reported.

We designed and prepared novel approach to synthesize polymethacrylate-functionalized polyhedral oligomeric silsesquioxane, which has seven vinyl groups (PMAvinylPOSS) that enable the introduction of functional molecules via a post-functionalization reaction. As the vinyl group generally reacts with radical species, we present the preparation of PMAvinylPOSS using anionic polymerization and explore the living nature of the polymerization. We also demonstrated the successful post-functionalization via a thiol-ene reaction, which lead to the formation of a preferred-handed static helical conformation. Furthermore, we reveal that the helical conformation is retained during the calcination process, resulting in chiral silica with a helical structure (Figure 1)[2].

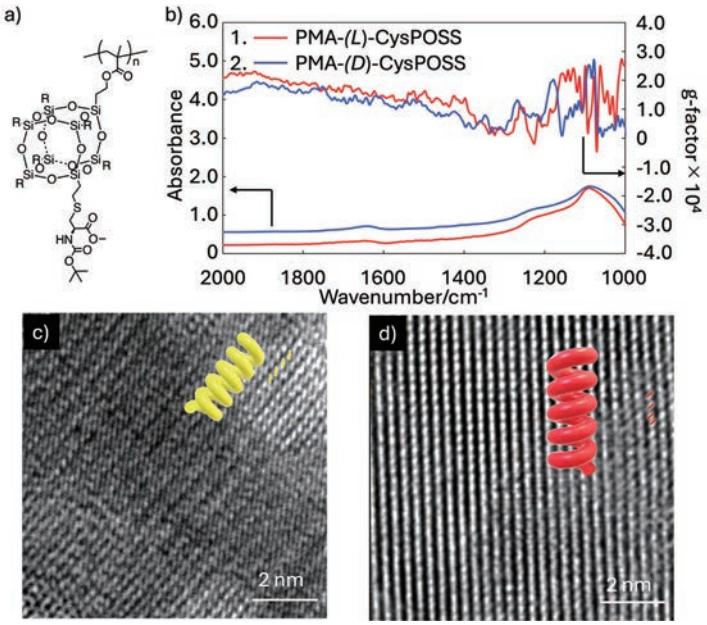


Figure 1. a) Chemical structure and b) VCD spectra of PMA-CysPOSS. c) and d) TEM image of chiral silica prepared from enantiomeric PMA-CysPOSS.

[1] Hirai, et al., *JACS Au* **2021**, *1*, 375-379.

[2] Hirai, et al., *Macromolecules* **2025**, *58*, 6534-6542.

有機高分子材料の重水素化技術の確立と中性子散乱による高次構造の解明

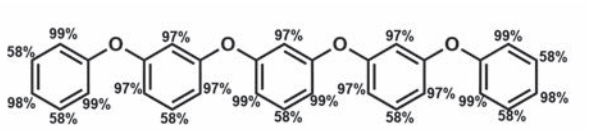
岡弘樹　東北大学

【研究目的】

現代社会を支える３大材料は高分子・金属・セラミックスであり、高分子材料は我々の生活を支える重要なものとなっている。高分子材料の高機能化・高性能化のために、散乱法（中性子散乱、X線散乱、光散乱）や顕微鏡法（透過型電子顕微鏡、走査型電子顕微鏡、光学顕微鏡）を用いて、ナノメータースケールからミクロンスケールにおいて微視的視点から高分子材料が作る階層的高次構造およびその形成機構を解明し、その制御法を確立することが極めて重要である。中性子線による研究においては、中性子線が水素原子に敏感であり、またその同位体である重水素原子を使うことで試料のコントラストを変えることが可能であるため、X 線などでは見えない構造を観るための手法として重要な役割を担っている。特に、有機分子の水素をその同位体である重水素でラベル化する手法は、試料のコントラスト変調、部分選択的構造解析、水素の非干渉性散乱に由来するバックグラウンド信号の低減など多くの利点があり、中性子研究を更に高度なものへと昇華する手法として重要な役割を担っている。しかし、中性子散乱に係る技術が成熟する一方で、高分子材料の重水素化は、研究遂行のうえでボトルネックとなっていた。そこで、本研究では、研究代表者独自の重水素化法により代表的な有機高分子材料（ポリフェニルエーテルなど）を重水素化し、化学研究所の共同研究者が得意とする中性子散乱によりその高次構造を解明することを目的としていた。

【結果と考察】

現在までに、代表的な有機材料であるポリフェニルエーテルの重水素化を試み、その高い重水素化率での重水素化に成功している（右図）。本年度



終了までに、1g スケールのサンプル提供に向けた反応条件の確定を目指す。本研究ではポリフェニルエーテルを“材料そのまま”重水素化し、重水素化によって、同材料の分子量（重合度）および分散度が変化しないようにする手法を確立することができた。また、本研究のもう一つの対象物質である安息香酸スクロースについても重水素化進行の兆しを確認でき、共同研究者から高純度なサンプルのご提供を受け次第、重水素化に取り組む予定である。さらに、今後、これらの重水素化サンプルを用いて、京都大学 化学研究所の共同研究者が得意とする中性子散乱によりその高次構造を解明する。

【成果報告】

本研究を通して、ポリフェニルエーテルおよびオレフィンポリマーの重水素化手法を確立することができた。同成果は、幅広く産業現場、研究機関で活用されることが期待できるため、まずは、一連の重水素化材料およびその中性子散乱の結果について取り纏め、知財の獲得に取り組み、その後、国際科学誌に共著論文を投稿する予定である。

液体界面におけるセルロースナノファイバー膜の粘弾性測定

横田慎吾　九州大学

近年、塗料や化粧品分野において、セルロースナノファイバー(CNF)と呼ばれる木質由来の繊維がエマルションやフォームの乳化安定化剤として注目を集めている。CNF による乳化安定化は、油滴(気泡)に吸着した CNF によって液体界面が膜のように覆われ、安定化されることに由来する。従って、エマルションやフォームの物性を制御する上では、液体界面に存在する膜の構造と物性の相関を理解することが不可欠である。しかし、CNF 安定化エマルションやフォームに関する研究の殆どはバルクでの評価に留まっており、界面膜の物性や構造に注目した研究は非常に少ない。

本研究では液体界面における疎水化 CNF 単層膜の粘弾性測定から、その構造と物性の相関について検討した。まず、幅約 20 nm の CNF をトルエン中でエステル化し、C8 のオクタノイル基を置換度 0.23-0.29 で導入した。なお、置換度 0.29 は CNF 表面の水酸基がほぼ全て反応した状態に相当する。レオメータ(MCR-302, Anton Paar)に界面レオロジー測定(IRS, Anton Paar)用水槽を取り付け、水面に対して疎水化 CNF を気液界面に希薄で展開した。続いて、水面に設置したバイコーン型のプレートによってせん断を加えることにより動的粘弾性測定を行った。線形領域内において、貯蔵弾性率(G')>>損失弾性率(G'')であり、かつ周波数に依存しないゴム状平坦部様の挙動が見られた。これは、気液界面において、疎水化 CNF が二次元的ネットワークを形成し、変形に抵抗していることを示唆する。また、G'の値は疎水化の度合いが強いほど高く、繊維間の凝集力を反映しているものと考えられた。さらに、このゴム状平坦部の弾性率を水面における繊維濃度毎に両対数プロットしたところ、$G'=kc^{\alpha}$ のべき乗則で表されることが分かった(図)。なお、3 次元の繊維分散系において、弾性率が濃度のべき乗で表され、べき数は繊維のネットワーク構造を反映することが報告されている。例えば、ランダムネットワーク構造の場合べき数は 2.25 であり、本実験で得られたべき数 2.3 に非常に近い。実際に水面上の疎水化 CNF 膜の構造を原子間力顕微鏡によって観察したところ、繊維は二次元的なランダム構造をとっていることが明らかとなった。なお、水-トルエン界面においても同様の測定を行ったところ、べき数は 2.7 と同程度であったことから液液界面においても類似した構造をとっているものと考えられる。本研究によって得られた知見は、ナノファイバー膜の構造物性相関の理解だけでなく、エマルションやフォームの安定性を理解し、制御する上でも重要であると考えられる。

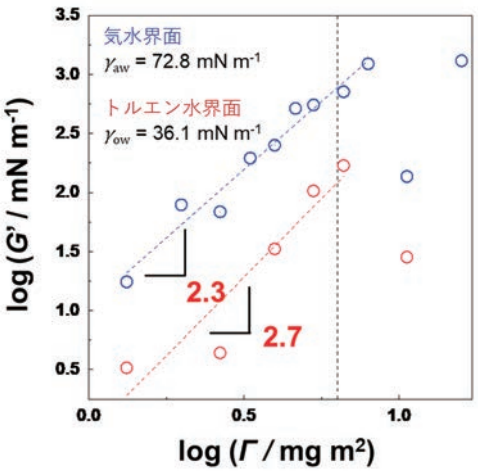


図　疎水化 CNF(置換度 0.29)の繊維濃度に対する貯蔵弾性率の両対数プロット

参考文献　1) Tatsumi, D., et al., Nihon Rheology Gakkaishi, 30, 27 (2002).

ナノ粒子超構造体における量子協同過程の超高速光電流計測

田原弘量　横浜国立大学

目的

コロイド半導体ナノ粒子は液相で合成される半導体量子ドットであり、内部に生成した電子とホールには強い量子閉じ込め効果が生じる。このナノ粒子内部の量子閉じ込め効果に加えて、集団のナノ粒子を結合させてナノ粒子同士の相互作用を利用することができれば、新しい集団的な量子光機能の発現が期待される。本研究は、集団のナノ粒子によって構築したナノ粒子超構造体の集団的量子光機能の発現メカニズムを解明することを目的として、超構造体の光学応答と光電流応答の計測を行った。

実験方法

本研究で用いたナノ粒子超構造体は、化学研究所の精密無機合成化学研究グループによって作製された $Cu_{2-x}S$ ナノディスク超構造体である。この超構造体はワンポッド液相合成によって、自己組織化によって作製したものである。$Cu_{2-x}S$ ナノ粒子が溶液中で結晶成長し、立体反発（斥力）とファンデルワールス力（引力）によってナノディスク配列積層構造が形成される。図１はナノディスク超構造体の光学顕微鏡像であり、長軸方向がナノディスクの積層方向に対応している。超構造体試料の光学特性を明らかにするために、波長可変フェムト秒パルスレーザーを用いて光吸収計測と光電流計測を行った。

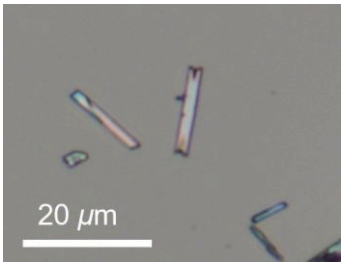


図１：$Cu_{2-x}S$ ナノ粒子超構造体の光学顕微鏡像.

実験結果・考察

近赤外光領域についてレーザーの波長を掃引しながら光吸収計測を行ったところ、0.9 eV を中心エネルギーとして 0.1 eV の幅を持ったブロードな局在表面プラズモン共鳴ピークが存在することを明らかにした。顕微分光によって単一超構造体の光吸収を１つずつ行うことで、局在表面プラズモン共鳴ピークのエネルギー位置は超構造体ごとに異なることが分かった。これは、ホールのドーピング度合いが超構造体ごとに異なることを意味している。レーザー光の偏光を回転させることで、局在表面プラズモン共鳴の光学異方性が存在することを明らかにした。さらに、超高速光電流の計測に向けて、くし型電極上に塗布した集団の超構造体に対する光電流計測を行った。バイアス印加によってバックグラウンド電流が流れることが分かり、ホールドープによるキャリアが強い影響を与えていることが分かった。

本研究ではフェムト秒パルスレーザーを用いた局在表面プラズモン共鳴の直接励起を行い、レーザー光の偏光に起因した吸収強度の光学異方性を明らかにした。バイアス印加による測定にも成功しており、ナノ粒子超構造体特有の協同過程を光電流として取り出せることが期待される。より詳細な計測に向けて、単一の超構造体に対する微細電極構造の作製を進めている。

塗布重合による 2 次元共有結合性有機構造体の精密成膜

鈴木充朗　大阪大学

【背景・目的】共有結合性有機構造体（covalent organic framework, COF）は，良好な構造秩序，大きな比表面積, 高い設計自由度などの特長をもち, 新たな機能材料として期待されている. しかし，高品質な薄膜を効率的に得るための手法は十分に確立されておらず, 薄膜材料としての研究開発はいまだ限定的である．そこで本研究では，高品質な COF 薄膜の形成を可能とする，良好な再現性と高い構造制御性を備えた成膜法の開発に取り組んだ.

【結果・考察】既知のイミン連結型 2 次元 COF である TAPPy–TA COF（Fig. 1a）をモデル化合物として,「塗布重合」による成膜を検討した．本手法では，モノマーを含む溶液を基板上に塗布し，その乾燥と同時に重合を進行させることで COF 薄膜を形成する. 成膜条件を系統的に検討した結果, 溶媒としてベンゾニトリルおよびジオキサン，触媒としてトリフルオロ酢酸を用いた溶液から，良好な結晶性と平滑性を備えた薄膜を形成することに成功した（Fig. 1b, c）．得られた薄膜を 2 次元微小角入射広角 X 線散乱（2D GIWAXS）により評価したところ，001 反射が q_z 軸方向で優先的に観測される一方，110 およびその高次反射は q_{xy} 軸近傍で比較的強く観測された（Fig. 1b）．この反射パターンは，COF の 2 次元共有結合ネットワークが基板に平行に配向した構造が，薄膜中で優先的に形成されていることを示しており，配向制御された COF 薄膜が塗布重合により形成可能であることを示唆する.

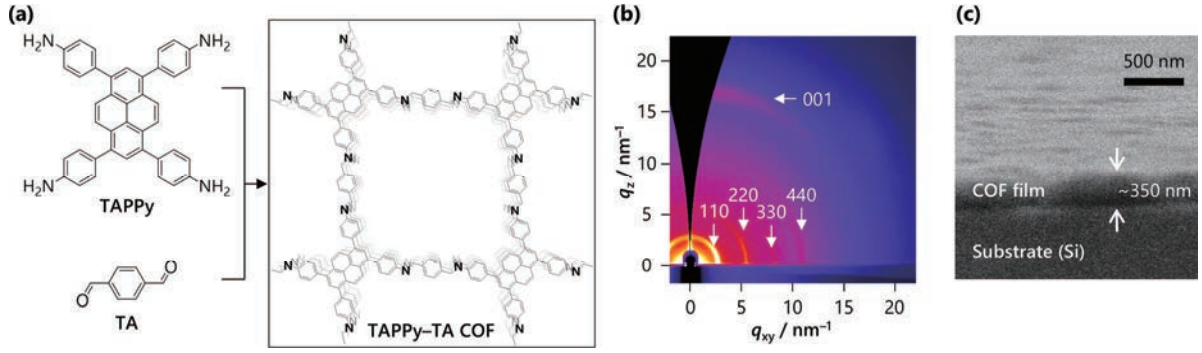


Fig. 1. (a) Chemical structures of the model compound TAPPy–TA COF and corresponding monomers. (b, c) 2D GIWAXS pattern and cross-sectional SEM image of a TAPPy–TA COF film prepared via the solution-deposition–polymerization approach developed in this study.

【成果報告】(1) Yamazaki, S. et al. Chemiresistive Sensing with Oriented Covalent Organic Framework Films Prepared via a Solution-Deposition–Polymerization Approach. 2025 KJF International Conference EASon Organic Materials for Electronics and Photonics (KJF-ICOMEP 2025), Aug. 2025. (2) Haze, S. et al. Crystallite Orientation in Covalent Organic Framework Films Prepared through a Solution-Deposition–Polymerization Approach. The 12th East Asia Symposium on Functional Dyes and Advanced Materials (EAS12), Sep. 2025. (3) 山崎 空ほか，塗布重合により成膜した共有結合性有機構造体における骨格構造と蒸気応答特性との相関，第 15 回 CSJ 化学フェスタ 2025，2025 年 10 月.

高い電気伝導率を指向した n 型有機金属半導体の開発

村田理尚　大阪工業大学

身の回りの廃熱を電力へ変換する熱電変換技術は、未利用熱の有効活用の観点から注目されている。熱電性能はゼーベック係数 S、電気伝導率 σ、熱伝導率 κ から定義される無次元性能指数 ZT ($ZT = S^2\sigma T/\kappa$) およびパワーファクター (PF = $S^2\sigma$) によって評価される。近年はフレキシブルデバイスへの応用を見据え、有機材料を用いた熱電材料研究が活発に行われている。p 型材料としては PEDOT:PSS が高性能を示す一方、n 型有機材料は大気安定性やドーピング効率に課題を有する。最近では高導電性と大気安定性を兼ね備えた n 型共役ポリマーPBDF が報告されている (Figure 1)[1]。π 共役配位高分子である NiETT 錯体も高い大気安定性と n 型熱電特性を示す材料として知られるが、溶媒への難溶性から加工性に課題がある[2-4]。

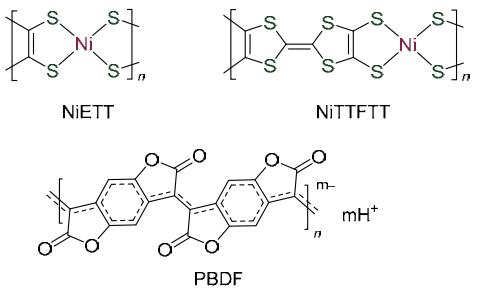
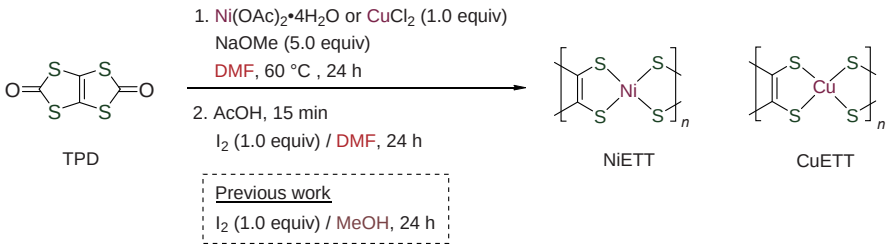


Figure 1. Structures of NiETT, NiTTFTT and PBDF.

本研究では NiETT の合成条件を最適化し、分散性向上と塗布膜の高性能化を目指した。TPD を出発原料とし、DMF 中で NiETT を合成し、ヨウ素酸化時の溶媒を従来のメタノールから DMF へ変更した (Scheme 1)。得られた懸濁液を遠心分離および超音波処理により精製し、NiETT/DMSO 分散液を調製した。これをドロップキャスト法で成膜し、70 °C 乾燥後 210 °C で熱処理した。DLS 測定の結果、分散液中の NiETT 粒子は、従来のボールミル法（650 nm）や水分散液（190 nm）と比較して著しく微細化していることがわかった。粒子の微細化は塗布膜における緻密な導電ネットワーク形成に寄与し、導電率は 320 S cm^{-1} へ向上した。その結果、PF は 57 μW m^{-1} K^{-2} を示し、従来報告値を上回った。UPYS 測定より仕事関数は 4.6 eV であり、従来膜よりも HOMO 準位が真空準位側へシフトしていることが示唆された。また、大気中 18 日間にわたり導電率を保持し、優れた大気安定性を示した。さらに、本知見を基に CuETT の成膜条件も改良し、CuETT/PVDF 膜においても導電性および PF の向上を達成した。

Scheme 1.



1) H. Tang, Y. Liang, C. Liu, Z. Hu, Y. Deng, H. Guo, Z. Yu, A. Song, H. Zhao, D. Zhao, Y. Zhang, X. Guo, J. Pei, Y. Ma, Y. Cap, F. Huang, *Nature* **2022**, *611*, 271. 2) J. Xie, S. Ewing, J.-N. Boyn, A. S. Filatov, B. Cheng, T. Ma, G. L. Grocke, N. Zhao, R. Itani, X. Sun, H. Cho, Z. Chen, K. W. Chapman, S. N. Patel, D. V. Talapin, J. Park, D. A. Mazziotti, J. S. Anderson, *Nature* **2022**, *611*, 479. 3) K. Ueda, R. Fukuzaki, T. Ito, N. Toyama, M. Muraoka, T. Terao, K. Manabe, T. Hirai, C.-J. Wu, S.-C. Chuang, S. Kawano, M. Murata, *J. Am. Chem. Soc.* **2022**, *144*, 18744. 4) R. Yura, T. Itoh, M. Ishihara, D. Suzuki, Y.-C. Kuo, S. Nagata, T. Yumura, S. Hosokawa, M. Murata, Y. Nonoguchi, *J. Mater. Chem. A* **2025**, *13*, 33685.

Resolving Pre-GOE Oxygen Whiffs and Post-GOE Redox State of Paleoproterozoic Oceans through Mo and W isotope Analyses of Sedimentary Rocks of the Dharwar Craton

Gurumurthy G.P.　Birbal Sahni Institute of Palaeosciences

Molybdenum (Mo) and tungsten (W) provide valuable insights into the evolution of ancient marine depositional environments. Their geochemical behaviour is strongly controlled by the oxidation state of the water column, sulfur availability, hydrothermal activity, and interactions with iron-bearing phases, making them important proxies for reconstructing palaeoredox conditions. In oxygenated environments, they occur as soluble oxyanions, whereas under reducing conditions they become scavenged into sediments through adsorption onto Fe–Mn oxyhydroxides, incorporation into sulfide minerals, or association with organic matter. Molybdenum has been extensively used as a proxy for euxinic and anoxic conditions due to its strong enrichment in organic-rich black shales deposited under sulfidic bottom waters. While, tungsten has emerged as a promising proxy for ferruginous and hydrothermal systems, particularly in Precambrian oceans where widespread euxinia was limited. The combined application of Mo and W concentration and their isotope ratios for understanding the links between ocean chemistry, climate evolution, and biogeochemical cycling through geological time. In this study, Mo and W concentration and their stable isotope ratios were measured to study the evolution of redox conditions in the marine sediments during the Precambrian. The project is part of the ongoing research collaboration with Prof. Yoshiki Sohrin and Dr Mahboob Alam, Institute of Chemical Research (ICR), Kyoto University, Japan. The sediment samples were acid digested with HNO_3 and H_2O_2 followed by HF in microwave digestions system (200^{o}C for 1hr). The digestion involved multiple steps to repeated microwave heating to achieve complete digestion. The digested samples were dried and redissolved in HCl. Mo and W were purified through two step chromatography involving TSK-8HQ and anion exchange resin (AG1 X8 resin). The purified Mo and W solutions were spiked with Ru and Re, respectively for isotope ratio measurement. To validate the analytical protocol, certified geological reference materials JMS1 and JMS2 were processed alongside the samples. The stable isotopes of δ^{98}Mo and δ^{186}W were measured in Neptune plus MC-ICP-MS, at the Research Institute for Humans and Nature (RIHN). The stable isotope ratios of δ^{98}Mo and δ^{186}W have been acquired for about 25 sedimentary rocks. The measured dataset is currently being interpreted to discuss the palaeoredox conditions and the development of variability in oxygen minimum zones in the geological past. The results will be published jointly in peer reviewed journal.

Trace metal elemental and isotopic composition in the North Pacific Ocean: sources and internal cycling (5)

Tung-Yuan Ho　Academia Sinica

Objectives:

The major objective of this extended joint study is to investigate the sources and internal cycling mechanisms of trace metals in the water column of the Northwestern and subarctic Pacific Ocean and to evaluate the impacts of aerosol trace metals on the cycling processes of material in the region. Prof. Yoshiki Sohrin is my host at ICR, Kyoto University.

Methods:

We have collected particulate samples in the subarctic Pacific Ocean through the Japanese GEOTRACES GP-02 program, in collaboration with Prof. Yoshiki Sohrin and Hajime Obata. My laboratory has also collected size-fractionated aerosol samples at Penjia Islet in the East China Sea. The elemental and isotopic compositions of trace metals in suspended particulate matter (SPM) and aerosol samples were determined using HR-ICPMS and MC-ICPMS. Detailed descriptions of the analytical procedures can be found in our previously published papers.

Results and Discussions:

We have completed all measurements of various trace metal concentrations and Fe isotopic compositions in the GP-02 SPM samples. Currently, we are preparing a manuscript focusing on the Fe elemental and isotopic composition in plankton assemblages (Ho et al., in prep.). In addition, Drs. Hsieh and Lu visited Prof. Sohrin's laboratory in February 2025 for one month, in which they completed the pretreatment and elemental analysis of aerosol samples. These new findings will be presented at the Goldschmidt 2025 Conference and are currently being prepared for publication.

Publications:

Prof. Sohrin and I, along with our laboratory members, have maintained close collaboration on the proposed topics. Over the past 5 years, our joint efforts have resulted in the publication of 5 peer-reviewed papers. In addition, 3 more collaborative manuscripts are either under review or currently in preparation. Below is a list of the newly prepared and submitted manuscripts:

Sohrin, Y., L.J. Zheng, C.-Y. Chan, Y. Nakaguchi, S. Takano, R. Sohrin, W.-H. Liao, and **T.-Y. Ho** (2025) Acid-leachability of metals from suspended particles in the Pacific Ocean (*under review*)

Ho, T.-Y., W.-H. Liao, C.-C. Hsieh, K.-F. Huang, S. Takano, **Y. Sohrin**, and Hajime Obata (2025) Fe quota and isotopic composition of phytoplankton assemblages in the subarctic Pacific Ocean (*in prep.*)

Hsieh, C.-C., S. Takano, K.-F. Huang, **Y. Sohrin**, and **T.-Y. Ho** (2025) Tracing Fe sources in size-fractionated aerosols from the Western Philippine Sea by using elemental and isotopic composition (*in prep*.)

Chain orientation in single electrospun fibers: diameter dependence and correlation with mechanical properties

Chi Wang　National Cheng Kung University

Background and objective

Biodegradable P(3HB) is strong but brittle because of high crystallinity and secondary crystallization. We identify how 3HH copolymerization improves ductility by resolving structural changes from the lamellar to submicron hierarchy during stretching.

Experiment

Unoriented press sheets of P(3HB) and P(3HB-co-11 mol% 3HH) were drawn uniaxially at room temperature (1 mm min^{-1}). USAXS/SAXS/WAXS were measured in situ at SPring-8 BL03XU.

Key Finding

Initial state: P(3HB) formed thick crystalline lamellae, regular stacks, and spherulites densely filled with fibrils. The copolymer had lower crystallinity and long-range crystal order, thinner lamellae, and looser fibril packing.

Near yield: P(3HB) yielded at 2.38% strain and showed a strong “abnormal butterfly” pattern in USAXS. It reflects large stress heterogeneity and density fluctuations on the submicron scale, followed by nanovoid formation and early fracture.

The copolymer yielded at 6.74% strain. Its butterfly pattern was weaker, while deformation proceeded through coarse slip and mechanical melting. A beta form developed after yield from chains extracted from alpha crystals, allowing drawing to continue after void formation.

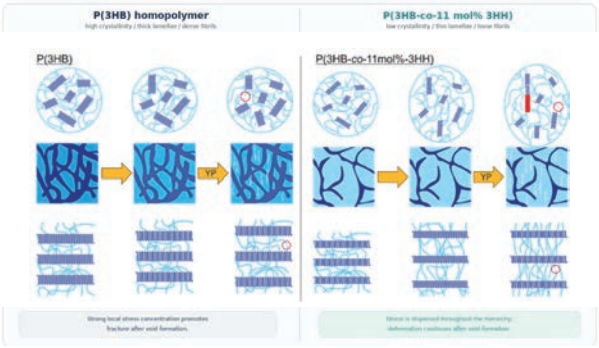


Fig. 3Summary schematic of hierarchical-structure model. 3HH copolymerization suppresses crystallization and reduces crystal stability, thereby moderating local stress concentration from the lamellar to submicron scale**.**

Conclusion

3HH incorporation does more than simply reduce crystallinity: it reorganizes the lamellar–fibrillar–spherulitic hierarchy and disperses stress. This weakens heterogeneous deformation around yield, prevents rapid fracture, and substantially enhances the ductility of P(3HB).

Imaging of Block Copolymer Morphology with Small Angle X-ray Scattering

Byeongdu Lee　Argonne National Laboratory

My research focuses on advancing x-ray imaging techniques to study complex material systems. Recently, my group developed a method combining x-ray ptychography and small-angle x-ray scattering (SAXS) to visualize DNA-programmable nanoparticle assemblies. These complementary techniques offer low-resolution real-space and high-resolution reciprocal-space information, respectively. While initially demonstrated for gold nanoparticle assemblies, this approach has the potential to be applied to soft material systems, such as block copolymers.

I have initiated collaboration with Prof. Mikihito Takenaka to apply advanced x-ray imaging techniques, including those based on Fourier synthesis, to his block copolymer systems. As a leading researcher in the field, Prof. Takenaka brings extensive expertise in block copolymer studies and SAXS applications. Together, we aim to explore various SAXS imaging methods for visualizing both standard and advanced block copolymer systems, further pushing the boundaries of this emerging approach.

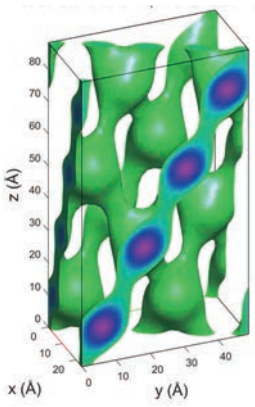


Figure 1. Electron density map obtained from SAXS data

In phase 1, we planned to apply my SAXS analysis software to reconstruct the unit cell structure of novel block copolymer systems developed by Prof. Takenaka's group. During this phase, I updated the software for analyzing soft materials. Figure 1 shows the electron density map calculated from one of Prof. Takenaka's SAXS data.

In phase 2, we anticipate to run samples at the APS 12-ID-E beamline and collect SAXS and imaging data on the same sample. Imaging may visualize the heterogeneity larger than ~100 nm, or its focusing optics can be used for scattering measurement of structures within the 100 nm domain. Upon the successful completion of the final phase, we will establish a novel nanostructure analysis method tailored for soft material systems. This advancement will have a broad impact across various fields of nanoscience, including colloidal science, nanoparticle research, molecular science, and polymer science. It will enable more accessible and accurate nanostructure analysis, allowing researchers to visualize their systems with greater ease and gain deeper insights into the underlying physics.

Elucidation of anti-stokes shifted photoluminescence from lead-based halide perovskite

Yasuhiro Tachibana　RMIT University

Introduction

Metal halide perovskite have recently attracted considerable attention as one of the most promising materials to be applied for optoelectronic devices such as light-emitting diodes (LEDs), solar cells and lasers, owing to their low-cost preparation process and attractive optical properties including high absorption co-efficient and a band gap tunability. In particular, their photoluminescence (PL) has attractive optical properties such as high PL quantum yield (PLQY) and anti-stokes shifts. Recently, we have developed a method to synthesize $MAPbI_3$ perovskite nanocrystals with a PLQY of ~100 % (manuscript in preparation). The anti-stokes shift of their PL spectra, i.e. higher energy emission band with lower energy excitation, has been reported.

In this proposal, we aim to identify the conditions to indicate anti-stokes shifts using steady state and transient PL spectrometers, and to elucidate the origin of this anti-stokes shifts using fs-ps transient absorption spectrometers. Professors Teranishi and Wakamiya at the ICR have expertise of developing metal halide perovskite structures and homogeneous perovskite films, and thus this project in collaboration with them will lead to innovative outcomes to elucidate the anti-stokes shift mechanisms.

Experimental

(1) Identifying conditions to show anti-stokes shifts

We will observe anti-stokes shifts of PL spectra and transient PL spectra of lead-based halide perovskite films using a fluorometer and a home-built transient emission spectrometer. A wide range of excitation wavelengths and intensities will be employed. Teranishi and Wakamiya will prepare perovskite films, and characterise film structures by employing X-ray spectroscopy and electron microscopies, while Tachibana and his PhD student will measure PL and transient PL spectra.

(2) Elucidation of the anti-stokes shift mechanisms

Ultrafast transient species will be observed by femtosecond-picosecond transient absorption spectrometers. The transient data will be analysed using global and target analysis to identify the reaction pathways and emission mechanisms. Tachibana and his student will conduct optical measurements.

Results and Discussion

Size tunable $CsPbCl_3$ nanocuboids (3~13 nm) with a small size distribution of ±1~2 nm were obtained by modifying synthesis conditions such as precursor or ligand concentration.[1] These nanocrystals show clear anti-stokes shifts of their PL spectra. We also found clear anti-stokes shifts of PL spectra obtained for mixed A-site cation lead bromide/iodide perovskite film prepared by Wakamiya's group.

We also found specific recipes can provide pure Cs_2SnI_6 nanocrystal formation. We will summarise and publish the most appropriate condition to control Cs_2SnI_6 nuclei formation and crystal growth.

We identified the relationship of spin-coating temperature with lead-based perovskite film morphology and solar cell performance.[2] We have also reviewed the parameters controlling charge carrier dynamics, and established key parameters to maximise solar cell performance.[3]

Outcomes

[1] **Teranishi, Tachibana** and co-workers, *J. Photopolym. Sci. Technol.*, **38**(5) 369-375 (2025).
[2] **Wakamiya**, **Tachibana** and co-workers, *ACS Appl. Energy Mater.*, **8**(3) 1437-1445 (2025).
[3] **Tachibana** et al., *Jpn. J. Appl. Phys.*, **64**(5) 050806 (2025).

Investigation of molecule arrangements in artificially abrupted self-assembled monolayers with surface specific spectroscopy techniques

Wei-Ssu Liao　National Taiwan University

Objectives In this collaboration with Hasegawa Group, we aim on utilizing the surface sensitive *p*-polarized Infrared Reflection-Absorption Spectroscopy (IRRAS) to qualitatively analyze the conformation of alkanethiol self-assembled monolayer (SAM).

Experimental Methods A unique solvent-sonication-washing (SSW) treatment of alkanethiol SAMs followed by re-insertion of another alkanethiol molecule is first characterized by IRRAS. In the SSW treatment, the 11-mercapto-1-undecanol (MCU)-covered Au samples were treated with a 1-min sonication in polar and non-polar solvents. Finally, the treated samples were immersed in alkanethiol solutions for 1 h of re-insertion. By setting the incident angle of the *p*-polarized IR source to ~80°, *p*-polarized IRRAS allows qualitative analysis of the orientation angles of vibrational groups.

Outcomes and Analysis We first examine the pure MCU-covered Au (MCU) as a reference (*blue solid line*), Figure 1. Four peaks are observable, with peaks at ~2922 cm^{-1} (CH_2-as) and ~2853 cm^{-1} (CH_2-ss) being the long carbon chain of MCU (*yellow shaded*). Potential environment contamination results in the CH_3-as mode as a weak shoulder at ~2964 cm^{-1} (*blue shaded*). Another peak at ~2875 cm^{-1} (α-CH_2-ss) appears much weaker since there is only one CH_2 next to the O-H terminal group (*green shaded*). For the SSW-treated sample (*orange dashed line*), the overall intensity decreases suggest the removal or orientation difference of the SAMs. Moreover, the CH_2-as and CH_2-ss peaks shift towards a higher frequency, indicating a more disordered (gauche conformation) environment. In the ODT re-insertion sample (*green dashed-dot line*), the peaks at ~2963 cm^{-1} (CH_3-as) and ~2875 cm^{-1} (CH_3-ss) indicate the successful re-insertion of ODT. Moreover, the CH_2-as and CH_2-ss peaks shift back, pointing to the restored order of SAM. In short, the SSW treatment can artificially disorder the original monolayer, allowing the re-insertion of molecules to form ordered mixed SAMs. Further tests on different substrate pretreatments are planned for molecular packing effect comparison. (The manuscript of this work is under preparation.)

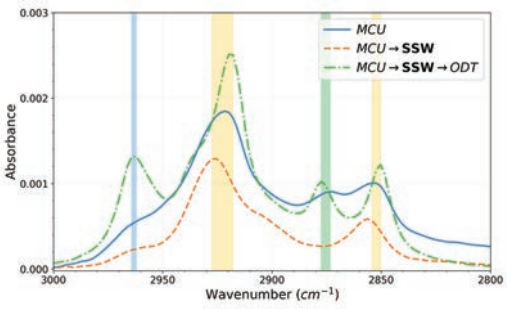


Figure 1. Representative IRRAS spectra of SAM on Au: MCU/Au (*blue solid line*), post-SSW-treated MCU/Au (*orange dashed line*), and post-SSW-treated MCU/Au followed by ODT re-insertion (*green dashed-dot line*). CH_2, CH_3, overlapped peaks are shaded in yellow, blue, and green, respectively.

Nonlinear Rheology of Dynamically Associative Ionomers

Quan Chen　Chinese Academy of Sciences

Nonlinear shear behavior was examined for a representative dually crosslinked elastomer, poly(vinyl alcohol) (PVA)/Borax hydrogel having both permanent and transient crosslinks, the former due to covalent bonds and the latter sustained by a complex of the hydroxy group and borate ion. The PVA chain backbone between the transient crosslinks behaved as the transient network strand partially relaxing on thermal dissociation and/or mechanical breakage of the transient crosslinks. For comparison, the nonlinear behavior was also examined for bulk SI(COOH)S block copolymer having glassy spherical domains of the S block as the permanent end-crosslinks for the I blocks and the hydrogen bonds between carboxyl groups as the transient crosslinks. The I block backbone between the carboxyl groups served as the transient network strands.

The nonlinearity can be straightforwardly tested under a shear strain γ shown in Figure 1: The strain γ is increased at a constant rate $\dot{\gamma}$ from time $t = 0$ to $t = t_m$, and then kept constant at $\gamma_m = \dot{\gamma} t_m$ for $t > t_m$. The resulting shear stress $\sigma(t)$ is compared with the linear viscoelastic (LVE) stress calculated from the relaxation modulus $G(t)$, $\sigma_{LVE}(t) = \int_0^t G(t-t')\dot{\gamma}(t')\,dt'$, to judge if the material remains in the LVE regime.

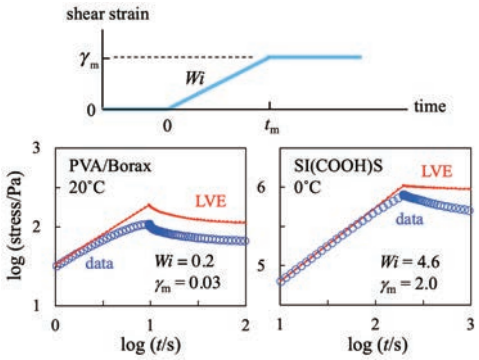


Figure 1. Test of nonlinearity of PVA/Borax and SI(COOH)S systems under shear strain.

It turned out that the PVA/Borax hydrogel shows strong shear-softening even under a very slow and small shear characterized with the Weissenberg number $Wi = \dot{\gamma}\tau = 0.2$ (with τ being the terminal relaxation time) and the total $\gamma_m = 0.03$. Namely, the LVE response of this gel vanished even under a very mild shear. The SI(COOH)S copolymer showed softening of a similar magnitude but under a stronger shear condition, $Wi = 4.6$ and $\gamma_m = 2.0$. These nonlinear features can be related to the shear-induced breakage of the transient crosslinks that results in anisotropy of the population of the network strands reformed in different directions as well as non-equilibrium motion of the strands connected to the broken transient crosslinks. The difference between the PVA/Borax hydrogel and the SI(COOH)S copolymer, the nonlinearity much stronger for the former, could be related to the mobility of the transient crosslinks (-OH/borate ion complex) along the PVA backbone and lack of the mobility of the carboxyl group along the I block backbone.

Stoichiometry of biologically active trace metals in Osaka Bay and its inflowing rivers (3)

Yuzuru Nakaguchi　Kindai University

Porpose) My research has focused on the distribution behavior of bioactive trace metals (hereinafter "trace metals") in Osaka Bay. Previous results revealed the vertical distribution of dissolved trace metals and showed high concentrations in the inner bay, suggesting supply from the Yodo, Kanzaki, and Yamato Rivers. This year, I analyzed total dissolvable trace metals (tdMs) in addition to dissolved trace metals (dMs). By subtracting dMs from tdMs, I was able to clarify the distribution of leachable particulate trace metals (lpMs).

Experimental Methods) Sampling stations are shown in Fig. 1. Seawater samples from Osaka Bay were collected in February 2023 using Niskin bottles. Samples for the measurement of total dissolvable trace metals (tdMs) were left unfiltered, adjusted to pH 2.0 using hydrochloric acid, and stored for more than six months before being filtered through a 0.45 μm filter. Trace metal analysis was performed by pre-concentrating the samples using an automated solid-phase extraction system equipped with a chelating resin (Nobias PA-1), followed by quantification using ICP-MS . The concentration of leachable particulate trace metals (lpMs) was calculated by subtracting the dMs from the tdMs.

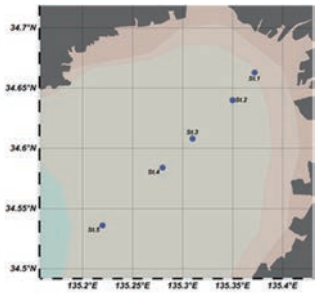


Fig.1 Sampling station

Results) Figure 2 shows vertical profiles of salinity, lpAl and lpCu. High concentrations of lpAl were observed in surface waters in the inner bay (St.1-3). Because surface salinity in this area was low, lpAl was considered to be derived from river water. Similar distribution patterns were also observed for lpFe and lpPb, suggesting that these elements were likewise of riverine origin. In contrast, lpNi, lpCu, lpCo, and lpZn were considered unlikely to be derived from river water. In addition, lpAl, lpFe, and lpPb showed high concentrations in the bottom layer (15-30 m) at St.3, St.4, and St.5, indicating a possible contribution from sedimentary sources. The enrichment factor relative to the crust (EFcrust= [lpMs/lpAl]/[Mcrust/Alcrust]), commonly used in atmospheric chemistry, was applied to river water and calculated. As a result, EFcrust(lpFe) was 2.1 ± 1.0, suggesting that river-derived lpFe originates from the Earth's crust (i.e., riverine erosion). EFcrust(lpCo) was 12 ± 12, indicating that lpCo was also likely of crustal origin. Other elements showed EFcrust values greater than 10; in particular, lpPb exhibited a very high value of approximately 1600. This suggests that although lpPb is river-derived, it is introduced into rivers largely through anthropogenic sources.

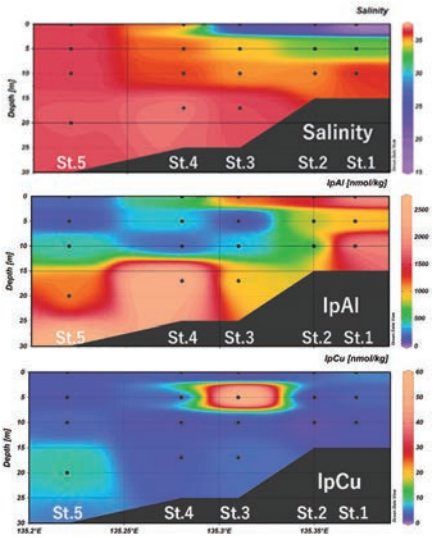


Fig.2 Cross sectional distributions of salinity, lpAl and lpCu

Separation and concentration of rare metals by a liquid membrane transport method using ionic liquid

Hiroshi Mukai　Kyoto University of Education

[Objectives] One of the problems in industrial use of rare metals is.difficulty in refining process. This study aim to develop the novel and efficient methods for separation and concentration of rare metals. A liquid membrane transport method using ionic liquids (ILs) was considered for the purpose. The membranes used were polymer inclusion membranes (PIMs) with hydrophobic ILs. In order to enhance the selectivity of metal ions, two improvements were attempted. One was to use the PIMs previously containing the complexes of the target metal ion with carrier molecules. The other was to apply alternative voltage to the supplying phase. The effects of these two attempts to metal selectivity were investigated.

[Experimental] (1) Membranes. 1-Phenyl-3-methyl-4-benzoylpyrazol-5-one (PMBP) of 0.014 g (5×10^{-5} mol) was dissolved in 1-butyl-3-dodecylimidazolium bis(trifluoromethanesulfonyl)imide ($[C_4C_{12}im][Tf_2N]$) or 1-dodecyl-3-methylimidazolium bis(trifluoromethanesulfonyl)imide ($[C_{12}C_1im][Tf_2N]$) of 1.000 g. The IL solution of 1.014 g was mixed with PVC of 0.100 g dissolved in tetrahydrofuran in the glass petri dish and dried. (2) Liquid membrane transport. The membrane was fixed at the center of a U-shaped reaction tube. The 30 cm^3 of aqueous supplying phase ($[Co(NO_3)_2$, $Zn(NO_3)_2$, $Cd(NO_3)_2$, $Pb(NO_3)_2] = 2.0\times10^{-5}$ mol dm^{-3}, $[CH_3COONa] = 0.01$ mol dm^{-3}, $[NaClO_4] = 0.1$ mol dm^{-3}, pH 5.0) and the 30 cm^3 of aqueous receiving phase ($[CH_3COONa] = 0.01$ mol dm^{-3}, $[NaClO_4] = 0.1$ mol dm^{-3}, $[HNO_3] = 0.1$ M, pH 1) were poured into each part of the reaction tube separated by the membrane and stirred fot 24 hours.

[Results and discussion] (1) Effect of complexes previously contained in PIMs. Cobalt ions were loaded as complexes in a PIM when target metal was cobalt. A site occupation rate was defined as a ratio of an amount of cobalt ions to a maximum amount of metal binding sites calculated from an amount of PMBP in a PIM. As shown in figure, cobalt complexes in the PIM with high site occupation rate exclude metal ions not targeted. (2) Effect of alternative voltage in the supplying phase. Effect of alternative voltage in the supplying phase was investigated using separation factors (α_{AB}) of metal A and B calculated from transport rates. Table shows enhancement of separation from cadmium by alternative voltage. This was caused by suppression of the transport of metal ions, especially cadmium ions, to the membrane phase by the influence of alternative voltage.

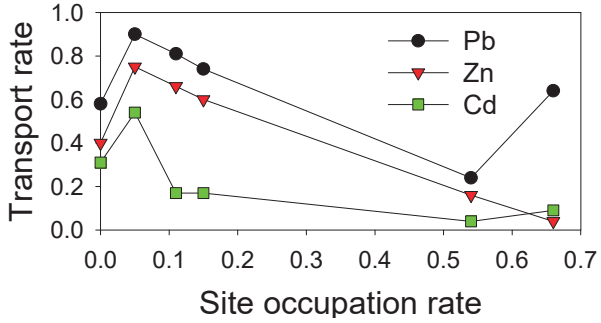


Figure. The dependence of transport rates on site occupation rates of cobalt ions in PIM.

Table. The α'_{AB}/α_{AB} values that show the influence of alternative voltage on separation of metal ions.

B \ A	Co^{2+}	Zn^{2+}	Cd^{2+}	Pb^{2+}
Co^{2+}	1	1.07	0.41	1.05
Zn^{2+}	0.94	1	0.38	0.98
Cd^{2+}	2.46	2.62	1	2.57
Pb^{2+}	0.96	1.02	0.39	1

時分割超小角・小角・広角 X 線散乱法による ゴム中フィラーの分散に関する研究

西辻祥太郎　山形大学

目的

ゴム/フィラー混合系材料においては、充填されているフィラーの分散状態が力学物性に影響を与える。したがって、高性能化に向けてフィラーの分散状態と力学物性の関係を理解することは極めて重要である。本研究では、時分割超小角・小角・広角 X 線散乱法を用いて、一軸伸張下におけるスチレン-ブタジエンゴム(SBR)中シリカの分散状態の変化を明らかにする。特にシランカップリング剤の効果について着目する。

実験方法

この研究では、SBR（重量平均分子量 $M_w = 500{,}000$）にシリカとシランカップリング剤をフィラーとして混合した。シリカは体積率で 1、3、5、10、15、20 vol%にて添加した。これらの試料に対して一軸伸長変形下で時分割超小角 X 線散乱測定を行った。また、デジタル画像相関法(DIC)を用いてサンプルの X 線が照射されている場所のひずみを測定した。測定は SPring-8 のビームライン BL03XU で実施した。

実験結果

時分割超小角 X 線散乱測定で得られた散乱パターンから、伸長方向と伸長に対して垂直方向の 1 次元プロファイルを得た。それらの散乱プロファイルに対して Polydisperse Born-Green Approximation(PBG)解析を適用し、凝集体間の相関距離を推定した。図 1 は、伸長に伴う平行方向および垂直方向の凝集体の相関距離を示している。平行方向の相関距離がひずみ増加とともに増加し、直交方向では減少している。

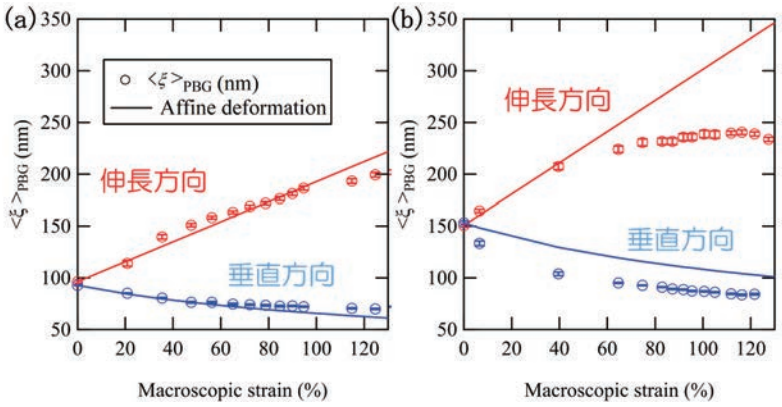


Figure 1. (a)SBR/シリカ/シランカップリング剤と (b)SBR/シリカの凝集体間の相関距離

考察

シランカップリング剤が混合されている場合、凝集体間の相関距離はアフィン変形に従う。つまり、ゴムとフィラーがシランカップリング剤で結合しているため、ゴムの変形に伴ってフィラーも変化することを示している。一方、シランカップリング剤が混合されていない場合、凝集体間の相関距離はアフィン変形に従わない。つまり、ゴムは変形する一方、フィラーは滑りが生じ変形しないということである。

成果報告

T. Yoshida, D. Iwahara, S. Nishitsuji, N. Amino, Y. Watanabe, M. Takenaka, International Rubber Conference 2025, 1-3 December 2025, BITEC, Bangkok, Thailand.

プラズモニック合金ナノ粒子を設計するための理論的指針の構築

飯田健二　北海道大学

自然界の限られた資源を有効活用するためには、様々な元素を組み合わせることで高性能な物質・材料を創造していくことが求められる。可視域に局在表面プラズモン共鳴(LSPR)吸収を示す材料の場合、周期表 11 族の単金属（Cu、Ag、Au）のみが使われてきた。そうした中で、京都大学化学研究所の寺西研究室において、*B*2（塩化セシウム）型や *C*1（フッ化カルシウム）型の合金ナノ粒子が可視域に LSPR 吸収を示すことが発見された。

我々は、規則合金の *B*2 型や *C*1 型の幾何的構造が LSPR の発現に重要な役割を果たすことを明らかにしてきた。そうしたなかで新たに、六方晶型の構造を有する PtSn のナノ合金が合成された。光吸収スペクトルについて、LSPR の発現に起因すると考えられる複数のピークが見出された。歪んだ *B*2 構造と見なされる構造を有しており、わずかな構造歪みで光物性が変化することが示唆される。そこで我々は、PtSn の光学応答の機構を明らかにするために、超並列第一原理計算プログラム SALMON を用いて研究を行った。

[計算手法] 本研究では、直径数 nm のナノ粒子の光電子物性を原子スケールで明らかにすることが求められる。そのために、高い並列化効率を有する第一原理計算プログラム SALMON を用いて、光励起電子ダイナミクスをシミュレーションした。PtSn の結晶構造(図 1)から直径約 3 nm のナノ粒子を切り出して計算した。

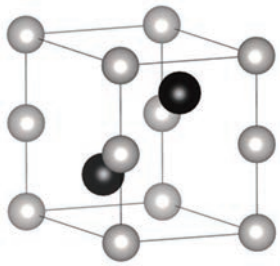


図 1. 用いた PtSn ナノ粒子の結晶構造。黒と白はそれぞれ Sn と Pt。

[結果と考察] 光吸収スペクトルを計算したところ、複数の光吸収ピークが見出された。また、偏光方向によってピーク位置が異なっており、実験と同様の結果が得られた。そこで、光励起電子ダイナミクスの解析を行った。その結果、Au などの LSPR と同じく、電子の集団運動が粒子表面で確認された。さらに、電子の集団運動が複数の光波長で生じていることが見出された。そこで、それぞれの光波長での励起の機構を明らかにするべく、粒子内部の電子ダイナミクスを解析した。その結果、幾何構造の歪みに起因して、偏光方向に応じて電子系の応答の仕方が異なり、そのために LSPR が複数の光波長で励起されることが分かった。

[学会発表]

1. 飯田健二，"ナノ物質の光や電圧に対する応答機構についての理論計算研究"，ナノ学会第 23 回大会，東京都立大学 (2025 年 5 月 14 日-16 日) [招待講演]

[論文]

2. Iida, K.*; Kato, S.; Hasegawa, J., Catal. Sci. Tech. **2025**, *15*, 3550–3560.

Structure analysis of liquid crystalline organic thin films

Shingo Maruyama　Tohoku University

Fabrication of high-quality crystalline organic semiconductor thin films is important for advances in organic electronics. As one method for fabricating organic semiconductor thin films with high crystallinity, our group has reported a technique to control crystal nucleation during crystallization from the liquid crystalline (LC) state by using temperature gradients during the post-annealing process of vacuum-deposited LC organic semiconductors (e.g. Tsujita et al., CrystEngComm, 2023, 25, 64‑71.). In this study, we attempted to use a nucleation-inducing layer as a new method for controlling nucleation and for preparing large-area single-crystalline C8-BTBT films without a special temperature-gradient. We used the grazing incidence X-ray diffraction (GIXD) instrument at ICR Kyoto University to measure in-plane alignment through φ scans.

C8‑BTBT films were deposited at room temperature on SiO_2/Si substrates by infrared laser deposition. Pentacene layer (1.5 nm) was introduced only in a defined nucleation region, followed by deposition of C8‑BTBT (200 nm) to form an adjacent growth region. After deposition, samples were annealed at 115 °C, above the LC transition temperature of C8‑BTBT (110 °C), to obtain a uniform LC phase. They were cooled to 107 °C to trigger nucleation, confirmed by in-situ polarized optical microscopy. After nucleation, crystal growth was continued either at 107 °C or at 109 °C. In-plane orientation of C8-BTBT thin films was evaluated by XRD φ-scans of the C8‑BTBT 020 diffraction peak using the ICR GIXD setup.

Nucleation in the C8-BTBT film appeared immediately in the pentacene-seeded region after cooling, and crystallization propagated laterally into the growth region. Fig. 1 shows in-plane φ-scans of the C8-BTBT 020 diffraction peak for the samples grown at 107 °C and 109 °C. A clear two-fold symmetric φ-scan profile was obtained, demonstrating uniaxial in-plane alignment induced by the seeded nucleation and subsequent lateral growth. Importantly, the post-nucleation growth temperature strongly affected the degree of alignment: when crystal growth was carried out at 109 °C, the φ-scan peak was sharp with a full width at half maximum (FWHM) of ~3°, whereas growth maintained at 107 °C resulted in a broader peak (FWHM ~8°). These results indicate that reducing the degree of supercooling after nucleation is effective for enhancing in-plane alignment in C8-BTBT films. This is likely because smaller supercooling promotes molecular rearrangement at the growth front while suppressing secondary nucleation and defect formation in the growth region, thereby narrowing the azimuthal distribution in the φ-scan.

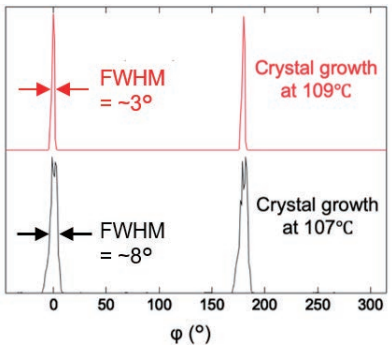


Fig. 1 In-plane φ-scans of the C8-BTBT 020 diffraction peak for the samples grown at 107 °C and 109 °C

Study on crystalline structure and transistor characteristics of liquid crystalline organic semiconductors

Hiroaki Iino　Institute of Science Tokyo

The liquid crystalline organic semiconductor, 2-decyl-7-phenyl-benzothienobenzothiophene (Ph-BTBT-10: Fig. 1(a)) is a promising material for organic field effect transistor (OFET). This is due to its ability to form uniform polycrystalline thin films with high crystallinity by solution process using its liquid crystallinity. However, the mobility of Ph-BTBT-10 thin films degrades after thermal process at temperature above 143 °C, which corresponds to the smectic E (SmE) liquid crystal phase. This is a significant issue because fabrication processes for organic electronics typically involve thermal stress around 150 °C. In this collaboration with Mr. Oka, Dr. Shioya, and Prof. Hasegawa at Kyoto University, we previously investigated the origin of Ph-BTBT-10 OFETs degradation following thermal stress at 150 °C and found that polycrystalline thin film fabricated with a slow cooling rate exhibit minimal degradation even after thermal stress [1]. In this collaboration study, we investigated the optimal additional thermal annealing conditions to recover OFET performance after thermal stress (150 °C) followed by rapid cooling.

Ph-BTBT-10 polycrystalline thin films were fabricated by spin-coating at the temperature of liquid crystal phase, heated at 150 °C (SmE phase), and then cooled to the crystalline phase at room temperature. Subsequently, the films were treated with additional thermal annealing to improve the crystallinity. The crystallinity and molecular packing structure were evaluated using X-ray diffraction (XRD) and infrared (IR) spectroscopy. FET performance was evaluated by transfer characteristics of bottom gate bottom contact type OFETs.

The XRD and IR spectroscopy analysis revealed that rapid cooling from the SmE phase causes partial disorder in the molecular packing and the conformation of the alkyl side chains. On the other hand, the analysis suggest that crystallinity of the thin films can be recovered by additional thermal annealing at 120 °C for 15 minutes.

In order to confirm the effectiveness of the additional annealing condition, we evaluated the charge carrier transport properties in channel region from OFET performance. Ph-BTBT-10 polycrystalline thin film after treated additional anneal at 120 °C for 15 minutes showed the high crystallinity and mobility of 1.3 cm^2/Vs (Fig. 1(b) "Additional annealed"), which is higher than that of rapid cooled films (Fig.1(b) "150 °C Rapid") and comparable to that of slowly cooled polycrystalline thin films (Fig.1(b) "150 °C Slow").

In conclusion, we succeeded to find the suitable prosses conditions to recover the performance of Ph-BTBT-10 polycrystalline film after thermal stress at 150 °C.

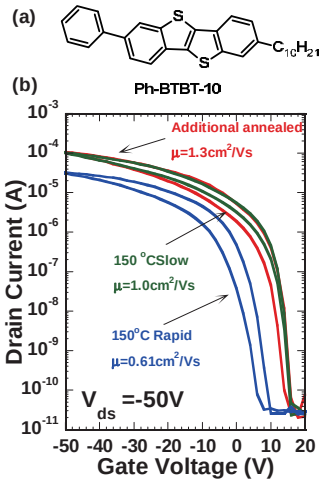


Fig.1 Ph-BTBT-10 transistors (a) Chemical structure, (b) transfer characteristics

[1] H. Nakano, T. Oka, N. Shioya, T. Hasegawa, H. Iino, Fall meeting of Jpn. Soc. Appl. Phys. 18pD63-6 (2024).

Relationship between primary structure of partially fluorinated phospholipids and membrane properties

Takafumi Shimoaka　Gunma University

In the past decade, our research group has been developed a variety of phosphatidylcholines (PCs) with partially fluorinated hydrophobic chains (C_nF_{2n+1}), and as a result of comprehensive studies of the bilayer membranes, the relationship between the membrane properties and their chemical structures is becoming clear.[1] Recently, one of the developed PCs is found to exhibit interesting phase behavior by mixing with a non-fluorinated PC with the same length of hydrophobic chains by calorimetric measurements, which implies that these PCs are mixed with each other. To reveal the molecular mechanism of the two-dimensional mixing of PCs, in this joint research, we focus on binary mixed monolayer films on the water surfaces, which have the following advantages.

1) Molecular packing in the mixed film can quantitatively be discussed by surface pressure (π)-surface area (A) isotherm measurements.
2) Brewster angle microscope (BAM) can be applied, which enables us to visualize mixing in the scale of several tens to hundreds μm.
3) Molecular packing and orientation of PCs can be discussed by vibrational spectroscopic measurements.

In this year's joint research, miscibility of dipalmitoylphosphatidylcholine (DPPC) and its partially fluorinated ones (F*n*-DPPCs) was investigated by BAM measurements. The miscibility of these PCs on the BAM scale was found to depend on the mixing ratio, and the differences in the BAM images were discussed by infrared spectrometry in terms of molecular packing of the hydrophobic chains. In addition, partially fluorinated palmitic acids (F*n*-PAs), a precursor of F*n*-DPPCs, were also investigated by the same techniques.

In addition, a new analytical method for investigating the molecular orientation of perfluoroalkyl groups using backscattering Raman spectrometry was established and reported in *Analytical Sciences*.[3] The paper was selected as one of the Hot Articles in the August issue.

References

1. K. Morita et al., *Chem. Lett.* **2019**, *48*, 1105., M. Miyazaki, et al. *BBA-Biomembranes* **2024**, *1866*, 184261.
2. T. Hasegawa, *Chem. Rec.* **2017**, *17*, 903.
3. T. Shimoaka et al., *Anal. Sci.*, **2025**, *41*, 1355.

Identification of bioactive gibberellins in the liverwort *Marchantia polymorpha*

Yoshihiro Yoshitake　Kyoto University

Gibberellins (GAs) are among the major phytohormones regulating plant growth and development. GA biosynthetic genes and receptors have been isolated mainly from *Arabidopsis* and rice plants. To systematically understand the origin of GAs and the molecular evolution of the GA signaling pathways, we focused on *Marchantia polymorpha*, a model bryophyte that belongs to the lineage sister to vascular plants. *M. polymorpha* lacks the enzymes required to catalyze the final steps of GA biosynthesis in angiosperms but is capable of producing GA precursors such as *ent*-kaurenoic acid (KA) and GA_{12}. The biosynthesis of these precursors is upregulated under far-red light (FR)-enriched conditions, whereas the disruption of the KA biosynthesis genes consistently inhibited FR-induced hyponastic growth and sexual reproduction. Exogenous application of KA fully rescues the biosynthetic mutants, suggesting that a GA-related compound functions physiologically in *M. polymorpha* (Sun *et al*., 2023 The Plant Cell). However, the active GA-related molecules (GA_{Mp}) remain unidentified. In addition, the receptor for GA_{Mp} is also unidentified, as the receptors for angiosperm GAs, GIBBERELLIN INSENSITIVE DWARF1 (GID1), are absent from the bryophyte lineage.

To identify GA_{Mp}, a bioassay method was developed for *M. polymorpha*. Fractionated samples were prepared from wild-type extracts using a two-phase partition method. The bioassay used sexual organ formation as an indicator, as GA biosynthesis mutants exhibit delayed sexual organ formation. Further analysis revealed that fractions containing low-polarity acidic substances accumulated and contributed to the restorative effect. Detailed HPLC fractionation using both reversed-phase and normal-phase columns showed that a specific fraction restored the timing of sexual organ formation in GA biosynthesis mutants. GC-MS analysis suggested that GA_{Mp}, found in this active fraction, has an *ent*-kaurane (KA) skeleton rather than an *ent*-gibberellane skeleton. Furthermore, we identified another crucial KA-related intermediate of GA_{Mp} that is shared by various plant lineages, including angiosperms. These results suggest that *M. polymorpha* produces these KA derivatives by adding a unique final biosynthetic step. The precise structure of GA_{Mp} will be determined in future studies using a combination of mass spectrometry and NMR.

Publication

Sun *et al.* Biosynthesis of Gibberellin-Related Compounds Modulates Far-Red Light Responses in the Liverwort *Marchantia Polymorpha*, Plant Cell 35, 4111–4132 (2023)

Conference reports

Okabe *et al*. Exploring the biosynthetic pathway of gibberellin-related compounds in the liverwort *Marchantia polymorpha* through the diversity of cytochrome P450. The 60th Annual Meeting of the Japanese Society for Chemical Regulation of Plants.

実験およびシミュレーションによる非絡み合い高分子のダイナミクスの統一的解析

佐藤健　金沢大学

高分子のダイナミクスを理解することは、高分子を用いた化学・成形プロセスの最適設計のために重要である。これまでの研究によって、高分子のダイナミクスを記述する標準的なモデルが構築され、歪みの小さい線形領域の粘弾性やダイナミクスの精密に再現することに成功している。一方で、化学・成形プロセスにおいて重要な非線形レオロジーについては、分子量が小さい非絡み合い高分子についてすら従来の標準モデルで精密に記述できていない。この理由の 1 つとして、非絡み合い高分子系では、微弱な信号強度の問題から非線形レオロジー計測が難しいことが挙げられる。特に、信頼できる伸長レオロジーデータが不足していることは、統一的な理解を阻んでいる。

本研究では、高分子の非線形レオロジーの基礎的理解の深化を最終目的として、非絡み合い状態の高分子溶液の伸長レオロジーをシンプルな装置によって評価することを目指した。具体的には、液柱の最小半径の経時変化から伸長緩和時間を評価する Dripping-onto-Substrate (DoS) 法 [J. Dinic *et al.*, *ACS Macro Lett.*, **4**, 804 (2015)] によって非絡み合い高分子流体のレオロジーを調べた。

測定試料は、当初計画していたポリイソプレン（PI）よりも容易に入手可能な分子量 100 万のポリエチレンオキシド（PEO）水溶液とし、濃度を 0.5wt％から 2.0wt%（いずれも非絡み合い領域）に調製した。Fig. 1(a および b)に、構築した DoS 法の測定系を示す。DoS 法では、シリンジからガラス基板へ検査対象の液滴を着滴させ、形成された液柱の破断過程を高速度カメラで撮影する。撮影した動画は、輝度値に基づいた処理を行うことで各フレームにおける液相と気相の境界を特定し、液柱径の時間発展を定量した。

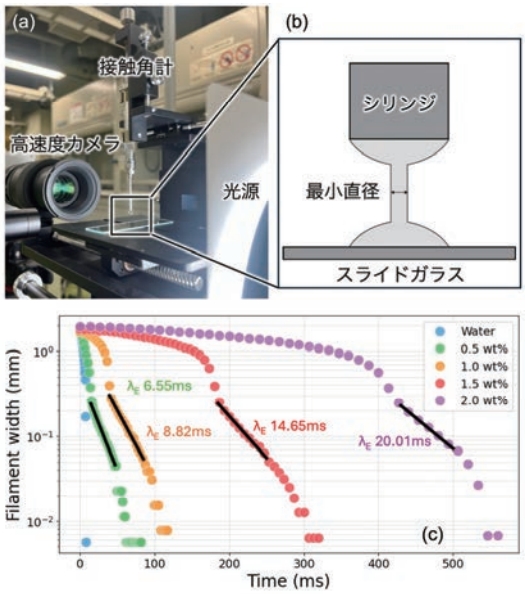


Figure 1：(a, b) 構築した DoS 法の概要と (c) 得られた結果の例。

Fig. 1(c)に、異なる PEO 濃度における液柱径の経時変化を示す。まず、純水においては、極めて短時間で破断に至った。これに対して、PEO 溶液では、急速な直径減少の後に液柱径の減少速度が緩やかになる領域が観測された。この領域において、円柱状の液柱が形成していることが観察された。この中間領域では、PEO 濃度の増加に従って液柱径の減少速度が緩やかになった。各 PEO 濃度における伸長特性を定量化するために、円柱状の液柱が形成されている領域を指数関数でフィッティングし、特徴時間として伸長緩和時間 λ_E を求めた（Fig. 1(c)の黒線）。PEO 濃度が 0.5 wt% から 2.0 wt% へと増加するに従って、λ_E は 6.55 ms から 20.0 ms へと増加する傾向を示した。以上の λ_E の測定値は文献値 [O. Arnolds *et al.*, *Rheol. Acta*, **49**, 1207 (2010)] と近く、測定系の妥当性を確認した。今後は、この測定装置を用いて PI を含む種々の高分子の伸長特性を計測し、非絡み合い高分子のモデリングを深化するための基礎データとしたい。

Exploring Spin Wave Dynamics: From Doppler Effects to Magnonic Black-Hole Analogues

Kab-Jin Kim　KAIST

Objectives: The main objective of this project was to explore spin wave dynamics in a metallic ferromagnetic CoFe film under applied charge current using optical measurements, and to investigate the critical current regime relevant to approaching the magnonic black-hole analogy.

Experimental Methods: A 10 nm CoFe thin film was prepared in a narrow constriction geometry, and its magnetic properties were characterized at KAIST. To effectively excite high-wavevector spin waves and maximize current-induced effects, nanoscale antenna structures with line widths ranging from 100 to 500 nm were fabricated in Prof. Ono's group at ICR. Spin wave propagation under applied current was investigated using a vector network analyzer (VNA) and a heterodyne magneto-optical Kerr effect (MOKE) system, in collaboration with Prof. Ono's group.

Outcomes: A low damping constant on the order of 10^{-3} was confirmed for the CoFe film. By optimizing the constriction width and antenna design, propagating spin waves with wavevectors ranging from 1 to 4 um^{-1} were observed and propagation properties such as decay length and the dispersion relation were directly extracted. Upon increasing the charge current up to the order of 10^{11} A/m^2, a measurable phase shift of the spin waves was observed, which can be attributed to spin transfer torque. The magnitude of the phase shift depended on the applied current and antenna geometry.

Analysis: Using both electrical measurements and spatially resolved optical measurement, we effectively characterized current-driven modifications of spin wave propagation. This work establishes a foundation for future studies targeting the critical current regime and for experimentally approaching the magnonic black-hole analogy.

Publications:

1. M. You, M. Song, D. Lee, S. Yoon, Y. Shiota, T. Ono, S. Kim, S. K. Kim, A. Park, K.-J. Kim, *Nature Communications, accepted* (2026)
2. D. Hayashi, Y. Shiota, M. You, A. Park, K.-J. Kim, H. Narita, R. Hisatomi, S. Karube, T. Ono, *Applied Physics Letters* 126, 082401 (2025)

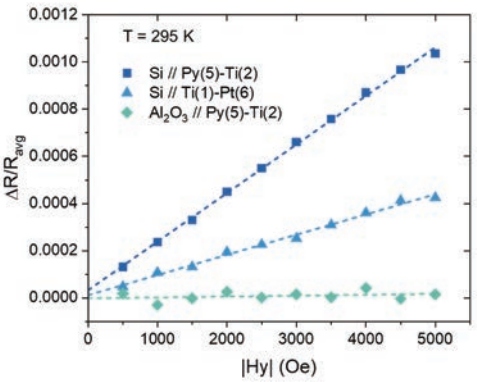
Possible Quantum Origin of Unusual Magnetoresistance in Thin-Film Magnetic Metals

Satoru Emori　Virginia Tech

Objectives: We aim to determine the underlying origin of peculiar electrical signals in metallic magnetic film strips, seemingly resembling the widely studied unidirectional magnetoresistance, but with an unexpectedly large magnitude and magnetic field dependence. In this project reporting cycle, we focused on (1) the influence of the substrate and (2) the role of ferromagnetism.

Experimental Methods: Strips of metallic magnetic films (4 micron wide, 20 micron separation between longitudinal contacts) were patterned with maskless photolithography and liftoff. We focused on the prototypical soft magnetic alloy of permalloy (Py = $Ni_{80}Fe_{20}$) on undoped Si and Al_2O_3 substrates, as well as non-ferromagnetic Pt on undoped Si. The longitudinal resistance was measured under DC currents ranging from 1 to 4 mA, under in-plane transverse magnetic fields of various amplitudes.

Outcomes: The figure summarizes the critical results, i.e., normalized resistance change as a function of applied magnetic field. The substrate makes a significant difference: Py on Si exhibits a clear linear increase of the response, whereas Py on Al_2O_3 exhibits no discernible response. Also surprising is the observation that the non-ferromagnetic Pt also exhibits a sizable response.



Analysis: We deduce that the underlying mechanism is a thermoelectric Nernst effect (not a quantum spin transport phenomenon that we initially set out to uncover), which emerges from the current-induced vertical thermal gradient and scales linearly with magnetic field. Yet, the magnitude of the effect appears to be unusually large – by more than an order of magnitude compared to ordinary Nernst effects in those metals. The conventional anomalous Hall effect from the magnetic film bulk should be constant with field, so it cannot account for the pronounced linear slope. We suspect that an ultrathin, nearly ferromagnetic layer of silicide (e.g., NiSi, PtSi) at the film-substrate interface plays a crucial (previously unrecognized) role. Further elucidation of the actual mechanism, to be pursued in the coming cycle, can provide insights into enhancing thermoelectric energy harvesting with manufacturing-friendly metal films on common Si wafers.

Products: G. T. Street et al., 2025 MMM conference, contributed talk DF-07.

Collaborators: Mr. G. Street, Prof. S. Karube, Prof. Y. Shiota, Prof. T. Ono

Research on Magnetic Octupoles in Non-Collinear Antiferromagnets

Sanghoon Kim　University of Ulsan

From this collaboration, we have studied full spin–orbit torque (SOT) switching of the magnetic cluster octupole in the noncollinear antiferromagnet Mn_3Sn using an industry-compatible sputtering process. Noncollinear antiferromagnets are attractive for spintronic applications due to their ultrafast dynamics and absence of stray fields, yet electrical control of their order parameters remains challenging. In Mn_3Sn, the kagome lattice hosts a chiral 120° spin structure that can be described by a collective magnetic octupole. **While SOT-induced switching of this order has been reported previously, deterministic full switching has been largely limited to single crystals or MBE-grown films, with sputtered films exhibiting only partial switching.**

To overcome this limitation, Mn_3Sn thin films were grown in W/Mn_3Sn/Ta heterostructures on MgO(110) substrates using a co-sputtering approach that enables precise control of Mn stoichiometry. Structural characterization reveals that suppressing Mn deficiency is essential for stabilizing single-phase Mn_3Sn and for preventing W interdiffusion at the interface. **Optimized stoichiometry yields atomically sharp W/Mn_3Sn interfaces, whereas Mn-deficient or Mn-rich films exhibit interfacial disorder, secondary phases, and enhanced spin scattering.**

These structural differences directly translate into SOT switching behavior. Hall-bar devices fabricated from optimized films show robust anomalous Hall signals and deterministic SOT-induced switching when current is applied parallel to the kagome plane, consistent with a damping-like torque mechanism. Switching does not occur when current is applied perpendicular to the kagome plane, highlighting the symmetry constraints of noncollinear antiferromagnets. **Switching efficiencies reach full 100% switching is achieved with atomically inert interface between W and Mn_3Sn layers.**

Overall, this study establishes that precise stoichiometric control enables interface engineering sufficient to achieve complete SOT switching in sputtered Mn_3Sn films. The results demonstrate that industry-compatible deposition techniques can reach epitaxial-level performance, providing a practical pathway toward antiferromagnetic SOT memory, ultrafast logic, and neuromorphic computing devices. Our study has reported in ACS nano in 2025, which was selected as a cover paper.

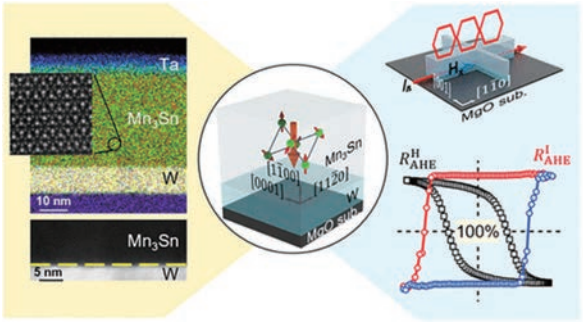


Figure 1. The layer structure based on Mn_3Sn captured by TEM (left) and observed 100% switching behavior of the magnetic octupole in Mn_3Sn.

○ **Paper information:** *ACS Nano* **19** (46), 39747-39756 (2025).

Research on high-sensitive quantum sensor with high quality diamond

Jörg Wrachtrup　Stuttgart University

Color centers in diamond have attracted considerable attention for applications in quantum information devices and quantum sensing. In particular, emission in the near-infrared (NIR) region is highly desirable because optical loss is minimized in both optical fibers and biological tissues, making it suitable for quantum communication and in vivo sensing. However, reports of diamond color centers exhibiting fluorescence in the NIR region remain limited, and further exploration is required.

In this study, we report the observation of a single color center emitting in the NIR region in a diamond sample consisting of a chemical vapor deposition (CVD) layer grown on a (111)-oriented type-Ib diamond substrate synthesized by the high-pressure high-temperature (HPHT) method. The sample was characterized using a confocal laser microscope with an excitation wavelength at NIR region and an objective lens with a numerical aperture of 1.35. Photoluminescence (PL) imaging revealed isolated bright spots within the HPHT substrate. Second-order autocorrelation measurements, $g^{(2)}(\tau)$, confirmed that these spots originated from single color centers.

The PL spectrum of an isolated emitter was measured at room temperature using a silicon detector. A sharp emission peak centered around NIR region was observed, indicating NIR fluorescence. To further investigate the nature of these emitters, polarization-dependent excitation measurements were performed on centers exhibiting similar spectral features. The results revealed two types of behavior: some centers exhibited orientations consistent with the crystallographic axes $[1\bar{2}1]$ and $[\bar{2}11]$, while others showed orientations that did not correspond to any principal crystal directions.

Moreover, certain centers displayed polarization dependences that could not be explained by a conventional two-level electric dipole transition model, suggesting a more complex electronic structure or transition mechanism. These findings indicate the presence of previously unreported NIR-emitting color centers in diamond. [1]

We also measured the single color centers at low temperatures using a confocal laser microscope in Stuttgart University. We observed sharp peaks around NIR region. Since this color center was observed in the NIR region, it is considered a promising candidate for applications in quantum cryptographic communication and life sciences, and its discovery in this study is therefore of significant importance.

[1] R. Shiotani, T. Nishikawa, N. Morioka, S. Miki, R. Kawase, H. Kawashima, N. Mizuochi, The 86th JSAP Autum Meeting 2025. Nagoya, Sep. 7-10, 2025.

Visualization of magnetization vector using magneto-thermo and magneto-optical effects

Kihiro Yamada　Institute of Science Tokyo

Research background & objective:

Toward realizing a sustainable society, the efficient recycling of waste heat is becoming an important issue as global energy consumption continues to rise. The anomalous Nernst effect (ANE) in thin magnetic metals can retrieve thermal energy as an electron motive force orthogonal both to the heat gradient and magnetization. When a local temperature is applied normal to a magnetic thin film, the resulting in-plane voltages reflect the in-plane magnetization components. This project aims to realize a comprehensive vector-resolved characterization of magnetic configurations using the laser-induced ANE in addition to the magneto-optical Kerr effect, which reflects the out-of-plane magnetization component. In this year, we realized the visualization of the in-plane magnetization components by measuring two orthogonal voltages resulting from the laser-induced ANE.

Experimental methods:

A magnetic bilayer consisting of Ru(5 nm)/Co(60nm) was deposited by dc magnetron sputtering on a sapphire (0001) substrate. The bilayer was processed to Hall devices with a channel size of 0.2 mm×0.2 mm by standard photolithography followed by physical etching procedures. The device fabrication processes were carried out at the Ono laboratory at the Institute of Chemical Research, Kyoto University. Laser-induced voltages were measured using an electrical set-up equipped with a continuous-wave laser [1] with a wavelength of 532 nm in our laboratory. The laser beams were focused onto the surface of the cross area to a spot radius of 6 μm. The laser intensity was modulated at a frequency of 100 kHz using a photo-elastic modulator in combination with a Gran-Tyalor prism. Two orthogonal voltages were simultaneously detected using two lock-in amplifiers. This configuration enabled measuring the local in-plane component of magnetization within the laser-irradiated area while scanning the sample position under a constant external magnetic field.

Experimental results & Discussion:

Figure 1 show the in-plane magnetization components when the macroscopic magnetization switches. The direction and amplitude of local in-plane magnetization are represented by vector and color map, respectively. The magnetization reversal proceeds through both coherent rotation of local magnetization and domain-wall motions. We find that magnetic vortexes emerge during the reversal process. The complementary use of the magneto-optical effect may allow full vector-resolved visualization of the complex magnetization switching dynamics in the magnetic film with an in-plane magnetic easy plane.

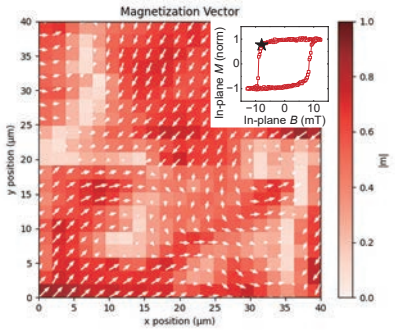


Fig. 1. Map of in-plane magnetization under magnetic field (B) of 7.7 mT. The inset shows the magnetic hysteresis loop of in-plane magnetization (M).

Reference

[1] S. Mochizuki, I. Sugiura, T. Narushima, T. Ono, T. Satoh, K. T. Yamada, Phys. Rev. Appl. 24, 044101 (2025).

Study on generation of spin-polarized current using insulating ferrite films

Masaaki Tanaka　Nagoya Institute of Technology

The spin-filtering effect, in which a spin-polarized current is generated via electron tunneling through a ferromagnetic insulator, is a promising candidate for spin injection. Magnetoplumbite-structured barium ferrite ($BaFe_{12}O_{19}$, BaM) is a ferromagnetic insulator whose (001)-oriented films grown along the [0001] direction exhibit perpendicular magnetic anisotropy (PMA). As a tunnel barrier film, BaM films are required to possess good magnetic properties, high surface flatness, and good insulating characteristics. However, post-annealing is required to crystallize the BaM films. As a result, the surface roughness deteriorates. In this study, we optimized the post-annealing conditions of the BaM films and investigated the tunneling properties of the magnetic tunnel junctions (MTJs) with BaM layers.

BaM films with various thicknesses were grown on MgO (001) substrates with Pt (111) buffer layers by pulsed laser deposition. The as-deposited films were subsequently annealed at 850°C in an oxygen atmosphere using an infrared lamp annealing system for various annealing durations. After the BaM films were annealed for 90 min, MgO/Co/$\{Tb/Co\}_{10}$ multilayer structures were subsequently deposited on top of the BaM layer to form MTJs. The MTJs, with junction diameters of several micrometers, were patterned by photolithography and argon ion milling. The entire microfabrication process was carried out at ICR, Kyoto University. Current-voltage (I-V) characteristics and magnetoresistance measurements of the MTJs were performed using a four-probe method.

With increasing annealing time, the crystallization and preferential (0001) orientation of BaM are enhanced, resulting in an increase in the saturation magnetization. However, this improvement is accompanied by an increase in surface roughness. The BaM layer annealed for 90 min exhibits favorable magnetic properties while maintaining a smooth surface. Figure 1 shows the I–V characteristics of the MTJ with a 7-nm-thick BaM layer, indicating good tunneling properties. The inset of Fig. 1 shows the BaM thickness dependence of the effective barrier thickness estimated using Simmons' model based on the I–V curves. The effective barrier thickness increases with increasing BaM thickness, suggesting that the BaM layer functions as a well-defined tunnel barrier with good insulating properties. Although a clear tunneling magnetoresistance effect has not yet been observed, the results suggest strong potential for spin-dependent transport. Further optimization of the barrier and interface properties is expected to lead to the realization of TMR in these MTJs.

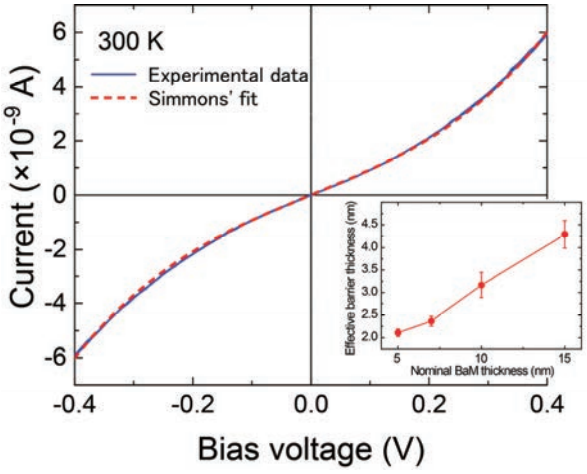


Fig. 1 I-V curve of the MTJ with a 7-nm-thick BaM layer.

Research on heat transport mechanism of MgO | Co-Fe-B structure

Minori Goto　Tokyo University of Science

Magnetic anisotropy control utilizing Joule heating in magnetic tunnel junctions has been reported as an effective approach for achieving fast and energy-efficient spin manipulation [1]. Such techniques are expected to contribute to advanced spin-based information and communication devices. To further improve device performance, it is essential to achieve efficient temperature rise in the ferromagnetic layer through Joule heating, which requires a fundamental understanding of heat transport phenomena involving interfacial thermal resistance between ferromagnetic and insulating layers. In our experimental system, the ferromagnetic layer is sandwiched between MgO layers (MgO | ferromagnetic layer | MgO), where interfacial thermal resistance is expected to play an important role in thermal confinement. However, heat transport characteristics in magnetic tunnel junctions with double-MgO structures remain insufficiently investigated. In this study, thermal resistance was evaluated in multilayer structures of [$Co_{16}Fe_{64}B_{20}$ (2 nm) | MgO (1 nm)]$_N$.

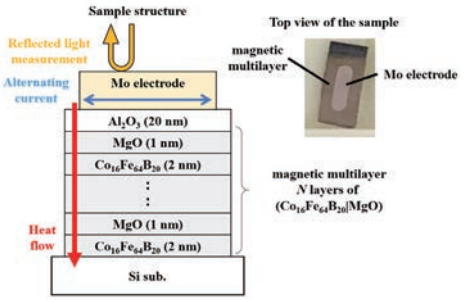


Figure 1 Schematic illustration of the sample structure and planar geometry used for thermal conductivity measurements. Thermal conductivity was evaluated by applying an AC current to the Mo electrode and detecting reflectivity modulation associated with temperature oscillations via lock-in detection (2ω method).

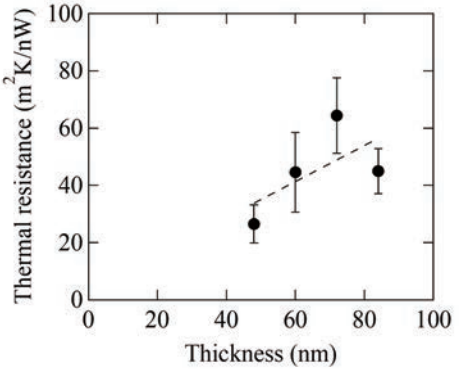


Figure 2 Thickness dependence of the total thermal resistance of [$Co_{16}Fe_{64}B_{20}$ (2 nm) | MgO (1 nm)]$_N$ multilayers. The dashed line represents linear fitting.

Film deposition was carried out using a magnetron sputtering system installed in the Ono Laboratory at the Institute for Chemical Research, Kyoto University, which has a proven track record in fabricating magnetic tunnel junctions. Multilayer films consisting of [$Co_{16}Fe_{64}B_{20}$ (2 nm) | MgO (1 nm)]$_N$ | Al_2O_3 (20 nm) | Mo were deposited on Si substrates, where N represents the number of bilayer repetitions (N = 16, 20, 24, 28). Thermal conductivity was evaluated by applying an alternating current to the Mo electrode and performing optical 2ω method. The measurements were conducted by our collaborator, Ishibe at University of Osaka. Figure 2 shows the thickness dependence of the total thermal resistance for the [$Co_{16}Fe_{64}B_{20}$ (2 nm) | MgO (1 nm)]$_N$ multilayers. Linear fitting (dashed line) yields a thermal conductivity of approximately 4 W m^{-1} K^{-1}, which is comparable to previously reported values for thin-film MgO [2]. Although thermal resistance was expected to increase monotonically with thickness, significant sample-to-sample variation was observed. This result suggests that heat transport in this multilayer system is sensitive to fabrication conditions and interfacial states. Further systematic investigations using samples fabricated under strictly controlled deposition conditions will be required to clarify the intrinsic thickness dependence.

[1] M. Goto, *et al.*, Nat. Nanotechnol., **14**, 40 (2019), [2] M. Walter, *et al.*, Nat. Mater, **10**, 742 (2011)

量子スピントロニクスのためのダイヤモンド半導体材料研究

徳田規夫　金沢大学

【緒言・目的】本研究では、ダイヤモンド中の窒素-空孔（NV）中心を用いた量子センサのさらなる高感度化を目的とし、(001)面方位ダイヤモンドにおける NV 中心生成の高効率化に関する検討を行った。NV 中心は室温環境下でも長い電子スピンコヒーレンス時間を有し、光照射によるスピン初期化・読み出しが可能であることから、磁場をはじめとする微小な物理量を高い空間分解能で検出可能な量子センサとして広く注目されている。センサ感度向上のためには、負電荷状態 NV 中心（NV^-）の濃度とスピンコヒーレンス時間（T_2, T_2^*）の積を最大化することが重要であるが、窒素濃度を単純に増加させると、置換型窒素欠陥（P1 中心）によるスピン雑音の影響で T_2 が低下する。このため、P1 中心から NV 中心への変換効率を高めることが、本質的かつ重要な課題となっている。

従来の研究では、(113)面方位基板を用いた化学気相成長（CVD）により比較的高い変換効率が達成されている一方で、デバイス応用上重要な(001)面では変換効率が 1%程度にとどまることが知られている。本研究では、(001)面基板を用いた CVD 成長において、ガス組成（H_2、CH_4、N_2）、基板温度、圧力などの複数の成長パラメータを系統的に変化させることで、NV 生成効率を高める条件の探索を行った。

【実験と結果】合成した試料については、共焦点顕微鏡を用いて NV^- 濃度およびスピンコヒーレンス時間の詳細な評価を行った。NV^- 濃度は、励起レーザー強度に対する発光強度の飽和挙動を解析し、単一 NV 中心の発光強度との比較により定量的に算出した。また、スピンコヒーレンス時間 T_2 はスピンエコー法により評価した。具体的には、$\pi/2–\pi–\pi/2$ および $\pi/2–\pi–-\pi/2$ のマイクロ波パルス系列を用いてスピン状態の読み出しを行い、その差分信号の減衰曲線をフィッティングすることで T_2 を導出した。

その結果、最適条件で合成した試料において、NV^- 濃度は 1.3×10^{17} cm^{-3}、スピンコヒーレンス時間 T_2 は 13.8 μs が得られた。さらに、既知の関係式（T_2 と窒素濃度の積が一定）を用いて変換効率を評価したところ、約 6.4%（SIMS 測定では 5.2%）と見積もられた。この値は、従来(113)面基板で報告されている高変換効率（約 7.8%）に匹敵するものであり、(001)面基板においても高効率な NV 生成が可能であることを明確に示している。特に、(001)面において 5%を超える変換効率を達成した点は、これまでの報告と比較して顕著な進展であり、材料開発の観点からも重要な成果である。

以上の結果から、(001)面方位ダイヤモンドにおいても、成長条件の精密な最適化により高い NV 変換効率を実現できることが明らかとなった。本成果は、NV 量子センサの高感度化に向けた材料設計指針を与えるとともに、実用的な量子センシングデバイスの開発にもつながる重要な知見である。今後はさらなるコヒーレンス時間の延長や欠陥制御技術の高度化を通じて、より高性能な量子センシング応用への展開が期待される。

【成果報告】[1] 川瀬 凜久、川島 宏幸、中川 大夢、加藤 宙光、徳田 規夫、山崎 聡、小倉 政彦、牧野 俊晴、森岡 直也、大木 出、水落 憲和、第 39 回ダイヤモンドシンポジウム、東京、2025.11.12 ~ 14.

量子センサの高感度化のためのリンドープダイヤモンド合成研究

牧野俊晴　産業技術総合研究所

【緒言・目的】 ダイヤモンドは、広いバンドギャップ、高い熱伝導率、および高い絶縁破壊電界といった優れた物性を有しており、次世代パワーデバイス材料として有望視されている。これらの応用を実現するためには、n 型電気伝導特性の向上が不可欠であり、そのための手法としてリン（P）ドーピングが重要である。さらに、リンドープダイヤモンド中に形成される窒素-空孔（NV）中心においては、負電荷状態（NV^-）の安定性が向上することが報告されている。加えて、室温において固体中で最長となる電子スピンコヒーレンス時間（T_2 = 2.4 ms）が実現されており、量子センサをはじめとする量子デバイス応用の観点からも、リンドープ技術の高度化は極めて重要である。一方、従来リン源として広く用いられてきたホスフィン（PH_3）は高い毒性および爆発性を有し、安全管理の観点から大きなコストを要する。この課題に対し、本研究グループでは、より低毒性かつ低爆発性の tert-butylphosphine（TBP）を用いたリンドープダイヤモンドの合成に取り組んできた。その結果、ホスフィンを用いた場合に匹敵する電子移動度（580 cm^2/Vs, リン濃度 3×10^{17} cm^{-3}）および、最長記録に近い電子スピンコヒーレンス時間（T_2 = 2.23 ms）を達成している[1]。本研究では TBP を用いたリンドープダイヤモンドにおいて、電子移動度の更なる向上を目的とし、リン濃度の異なる試料を作製して電気伝導特性を系統的に評価した。

【実験方法】リンドープダイヤモンドの合成には、水素（H_2）、メタン（CH_4）、およびリン源として TBP を用い、ARIOS 社製マイクロ波プラズマ CVD 装置により成長を行った。基板には、高温高圧法（HPHT 法）で合成された Ib 型(111)面ダイヤモンドを使用した。合成時の圧力および原料ガス流量を変化させることで、リン濃度の異なる複数の試料を作製した。試料中の不純物濃度は二次イオン質量分析（SIMS）により評価し、電気伝導特性はホール効果測定により解析した。測定は室温から 900 K の温度範囲で実施し、電子移動度およびキャリア濃度の温度依存性を取得した。さらに、キャリア濃度のアレニウスプロットからドナー準位および補償比を算出した。

【結果および考察】各試料の合成条件および室温におけるホール移動度を計測した結果、TBP を用いた n 型ダイヤモンドとしては最高値となる電子移動度 719 cm^2/Vs を達成した。また、従来のホスフィンを用いた試料と同等レベルの高い移動度が得られた。更に、高い移動度を示した試料では補償比が低い傾向が確認された。このことから、移動度向上に対する補償比の影響が示唆される。そこで、合成条件と補償比の相関について検討を行った結果、合成時の圧力が低いほど補償比が低減する傾向が明らかとなった。以上の結果より、TBP を用いたリンドープダイヤモンドにおいては、合成条件、特に成長圧力の最適化が補償比の低減および電子移動度の向上に重要であることが示された[2]。今後は、電子スピンコヒーレンス時間（T_2）との相関についても詳細な検討を行い、量子デバイス応用に向けた材料特性の最適化を進める予定である。

【引用文献】[1] R. Kawase, H. Kawashima, H. Kato, N. Tokuda, S. Yamasaki, M. Ogura, T. Makino, N. Morioka, and N. Mizuochi, *Applied Physics Letters*, 126, 074002 (2025).

[2] 中川大夢，川瀬凜久，川島宏幸，山口翔真，加藤宙光，徳田規夫，山崎聡，小倉政彦，牧野俊晴，重松英，森岡直也，水落憲和、第 73 回応用物理学会春季学術講演会、東京、2026 年 3 月 15-18 日.

Research on the efficient color centers creation in nanodiamond for bio-application

Takuya F. Segawa　ETH Zürich

Group-IV color centers in diamond have attracted considerable interest due to their strong zero-phonon lines (ZPLs), making them promising candidates for single-photon sources in quantum information technologies. In addition, their optical properties enable applications as fluorescent probes and all-optical temperature sensors in biological environments. Among various fabrication approaches, we focus on the formation of group-IV color centers in detonation nanodiamonds (DNDs). The detonation method enables mass production of ultra-small nanodiamonds with particle sizes below 10 nm, which are suitable for intracellular applications, including targeting subcellular structures such as the cell nucleus. We have previously demonstrated the formation of silicon-vacancy (SiV) and germanium-vacancy (GeV) centers in DNDs, and recently reported the formation of tin-vacancy (SnV) centers. Although the formation efficiency of SnV centers is limited due to the large atomic radius of tin, they are attractive because of their longer electron spin coherence times compared to SiV and GeV centers. In this study, we report the identification of single SnV centers in Sn-doped DNDs with an average particle size of approximately 5 nm using second-order autocorrelation measurements.

Sn-doped DNDs were synthesized by detonation of mixed explosives containing tin dopants, followed by purification and cleaning processes. The samples were further treated with thermal mixed-acid cleaning (H_2SO_4 + HNO_3 at 130 °C) for three days to remove surface impurities. A suspension of the cleaned DNDs (1 mg/mL) was drop-cast onto a cover glass and dried under ambient conditions. The samples were characterized using a laser confocal microscope, and bright emission spots were further analyzed by photoluminescence spectroscopy and second-order autocorrelation measurements.

The photoluminescence spectrum of an isolated emission spot exhibited a clear ZPL at 618 nm, characteristic of the SnV center. The second-order autocorrelation function showed $g^{(2)}(0) < 0.5$after background correction, confirming single-photon emission [1]. These results demonstrate that Sn-doped DNDs can host single SnV centers even at particle sizes of ~5 nm, highlighting their potential for quantum photonics and nanoscale bioimaging applications.

References

[1] M. Fujiwara, M. Ohori, F. T. K. So, Y. Makino, N. Morioka, I. Ohki, R. Igarashi, M. Nishikawa, N. Mizuochi, *Discover Nano*, 20, 81 (2025).

Synthesis of Pyrene-based Materials with Diradical Character

Graham J. Bodwell　Memorial University of Newfoundland

Objectives: Pyrene-based nonplanar π-systems are attractive platforms for materials with unusual electronic structures, including potential diradical character, because their π-conjugation and through-space interactions can be tuned by curvature and strain[1]. Incorporating carbonyl groups into such frameworks is expected to further perturb the electronic structure by introducing low-lying π^* orbitals and carbonyl-centered n–π^* states[2]. In this study, we examined a cyclic diketone incorporating pyrene units and evaluated the bending of the pyrene units and the strain associated with macrocyclization.
Methods: The structure was optimized by DFT calculations at the B3LYP/6-31G* level. The bending deformation was evaluated by the bend angle θ between the C1–C2–C3 and C10–C11–C12 planes of the pyrene unit[1]. The strain energy was estimated using appropriate non-cyclic or fragment-based reference models[3].
Outcomes: The optimized structure showed moderate bending of the pyrene units, with a bend angle θ of 66.4°. This value is in the middle of the range reported for [n](2,7)pyrenophanes (θ = 34.6–109.2°). In contrast, the strain energy was estimated to be 365.8 kJ mol^{-1}, which indicates rather high, but by no means unprecedented, strain stored in the macrocyclic framework. The closest distance between the two pyrene systems (C2–C2') was found to be 2.44 Å.
Analysis: The levels of curvature and strain in the pyrene-based π-system are well within those previously achieved, which indicates that the compound should be amenable to synthesis and stable. The proximity of the ends of the two pyrene systems bodes well for through-space electronic interactions. The ketone units, such deformation may perturb the electronic structure through carbonyl-centered π^* and n–π^* contributions. As a whole, the target molecule provides a useful platform for examining how curvature, strain, and carbonyl functionality influence the electronic properties of pyrene-based π-materials.
Publications: No publications or presentations directly related to this project have been reported at this stage.

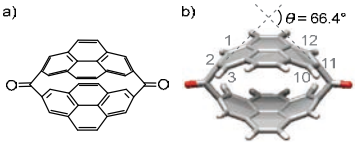


Fig. 1.　Target Pyrene-based Materials; a) Cyclic Pyrene-based Aromatic Diketone. b) Optimized Structure by DFT Calculations (B3LYP/6-31G*).

References　1) Bodwell, G. J. *et al. Chem. Soc. Rev.* **2015**, *44*, 6494. 2) Abe, M.; Yamago, S. *et al. Angew. Chem. Int. Ed.* **2025**, *64*, e202509754. 3) Itami, K. *et al. Angew. Chem. Int. Ed.* **2009**, *48*, 6112.

Investigation of geometric magnetic frustrated materials with structure design and high-pressure synthesis

Wei-Tin Chen　National Taiwan University

[Introduction] High-pressure high-temperature (HPHT) techniques is one of most powerful methods to prepare novel quantum matters and functional materials such as geometric magnetic frustrated materials and superconductors. Within the binary Ba–Ge system, numerous compounds with different stoichiometric ratios have been reported, exhibiting rich structural diversity and intriguing electronic properties. Nevertheless, no stable phase with a Ba:Ge = 1:3 stoichiometry exists under ambient-pressure conditions, leaving a notable gap in the Ba–Ge phase diagram and motivating exploration under high-pressure synthesis conditions. In 2011, Fukuoka *et al.* successfully synthesized $BaGe_3$ using HPHT techniques and reported superconductivity with a transition temperature of approximately 4.0 K. Subsequent theoretical work by Zurek and Yao (2015) predicted pronounced structural polymorphism in $BaGe_3$, demonstrating that its crystal structure is strongly pressure dependent, different polymorphs may exhibit distinct superconducting properties. In this work, we aim to synthesize high-pressure phases of $BaGe_3$ using HPHT techniques in collaboration with the Advanced Solid State Chemistry Laboratory (Prof. Shimakawa), followed by detailed structural characterization using high-resolution synchrotron X-ray diffraction (SXRD) at the Taiwan Photon Source (TPS).

[Results and discussion] $BaGe_3$ was initially synthesized in the hexagonal $P6_3/mmc$ (No. 194) structure, characterized by face-sharing Ge trigonal units stacked along the *c* axis, forming a quasi-one-dimensional Ge framework. Under higher-pressure synthesis conditions, $BaGe_3$ can be stabilized in the tetragonal $I4/mmm$ (No. 139) structure, where the Ge sublattice reorganizes into Ge–Ge dumbbell units within a more compact three-dimensional framework. This high-pressure polymorph is the primary focus of the present study and was synthesized using a Kawai-type multianvil apparatus. Rietveld refinement of the SXRD data indicates that the target $BaGe_3$ phase constitutes approximately 85% of the sample, with a minor impurity phase of $BaGe_5$. Magnetic measurements reveal the onset of diamagnetic behavior at around 6.7 K, together with a clear separation between zero-field-cooled and field-cooled curves, consistent with superconductivity and suggesting type-II superconducting state. However, presence of the non-superconducting $BaGe_5$ impurity likely suppresses the bulk superconducting response. Further electrical resistivity and heat-capacity measurements are therefore required to establish the superconducting transition and to clarify the underlying superconducting mechanism.

Development of solution-processable multi-resonant TADF emitters

Eli Zysman-Colman　University of St Andrews

We have worked on three collaborative studies between the Zysman-Colman and Kaji labs involving solution-processable thermally activated delayed fluorescence (TADF) molecular design and their use in OLEDs.

In the first project, which has been published in *Org. Chem. Frontiers* (DOI: 10.1039/D5QO00146C), we highlight the impact of regiochemistry in the donor dendron design of the MR-TADF emitter. **2,7-tBuCzNB** shows narrowband green emission at 498 nm (full-width at half-maximum of 47 nm) and is relatively less sensitive to aggregation-caused quenching thanks to the steric shielding provided by the donor dendrons. Given the sufficiently small ΔE_{ST} of 150 meV to enable TADF and a high photoluminescence quantum yield, Φ_{PL}, of 86%, the 5 wt% doped films in mCP showed prompt and delayed fluorescence lifetimes of 9.9 ns and 1.89 ms. Despite the resulting slow k_{RISC} (5.4×10^2 s^{-1}) solution-processed OLEDs employing **2,7-tBuCzNB** showed EQE_{max} values of 11.4% at CIE coordinates of (0.16, 0.56).

In a second project, we developed a donor dendron decorated derivative of the fast k_{RISC} donor-acceptor TADF emitter **DOBNA-SpAc** (**TDBA-SAF**). **DOBNA-SpAc-DCz** emits in the sky-blue at 474 nm in 20 wt% doped films in PPF, and has a high Φ_{PL} of 93% and a short delayed lifetime of 2.04 µs. The resulting fast k_{RISC} of 1.7×10^6 s^{-1} enables the fabrication of highly efficient solution-processed OLEDs with EQE_{max} of 29.4% at CIE coordinates of (0.14, 0.21). By a comparison of different electron transport materials within the device it has been shown that **DOBNA-SpAc-DCz** enables enhanced hole transport compared to its parent emitter **DOBNA-SpAc**, owing to the hole-transporting properties of the *ter*-carbazole donor dendrons. A manuscript for publication is currently in preparation.

The third collaborative research project involves the investigation of liquid crystalline donor-acceptor TADF emitters (Figure **1**). This would be the first example of a columnar liquid crystalline D-A TADF material and one of the first to be used in an OLED. A manuscript for publication is currently in preparation.

Design of novel organic emitters for highly efficient OLED: Theory meets Synthesis

Francesco Di Maiolo　University of Parma

The aim of this 1-year project was to devise and characterize new organic systems as light emitters for highly efficient OLEDs, with special emphasis on emitters featuring an inverted singlet-triplet (InveST) gap, which allows triplet harvesting and potentially revolutionizes OLED efficiency. The theoretical foundation exploited the Pariser-Parr-Pople (PPP) model for correlated π-electrons, providing computationally affordable screening of different molecular structures. The collaboration with the ICR partner researcher (Prof. Hironori Kaji, Kyoto University) provided complementary expertise: synthesis (ICR: Dr. Heekyoung Choi), DNP-NMR characterization (ICR: Prof. Katsuaki Suzuki), and theoretical support (ICR: Prof. Hironori Kaji).

The core theoretical framework relies on the PPP model combined with a restricted active space configuration interaction (RASCI) approach (PPP-RASCI). This approach captures the dynamical spin-polarization corrections that are critical for predicting ST inversion in π-conjugated nitrogen-doped systems. The PPP-RASCI results were systematically benchmarked against high-level *ab initio* CASSCF/QD-NEVPT2 calculations, validating the reliability and predictive power of the model across a broad set of molecular structures.

Three publications resulted from this project: 1) DOI: 10.1021/acs.jctc.5c01571 presents a molecular design strategy for organic diradicals bridged by InveST units targeting optical-spin interfaces; 2) DOI: 10.1021/acs.jpca.5c08128 discusses potentially luminescent organic radicals that could be connected to the InveST unit; 3) DOI: 10.26434/chemrxiv-2026-d65ps is currently in peer review and presents additional InveST-bridged organic diradicals.

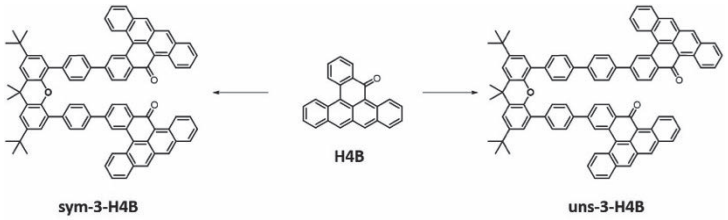
A key outcome was the initiation of a fruitful collaboration with Prof. Hironori Kaji and Prof. Katsuaki Suzuki (ICR, Kyoto University). The project travel funds (220,343 JPY) supported a research visit of the PI and his PhD student Matteo Bedogni to ICR members to discuss the synthesis and DNP-NMR characterization of systems closely related to those computationally designed in Paper 1.

Results were presented at three conferences: two invited talks at the Donegani Conference (Accademia dei Lincei, Rome, November 25-26, 2025) and at QMChem@SSM (Naples, Italy, February 4-6, 2026), and one contributed talk at Optical Probes 2025 (Fukuoka, Japan, September 21-26, 2025). The PI has also been invited to deliver a Keynote Lecture at the Journées Méditerranéennes des Jeunes Chercheurs 2026 (JMJC), Nice, France (October 8-9, 2026).

Synthesis of higher acene derivatives and the evaluation of their singlet-fission properties

Andrej Jancarik　CRPP-CNRS

Experimental Methods, Outcomes and Analysis : In the course of the project, the team at CRPP‑CNRS focused on the synthesis of novel acene-based polyaromatic hydrocarbons suitable for singlet fission. We in CRPP-CNRS and Yamada's team in ICR were responsible for synthesizing the acene materials for singlet fission and we successfully developed a new and robust synthetic strategy for stable tetracene derivatives. This short and straightforward approach enables the preparation of a diverse range of tetracene derivatives on a relatively large scale (>100 mg), making them promising candidates for singlet fission studies. Prof. Hasobe's team in Keio Univ. is internationally recognized for their expertise in singlet fission and transient absorption spectroscopy, which significantly contributed to the rational design of new structures exhibiting singlet fission properties. In the first stage of the project, we synthesized a prototype tetracene derivative, **H4B**. Since singlet fission is a bimolecular process, its verification in **H4B** required investigation in the solid state. Therefore, **H4B** was sublimated onto quartz plates to form an amorphous solid and subsequently characterized by Prof. T. Hasobe's team. Thorough spectroscopic studies confirmed that **H4B** undergoes singlet fission, efficiently generating two separated triplet states (T_1) with a high yield of approximately 70%. In the next stage of the project, we focused on molecular engineering to control the formation of separated T_1 states during the singlet fission process. New structures were designed in which two **H4B** chromophores were symmetrically and unsymmetrically attached to a xanthene bridge (**sym-3-H4B** and **uns-3-H4B**). Owing to the close proximity of the two chromophores, singlet fission could be studied in solution, which is experimentally more convenient than solid-state measurements.

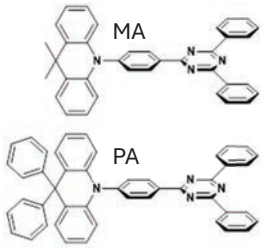


Conclusion: Thanks to the Collaborative Research Program of ICR, Kyoto University, the CRPP‑CNRS team established a highly important collaboration with a Japanese partner, which proved essential for the development of this project. The project is already well advanced and shows very promising results, a considerable amount of work still lies ahead before publication. The project will continue in the coming years.

Modelling, design and synthesis of chiral dyes for CISS and CPL

D. K. Andrea Phan Huu　University of Parma

Objectives: As a first step towards modelling and design axially chiral TADF dyes, we investigated a series of achiral TADF emitters, designed by the ICR partner group by substitution of the donor unit of MA (Fig. 1). Chiral analogues can be obtained exploiting axial chirality.



Experimental methods: Steady state and time resolved UV-vis spectroscopy in solution. Photophysical rates were estimated from fitting of the time evolution of the integrated luminescence.

Structure of theory: TD-DFT computational study was performed to address excited states and conformational degrees of freedom. The model for MA proposed in Ref 1 by some of us was modified and parametrized to describe PA. Interestingly, additional conformational relaxation in PA must be introduced to properly address ISC and RISC rates. ISC and RISC rates in solution are estimated for PA using the approach proposed by some of us in Ref. 2 (Fig. 2 and Fig. 3).

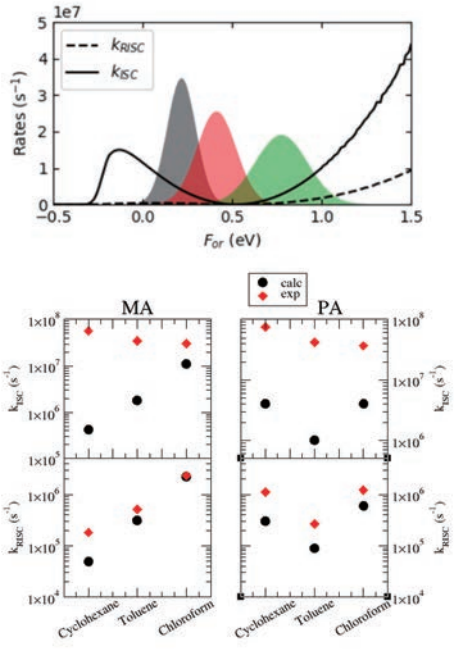


Fig. 2: RISC and ISC rates of PA-TRZ vs orientational field, and solvent distributions for cyclohexane (black), toluene (red), and chloroform (green). Comparison of experimental and theoretical ISC and RISC rates.

Outcomes: The experimental characterization revealed that up-conversion mechanism of MA and PA are similar. Computational analysis revealed that the CT state in PA is closer in energy to ^{3}LE states, affecting SOC at the GS equilibrium, but additional relaxation makes this difference less pronounced.

Analysis: Once solvent effects and additional vibrational relaxation pathways are considered, similar rates are obtained for MA and PA, despite their different excited state properties in gas phase.

Publications: One paper is in preparation.

References: [1] Dhali et al. PCCP, 2021, 32, 1, 378 [2] Phan Huu et al. JACS 2022, 144, 33, 15211

High-Performance Solution-State Light-Emitting Devices through Excimer-Formation

Malte C. Gather　University of Cologne

This study addresses the low luminance and short operational lifetime of electrochemiluminescent devices (ECLDs) by introducing electrochemically induced hyperfluorescence (ECiHF), achieving higher brightness, improved efficiency, and longer device lifetime. Charge-transfer (CT) excimers formed by the TADF molecule TpAT-tFFO act as triplet-sensitizing states, enabling efficient energy transfer to the fluorescent emitter TBRb and resulting in performance far exceeding that of conventional ECLDs.

Objectives

The objective is to establish the ECiHF mechanism based on CT excimer formation and to demonstrate its potential for high-performance ECLDs and display applications.

Experimental Methods

TpAT-tFFO and TpATtBu-tFFO were characterized using concentration-dependent, time-resolved, and variable-temperature photoluminescence, along with absorption spectroscopy and spectroelectrochemistry. ECL devices using TBRb were fabricated, including parallel-electrode ITO, mirror-assisted, and floating bipolar electrode structures for display demonstrations.

Outcomes

TpAT-tFFO showed a transition to CT excimer emission at high concentration while retaining TADF behavior. Efficient FRET to TBRb enabled ECiHF, achieving maximum luminance of 3,650 cd/m² (glass–glass) and 6,220 cd/m² (glass–mirror). The LT50 reached 369 s (potentiostatic) and 1,252 s (galvanostatic) at 100 cd/m², exceeding previous ECLDs. A 10 μm-resolution calligraphic display was also demonstrated.

Analysis

In TpAT-tFFO, electrochemically generated species form CT excimers, followed by ISC/RISC cycling and singlet energy transfer to TBRb, resulting in high exciton utilization. TpATtBu-tFFO showed poorer energy alignment, mixed emission pathways, and lower performance. Maintaining HOMO/LUMO offsets below 0.4 eV is a key design guideline for efficient ECiHF.

Publications

This work has been published as:

Electrochemically Induced Hyperfluorescence Based on the Formation of Charge-Transfer Excimers, C.-K. Moon, Y. Yasuda, Y. Kusakabe, A. Popczyk, S. Fukushima, J. F. Butscher, N. Pathak, J. Schlecht, K. Ishihara, O. Dumele, H. Kaji,* M. C. Gather,* ***Nat. Commun.*** **2026**, *17*, 3753.

生命科学分野への応用に向けたナノダイヤモンド高感度化研究

五十嵐龍治　量子科学技術研究開発機構

【緒言・目的】ダイヤモンド中の NV 中心は、室温でも長い電子スピンコヒーレンス時間（T_2）を維持し、光照射によってスピン状態の初期化と読み出しが可能で、光検出磁気共鳴（ODMR）測定が可能である。この ODMR 信号を活用することで、NV 中心は磁場、電場、温度、圧力などの物理量変化を検出可能な高感度量子センサとして機能する。特にナノダイヤモンド（ND）中に含まれる NV 中心は、その優れた量子特性を保持しつつ、生体毒性が低く表面修飾による多機能化が可能なことから、細胞内の微小領域における非侵襲的な磁気センサや温度センサとしての応用が期待されている。

これまで ND 中の単一 NV 中心を用いた磁場センシングについては、例えば、平均粒径 30 nm の ND において交流磁場感度 $\eta = 500$ nT/(Hz)$^{1/2}$、また 23 nm の ND において 140 nT/(Hz)$^{1/2}$ といった成果が得られている。しかし、生体活動に伴う磁場強度の計測の場合、イカ軸索などの神経細胞発火信号であれば μT ~ nT レベルの感度で観測可能であるが、心磁などのより微弱な信号検出には nT ~ pT レベルの高い感度が要求される。更に、細胞内での非侵襲的な計測を実現するためには、ND のさらなる小粒径化が不可欠である。我々は、小粒径の ND を安価かつ大量に合成可能な爆轟法に着目し、爆轟ナノダイヤモンド（DND）を用いた高精度な磁場センシングの実証に取り組んだ。

【実験と結果】実験においては、まず混合火薬を爆轟させることで DND を生成し、その後の洗浄・精製プロセスを経て試料を得た 。透過型電子顕微鏡を用いた画像解析の結果、得られた DND の平均粒径は 11.2 nm と確認された。更に、DND 表面に残留する不純物や欠陥を除去するため、72 時間にわたる熱混酸洗浄を行った。精製された DND はスライドガラス上に滴下・乾燥させ、自作の共焦点顕微鏡による測定に供した。励起光源には波長 532 nm、強度 200 μW のレーザーを用いた。DND からの発光はピンホールを通過させた後、単一光子検出モジュールを用いて高精度に記録した。

磁場センシングの実施に際しては、まず共焦点画像から DND の凝集体である発光輝点を特定し、静磁場印加条件下で ODMR スペクトルを測定した。この際、NV 軸が静磁場と平行に近い個体を選択するため、事前に全 NV 中心が同一方向に配向した CVD ダイヤモンド基板を用いて静磁場の方向と強度を精密に校正し、その共鳴周波数に近い輝点を探索する手法を採用した。選別された輝点に対して Rabi 振動測定を行い、πパルス長を決定した後、Pulse Echo 測定によってスピンコヒーレンス時間を算出した。その結果、$T_2 = 4.1$ μs という値を記録した。これは本研究グループがこれまでに調査した DND の中でも最長の T_2 である。この輝点に対し、ダイナミカルデカップリング法を適用して交流磁場測定および磁場感度測定を行ったところ、最終的に $\eta = 910$ nT/(Hz)$^{1/2}$ という感度を得るに至った。

本研究の成果により、DND 中の NV 中心を用いた交流磁場センシングが実証された。得られた感度は更なる向上が望まれるものの、磁場感度が報告されている ND の中では世界最小の粒径を実現した点に意義がある。今後、この極小径の DND を活用することで、細胞内局所領域における磁場や温度の超高解像度センシングといった、次世代のバイオ量子計測技術への応用が期待される。

【成果報告】藤原正規、神山直也、大堀真尚、蘇梓傑、牧野有都、E. D. Herbschleb、西川哲理、重松英、大木出、森岡直也、五十嵐龍治、水落憲和、第 39 回ダイヤモンドシンポジウム、東京、2025.11.12 ~ 14.

Elucidation of electronic state for bis-homo in-plane aromatic molecules

Eiichi Kayahara　roshima University

Diaryl ketones are valuable compounds with diverse applications in scientific and industrial fields. Among them, diaryl ketones with a distorted cyclic skeleton have attracted attention for their potential to alter physical properties. However, the synthesis of such ketones is still limited. In this collaboration research, we succeeded in the synthesis of a series of [*N*]cycloparaphenylene ketone, [*N*]CPP-CO (Figure 1), in which a carbonyl group is inserted into [*N*]CPP framework, representing the first examples of diaryl cyclic monoketones with a distorted yet fully conjugated tether group, and investigate their structures and physical properties.[1]

[*N*]CPP-CO (*N* = 6, 7, 8, and 10) was synthesized by a coupling reaction between a CPP precursor and a ketone unit, followed by reductive aromatization. Single crystal X-ray diffraction analysis and DFT calculations confirmed their Möbius topology and significant molecular strain as characterized by the deviations in bond angles at the carbonyl carbon. The strain was also evidenced by size-dependent 20–50 cm^{-1} shifts in the carbonyl IR stretching bands. The CPP units in [*N*]CPP-CO significantly alter the electronic properties, particularly the relative orbital energies. Due to the elevation of the energy level of the occupied π-orbitals by CPP units, the highest occupied molecular orbital (HOMO) in [*N*]CPP-CO is the conjugated π system, in contrast to benzophenone, where the HOMO is the non-bonding n-orbital. Consequently, the lowest excited state of [*N*]CPP-CO is the singlet state (S_1) with π–π* character rather than the conventional n-π* triplet (T_1) state. Furthermore, intersystem crossing from the S_1 state to the T_1 state, which is a characteristic process for typical aromatic ketones, does not occur efficiently. As a result, [*N*]CPP-CO exhibits unique photophysical properties opposite to those of typical aromatic ketones, such as fluorescing but not phosphorescing. Furthermore, the S_1 state of [*N*]CPP-CO was quenched by molecular oxygen, most likely by the energy exchange mechanism. Optical and electrochemical properties showed a clear dependence on ring size, with smaller rings exhibiting greater strain, lower oxidation potentials, and red-shifted absorption and emission.

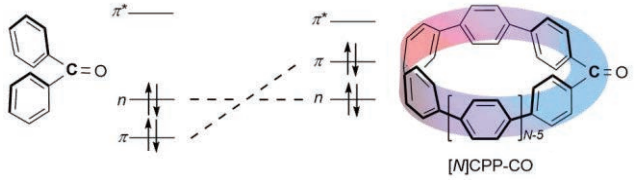


Figure 1. Schematic image of this collaboration research.

These findings highlight the unique interplay between molecular topology, strain, and photophysics in CPP-based ketones and provide a foundation for designing novel π-conjugated materials with tailored excited-state properties.

References

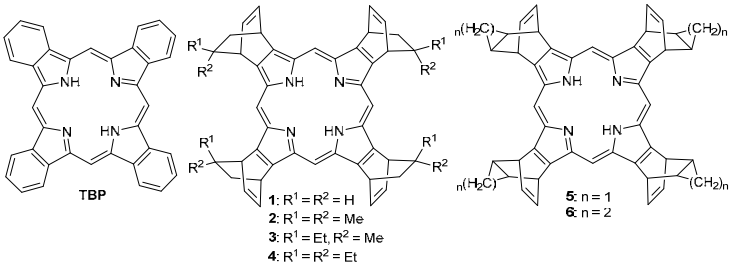
Kayahara, E.; Okahara, R.; Shibata, A.; Abe, M.; Yamago, S. *Angew. Chem. Int. Ed.* **2025**, *64* (33), e202509754. DOI: https://doi.org/10.1002/anie.202509754.

熱変換型π電子系有機材料の合成と半導体素子の作製

奥島鉄雄　愛媛大学

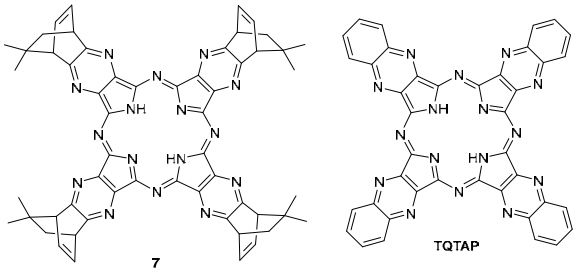
Introduction

Organic semiconducting molecules have attracted considerable attention due to their potential applications in electronic devices such as organic field effect transistors (OFETs). Tetrabenzoporphyrin (TBP) and phthalocyanine offer several advantages, including easy optimization of molecular structure, low HOMO-LUMO energy gap, and thermal and chemical stability. We have previously reported thermally convertible precursors of TBPs **1**–**6** and their application in solution-processed OFET fabricated. In this collaborative project, we fabricated an n-type OFET based on electron-deficient tetra(quinoxalino)tetraazaporphyrin (TQTAP).

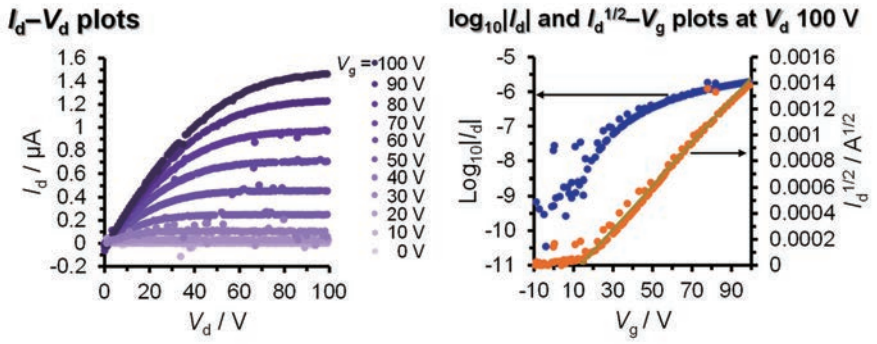


Results

TQTAP precursor **7** was synthesized *via* Diels–Alder reaction of 5,5-dimethyl-1,3-cyclohexadiene and vinylene carbonate, followed by hydrolysis, Swern oxidation, condensation with 2,3-diaminomaleonitrile, and the subsequent formation of TAP.



OFET fabrication was conducted in the Yamada laboratory at the Institute for Chemical Research, Kyoto University. A thin film of TQTAP was prepared by spin-coating a 0.5wt% solution of **7** at 1,000 rpm for 1 min, followed by thermal treatment at 220 °C for 30 min in a glove box. The fabricated FET device exhibited an n-type semiconductive behavior. The field-effect mobilities μ was evaluated in the saturation regime, and the on/off current ratio (I_{on}/I_{off}) was determined from the source-drain current (I_d) measured at the gate voltages (V_g) of 0 and 100 V. A good μ of 1.10×10^{-3} cm^2 V^{-1} s^{-1}, and an I_{on}/I_{off} of 3.71×10^3, and the threshold voltage (V_{th}) of 13.3 V were obtained. Further improvement of device performance will be pursued through optimization of thin-film morphology and modification of device structures.



村上晴哉・菊池 誠・三谷知妙・秋山泰士・森 重樹・髙瀬雅祥・宇野英満・山田容子・小野 昇・奥島鉄雄，熱変換型ナフタロシアニン前駆体の合成，2025 年日本化学会中国四国支部大会香川大会，高松（徳島文理大学高松駅キャンパス）2025 年 11 月 23-24 日（ポスター）

固体 NMR と EDMR・ODMR の連携による電子・正孔対の挙動解析

森下弘樹　東北大学

目的

有機 EL（OLED）内の電子・正孔対は、励起子生成の前駆体として、電荷輸送や電荷再結合に深く関わっていることが知られている。近年、発光ドーパントとして注目されている熱活性化型遅延蛍光（TADF）材料は、一重項-三重項励起状態間のエネルギー差が小さく、三重項-一重項間の逆項間交差が、室温においても可能であることから高効率な OLED の発光材料として注目されている。一方、電荷注入下と光励起下における電子・正孔対の挙動については未だ明らかにされていない部分が多い。そこで本課題では、これまで種々の高効率 TADF 材料を報告している京都大学 梶と鈴木と共同研究を行い、申請者がこれまで研究を進めてきた、電子・正孔対の選択的検出が可能な電流検出 ESR (EDMR)や光検出 ESR（ODMR）法を TADF 材料に展開する。EDMR や ODMR 法を用いて電子・正孔対に働く磁気相互作用の定量評価に取り組み、非晶状態における TADF 材料の電子・正孔対の学理を構築するとともに、高性能な TADF 材料開発の分子設計指針を確立する。

実験方法ならびに結果

Bruker 社製の X-band 電子常磁性共鳴（EPR）装置を用いて、EDMR および ODMR 測定系を構築した（図 1）。本測定系では、TADF 材料を用いた OLED 素子を電磁石中に設置し、定電流源から電流を印加する。磁気共鳴に伴う電流応答は、電流アンプおよびサンプリングオシロスコープを用いて検出し、EDMR 測定を行った。測定プログラムでは、照射マイクロ波の周波数を掃引しながら、有機 LED に流れる電流の時間応答を取得することで EDMR 信号を計測する。一方、ODMR 測定では、光検出器から得られる電流の時間応答を測定する。さらに、本プログラムではこれら 2 種類の電流応答を同時に取得可能なシステムを構築し、両者の応答の違いを詳細に比較できるようにした。その結果、EDMR および ODMR 測定に必要な装置制御およびデータ取得が可能となった。

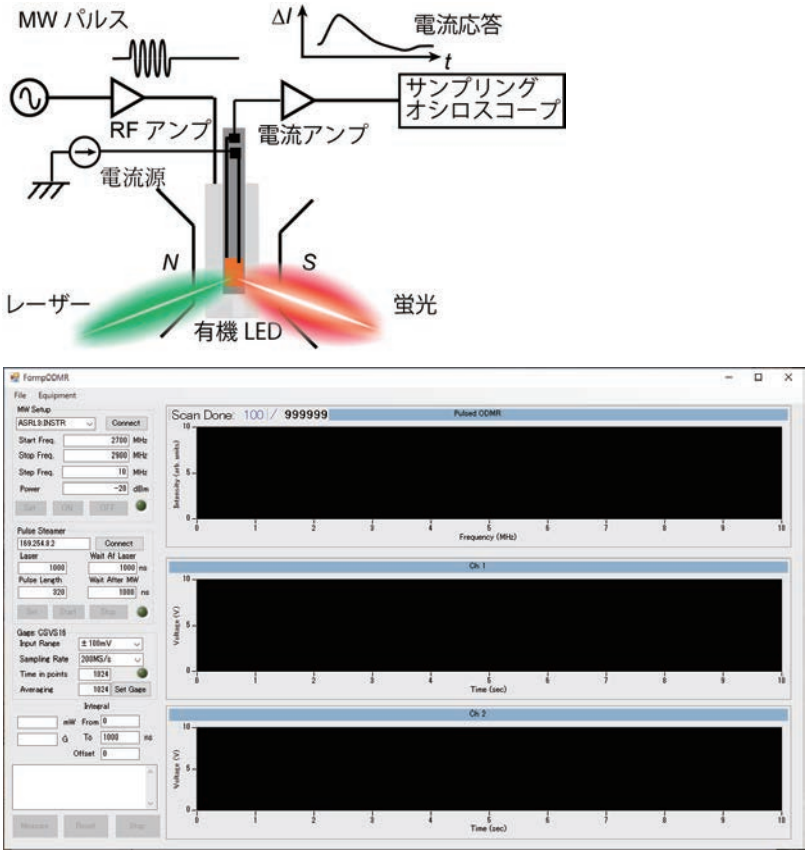


図 1　システムの概要と作成した測定プログラム

Visualization and Analysis of Cellular Phase-Separating Proteins

Kazuya Kikuchi　Osaka University

Building on our previous development of fluorescence-based tools to visualize and quantify liquid-solid transitions of biomolecular condensates, our collaboration with Kyoto University's Uesugi Group was further strengthened in FY2025 through a comprehensive omics-based investigation of condensate states. This collaborative effort resulted in a publication in *Journal of American Chemical Society* in 2025.

In FY2025, we established a workflow that combines live-cell labeling of phase-separating proteins with fluorescence-activated cell sorting (FACS) to isolate cell populations harboring condensates in distinct physical states: liquid, intermediate, and solid. This strategy enabled, for the first time, systematic downstream transcriptomic and proteomic analyses directly linked to the material properties of intracellular protein condensates.

Using cells expressing PYP-tagged FUS(P525L), we sorted three populations corresponding to liquid condensates, solid aggregates, and an intermediate transition state. RNA-sequencing analysis revealed that cells containing solid or intermediate condensates exhibited coordinated transcriptional changes compared to cells with liquid condensates. Complementary quantitative proteomic analyses further demonstrated that condensate solidification is accompanied by a pronounced increase in extracellular matrix (ECM) proteins. Gene ontology enrichment consistently identified extracellular matrix organization as the most significantly upregulated biological process in cells harboring solid aggregates. Key ECM components, including collagen and laminin family proteins, were validated as being progressively upregulated along the liquid-to-solid transition axis. This finding reveals a previously unrecognized link between intracellular condensate solidification and extracellular matrix remodeling.

Collectively, the FY2025 outcomes extend our earlier biophysical and imaging-based studies into the cell biological studies with previously unrecognized insights. This work establishes an integrated chemical biology-omics platform for dissecting the biological consequences of protein phase transitions and provides a conceptual framework for understanding how aberrant condensate solidification may contribute to disease-associated cellular states. We sincerely acknowledge the continued and productive collaboration with Kyoto University's Uesugi Group, which was essential for achieving these advances.

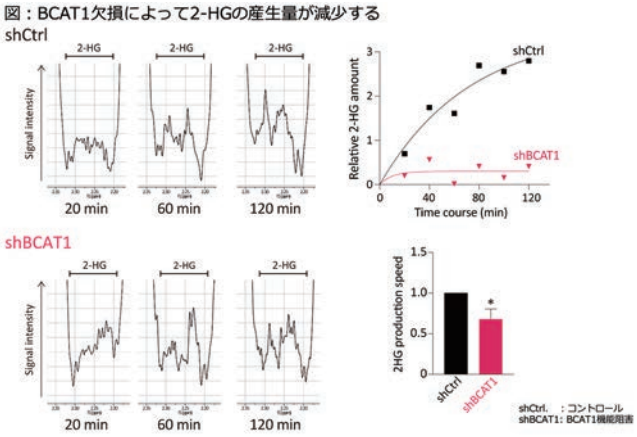
HR-MAS 法を用いた悪性腫瘍の代謝プロファイリング

服部鮎奈　京都大学

目的

がん細胞は、正常細胞とは異なる代謝活動を行うことが知られている。一方で、代謝酵素の多くが反応を両方向に触媒する活性を持つこと、代謝物の多くが細胞内の別経路からも産生されることから、代謝の方向性を明らかにすることや、BCAA 代謝がどのように腫瘍維持に機能するのか、その分子メカニズムを明らかにすることは困難であった。本研究では、安定同位体標識基質を用いた High Resolution NMR MAS（HR-MAS）技術により、生細胞・組織を非破壊で測定し、代謝の方向性を決定づけるとともに、BCAA 代謝による腫瘍維持機構の解明を目的とした。

結果と考察



化学研究所分子材料化学研究領域梶研究室との共同研究により、軟骨肉腫細胞を対象に、^{13}C 標識基質を用いた HR-MAS 解析を実施し、分岐鎖ケト酸（BCKA）から分岐鎖アミノ酸（BCAA）が産生される反応を、生細胞条件下で検出した。さらに、BCAA アミノ基転移酵素 BCAT1 の阻害を行うと BCAA 産生が低下したことから、BCKA から BCAA への反応を担う主要酵素が BCAT1 であることを示した。加えて、BCAT1 反応では BCAA と共役して α-ケトグルタル酸（α-KG）が生成されることに着目し、軟骨肉腫で高頻度に認められる IDH1/2 変異との関連を検討した。IDH 酵素はイソクエン酸と α-KG の代謝に関与する酵素だが、点変異型 IDH は α-KG から腫瘍代謝産物 2-hydroxyglutarate（2-HG）を産生する。そこで、BCAT1 由来 α-KG が 2-HG 産生に寄与するかを解析した結果、BCAT1 阻害により 2-HG 産生量が低下することを明らかにした（図）。乳がんにおいても、悪性度と BCAA 産生速度の相関があることがわかった。以上より、BCAA 代謝経路は広汎ながん種に保存された代謝脆弱性である可能性が示唆された。現在、共同研究成果となる以下の２報の論文がリバイス中である。

1. Yamamoto, Y., Nakagawa, M., Glushka J, Maeno A, Tsunoda, M., Shimada, E., Nakatani, F., Ichihara, K., Matsumoto, A., Edison, A. S., Kaji, H, Toguchida., J, Alman, B, Ito, T., Hattori, A.* BCAA transaminase as a critical regulator of human chondrosarcoma progression and differentiation through enzymatic and non-enzymatic mechanisms. *British Journal of Cancer*, In revision (2026)
2. Matsuura K., Shinonaga R., Yamamoto M., Okuda K., Inoue H., Imotani S., Glushka J., Watanabe Y., Takada M., Inoue J., Kaji, H, Hattori A., Imamura H., Ito T.* Unique Metabolic Dependency on BCAA Defines Cancer Stemness and Malignancy in Human Triple-Negative Breast Cancer. *Cell Reports*, In revision (2026)

Chemical Genetics of XZA-1

Lu Zhou　Fudan University

This collaboration with Professor Uesugi at the Institute for Chemical Research (ICR), Kyoto University, focused on elucidating the chemical and metabolic regulation of hypoxia-inducible factor-1α (HIF-1α) signaling in cancer. Professor Uesugi provided critical guidance on chemical biology strategies throughout the project. The collaborative work resulted in a research article published in *Cell Chemical Biology* in 2025.

HIF-1α is a master transcriptional regulator of hypoxic responses and is frequently hyperactivated in solid tumors through post-translational modifications, including SUMOylation. CBX4 functions as a SUMO E3 ligase that enhances HIF-1α transcriptional activity; however, regulatory mechanisms controlling CBX4 itself were previously unclear.

Through large-scale phenotypic screening of over 100,000 compounds, we identified XZA-1 as a potent small-molecule inhibitor of CBX4-dependent HIF-1α activation. Mechanistic studies revealed that XZA-1 directly activates 3-hydroxyacyl-CoA dehydrogenase (HADH), a mitochondrial enzyme involved in fatty acid β-oxidation. HADH activation leads to intracellular accumulation of acetoacetyl-CoA, a metabolite that induces acetoacetylation of CBX4 at lysine 106. This post-translational modification suppresses CBX4 SUMO E3 ligase activity, resulting in reduced SUMOylation and transcriptional activity of HIF-1α.

Importantly, the biological relevance of this pathway was validated in multiple cancer cell lines, xenograft mouse models, and human hepatocellular carcinoma (HCC) tissues. Elevated levels of CBX4 K106 acetoacetylation correlated with improved overall survival in HCC patients, highlighting its potential clinical significance. This study establishes acetoacetyl-CoA as a bioactive antitumor metabolite and proposes HADH activation as a novel pharmacological strategy to modulate hypoxia signaling.

Professor Uesugi’s expertise in chemical biology was instrumental in ensuring rigorous experimental design. This collaboration exemplifies the value of interdisciplinary supervision.

Exploration and Analysis of Fluorescent Probes for Biomolecular Condensates

Young-Tae Chang　POSTECH

Protein condensation through liquid-liquid phase separation (LLPS) has emerged as a fundamental mechanism underlying cellular organization, particularly driven by intrinsically disordered, low-complexity protein regions. In this collaboration, the Uesugi Group at the Institute for Chemical Research (ICR), Kyoto University, and our research group at POSTECH aimed to develop fluorescent probes that selectively label protein condensates and enable real-time analysis of their dynamic formation and transitions.

In FY2025, the collaboration was strengthened through direct interactions. An in-person meeting was held at POSTECH in May with Prof. Uesugi and members of his laboratory to accelerate scientific exchange and align research strategies. Subsequently, during the summer, our laboratory hosted a graduate student from ICR for one month. The student conducted a large-scale screening of approximately 1,700 fluorescent compounds to identify probes that preferentially accumulate in LLPS droplets formed by p62 and FUS(P525L). Although this screening did not yield probes with the desired selectivity, the effort provided valuable technical insights and informed subsequent directions.

Importantly, this initial outcome prompted the development of an alternative and more innovative strategy. By integrating the Uesugi Group’s protein-tagging and photodamaged-protein isolation technology (*JACS*, 2022) with our expertise in fluorescent probe discovery, we established a new proximity-based protein capture approach. Many fluorescent probes, particularly those excited by high-energy blue light, generate localized reactive oxygen species upon photo-irradiation. Leveraging this property, we developed a method to capture and identify proteins in close proximity to fluorescent probes in live cells.

This newly developed technology has enabled us to determine the subcellular localization and protein environment of existing fluorescent probes, as well as to elucidate the molecular context of previously “mysterious” probes discovered in our laboratory that exhibit characteristic staining patterns in senescent cells. We consider this co-developed technology to be highly promising, with strong potential to yield biologically significant insights into cellular organization and disease-related states. On this basis, we are highly motivated to further deepen and expand this collaboration in the coming years.

Synthetic and Functional Investigation of Arvenin I

Xiaoguang Lei　Peking University

This collaborative project with the Uesugi group at ICR focuses on elucidating the structural and functional requirements of arvenin I, the first covalent kinase activator discovered by the Uesugi group. Arvenin I enhances anticancer immune responses by covalently binding to MKK3 and activating the MKK3–p38 MAPK signaling pathway in T cells. Arvenin I restores mitochondrial fitness in exhausted T cells, highlighting its strong potential as a novel immunotherapeutic agent.

A key finding from the Uesugi group is that the glycosylated form of arvenin I exhibits markedly higher biological activity than its aglycone counterpart. This observation suggests that the glucose moiety plays a critical role in cellular uptake and/or molecular recognition. Accordingly, the primary objective of this collaboration is to clarify how glycosylation governs the transport, target engagement, and biological activity of arvenin I through integrated chemical and biological approaches.

Substantial progress was achieved during FY2025 through close coordination with the Uesugi group. In vitro kinase assays demonstrated that arvenin I, arvenin III, and non-glycosylated derivatives all activate the MKK3–p38 MAPK signaling cascade. These results indicate that the reduced activity of the non-glycosylated derivatives (CuB and CuD) observed in cellular IL-2 assays is likely attributable to factors such as cellular permeability or selectivity, rather than a loss of intrinsic kinase activation. PAMPA assays showed that arvenin I and arvenin III are non–cell-permeable, whereas CuB and CuD display limited membrane permeability. Arvenin I–mediated IL-2 restoration was abolished by the pan-GLUT inhibitor phloretin, indicating that arvenin I utilizes a glucose transporter for cellular entry.

In parallel, multiple 2-OH carbamate derivatives of CuB were successfully synthesized, generating an initial compound set for structure-activity relationship studies. In addition, chemoproteomics experiments comparing arvenin I and CuB were initiated, with ongoing optimization to improve sensitivity and target coverage.

Plans for FY2026 include completion of the chemoproteomics studies, further expansion and functional evaluation of CuB derivatives, and the synthesis of an azide-labeled arvenin I derivative to enable imaging-based analyses of cellular uptake and target engagement.

Biogenesis, functions, and application of bacterial extracellular membrane vesicles

Wei Yunlin　Kunming University of Science and Technology

A Gram-negative bacterium, *Shewanella vesiculosa* HM13, isolated by the group of the ICR partner researchers from the intestinal contents of horse mackerel, abundantly produces EMVs. Their major cargo protein of unknown function, with a molecular mass of 49 kDa and designated P49, is loaded onto EMVs through interaction with capsular polysaccharide (CPS) on the EMV surface. To gain insights into the structural moiety of P49 responsible for interaction with CPS, we performed crystallographic analysis in collaboration with researchers at Kyoto University.

In 2025, our research advanced bacteriophage–host interaction studies with a translational emphasis on: (i) Developing and validating phage candidates to control *Pseudomonas syringae* (Pss) for reduced antibiotic dependence; and (ii) Synthesizing emerging “communication” frameworks (quorum sensing-like systems) that govern phage infection strategies and shape microbial ecology, together with insights into bacterial oxygen adaptation relevant to persistence and pathogenicity.

Publications (2025): 1) Frontiers in Microbiology (published 12 Nov 2025): “Characterization of two novel bacteriophages (PSV6 and PSV3) as biocontrol agents against Pseudomonas syringae.” DOI: 10.3389/fmicb.2025.1633072. 2) Viruses (published 26 Feb 2025): QS and lysis–lysogeny decision review. DOI: 10.3390/v17030317. 3) Microorganisms (published 4 Sep 2025): Arbitrium (ARM) communication system review. DOI: 10.3390/microorganisms13092058.

Funding Information: Yunnan Province Science and Technology Plan Project (202201AU070003) and Yunnan Provincial Department of Education Science Research Fund (2024J0546).

Future plan: (i) Develop stable formulations and conduct field trials for PSV6/PSV3-based biocontrol; (ii) Build QS/ARM-informed predictive frameworks to guide phage selection and dosing strategies under ecological constraints; (iii) Extend oxygen-adaptation multi-omics to infection-relevant models to identify intervention targets that disrupt persistence and virulence.

Structural and functional analysis of the surface polysaccharides of outer membrane vesicles released by bacteria

Maria Michela Corsaro　University of Naples Federico II

Objectives This study aims to determine the structures and functions of surface glycans of *Shewanella vesiculosa* HM13, a hyper-vesiculating Gram-negative bacterium. Capsular polysaccharide (CPS) is a major surface component of this bacterium's outer membrane vesicles (OMVs) and plays a key role in protein loading onto OMVs and their biogenesis. CPS consists of a pentasaccharide repeating unit with neutral and amino sugars (Casillo et al., 2022), one of which has an *N*-acetimidoyl group derived from an *N*-acetyl group. Because our previous studies suggested that the surface properties of OMVs are affected by the deletion of *wecA*, we will focus on a structural analysis of polysaccharides from the *wecA* mutant strain. The monosaccharide composition was obtained by derivatisation into acetylated methyl glycoside (AMG) and GC-MS analysis.

Experimental To obtain structural information on surface glycans, the *wecA* mutant cells were extracted by phenol/chloroform/petroleum ether (PCP) 2:5:8 *v/v* and water/phenol method. All the extracts were dialysed against water (cut-off 3500 Da) and freeze-dried. The obtained extracts were analysed by DOC-PAGE and visualised after silver staining. The monosaccharide composition was obtained after derivatization into AMG.

Results The cells of the *wecA* mutant of *S. vesiculosa* HM13 were extracted by PCP and hot phenol/water methods. After precipitation of the lipooligosaccharides (LOSs), the residual phenolic and aqueous phases were dialyzed against water. The GC-MS analysis of monosaccharides derivatised as AMG disclosed the presence of glucose (Glc), 2-amino-2-deoxy-glucose (GlcN), and heptoses (Hep), as already reported for the LOS isolated from the wild-type (Casillo et al., 2019). The AMG chromatograms of phenolic and aqueous extracts disclosed the presence of monosaccharides attributable to the LOS (glucose and heptoses). Furthermore, no peak assigned to rhamnose was detected, thus indicating that the CPS isolated from *S. vesiculosa* HM13 wild-type was not produced by the *wecA* mutant.

References Casillo, A. et al. Marine Drugs (2019), 17, 34; Casillo et al., Carbohydrate Polymers (2022), 297, 120036.

Exploration of useful bacteria for nanobiotechnology

Douglas Bartlett　UC San Diego

Objectives: Membrane vesicles are membrane-encapsulated nanoparticles secreted by all organisms, such as humans, plants, and bacteria. These nanoparticles play important physiological roles in various biological activities. In bacteria, these vesicles are generally called outer-membrane vesicles (OMVs) and extracellular membrane vesicles (EMVs). Bacterial membrane vesicles (MVs) contribute to inter- and intraspecies communication, including infection and microbiome formation, to support bacterial survival. Moreover, MVs have attracted great attention across various bio-industrial fields and are expected to be used as platforms for novel vaccines and nanoreactors as natural nanocarriers. This study aims to screen for novel bacterial strains that produce large amounts of MVs and to elucidate the molecular basis of MV formation.

Results and Discussion: *Shewanella vesiculosa* HM13, a gram-negative bacterium isolated from the fish intestine, produces a large amount of MVs compared to *E. coli* and lactic acid bacteria, and the related *Shewanella* species. Previously, we developed a novel peptide-based tool that enables rapid *in situ* screening of mutants for changes in MV production from the transposon random mutant library (Inoue, 2025). Using this approach, multiple genes involved in MV production were identified. One of the identified genes, *hm2929*, encodes a RadD homolog, a putative DNA helicase containing a conserved DNA-binding motif. Transposon insertion into *hm2929* resulted in approximately a two-fold increase in MV production. To investigate the molecular basis underlying this phenotype, whole-cell proteomic analysis was performed. The results revealed that, in the *hm2929*-deletion mutant, the relative abundance of a putative phospholipid transporter, LetB, encoded by *hm2719*, was significantly reduced. Consistent with this observation, deletion of *hm2719* also led to increased MV production. In gram-negative bacteria, LetB transports excess phospholipids from the outer membrane to the inner membrane, thereby maintaining outer membrane integrity. LetB-deficient mutant of *S. vesiculosa* HM13 (ΔLetB) also exhibited increased SDS sensitivity, indicating outer-membrane destabilization. Comparative lipidomic analysis revealed that the cellular phospholipid composition of the parent strain and ΔLetB was comparable. In contrast, MVs derived from ΔLetB showed a marked increase in the relative abundance of phospholipid species containing a palmitoyl acyl chain (16:1-PLs). Furthermore, nanoparticle tracking analysis demonstrated that loss of LetB markedly altered the MV size distribution. While *S. vesiculosa* HM13 predominantly produced MVs with a uniform diameter of approximately 70 nm, ΔLetB generated a broader and more heterogeneous MVs, with vesicles larger than 200 nm being frequently observed. These observations indicate that LetB plays a key role in maintaining the outer-membrane lipid homeostasis and vesicle size fidelity.

Recycling of polymer-matrix composites by subcritical/supercritical water II

Maya Endoh　Stony Brook University

Objective: Recently, Mitsubishi Chemical Corporation and ENEOS Corporation announced their SCW-based plastic-to-oil project in Japan.Polymer degradation under subcritical/supercritical water (subCW/SCW) conditions is receiving much attention because of a rapid and catalyst-free reaction, the high conversion rate to hydrocarbons, and no use of toxic organic solvents. Supercritical water environments will be used to probe rapid depolymerization pathways, while subcritical conditions will enable controlled observation of intermediate structures and degradation mechanisms. Despite the aforementioned potentials over other technologies, the use of SCW for handling organic systems is very limited. This project aims to establish a mechanistic understanding of polymer degradation under supercritical and subcritical water conditions by leveraging advanced X-ray scattering techniques. By integrating in situ small- and wide-angle X-ray scattering (SAXS/WAXS), we will resolve structural evolution across multiple length scales during hydrothermal degradation. Ultimately, the objective is to develop predictive structure–processing–degradation relationships that inform the design of polymers with tunable lifetimes and improved recyclability. This work will provide a foundation for sustainable materials processing and closed-loop polymer lifecycle engineering.

Experimental Method & Results: We have successfully finished developing a new high-pressure cell for X-ray scattering experiments. The cell was constructed by Kouatsu System, Co., LTD (Saitama, JP) (See Figure 1). We have validated the safe performance of the cell, as it operates at pressures up to 30 MPa and temperatures up to 400 °C. We found that the materials of the O-ring packing at the diamond window cannot be polytetrafluoroethylene (PTFE) or polyimide as subCW/SCW degrade polymers. While this suggests that subSC/SCW may degrade polymers that are not easily decomposed under heat, we have decided to use pure gold for the O-ring. We confirmed that the pressure drop was minimal while keeping the temperature constant, thus it passed the safe performance test.

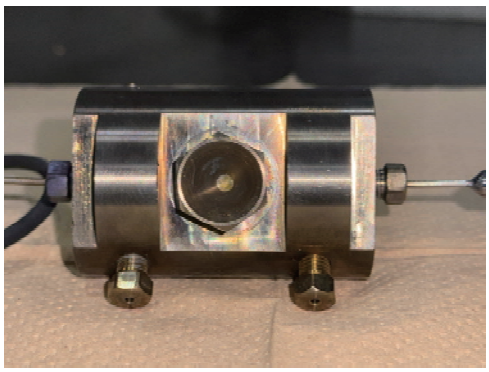


Figure 1: Front view of the high-pressure cell for X-ray scattering.

To compare with the SCW depolymerization process, we investigated the degradation process of polylactic acid (PLA) in an aqueous solution at room temperature. To initiate the reaction, we used the enzyme (proteinase K). We conducted X-ray scattering based scanning tomography for imaging and structural characterization at the LiX beamline, NSLS-II, Brookhaven National Laboratory, USA. The wide-angle X-ray scattering (WAXS) tomography images show PLA degraded by Proteinase K from week 1 to week 5. Each WAXS image exhibits local heterogeneity in PLA's crystallinity. We will continue to examine the degradation process under ambient condition and subCW/SCW conditions.

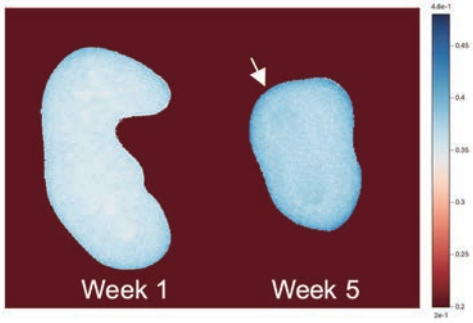


Figure 2: X-ray scattering tomography images of PLA degraded by Proteinase K from week 1 and week 5 are shown. The arrow indicates that the outer shell has higher crystallinity.

Synthesis and Tribological Applications of Polyether-Brush-Coated Particles

Kohji Ohno　Osaka Metropolitan University

INTRODUCTION Lubricants are widely utilized in industrial products and manufacturing processes to minimize friction and wear between moving parts. A key research challenge in recent years has been the development of functional additives to enhance lubricant performance and efficiency. Achieving this goal holds the potential to address economic and environmental concerns, thereby contributing to a more sustainable society. While the incorporation of fine particles into lubricating fluids has been explored, the impact of structural parameters such as particle size and surface properties on lubrication performance remains insufficiently understood. The present study aims to synthesize hybrid nanoparticles grafted with polyether brushes that exhibit a range of structural parameters, utilizing surface-initiated ring-opening polymerization of epoxides.

RESULTS AND DISSCUSION Surface-initiated ring-opening anionic polymerization (SI-ROAP) were employed to modify the surfaces of alumina nanoparticles (AlNPs) with polyether brushes. AlNPs with a diameter of 20 nm were treated with a silane coupling agent containing thiol group to introduce initiation sites on their surfaces. Subsequently, polye pichlorohydrin (PECH) was grafted onto AlNPs via SI-ROAP, resulting in PECH-grafted AlNPs (PECH-AlNPs). A TGA result from these nanoparticles is shown in **Figure 1**, suggesting the polymer brushes are attached to the surface. The graft polymer was cleaved from the nanoparticle surface to determine its molecular weight. Typically, PECH-AlNPs (30 mg) were dispersed in 5mL of toluene and stirred vigorously overnight to ensure suitable dispersion. Then, a phase transfer catalyst, tetraoctylammonium bromide (30 mg), followed by 48% HF (1mL) was added and the dispersion was stirred overnight. Using thus determined molecular weight of graft polymer, the graft density of PECH chains on the AlNP surfaces was calculated to be 0.8 chains/nm², indicating high-density grafting. By varying the polymerization conditions, hybrid particles with varying graft chain molecular weights were synthesized. Future efforts will focus on investigating the lubrication performance of a liquid prepared by dispersing PECH-AlNPs in an ionic liquid and then optimizing nanoparticle structures to prepare nanoparticle-based additives exhibiting superior lubrication properties.

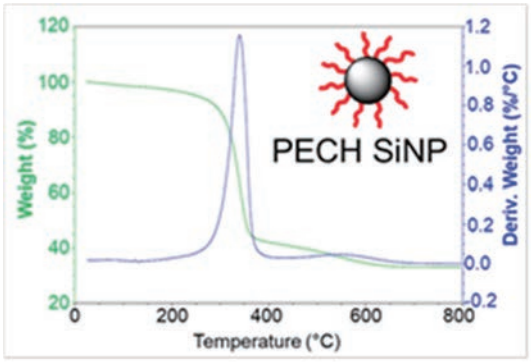


Figure 1. TGA showing the degradation of PECH grafted to the surface of the nanoparticle.

Real-time observation of self-assembly and phase transformation of nanocrystals

Oh-Hoon Kwon　KAIST

Palladium (Pd)-based catalysts play a key role in a variety of industrially important reactions. However, sulfur-containing impurities like alkanethiols may hamper catalytic activity and alter reaction selectivity. Therefore, understanding the formation Pd–S phases and their kinetic pathway is essential for elucidating sulfur poisoning mechanisms and improving catalyst durability. It has been reported that thiol–Pd interactions induce the formation of Pd_xS_y phases beneath the thiolated surface, although the continuous structural evolution during the phase evolution could not be directly tracked. Here, we investigate the sulfidation of Pd nanocrystals (NCs) with temperature in real time, focusing on the temperature-dependent phase evolutions towards forming Pd_4S, and the timescale of the structural transformation.

The in situ heating X-ray diffraction (XRD) results (Fig. 1A) show that, at approximately 480 K, the diffraction peaks exhibit pronounced broadening, accompanied by a splitting of the Pd (111) peak into peaks corresponding to the (210) and (112) reflections of Pd_4S. This behavior indicates the onset of the structural evolution associated with the formation of palladium sulfide phases. High-resolution transmission electron microscopy (HRTEM) analysis (Fig. 1B–D) reveals that the sulfidation reaction does not proceed through a monotonic transformation from Pd to Pd_4S. Instead, multiple intermediate Pd_xS_y phases were observed. Notably, even at the same temperature, different NCs exhibit distinct crystallographic phases, demonstrating significant heterogeneity in the phase evolution behavior. These findings suggest that the reaction is not governed solely by thermodynamic equilibrium but is strongly influenced by kinetic factors that may depend on a particle size, a defect density, and a local sulfur diffusion rate.

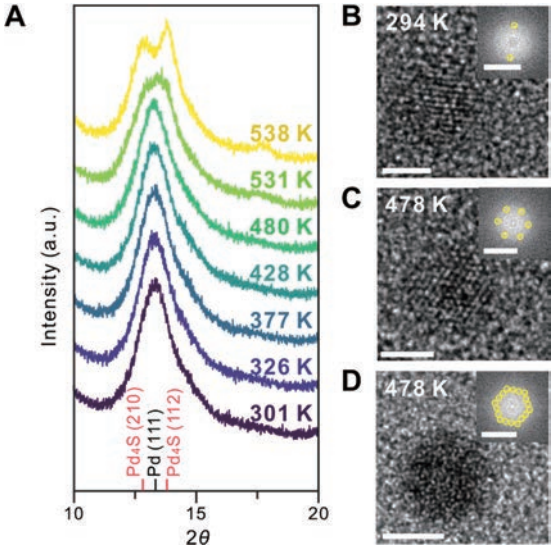


Fig. 1. (A) Temperature-dependent in situ heating XRD patterns of Pd NCs during sulfidation, (B-D) HRTEM images and FFTs of Pd NCs at 294 K. (B, C) HRTEM images of the same Pd_4S NC, but at different temperatures. (D) HRTEM image of a different NC in the $Pd_{16}S_7$ phase at 478 K. Scale bars: 2 nm for HRTEM images and 10 nm^{-1} for FFTs.

Ultrafast measurement of relativistic laser-generated plasma

Masato Ota　National Institute for Fusion Science

Objectives

With the development of chirped pulse amplification, high-intensity short-pulse lasers, which have sub-picosecond pulse widths, reached a relativistic regime, where electrons are directly accelerated by electromagnetic fields of the laser pulses. This property is promising for various applications such as next-generation accelerators and inertial confinement fusion. Relativistic laser-plasma acceleration has been studied for decades. However, experimental study on elemental process of laser-plasma interaction was not fully explored because the time scale of the phenomena is short (picoseconds), and ultrafast diagnostics were very limited. In this research, we apply ultrafast diagnostics to relativistic laser-generated plasmas at ultra-high-intensity ultra-short pulse laser system “T6 laser” of Tokita Laboratory (energy of 300 mJ, pulse width of 30 fs, and central wavelength of 800 nm).

Experimental Methods

In the experiment, we utilized sequentially timed all-optical mapping photography (STAMP) to obtain the temporal evolution of the two-dimensional plasma density profiles. STAMP consists of a diffractive optical element (DOE), a band-pass filter, and two Fourier transform lenses. By employing a linearly frequency-chirped pulse by temporal mapping device (TMD) and mapping the wavelength to the time axis by spatial mapping device (SMD), single-shot ultrafast burst imaging is achieved.

Outcomes

Figure 2 shows the STAMP measurement results obtained in the experiment. Each frame corresponds to delay times (T) of 20, 50, 377, 740, and 1630 ps between the pump irradiation and the arrival of the probe beam at the copper wire. At T = 20 ps, plasma formation occurs instantaneously over a wide area centered at the focal spot. Until T = 740 ps, the plasma expand monotonically; however, after that, the growth of filamentary structures appears. These filamentary structures are not observed at non-relativistic laser intensities and are considered to be instabilities unique to high-energy plasmas. The present measurement technique has potential to serve as a platform for high-energy plasma experiments, which has low reproducibility such as plasma instabilities and sudden transient events.

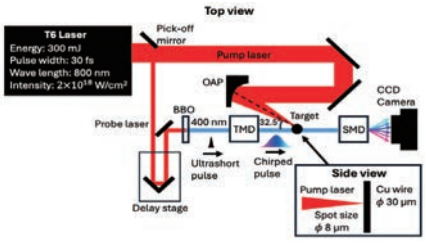


Fig. 1. Experimental setup of STAMP.

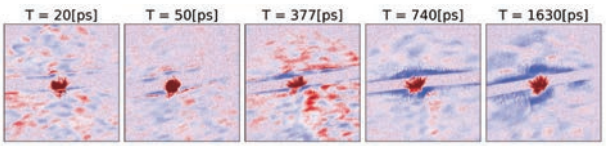


Fig. 2. Spatiotemporal profile of the laser-generated plasma obtained by STAMP.

Search for four-wave-mixing in the vacuum – Unveiling dark components in the Universe –

Kensuke Homma　Hiroshima University

Purpose and Method

The aim of this study is to investigate Four-Wave-Mixing (FWM) phenomena within a vacuum environment, with the goal of shedding light on the dark components present in the Universe. To this end, we have developed and refined an ultra-high vacuum chamber at ICR for this purpose. Within this vacuum chamber, two-color laser pulses are combined collinearly and focused into the vacuum along the same optical axis. If photon-photon interactions occur within this vacuum setting, the production of intrinsic FWM photons through the stimulated interaction $\omega+\omega\rightarrow(2\text{-u})\,\omega+\mathrm{u}\,\omega$ is expected to be amplified. Here, ω represents the energy of the creation laser pulse, while $\mathrm{u}\,\omega$ denotes the energy of the inducing laser pulse with $0<u<1$. The energy of the signal photon generated in this scattering process corresponds to $(2\text{-u})\omega$.

Progress and Achievements

We have developed an eclipse filtering system to suppress the entrance of the background FWM photons from the optical components into the photon counter using an image intensifier camera in order to capture the 2-dimensional image of the weal background FMW photons. With this filtering system, we have furthermore extended the search by increasing laser intensity and the null result has been published in [1]. Furthermore, in order to access the eV mass range of dark components, we have performed a search based on the same detection concept with a three-beam collider and published the null search result [2].

We summarize the published papers relevant to these related subjects during FY2025 as follows:

Published papers

[1] “Search for sub-eV axion-like particles in a quasi-parallel stimulated resonant photon-photon collider with “coronagraphy””

Yuri Kirita, Airi Kodama, Kensuke Homma* et al. (SAPPHIRES collaboration)

Published in: JHEP 06 (2025) 138（acknowledge the support by ICR）

DOI: 10.1007/JHEP06(2025)138,

[2] “Single-Point Search for eV-scale Axion-like particles with Variable-Angle Three-Beam Stimulated Resonant Photon Collider”

Takumi Hasada, Kensuke Homma* et al. (ᵗSAPPHIRES collaboration)

Published in: Universe 2026, 12(1), 17（acknowledge the support by ICR）

DOI:10.3390/universe12010017.

Flow Chemistry for the investigation of sustainable cyclisation conditions

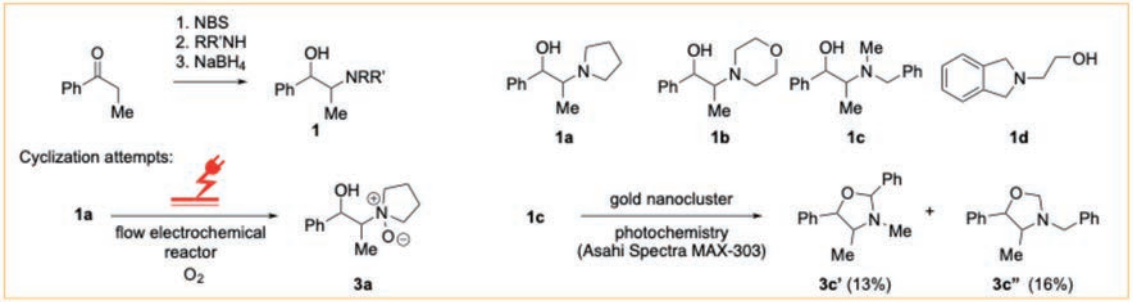
Thomas Wirth　Cardiff University

This report builds on our previous collaborative research with the Nakamura group (ICR partner researcher). As the original starting materials **1** for the proposed study were no longer commercially available, we successfully developed and extended a synthetic route, enabling the preparation of compounds **1** in good yields and sufficient quantities. These materials were also supplied to the Nakamura group, allowing the planned experiments to proceed as intended. Selected results were discussed in depth with the Nakamura research team during a highly engaging and productive visit in September 2025.

While the electrochemical cyclization of the target molecules in the presence of elemental oxygen did not yield the desired products, extensive efforts, including alternative non-photochemical methods for the generation of singlet oxygen ($^1O_2$), provided valuable insights. Although these approaches did not lead to productive cyclizations, the outcome is scientifically informative and contributes to a clearer understanding of the role of gold nanoclusters in the cyclization reaction.

Compounds **1** have been synthesized successfully but the electrochemical reaction produced only *N*-oxide products which were observed in the crude NMR. About 100 electrochemical reactions have been attempted using different reaction conditions. However, the reactions using gold nanoclusters (AuNCs) as photocatalysts for the oxidative cyclization of amino alcohols (*ACS Catal.* **2021**, *11*, 13180–13187) seem to provide small amounts of products as the compounds **3c'** and **3c"** have been isolated and characterized resulting from either a cyclization *via* the benzyl group (**3c'**) or *via* the methyl group (**3c"**).

We have already written a draft manuscript on the starting material synthesis and the comparative cyclization reactions, which we hope to be able to submit soon for publication.

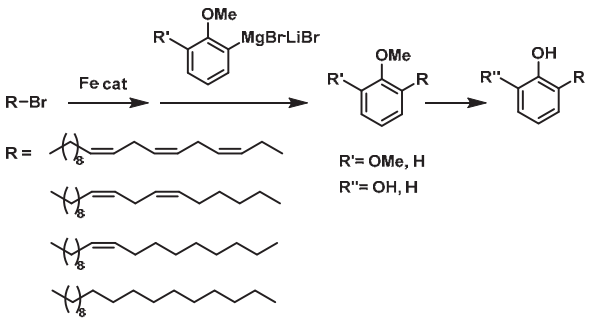


Synthesis and characterization of raw and polymerized Asian lacquer samples: towards the development of a comprehensive collection of lacquer reference samples for materials science and conservations studies

Bonaduce Ilaria　University of Pisa

Asian lacquer is obtained from the viscous sap collected from the *Toxicodendron vernicifluum* tree. Urushi is a natural product, a water-in-oil emulsion composed of urushiol (60-80%), water (10-30%), gum (3-6%) and enzymes (2-3%). The urushiol fraction contains a mixture of phenolic lipids which undergo enzymatic and auto-oxidative cross-linking to form the solid urushi film. Due to the well-known resistance of urushi against attacks by acids, bases and all types of solvents, one of the few techniques available to characterize both fresh and ancient urushi films is pyrolysis-gas chromatography-mass spectrometry. Despite the versatility of this technique, it has been difficult so far to unequivocally attribute the origin of the peaks in the complex pyrograms. In order to reliably understand the data obtained from the analysis of ancient urushi artifacts, it is of the outmost importance to compare the results from the natural material with those relative to the pure components of urushi. Access to synthetically prepared urushi monomers represents a powerful tool for model studies aimed at disentangling the mechanisms of film formation. Such an approach not only provides new insights relevant to conservation strategies, but also contributes to a deeper understanding of how urushi films can be deliberately modulated to improve durability or tailor specific final properties. Currently, the ICR team is working on the total synthesis of the main urushiol components, (8Z, 11E, 13Z)-trienyl pentadecylcatechol, and of several urushiol analogs via iron-catalyzed reaction, see Scheme 1. The synthetic routes have been systematically optimized and validated for large-scale production, ensuring the availability of sufficient quantities of reference compounds for analytical, mechanistic, and materials-oriented investigations. In addition, on 12–13 February 2026 an international workshop entitled *“Urushi and Asian lacquers in Western collections: scientific and conservation challenges”* was held at the British Museum (UK). The event was co-organized by all members of this collaborative team (Bonaduce, Pincella, Tamburini, Mineo) and brought together an international group of scientists, conservators, and material specialists from Europe, Asia, and North America. The workshop provided a dedicated forum to discuss the current state of the art, emerging analytical approaches, and unresolved challenges in urushi research, with a particular focus on the chemical characterization of lacquer materials and their implications for conservation practice.

Scheme 1



DNA-binding properties of chemically modified homeoproteins

Fabienne Burlina　Sorbonne University

Objectives. Homeoproteins (HPs) are transcription factors having the remarkable capacity to transfer between cells. This process, associated to their paracrine activity, is mediated by their cell-penetrating domain located in their homeodomain, which also functions as the DNA-binding domain.[1] Studies on HPs have led to the discovery of one of the first cell-penetrating peptide (CPP),[2] now widely used as a vector for drug delivery. HPs themselves are promising candidates for clinical development given their combined capacity for gene regulation and cell-penetration.[1] The aim of the project is to design HP derivatives with increased cellular uptake and preserved DNA-binding properties.

References: 1) Joliot A., Prochiantz A. Front Cell Dev Biol 2022, 10:926421. 2) Derossi D., Joliot A.H., Chassaing G., Prochiantz A. J Biol Chem 1994, 269,10444.

Experimental Methods. To improve HP interactions with their partners (membrane components, DNA), a key residue of their CPP domain was substituted with non-natural residues featuring tuned physico-chemical properties. The substitutes were first introduced on a HP-derived CPP and were evaluated at different levels: i) cellular uptake quantification by fluorometry, ii) secondary structure analysis by CD and/or NMR, iii) affinity for membrane partners analysis by calorimetry, iv) affinity and selectivity for the DNA target analysis by EMSA and fluorescence anisotropy. Selected substitutes have already been introduced in truncated HP derivatives containing the essential domains for cell penetration and DNA-binding. An optimised solid-phase synthesis procedure using backbone amide protecting groups introduced at key positions allowed the synthesis of the small proteins (60-80 residues long) with good yields.

Outcomes. So far, we have identified several substitutes improving the entry of the CPP and one, also increasing the entry of the truncated HP and showed that these substitutions do not perturb the peptide/protein secondary structures. Studies on DNA binding are ongoing. On the long-term, the data will support the design of an HP with improved properties for therapeutic applications.

Oral communication: L. Cano-Gonzalez, M. Samapour, F. Illien, D. Ravault, A. Walrant, O. Lequin, M. Larregola, F. Burlina. Designing new cell-penetrating peptides and therapeutic homeoproteins. French-Italian Joint Meeting GFPP24. Aussois, France, 22-26/06/2025.

Analysis of intracellular delivery mechanism of nanomedicine

Sílvia Pujals　Institute for Advanced Chemistry of Catalonia

Nanomedicine has been widely explored as a strategy to improve therapeutic efficacy while reducing side effects through selective drug delivery. However, the limited clinical success of nanomedicine indicates that intracellular behavior, including uptake pathways and endosomal escape, remains insufficiently understood. This collaborative project aimed to strengthen cooperation between my group and the Kawaguchi group at Kyoto University and to discuss strategies for analyzing intracellular delivery mechanisms of nanomedicines. During this reporting period, the activities focused primarily on scientific exchange, discussion, and technical training.

In September, I visited Kyoto University and delivered a seminar introducing our work on nanoparticle design, structural characterization, and intracellular imaging approaches. This visit enabled detailed discussions on nanoparticle architecture, physicochemical properties, and strategies for evaluating intracellular behavior. These exchanges helped identify complementary expertise between the two laboratories and refine ideas for future collaborative studies.

In October, my postdoctoral researcher Dr. Monika visited Kyoto University and received practical training in intracellular delivery experiments. The training included cell-based uptake assays, fluorescence imaging, and approaches to analyze uptake pathways. She also delivered a seminar presenting ongoing research from our laboratory. These activities promoted technical exchange and improved mutual understanding of experimental methodologies.

Through these visits, the collaboration strengthened the connection between the two laboratories by facilitating researcher exchange, knowledge sharing, and methodological alignment. The discussions clarified key challenges in intracellular delivery of nanomedicines and highlighted promising directions for future research. In particular, we recognized the importance of integrating nanoparticle engineering with delivery-active components to improve intracellular access and therapeutic performance.

In summary, this project effectively promoted international collaboration through seminars, discussions, and technical training. The exchanges clarified research directions and established a strong foundation for future collaborative studies aimed at improving intracellular delivery efficiency of nanomedicines.

Visualizing RNA Editing in Action: Developing Single-Molecule Resolution Techniques for Live Cells

Tim Stasevich　Colorado State University

RNA editing offers a reversible alternative to genome editing, but current assessment methods rely on bulk experiments that cannot capture the dynamic nature of RNA modifications. The objective of this project was to develop methods for visualizing RNA editing at single-molecule resolution in living cells, in collaboration with Dr. Miki Imanishi's group. We designed a reporter construct where translation of a fluorescent signal is conditional upon RNA editing. A stop codon in the mRNA is converted to a sense codon through A-to-I editing, allowing translation to proceed only when editing occurs. This design ensures that fluorescent signals are observed only when RNA editing has successfully occurred, enabling us to monitor editing events at the single-molecule level. The Imanishi group has been developing sequence-specific artificial RNA binding proteins, which could potentially be used to modulate RNA editing by recruiting or blocking editing factors at specific sites. We successfully developed and validated our RNA editing reporter system. As shown in Figure 1, bright fluorescent spots indicating active translation were observed in cells expressing the RNA editing machinery (A), while cells without the editing machinery showed only diffuse background signal with no translation spots (B). These results demonstrate that we now have a functional platform for monitoring RNA editing in live cells. The successful validation of our reporter system establishes a foundation for the next phase of research. With a functional imaging platform in place, we are now ready to test the RNA binding proteins from the Imanishi group, which will allow us to modulate and observe RNA editing in real time. We are excited to continue this collaboration in the coming year.

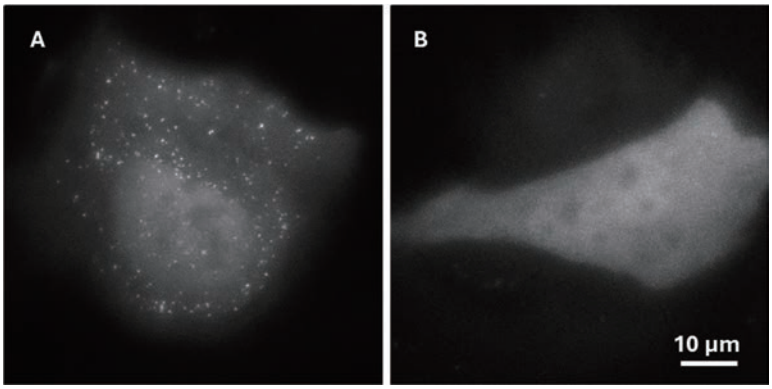


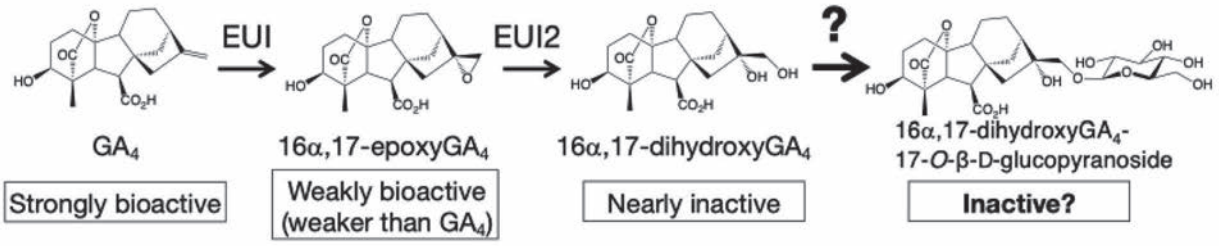
Figure 1. Translation signals detected in cells with RNA editing.

Molecular mechanisms for the inactivation of a growth hormone in rice

Zuhua He　Chinese Academy of Sciences

Objectives: Bioactive gibberellins (GAs) are a group of plant hormones that regulate such diverse developmental processes as seed germination, leaf expansion and stem elongation. They are tetracyclic diterpenoid carboxylic acids that are biosynthesized from the methylerythritol phosphate pathway in the plastid. Bioactive GAs play critical roles in promoting growth, including internode (stem) elongation of rice. The *elongated uppermost internode 2* (*eui2*) mutant of rice shows a tall phenotype due to its elongated uppermost internode. Because of this reason, this mutant has been utilized in hybrid rice breeding in order to eliminate panicle enclosure in male sterile parents. We have previously shown that EUI2 is an uncharacterized protein that belongs to the α,β-fold hydrolase superfamily. In collaboration with Shinjiro Yamaguchi's group, we have found that *EUI* encodes a cytochrome P450 enzyme that deactivates GAs via 16α,17-epoxidation. Based on these results, we speculated that EUI2 might act as an epoxy hydrolase and further deactivate epoxidated GAs in the uppermost internode of rice. Our goal is to fully understand the molecular mechanism for inactivation of GA_4 in rice.

Experimental methods: 16α,17-dihydroxyGA_4 was chemically synthesized, and its biological activity was determined using the uppermost internode of rice. Endogenous levels of epoxy GAs in the uppermost internode of WT and *eui2* mutant rice plants were determined by LC-MS/MS using deuterium labeled epoxy GAs as internal standards. We have also started to look for enzymes responsible for metabolizing 16α,17-dihydroxyGA_4 to its glucose conjugate.



Experimental results: We found that 16α,17-epoxyGA_4 was weakly, but significantly active in promoting the elongation of uppermost internodes of rice in comparison with 16α,17-dihydroxyGA_4. We also found that 16,17-dihydroxyGA_4 could still very weakly interact with the GA receptor GID1. Therefore, to fully understand the mechanism for inactivation of GA_4 in rice, it is necessary to identify the enzyme responsible for the metabolism of 16,17-dihydroxyGA_4. As a first step toward this goal, we started to look for UDP-sugar-dependent glycosyltransferases (UGTs) that could be involved in the conversion of 16,17-dihydroxyGA_4 to 16α,17-dihyroxyGA_4-17-*O*-β-D-glucopyranoside, a previously identified metabolite in rice.

Publications: Toshiaki Ishida, Yingying Zhang*, Hongbo Zhu, Shoko Fudano, Yu Peng, Yoshiya Seto, Kiyoshi Mashiguchi, Jiyun Liu, **Zuhua He**, Shubiao Zhang*, **Shinjiro Yamaguchi*** (2025): Stepwise deactivation of gibberellins during rice internode elongation. ***Proc Natl Acad Sci USA,*** 112(23):e2415835122DOI：10.1073/pnas.2415835122

Identification of biosynthetic genes for a novel signaling molecule that modulates plant development

David C. Nelson　University of California, Riverside

[Objectives]

Karrikins (KARs) are a group of smoke-derived butanolide compounds that can stimulate seed germination of many plants. A receptor, KARRIKIN INSENSITIVE2 (KAI2), is required for the perception of KARs in plants. Interestingly, disruption of KAI2 does not only diminish KAR responses, but also affects seed germination, seedling development and drought resistance in the absence of KAR, suggesting that it also mediates the response to a hormonal ligand endogenously produced in the plant, named as KAI2 ligand (KL). Despite the functional importance of KL in plants, the chemical structure and biosynthesis route of KL is still unclear.

Given that plant hormone biosynthesis is often regulated via negative or positive feedback mechanisms, we hypothesized that disruption of genes involved in KL signaling or treatment of plants with KAR might affect the expression of KL biosynthetic genes. By comparing the transcriptome data between several mutant and wild-type plants in *Arabidopsis thaliana*, as well as KAR-treated and untreated plants, we identified several KL biosynthetic gene candidates, designated ***KL Biosynthetic gene CAndidates selected by Transcriptome*** (KBCATs). This research aims to characterize these genes both genetically and biochemically, and verify if they play a role in the biosynthesis of KL.

[Experimental Methods and Outcomes]

For the genetic analysis, we obtained and confirmed T-DNA insertion mutants for four KBCAT genes and evaluated the phenotype. One of the mutants showed significant decrease in the hypocotyl length, which suggested that the gene might act in an opposite direction to KL signaling. We are currently examining the expression of KL-related marker genes and the genetic interaction between this candidate gene and the KL signaling pathway.

For the biochemical analysis, we are establishing a method to isolate bioactive KL from plant materials and evaluate the activity via bioassays. Plant extracts were separated with open-column chromatography and HPLC, and the fractions were applied to both wild-type and *kai2* mutants. We confirmed that a certain fraction can trigger KL responses in this system, which provided a basis for comparing KL activity in different mutants.

[Publication]

No publications from the collaboration in FY2025.

Analysis of novel transporters for strigolactones or their biosynthetic intermediates

Yunde Zhao　University of California San Diego

Objectives: Strigolactones (SLs) are carotenoid-derived plant hormones that regulate various processes of plant growth and development. They are also secreted from plant roots into the rhizosphere and function as allelochemicals for symbiosis with arbuscular mycorrhizal fungi and for stimulating the seed germination of parasitic plants. Classical grafting studies have suggested that SL and/or its biosynthetic intermediate(s) can move from the root to the shoot; however, SL transport has not been fully elucidated. We have previously identified candidate transporters of SLs or their biosynthetic intermediates in rice. The knockout mutants of the transporters increased the number of tillers, which is phenotypically similar to the well-characterized SL biosynthetic and signaling mutants. The physiological and biochemical roles of the identified transporters need to be experimentally demonstrated.

Experimental methods:

Our group • Phenotypic and genetic interaction studies of mutants whose ability to transport SLs or SL biosynthetic intermediates has potentially been compromised.

• Generation of additional mutants using CRISPR/Cas9 gene-editing technology.

ICR partner researchers (Dr. Kiyoshi Mashiguchi, Prof. Shinjiro Yamaguchi)

• Analysis of endogenous levels of SLs and SL biosynthetic intermediates by LC-MS/MS to identify substrate (s) of transporters.

• Elucidation of SLs and SL biosynthetic intermediates that can move from roots to shoots

• Evaluation of transporter-mediated export/import activity for the candidate compound(s).

Experimental results: We further conducted genetic studies on putative SL transporters this year. Previously, ICR partner researchers detected hydroxy-carlactonoic acid derivatives (OH-CLAs) in the xylem sap of Arabidopsis and rice. This year, they found that OH-CLAs were accumulated in the CLA METHYLTRANSFERASE-defective mutant, suggesting that OH-CLAs are converted into their methylated forms to exhibit bioactivity. They also identified a candidate ABC transporter that transports OH-CLAs from roots to shoots in Arabidopsis.

Publications: No publications from the collaboration in FY2025.

Cycloparaphenylene/Fullerenes Supramolecular Complexes in Chiroptical Applications

Matthew Fuchter　University of Oxford

This project is a continuation of our ongoing efforts to show – for the first time – complexation of chiral open cage fullerenes (cOCFs) and [10]Cycloparaphenylene ([10]CPP) and to study the chiroptical properties of such complexes. Previously, we could show that a chiral, open cage fullerene (cOCF), derived from C_{60} (provided by the group of Prof. Y. Murata, Kyoto University) is a very good match for complexation with [10]CPP. This was shown by strong emission quenching in fluorescence titration experiments. Other types of chiral fullerenes (e.g., bis-PCBM derivatives) and differently sized CPP's (e.g., [11] or [12]) did not give promising results.
We were also able to confirm that there is indeed a change in the chiroptical properties of cOCF upon complexation, leading to a slight decrease in the circular dichroism (CD) at most transitions. While the CD changes are rather small due to the low absorption in the areas of interest, this still corresponds to a significant change in the optical dissymmetry (g-factor). Our results therefore remain in good agreement with the computational data generated by our collaborator, Prof. M. Zwijnenburg (University College London).

While initial fluorescence titration experiments showed a clear quenching upon complexation, the quenching was not linear, as expected and as observed for the [10]CPP – C_{60} pair. Similarly, the Jobs plot titration, which is used to determine the ratio in the complex indicated a 2:1 of [10]CPP to C60 instead of a more intuitive 1:1 as in [10]CPP – C_{60}. To resolve these discrepancies, one lab member recently visited the group of Prof. Shigeru Yamago to draw from their wealthy experience with such titration experiments. Indeed, repeated fluorescence titrations now reveal linear behavior with a Stern-Volmer constant K_{SV} of 1.05×10^6 L/mol - similar to reported values for C_{60} and [10]CPP (4.34×10^6 L/mol). We also repeated Job's plot titrations via UV/Vis and could now confirm a 1:1 complex between cOCF and [10]CPP as indicated by a maximum of ΔA at 0.5 cOCF/(cOCF+[10]CPP).

With our greater experience in the titration experiments of these compounds, we are performing final repeats of the CD and UV/Vis experiments to confirm the changes in chiroptical response upon complexation. This data will be gathered immediately upon arrival of our new CD spectrometer at Oxford, which will ensure high quality data for final interpretation and publication of the results.

Synthesis and Electrocatalysis of Hetero-Metal Porphyrin(2.1.2.1) Arrays

Songlin Xue　Jiangsu University

Objectives: Efficient organic synthesis of porphyrin oligomers, physical and chemical properties, and electrocatalysis property are interesting and need to developing. This project want to provides a novel strategy for hetero-/multi-metal porphyrin electrocatalysis catalyst synthesis, while the multiple active sites provided by the multi-metallic cavity enhance interactions among metal ions. The exploration of metal porphyrin oligomers emerges as an intriguing path forward, as the potential for varied out-comes arising from different metals holds immense promise for diverse applications.

Outcomes: In this joint project, Prof. Dr. Hiroko Yamada and us focus on exploring to synthesis three kinds of porphyrin oligomers, and further investigated properties and application of electrocatalysis of them, such as oxygen evolution reaction (OER) and hydrogen evolution reaction (HER).

1, Fe Porphyrin(2.1.2.1) Dimer（*Inorg. Chem.*, 2025, *64, 22262−22268*）

We have synthesized an Fe(III) porphyrin(2.1.2.1) oxo-bridged dimer complex using porphyrin(2.1.2.1) as a bent ligand. TD-DFT simulations reproduce the main features of the UV−vis spectrum, revealing LMCT transitions. The OER study and DFT mechanistic calculations demonstrate that the presence of the bridging oxygen atom enhances electrocatalytic oxygen evolution activity, lowering the overpotential of the RDS.

2, Face-to-Face Porphyrin Nanoring（*Org. Lett.*, 2025, *27, 10868−10873*）

Two new porphyrin nanorings were synthesized and characterized. PR forms an interesting face-to-face porphyrin nanoring structure. NMR and ACID analyses indicated that both dimers exhibit local aromaticity rather than global 3D aromaticity. Steady state fluorescence, TCSPR, and nanosecond TA studies revealed no significant π−π interactions between the porphyrin unit. $^1O_2$ generation studies under blue and red light irradiation demonstrated that dimers act as highly efficient type II photosensitizers.

3, Wave-Shaped Cu Porphyrin Arrays（*Chem. Sci.*, 2025, *16, 22498–22503*）

Wave-shaped porphyrin(2.1.2.1) arrays were succeed obtained. Due to their rich N4 cavity, dinuclear and trinuclear Cu(II) porphyrin(2.1.2.1) arrays were obtained through coordination reactions. As a result of π-ligand surface and three catalytic Cu(II) ions, the trinuclear Cu(II) porphyrin(2.1.2.1) array exhibits remarkable HER activity, with a lower overpotential, faster HER and charge transfer kinetics, and longer catalytic stability than mono- and dinuclear Cu(II) porphyrin(2.1.2.1) complexes.

Publications: 1. *Inorg. Chem.,* **2025**, *64,* 22262−22268; 2. *Org. Lett.,* **2025**, *27,* 10868−10873; 3. *Chem. Sci.,* **2025**, *16,* 22498–22503.

Vacuum-deposited Perovskite Optoelectronic Devices with Advanced Hole-selection Materials

Hao-Wu Lin　National Tsing Hua University

This research study summarizes the outcomes of the vacuum-deposited inverted perovskite solar cells (PSCs). Utilizing thermal evaporation as the fabrication method in our group, we aim to improve the performance of solvent-free perovskite optoelectronic devices by investigating the effect of post-annealing humidity on perovskite films and device characteristics, thereby establishing a reproducible and stable fabrication approach for inverted perovskite solar cells.

Figure 1a reveals that annealing at saturated-humidity condition improves the device performance. PSCs employing 3PATAT-C3 as the hole-transport layer exhibited higher efficiency when the perovskite absorber was annealed at RH 99%, compared with devices annealed uZnder dry nitrogen or ambient air. This improvement is accompanied by moderate increases in open-circuit voltage and fill factor, as well as a noticeable reduction in hysteresis. Furthermore, the applicability of this annealing strategy was examined by incorporating Me-4PACz as the hole-selective contact. A significant increase in open-circuit voltage was observed, leading to a champion efficiency exceeding 21% (Figure 1b). These results suggest that the high-humidity annealing process can be applied across different interfacial configurations in inverted PSCs.

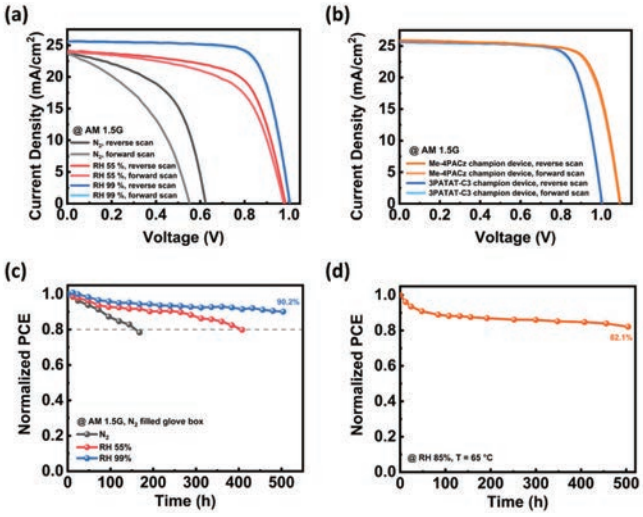


Figure 1. *J*–V characteristics of a) PSCs with 3PATAT-C3 fabricated under different annealing humidity conditions. b) Champion devices employing different hole-selective interfaces. c) Stability of 3PATAT-C3-based PSCs annealed under different humidity conditions measured in an N_2-filled glovebox. d) Stability of an unencapsulated device incorporating Me-4PACz evaluated at 65 °C and RH 85%.

In addition to efficiency, the operational stability of devices fabricated using saturated-humidity annealing was evaluated (Figure 1c and d). Under continuous illumination in an inert atmosphere, devices annealed at RH 99% retained most of their initial efficiency, while those processed under lower humidity showed accelerated degradation. The device employing Me-4PACz also maintained stable performance under combined thermal and high-humidity stress. These results indicate that the high-humidity annealing strategy contributes to improved operational stability.

Table 1. Performance of 3PATAT-C3-based PSCs with various annealing conditions.

	Voc (V)	J_{SC} (mA cm^{-2})	FF (%)	PCE (%)
N_2-R	0.62	23.7	53.2	7.9
N_2-F	0.55	23.7	41.6	5.4
RH 55%-R	0.98	24.1	65.6	15.6
RH 55%-F	0.98	23.9	60.4	14.1
RH 99%-R	1.00	25.6	75.8	19.5
RH 99%-F	1.00	25.5	75.4	19.3

Table 2. Performance of the champion cell fabricated with optimized post-annealing process employing Me-4PACz as the HTL.

	Voc (V)	J_{SC} (mA cm^{-2})	FF (%)	PCE (%)
Reverse	1.10	25.9	75.2	21.3
Forward	1.09	25.8	74.7	21.1

These results highlight the complementary expertise of both groups and establish a strategic framework for further innovations in perovskite optoelectronic applications. This work was supported by the International Collaborative Research Program of Institute for Chemical Research, Kyoto University (2025-111).

Elucidating molecular functions of plant hormones in light-responsive morphological plasticity in *Arabidopsis thaliana*

Eiji NAMBARA　University of Toronto

Experimental Project:
Plants cannot move from the place where they germinate. However, they can sense environmental changes and adapt to surrounding environments by altering their morphology. One example is leaf hyponastic movement, in which leaf angles become more vertical during the day to capture light efficiently. Plant hormones play an important role in this process. We have demonstrated that calcium signaling pathways are involved in hormone-mediated growth regulation during these environmental responses. This project aims to establish an efficient and accurate phenotyping system for analyzing diurnal leaf movements in Arabidopsis through collaboration with Dr. Tomohiko Tsuge (ICR, Kyoto University), an expert in photobiology and plant development, and Dr. Miki Fujita (RIKEN Tsukuba), who has developed high-throughput phenotyping platforms.

Objectives: Investigate the role of plant hormones and calcium signaling in leaf movement in response to environmental factors, particularly light and the day-night cycle, in *Arabidopsis thaliana*

Experimental methods:
1. Verification of light sources for plant growth conditions across the three labs.
2. Establishment of a night vision system for observing plant movements in the dark at 940 nm.
3. Optimization of time-lapse camera observation.
4. Establishment of an automated system for measuring leaf angles from video recordings.
5. Compare leaf movements in response to diurnal changes in wild type and calcium signaling mutants.

Results and discussion:
A night vision system using Chatbot security camera and PiOlan Matte Tape Kagemusha (for reflection reduction) successfully captured nighttime images of Arabidopsis plants. In combination with an automated measurement program modified from Oskam *et al*. (2024) (https://doi.org/10.1093/plphys/kiae097), enabled automated measurement of leaf angles from time-lapse images at relatively high throughput. We recorded leaf movements in Col wild type and *cngc2* and *cngc4* mutants under diurnal conditions and compared their responses (Fig. 1).

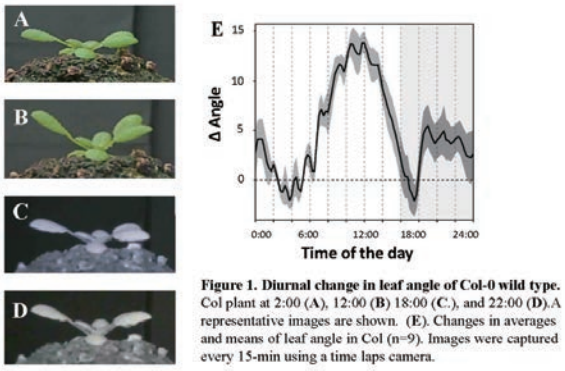


Figure 1. Diurnal change in leaf angle of Col-0 wild type. Col plant at 2:00 (**A**), 12:00 (**B**) 18:00 (**C**.), and 22:00 (**D**).A representative images are shown. (**E**). Changes in averages and means of leaf angle in Col (n=9). Images were captured every 15-min using a time laps camera.

Wild-type plants exhibited typical diurnal leaf movement, characterized by two hyponastic movements per day: one during the daytime and another at night. In contrast, *cngc2* and *cngc4* mutants showed reduced amplitude of leaf movement and delayed initiation of daytime hyponasty, while initiation of nighttime hyponasty remained unaffected. This phenotype may reflect defects in circadian regulation or in light-dependent responses independent of the circadian clock. Further experiments will be proposed to distinguish between these possibilities in the continuous year proposal.

Our findings indicate that *CNGC2*- and *CNGC4*-mediated control contributes to daytime hyponasty initiation but not to nighttime movement. In Arabidopsis, growth in darkness is fundamental to agriculture, yet its underlying mechanisms remain poorly understood. The observation that nighttime hyponasty occurs independently of *CNGC2/4* function may offer novel insights into the regulatory components of plant growth and development.

Outcomes: Invited talks
(1). Nambara E. Phytochemical Society of North America 2025. Toronto, Canada. (June 25, 2025)
(2). Nambara E. Canadian Society of Plant Biologists. Halifax, Nova scotia, Canada (August 10, 2025)
(3). Hussain S, *et.al.* ICR Seminar. Kyoto, Japan (December 15, 2025)

Imaging analysis of zinc transporter and lipid kinase-associated pollen vesicle transport

Miki KAWACHI-REUSCHER　Georg-August-Universität Göttingen

Objectives

Plant sperm cells exist within a vegetative cell and are enclosed by the peri-germ cell membrane. Although this membrane is enriched in $PI(4,5)P_2$, which plays a key role in membrane trafficking, its function during pollen development remains unclear. Based on previous experimental observations, we examined the possibility that pollen-derived vesicles carrying small RNAs (sRNAs) are transported across the peri-germ cell membrane via exocytosis for intercellular communication, using imaging analyses of *Arabidopsis* mutants with defects in membrane integrity and trafficking.

Experimental Methods

To visualize exocytosis, SEC3A, EXO70A1, EXO70A2, and PRP3 were fused to a fluorescent protein, and the resulting marker proteins were introduced into the wild type, the *pip5k4pip5k5pip5k6*, and the *iar1* mutants. Pollen was treated with the exocytosis inhibitor Endosidin 2. RNA distribution was examined using the RNAselective fluorescent dye SYTOR®RNASelect™. Observations were performed using confocal laser scanning microscopy and fluorescence microscopy.

Outcomes & Analysis

RNA staining suggested that RNA levels near sperm cells were lower in *iar1* pollen than in wild-type pollen. Differences in RNA fluorescence within sperm cells across the peri-germ cell membrane between wild-type and *iar1* pollen were not clearly detected. Co-localization analysis with exocytosis markers, which localize to the peri-germ cell membrane and the pollen germination site, indicated that RNA concentration was relatively higher at the germination site in wild-type pollen. A seminar entitled “Identification and Characterization of Pollen Vesicles Carrying Small RNAs — Toward Understanding Epigenomic Regulatory Mechanisms in Reproductive Cells” was also presented on Oct. 21, 2025 as part of this research project.

Publications

Sugi, N. *et al*. Nomenclatural revision of the membrane enclosing germ cells in flowering plants. *Plant Morphology*, submitted.

Crossroads of proteostasis and RNA processing in Arabidopsis photomorphogenesis

Vicente RUBIO　National Center of Biotechnology

Experimental Project:
To ensure survival, plants must rely on efficient signalling pathways that allow them to adjust rapidly to sudden changes and external cues. Such responses depend not only on the precise control of protein abundance but also on the coordinated regulation of gene expression. This dynamic control of gene expression is achieved, in part, by the regulatory function of posttranscriptional machineries such as mRNA processing factors. In recent years, several E3 ubiquitin ligases have been shown to influence mRNA processing in plants although this convergence between mRNA processing and proteostasis machineries has been relatively understudied. However, given that posttranscriptional control of gene expression underpins multiple stress responses and developmental transitions, understanding how mRNA processing and proteostasis shape these processes provides a valuable perspective on plant biology while also opening new possibilities for improving crop performance in increasingly variable environments. To dissect the mechanism by which mRNA processing and proteostasis machineries interlock to control plant development and stress tolerance, using Arabidopsis as model plant species, a collaboration between Dr. Tomohiko Tsuge (ICR, Kyoto University), an expert in mRNA processing and plant development, and Dr. Vicente Rubio (CNB-CSIC, Madrid, Spain) was established.

Objectives: To map the protein-protein interaction network between mRNA processing and proteostasis machineries in Arabidopsis.

Experimental methods:
1. Tandem Affinity Purification (TAP)assays to isolate mRNA processing and proteostasis machineries.
2. Yeast two hybrid assays to test for direct protein-protein interactions.
3. Semi-in vivo pulldown and coimmunoprecipitation assays to confirm protein interactions *in planta*.
4. Bimolecular Fluorescence Complementation assays for subcellular localization of complexes.

Results and discussion:
In plants, CRL4 ubiquitin ligases regulate photomorphogenesis, DNA repair, drought tolerance, and nutrient signaling. CRL4 comprises a CUL4 scaffold bound at its C-terminus to ROC1/RBX1 and at its N-terminus to DDB1, which recruits substrate receptors. Interestingly, DDB1 and the mRNA processing protein SAP130L share very significant similarities at the protein sequence and structural levels. DDB1 associates with accessory proteins such as DDA1, a small protein with and intrinsically disordered region at its C-terminal portion that facilitates substrate. In the context of this proposal, we found by TAP assays that DDA1 associates with SAP130L, suggesting that SAP130L might be incorporated into CRL4 complexes together with DDA1, e.g. by replacing DDB1, or that DDA1 is part of specific SAP130L-containing complexes yet to be characterized. A map of the protein-protein interaction network connecting DDA1 and SAP130L complexes has been the focus of this project. Functional characterization of their role in plant molecular and cellular processes is of great interest to better understand plant plasticity and adaptation to ever fluctuating environmental conditions.

Outcomes: Invited talks:

(1). Rubio V. Invited seminar at La Sapienza University. Rome, Italy. (March 21st, 2025)

(2). Rodrigues-da Silva *et al.,* Annual Meeting “EpiSeedLink” MSCA-DN Action. Galway University, Ireland (June 3rd-7th, 2025)

(3). Rubio V. Invited talk at Santiago de Compostela University. Spain. (October 21st24th, 2025)

Development of Covalent Small Molecules That Potentiates Antitumor Immunity

Misao Takemoto　Fukushima Medical School

Compounds that enhance T-cell immune functions represent promising therapeutic options for cancer immunotherapy. To identify such compounds, the applicant developed a unique cell-based assay that mimics T cells in the tumor microenvironment while working in the Uesugi laboratory. Using this assay, our collaborative research team identified arvenin I, a plant-derived natural product, as a potent immunomodulatory compound. Mechanistic studies revealed that arvenin I covalently binds to MKK3, enhances its kinase activity, and promotes mitochondrial function essential for T-cell activation via the p38 MAPK signaling pathway. In vivo studies further demonstrated that administration of arvenin I, either alone or in combination with immune checkpoint inhibitors, significantly enhanced antitumor immune responses in mice.

During immune checkpoint inhibitor therapy, tumor-reactive $CD8^+$ T cells are primed in draining lymph nodes (DLNs), and their circulation between DLNs and tumor sites (called the cancer–immunity cycle) is critical for therapeutic efficacy. In FY2025, our collaborative effort with the Chamoto and Uesugi Groups at Kyoto University demonstrated that combined treatment with arvenin I and a PD-L1 antibody markedly enhanced mitochondrial respiration and proliferation (Ki67 expression) of $CD8^+$ T cells in DLNs, accompanied by increased TNF-α production downstream of MKK3 signaling. Consistent immunological improvements were also observed in tumor tissues, including a reduction in terminally exhausted $CD8^+$ T cells ($PD\text{-}1^+$ $Tim3^+$) and an increase in less exhausted populations ($PD\text{-}1^+$ $Tim3^-$). These findings indicate that arvenin I synergizes with PD-L1 blockade to enhance $CD8^+$ T-cell activation while alleviating intratumoral T-cell exhaustion.

These collaborative results were summarized and published in *Journal of the American Chemical Society* (2025). In parallel, the derivative optimization of arvenins conducted in the Uesugi laboratory led to the successful synthesis of seven derivatives. Biological evaluations of these compounds were jointly performed by the applicant and graduate students in the Uesugi laboratory, laying a strong foundation for future therapeutic development.

Machine-Learning Prediction of Self-Assembly Compounds

Daniel Packwood Kyoto University

Self-assembly is the formation of complex structures from simple molecular building blocks. The Uesugi of ICR developed a self-assembled vaccine enhancer, also known as an adjuvant, that boosts immune responses. The molecular building block of this assembly, cholicamide, consists of two sterols connected by an amide linkage with an alkane spacer, and its assemblies exert the adjuvant activities through endosomal Toll-like receptor 7 (TLR7).

In FY2025, we employed computational approaches that provide molecular-level insights beyond the reach of current experimental methods. Specifically, we performed all-atom (AA) molecular dynamics (MD) simulations of a single cholicamide molecule and three of its derivatives (1 active, 2 inactive). These simulations show that all compounds interconvert between folded and extended conformations. However, we did not observe a correlation between these conformations and bioactivity. This suggests that bioactivity arises from the assembly level.

All-atomistic simulations, while accurate, are limited to small systems. As a result, the self-assembly processes were modeled using a coarse-grained (CG) approach. In this approach, several atoms are grouped into particles, speeding up the process by 2-3 orders of magnitude and enabling the study of self-assembly. We have carefully parametrized the molecule to reproduce the intramolecular and intermolecular interactions. We performed a self-assembly simulation of a 20 x 20 x 20 nm3 box containing 150 cholicomide molecules (~0.30 mM). Molecules self-assemble into small, compact, amorphous nanoparticles. Analysis shows that hydroxyl and amide groups are evenly spread on the surface of the nanoassembly.

We are currently converting the coarse-grained representation of the nanoassembly into an all-atomistic representation to characterize surface features at the atomic level, which may explain why this nanoparticle triggers an immune response. In parallel, we plan to perform coarse-grained molecular dynamics simulations of the active and inactive derivatives to determine whether differences in assembly structure correlate with immunological activity. Moreover, because the nanoparticle must cross the cellular membrane to reach endosomal TLR7, we will model its interaction with lipid bilayers. Lastly, we aim to simulate the TLR7 receptor in complex with cholicamide to assess whether direct binding is feasible.

Analysis and application of the physiological functions of extracellular vesicles secreted by intestinal bacteria

Shino Yamasaki　Kansai University

Introduction:

Intestinal bacteria contribute to host physiological homeostasis through the production of diverse metabolites. In addition to these metabolites, extracellular vesicles (EVs) released by intestinal bacteria have been recognized as mediators of host–microbe interactions; however, it remains unclear which bacteria produce EVs in the gut, how their production is regulated, and how these vesicles influence host responses. In this study, we investigated the bacterial origins of gut-derived EVs, evaluated their effects on host cells, and analyzed the mechanisms underlying EV formation.

Results:

1. Characterization of EVs produced by intestinal bacteria

To identify the bacterial origins of gut-derived EVs, EVs were isolated from mouse feces and cecal contents by differential and density gradient ultracentrifugation, and typical vesicular morphology was confirmed by electron microscopy. DNA enclosed within the vesicles was extracted and subjected to 16S rRNA gene sequencing to estimate their bacterial origins. Comparison with the corresponding gut microbiota revealed that EV-producing patterns differ among bacterial taxa and vary depending on intestinal location.

2. Bacterial EVs as possible mediators of intestinal inflammatory resolution

In the intestinal mucosa, immune cells coordinate inflammatory induction and resolution to maintain immune homeostasis. Apoptosis of antigen-activated T cells is one of several key mechanisms in inflammatory resolution. Using leukemia-derived Jurkat T cells as an *in vitro* model, we found that EVs from *Bifidobacterium dentium* and *Limosilactobacillus fermentum* each induce apoptotic cell death. These findings indicate that bacterial EVs can modulate T-cell survival *in vitro* and may be relevant to intestinal inflammatory resolution.

3. Mechanistic analysis of EV formation by *Shewanella vesiculosa* HM13

S. vesiculosa HM13, isolated from fish intestines, produces abundant EVs. We found that disruption of *letB*, involved in outer membrane lipid homeostasis, increased SDS sensitivity and EV production and led to the generation of unusually large EVs. Lipid analyses showed that parental EVs were enriched in saturated phospholipids, whereas EVs from the *letB*-disrupted strain contained more unsaturated fatty acyl chains. These results suggest that LetB-mediated lipid homeostasis regulates EV morphology by controlling lipid composition at EV-forming sites.

Analysis of membrane lipid-dependent fermentation stress response in acetic acid bacteria

Yosuke Toyotake　Ritsumeikan University

[Introduction] Acetic acid bacteria uniquely utilize phosphatidylcholine (PC) as a major membrane component, similar to eukaryotes. However, its physiological role remains unclear. We previously constructed an *Acetobacter pasteurianus* mutant, Δ*pmtA*+*pcs*, that produces PC in a choline-dependent manner. This strain exhibits differential PC requirements in response to strong and weak acid stress, requiring higher PC levels under strong acid stress and lower levels under weak acid stress. These observations provide new insights into the mechanisms of acid-stress response in *A. pasteurianus*.

[Results and Discussion] To evaluate acid stress response, we performed spot assays. Cells were grown in YPG medium for 24 h, harvested, adjusted to OD_{600} = 1, serially diluted (10-fold), and 3 µL of each dilution was spotted onto YPG agar plates adjusted to pH 3.5 with either acetic acid or HCl. Choline chloride was added at increasing concentrations, and plates were incubated at 30 °C until colonies were formed (**Fig. 1**). Under acetic acid stress, growth of the Δ*pmtA*+*pcs* strain was alleviated by ≥40 µM choline and fully restored at 200 µM (**Fig. 1A**). Under HCl stress, growth inhibition was more severe; ≥400 µM and 1,000 µM choline were required for partial and complete restoration, respectively (**Fig. 1B**). These results indicate that higher PC levels are required for response to inorganic acid stress than to organic acid stress. Previous phospholipid composition analysis (Collaborative Research Program of ICR, Kyoto University, 2024-113) showed that 200 µM choline did not restore PC to parental levels in the Δ*pmtA*+*pcs* strain. Nevertheless, this concentration fully restored growth under acetic acid stress. Thus, tolerance to acetic acid does not strictly correlate with membrane PC abundance. PC may instead functionally contribute, for example, by supporting the acetic acid efflux systems or by stabilizing membrane-associated transport proteins.

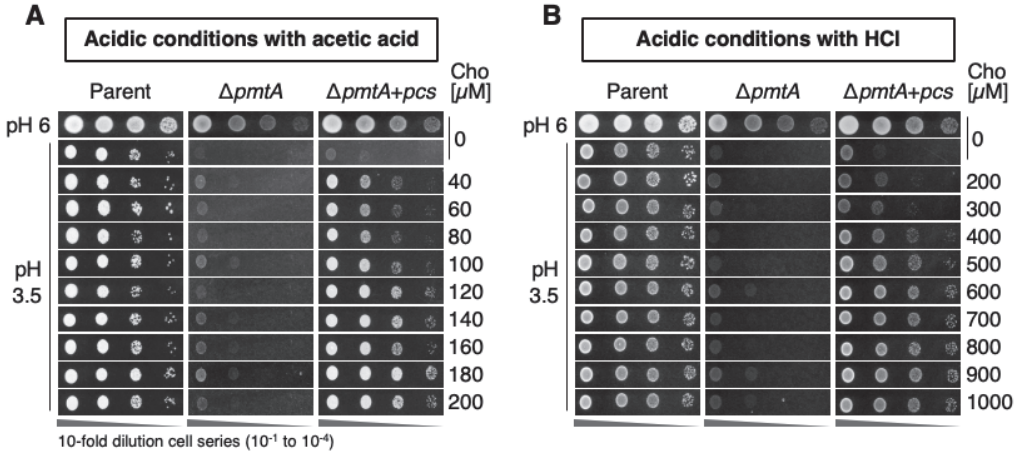


Fig. 1 The effect of different PC levels on growth under acidic conditions. Serial dilutions of parental, Δ*pmtA* (PC-deficient mutant), and Δ*pmtA*+*pcs* strains were spot-incubated on acidified YPG agar plates adjusted to pH 3.5 with acetic acid (**A**) or HCl (**B**) and supplemented with choline (Cho).

溶媒含浸樹脂を用いた連続的分離法による希土類元素分離の最適化

倉橋健介　大阪公立大学工業高等専門学校

１．目的

固相抽出法は溶媒抽出法などと比べ、人体や環境に有害な揮発性溶媒の利用が少ない利点を持つ。先行研究では、安価で広く流通されている界面活性剤を利用した溶媒含浸樹脂（SIR）が、レアメタルであるランタノイド元素を抽出可能で、酸を用いて回収できることを見出した。しかし、ランタノイド元素の抽出能は、2 価遷移金属イオンなどと比べると高いものの、一度の抽出操作で分離可能なほどではなく、バッチ法で多階抽出を行うと pH 調整のために液量が増加してしまう問題があった。そこで本研究では、この溶媒含浸樹脂をカラムで使用することで、ランタノイド元素の連続的な分離・回収手法を確立することを目的とした。

２．実験方法

エタノールで洗浄し、減圧乾燥機で 1 日乾燥させた多孔性樹脂 Amberlite XAD-7HP 1 g に、界面活性剤としてドデシル硫酸ナトリウムを 0.2 mmol 溶解させたエタノール溶液 20 mL を加え、1 日間含浸させた。減圧留去で溶媒を除き、減圧乾燥機で 1 日間乾燥させて SIR を調製した。調整した SIR 1.5 g を、純水に懸濁し、長さ 10 cm，直径 1.0 cm のカラムに詰めた。0.1 mM の La と Eu を含んだ溶液を pH 6 に調整し、1.25 mL/min で 60 mL 通液し、カラム内の SIR に金属イオンを吸着させた。その後、純水を 10 mL 流し入れてカラム内を洗浄し、0.5 M HCl を 70 mL 流し入れて金属イオンを溶離した。サンプルは 5 mL ごとに採取し、誘導結合プラズマ発光分光光度計(ICP-OES)を用いて測定することで、カラム出口における金属イオン濃度を測定した。

３．結果と考察

カラム実験に先立ち、pH 2.5 の金属溶液をバッチで SIR に吸着させ、逆抽出に用いる溶液を変更した際の、回収率の違いを観察した。その結果、回収率は HCl > HNO_3 > NaCl > KCl となったことから、カラム分離に用いる溶離液は 0.5 M HCl とした。

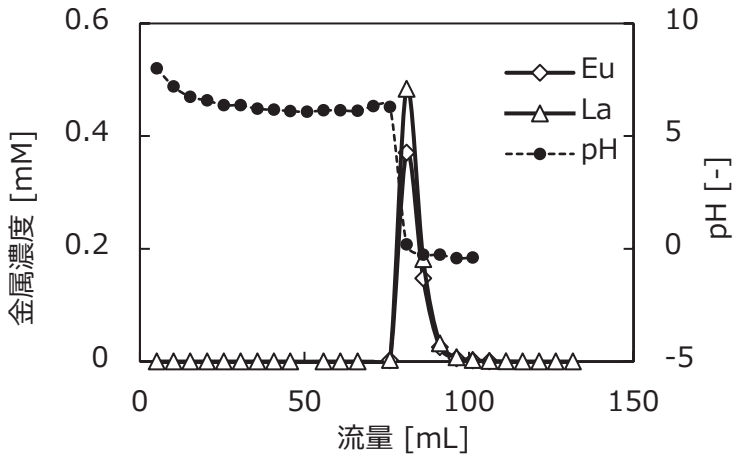


図１ カラム出口における金属濃度の変化

カラムに詰めた SIR に対して、La, Eu の吸着と溶離を行った結果を図 1 に示す。カラム出口の pH が急激に低下するとともに、La, Eu の鋭いピークが現れたことから、SIR に吸着された金属イオンが HCl によって迅速に溶離し、カラム操作を行うことでランタノイド元素を濃縮できることがわかった。

3D プリンティング技術を用いた 3 次元構造化モノリス造形

村瀬浩貴　共立女子大学

多孔材料は，各種の分離フィルタ，各種電池セパレータ，透湿防水布としての快適性衣料，海水淡水化膜や水浄化膜などの環境関連材料，血液透析膜や細胞培養基材などの医療材料など幅広い分野で利用されている。これまで，様々な多孔材料が実用化されてきたが，モノリス(Monolith)は３次元ネットワーク状の骨格構造を持ち，ネットワークの骨格サイズと，その空隙である連続空孔のサイズを独立に制御できる次世代多孔材料として注目されている。京都大学化学研究所の辻井敬亘教授と榊原圭太氏（元化学研究所助教、現産業技術総合研究所）は，界面化学的手法を駆使して，重合誘起スピノーダル分解を経由するエポキシ系ポリマーモノリスで新規な多孔材料を創生してきた。一方，報告者はこれまで、Additive Manufacturing（AM，3D Printing とも呼ばれる）の技術を応用して，新規な構造を有する複合繊維や繊維−樹脂複合型布帛の開発，セルロースナノファイバーの３次元造形に取り組んできた。本研究では AM の技術と，辻井教授らの界面制御技術・高性能モノリス合成技術を融合し，３次元構造を制御した新規ポリマーモノリスを創生することを目的とする。

本年度は、3D プリンタ用の光硬化樹脂にポロゲンとして様々な分子量のポリエチレングリコール（PEG）を混合し、３D プリンタ造形可能かつ多孔化できる組成を探索した。すでに同様の試みとして、メタクリレート系モノマーに光硬化開始剤とポロゲン（シクロヘキノールや１-デカノール）を混合した系で 3D プリンティングにより造形した任意形状のモノリスが報告されている[1]。本研究では、分子中にホスト分子とゲスト分子を有して自己修復性を発揮するエラストマー（Wizard EM-630, 685, 株式会社ユシロ製[2]）に PEG を混合すると、紫外線照射後に重合誘起相分離を発現することを見出した。さらに、光造形型 3D プリンタを用いて重合誘起相分離を発現させながら造形し、造形後に水洗することで多孔化することを確認した。図 1 左が中空円筒造形物（外径 6 mm 内径 4 mm 高さ 10 mm および外径 8 mm 内径 6 mm 高さ 10 mm）と、その表面の走査型電子顕微鏡写真（図 1 右）である。数μm 程度の孔が多数観察された。また、造形物はナイフ切断後に再接合する自己修復性も示した。自己修復性を有する多孔材料を、3D プリンティングにより任意の形状に造形できる可能性を示すことができた。

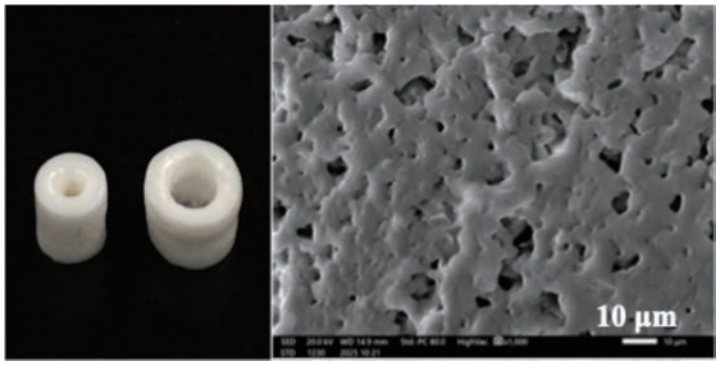


図 1．光造形型 3D プリンタで造形した自己修復性ポリマーモノリス

1)　Dong, Z., et al., *Nature Communications*, (2021)12:247.
2)　株式会社ユシロ, Wizard Series, https://www.yushiro.co.jp/products/wizard (2026.2.10 参照)

カチオン交換非平衡単一半導体ナノプレートのエネルギー準位の解明

真島豊　東京科学大学

半導体ナノ粒子に対してイオン交換を行うことで、原子層配列の異なる平衡構造および非平衡構造を創成することができる。ナノギャップ電極間に単一半導体ナノプレート(NP)を化学吸着させると、化学結合により安定なデバイス構造を形成できるため、デバイスを溶液中でイオン交換することが可能となる。単一半導体 NP デバイスでは、電極のフェルミ準位と NP の量子化エネルギー準位が一致した際に、共鳴トンネル現象を観察される。したがって、イオン交換に伴う構造変化を共鳴トンネル特性として測定することにより、平衡構造のみならず、非平衡構造における半導体 NP のエネルギー準位を解明することが期待される。本研究では、$Cu_{2-x}E$(E: S, Se)NP をナノギャップ電極間に化学吸着させ、共鳴トンネル現象を測定することにより、非平衡構造を有する半導体 NP のエネルギー準位を解明することを目的とした。

半導体 NP のサイズ(20 nm)と同じギャップ長、電極幅を有する Pt ナノギャップ電極を電子線リソグラフィにより作製し、ナノギャップ間に $Cu_{1.8}S$ NP を化学吸着した単一 $Cu_{1.8}S$ NP トランジスタを作製した。単一 $Cu_{1.8}S$ NP トランジスタのドレイン電流―ドレイン電圧を測定し、微分コンダクタンス特性を得た(図 1 (a))。また、$Cu_{1.8}S$ NP がスタックした $Cu_{1.8}S$ NP トランジスタを Co でカチオン置換し、非平衡 CoS がスタックした CoS NP トランジスタのトランジスタ特性の測定を試みた。単一 $Cu_{1.8}S$ NP トランジスタおよびカチオン置換後の非平衡 CoS NP がスタックしたトランジスタは、非常に類似した微分コンダクタンス特性を示した。単一 $Cu_{1.8}S$ NP は、ナノギャップ間に短いアルカンジチオールを介してドレイン電極側に片側吸着しており、ドレイン電極に NP のエネルギー準位はピニングされている。

単一 $Cu_{1.8}S$ NP の微分コンダクタンスの立ち上がり電圧は、-0.75 V と 0.80 V であり、0.55V に微分コンダクタンスが若干増加している。このことから、バンドギャップエネルギーは 1.55 eV となる。正電圧側は伝導体側のエネルギー準位を介した共鳴トンネル電流と考えられる。電流が立ち上がった後、コンダクタンスピークが 1.05 V($Cu_{1.8}S$ NP)に見られる。これらの結果より、伝導帯側のエネルギー準位は量子化しており次の準位までのエネルギー差が大きい。また、0.55V でコンダクタンスが増加していることから、伝導体近傍にトラップ準位があることが示唆される。

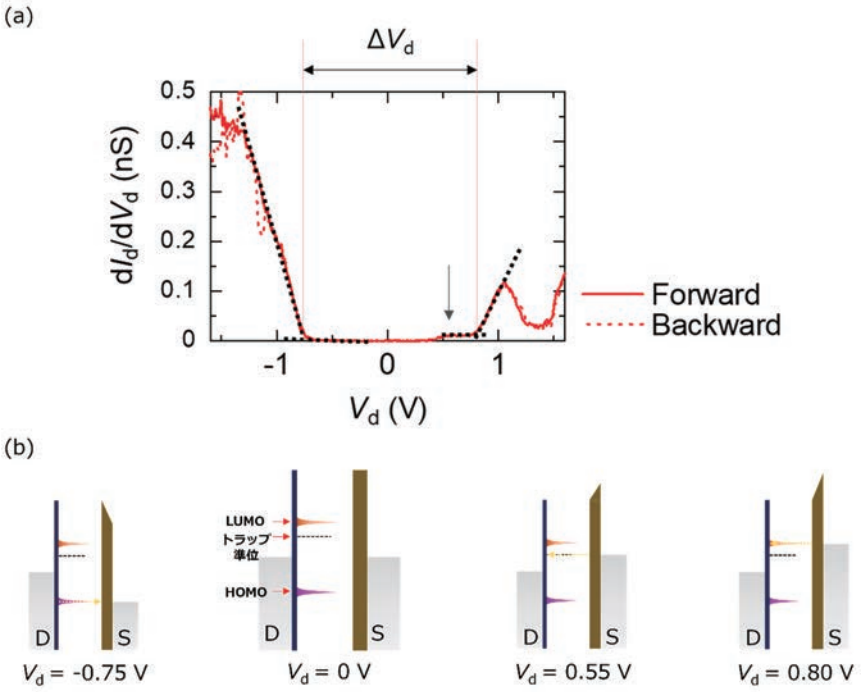


図 1 (a) 単一 $Cu_{1.8}S$ NP トランジスタの微分コンダクタンス特性 (9 K)、
(b) 単一 $Cu_{1.8}S$ NP のエネルギー準位と、各 V_d におけるバンド図

大型レーザー装置を利用した
電荷交換反応の地上再現実験と天体放射モデルの構築

内田裕之　京都大学

近年天文学の分野では、宇宙の局所非平衡環境に注目が集まっている。これらは近い過去に何らかの激しいエネルギー注入があった痕跡であり、宇宙線加速や超新星爆発など、未知の機構を解く鍵となる。申請者はこれまでのX線観測で、水素の軌道電子がイオンに捕捉される「電荷交換反応」の兆候を発見し、間接的ながら衝撃波が乱流を介して中性ガスと相互作用する証拠を掴んだ。2023年9月打ち上げのXRISM衛星は、史上初の精密X線分光を実現し、電荷交換によるカスケード輝線の直接検出を可能にした。実際、最初に観測した超新星残骸 N132D の S 輝線から電荷交換反応を示唆する輝線構造が検出されている（Gu, Uchida et al., 2025）。今後も様々な天体から電荷交換反応は発見されると予想される。しかし、電荷交換のモデル化は世界的にも進んでおらず、理論計算は精度が悪く、地上試験は広範なパラメータ領域を網羅しているとは言い難い。そこで本研究では、レーザー物質科学研究領域の超高強度レーザーを利用して、電荷交換反応の地上再現実験を行う。

電荷交換反応の地上実験は Electron Beam Ion Trap を用いる手法が現在の主流である。この手法では相対速度を網羅的に探索するのが難しく、モデル化の整備は進んでいない。プラズマの衝撃波速度はレーザー強度に依存するため、相対速度を調整しやすく、宇宙に近い環境を再現できる。このことが高出力レーザーを用いる大きな利点である。本研究が成功すれば、天文学的に重要な電荷交換反応の再現試験の新手法を提示できる。日本が XRISM 衛星を成功させたことにより、2030 年代を目処に追随する精密 X 線分光ミッションが世界中で計画されている。また、惑星科学の分野でも、太陽系小天体の組成を探る上で電荷交換反応の検出が重要視されている。電荷交換反応は宇宙の至る所で見つかるはずで、本研究が行おうとする地上再現試験は、将来的な放射モデル構築のための極めて重要な一歩である。

大阪大学の藤岡研究室のグループと実験の概念検討を行った後、2024年12月から、高出力レーザーを各種試料に照射し、発生したプラズマと外気の中性ガスの間で電荷交換反応を起こしてX線を実測する実験を開始した（図１）。京都大学化研の時田教授と升野研究員の監修のもと、照射源として10TW高強度レーザーを利用し、ターゲットとして単体のSi板とSiO_2板を設置した。ターゲットには5 Hzの頻度でレーザーを照射し、発生したプラズマを結晶分光器を介してCCD検出器で分光撮像した。またプラズマのサイズを別方向から用意したピンホールカメラで常時モニタする。プラズマ化した試料を外気と接触させて電荷交換反応を模擬するために、大気とHeガスのそれぞれの場合について、結晶分光したX線放射の測定を行った。この結果、X線スペクトルを取得し、イオン化したSiからの輝線の分光に成功した。特に、He様まで電離したSiからのtriplet輝線を明瞭に分離することができた。仮に電荷交換反応が起きていれば、禁制線の強度が通常より高くなる等、輝線強度比に変化が現れると予想される。そこで、2025年12月の実験では、統計の向上を目指してカメラシステムや結晶分光器の改良などを行い、輝線強度比の変化が顕著に現れるSiの高励起輝線群を捉える追試験を行った。しかし装置の不具合等により有意なデータを取得することはできなかった。この結果を踏まえて、次年度早々にこの実験を改良・拡張して種々の外気での輝線強度比の違いを調べることで、電荷交換反応由来の輝線の抽出を行う予定である。

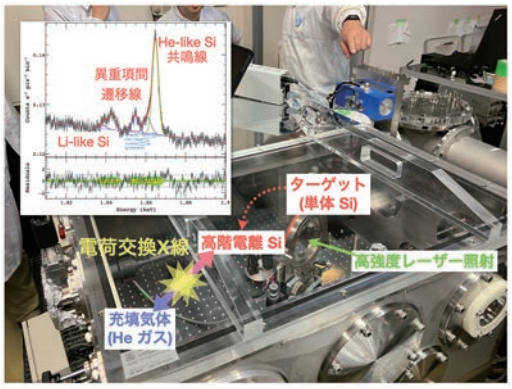


図 1 : T6 レーザー施設での実験の様子と Si 板に高強度レーザーを照射したときのプラズマの X 線スペクトル。

高強度レーザーと構造性ターゲットとの相互作用による水素・ホウ素核融合等価プラズマ生成と緩和・閉込め過程の検証

岸本泰明　京都大学

研究背景と目的：重水素・三重水素(DT) による核融合研究(D+T→^{4}He+n)が進展する中、燃料の三重水素は放射性物質であり、生成物の中性子は炉材料を脆化させるなど、課題が残されている。一方、水素・ホウ素(PB)による核融合(^{1}P+^{11}B→3^{4}He)は、これらの元素を含まないことから、より安全性の高いエネルギー源と考えられる。しかし反応断面積は小さく、DT 反応よりはるかに高い~300keV もの高温プラズマを長時間「閉じ込める」必要がある。これを実現する方法として、この PB が 1:1 割合で含む高純度で安定な二次元ホウ化水素シート(ボロファン)が発見されたこと(**図 1**)、一方、本拠点で開発してきたサブ μm サイズの微細構造体(シリコン)と相対論領域の高強度レーザーの相互作用によって PB 反応核融合温度に匹敵する数 100keV の高エネルギー密度プラズマの生成されること、これを慣性時間を超えて閉じ込める方法論(レーザー生成高強度磁場の自己組織化)が数値計算で見出され、実験でもその素過程が実証されつつあることを受け、これらの成果を融合することで PB 核融合を実現する新しい方法論を開拓することを目的している。

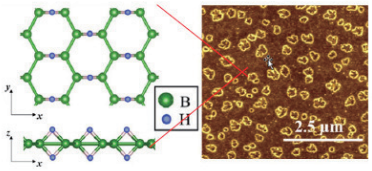


図 1　近藤等による 2 次元状ホウ素化水素(ボロファン：PB)の原子配列とナノシート(上段)、：JXTG Technical Review・第 60 巻　第 2 号(2018 年 7 月)

研究方法と成果：上記ボロファンからなる粒状物質を数 100 気圧で圧縮することで生成したバルク化した PB 燃料表面は、現状では 10μm 程度の“粗さ”を持つ(**図 2(a)**)。レーザー照射・吸収の一様性を保ち、高温プラズマを生成するため、燃料表面の粗さをレーザー波長(λ_L~0.8μm)程度に抑えるとともに、燃料を任意形状に整形・加工する技術基盤を構築する必要がある。本年度は、ボロファン素片集合体が複雑な構造変化を受けながら圧縮される過程において、圧力を準静的に変化させることにより表面がより滑に整形されることを見出すとともに、その厚さを±1μm 以下に抑制できることが分かった。また、これらの PB 燃料の表面構造を触診段差計や SEM 写真などで同定することができた(**図 2(b)**)。

これらの表面構造の差異は、高強度レーザーを照射したときのエネルギー吸収率の差異に現れる可能性があるとともに、より多くの粒子にエネルギーが配分されることから、高エネルギー電子および高エネルギーイオンの生成が抑制されることが期待され、これによって PB 核融合の反応温度に最適なプラズマを生成・制御できる可能性がある。この準静的圧縮方法を基盤に PB 燃料の微細加工の実現を目指す。

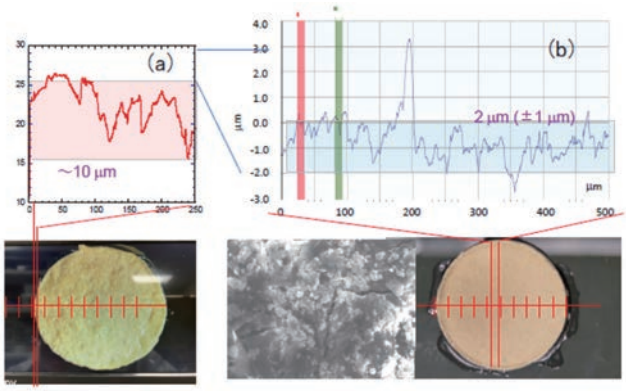


図 2 (a) 300 気圧を瞬時的に印可して作成した PB 燃料と(b)準静的に印可しながら 300 気圧の準定常状態にした場合の表面構造の差異(高精度触診段差系による)

参考文献：2024 年度報告書(2024-121_岸本泰明)

2025-124

On demand design of peptides targeting RNA structures

Tamaki Endoh　Konan University

Research fields of drug discovery have been developed by targeting proteins. However, concerns about the depletion of proteins that could serve as drug targets have been raised. In this context, RNAs are gaining attention as the targets to bring a new breakthrough in the drug discovery. In this study, peptide was selected as a modality for the RNA-targeting drug discovery, and large-scale screening system of interaction pairs between given peptide and RNAs forming various structures was constructed.

The screening system was constructed based on RNA-capturing microsphere particles (R-CAMPs), which immobilize RNA and DNA clones derived from initial library of interest (T. Endoh et al., 15, 1805062 (2019)). Recently, we have demonstrated screening of RNA targets, which interacted with METTL3/METTL14 heterodimer, an RNA methyltransferase (T. Endoh, M. Imanishi et al., ***ChemBioChem***, 26, e202500006 (2025)). Here, we have expanded the screening system by using 8-repeats of glycine-arginine dipeptide (GR_8) as a model peptide. Glycine-arginine repeats is a possible translated product from GGGGCC repeats on C9orf72 mRNA, in which expression is involved in neurodegenerative disorders. We have constructed R-CAMPs from a library derived from total RNA of human cells. The R-CAMPs were mixed with fluorophore labeled GR_8 and RNAs interacted with the peptide were isolated based on the fluorescence signals on the particle using fluorescence activated cell sorter. After the sequencing, we found RNAs that interacted with the fluorophore-labeled GR_8. One of the selected RNAs (Figure 1A) exhibited the association constant of 1.34×10^7 M^{-1} with fluorophore-labeled GR_8 (Figure 1B). Based on the screening system, it would be possible to construct a large-scale database for RNA-peptide interactions. The database provides on demand design strategy of peptides that interact with functional RNAs as a new therapeutic modality.

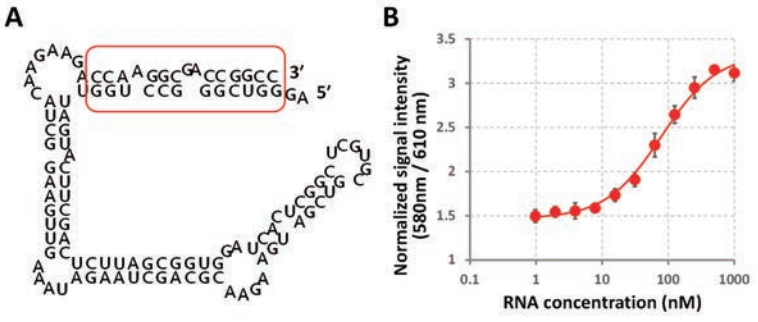


Figure 1. (A) Sequence and predicted secondary structure of selected RNA. (B) Interaction between TMR-labeled GR_8 and RNA region highlighted with square in (A).

- Publication

T. Endoh, Y. Ling, S. Okuda, M. Imanishi, Identification of Endogenous Sequences Interacting with METTL3/METTL14 RNA Methyltransferase, ***ChemBioChem***, 26, e202500006

インクジェットプリンターによる
細胞内への機能性ペプチド送達研究

中瀬生彦　大阪公立大学

膜透過性ペプチド（cell-penetrating peptides, CPPs）は、高い細胞内移行性を有し、臨床研究も含め、タンパク質や核酸などの細胞内送達に広く利用されている。研究代表者はこれまでに多数の CPPs を開発し、その細胞内移行機構、特にマクロピノサイトーシスを含む取り込み経路の解析を進めてきた[1]。近年では、CPPs の細胞内導入の際に、新たな工学的な組み合わせとして、狙った細胞群へ分子を精密に導入するため、インクジェットプリンターを用いた新規細胞内送達基盤技術を開発している[2]。本手法により、機能性ペプチドや蛍光タンパク質、IgG 抗体などを、特定の細胞群のサイトゾルへ高効率に導入できることを示してきた[2]。

本共同研究では、このインクジェット送達技術に、疎水度や二次構造、電荷等が異なる各種 CPPs を利用することで、送達範囲、細胞内移行量、細胞内局在をより厳密に制御可能な細胞内送達手法の確立を目的とした。本研究では、単に細胞内へ導入するだけでなく、導入量・局在・対象細胞数を精密に制御することが重要であり、ペプチド化学に強みをもつ川口助教との連携により、本技術の高度化が期待される。具体的には、合成した各種 CPPs を利用して、研究代表者が構築したインクジェットシステムに搭載し、細胞内移行効率、送達範囲、局在、及び、細胞毒性の評価を行った。

本研究の成果の一部として、インクジェットシステムと CPPs を組み合わせた細胞内導入技術に関する研究を、現在、川口助教と共同で投稿中である。本論文では、アルギニン残基数や疎水性の異なる CPPs を用いて細胞取り込み効率、膜透過性、及び、送達細胞範囲を評価した。インクジェットシステムにより滴下体積（1 滴が 30 pL 程度）、吐出速度（ピエゾ素子）、位置を精密に制御し、CPPs の細胞内導入効率を検証した。また、アポトーシス誘導ペプチドを搭載することで抗がん応用への可能性も示した。本成果は、目的分子を必要な細胞へオンデマンドで導入するための基盤技術として重要な知見を提供するものである。

以上より、本共同研究は、インクジェットによる空間制御送達技術と CPPs による細胞内移行制御を統合することで、1 細胞レベルでの分子導入制御や医療応用へ発展可能な細胞内送達基盤の構築に貢献するものである。今後は、本技術を顕微鏡手術や細胞治療などへの応用に展開することが期待される。

＜参考文献＞

[1] Futaki, S., Nakase, I. *Acc. Chem. Res.* **50**, 2449-2456 (2017)

[2] Omura, M. *et al. ACS Appl. Mater. Interfaces*, **15**, 47855-47865 (2023)

Identification of novel strigolactone biosynthetic inhibitors.

Yoshiya Seto　Meiji University

【The aim of this study】 Strigolactones (SLs) are plant hormones that regulate shoot branching, as well as being known to be rhizosphere signals that control symbiotic and parasitic relationship with Arbuscular mycorrhizal fungi and root parasitic plants, respectively. SLs are biosynthesized from carotenoids via a key intermediate molecule called carlactone (CL). In a model plant, Arabidopsis, CL is further converted into carlactonoic acid (CLA) by a cytochrome P450 monooxygenase, MORE AXILLARY GROWTH1 (CYP711A). We previously identified methyl esterified derivative of CLA, methylcarlactonoate (MeCLA) in Arabidopsis, and found that MeCLA can interact with the Arabidopsis SL receptor protein, AtD14. On the other hand, CL and CLA could not interact with AtD14, suggesting that the methyl esterification step is critical to convert a biologically inactive precursor to a bioactive hormone molecule. We have previously identified a CLA methyltransferase (CLAMT) in Arabidopsis, and found that the Arabidopsis *clamt* knockout mutant shows an increased shoot branching phenotype. Therefore, the CLAMT pathway is important in producing the shoot branching inhibitor in Arabidopsis. We also found that tomato *clamt* knockout mutant shows an increased shoot branching phenotype. Interestingly, the tomato *clamt* mutant was found to produce some SLs such as orobanchol in root. It has been reported that CYP722C has a critical role in the orobanchol biosynthesis in tomato. Therefore, in tomato there are two branched pathways for SL biosynthesis, and the CLAMT pathway is important for the shoot branching inhibition whereas the CYP722C pathway is necessary to produce SLs as rhizosphere signals (Fig. 1). If we can selectively inhibit inhibit the CLAMT pathway, it is expected that shoot branching can be increased without impairing SL function in the rhizosphere. Against this background, the present study aimed to identify the CLAMT inhibitors (Fig.1).

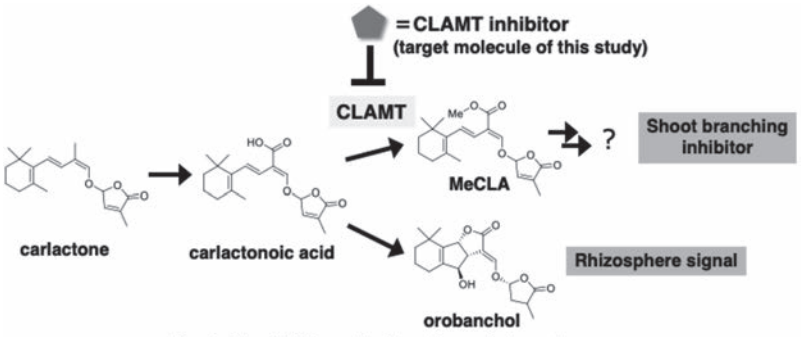


Fig. 1. The SL biosynthetic pathway in tomato

【Results】 We have performed a screening of chemicals that can interact with SlCLAMT by using thermal shift assay. We successfully identified three chemicals that can increase the melting temperature of SlCLAMT. We also clarified that these three chemicals inhibit CLAMT activity *in vitro*. To investigate the function of these three compounds *in vivo*, it is necessary to prepare these compounds in relatively large quantities. Thus, we attempted the chemical synthesis of these three compounds and succeeded in synthesizing them. We further found that the application of one of these three compounds to tomatoes resulted in a phenotype similar to that of the *clamt* knockout mutant, suggesting that this compound inhibits CLAMT *in vivo.*

揮発性性植物ホルモン様分子による生長制御機構の解析

深澤壽太郎　広島大学

目的：ジベレリン（GA）は、植物の発芽、伸長成長、花成を促進する植物ホルモンである。申請者は、GA 信号伝達の抑制因子 DELLA タンパク質の相互作用因子として GAF1 転写因子を同定した。DELLA-GAF1 複合体が GA 依存的に標的遺伝子の発現を制御することにより、GA フィードバックや、GA 花成経路を制御することを明らかにした。GAF1 標的遺伝子である ELF3 の変異体 ***elf3*** は、花成と伸長成長が促進される。さらに、***elf3*** の徒長型の表現型は、近隣の植物体にも伝播することから、***elf3*** は揮発性の植物ホルモン様分子 GA-X を放出すると考えられた。***elf3*** を用いた GA 生合成変異体の回復実験から、GA-X は、GA 中間体または、その派生分子である可能性が示唆された。広島大学では、ELF3 による GA-X 生合成の制御機構の解明とバイオアッセイにより ***elf3*** が放出する GA-X の絞り込みを行う。化学研究所・生体触媒化学研究領域との共同研究により、GA 中間体などの分析が可能な GC-MS を利用し、***elf3*** が放出する揮発性分子 GA-X の同定に挑戦する。

実験方法１：*elf3* 変異体を用いた GA 量の定量と ELF3 による GA 生合成遺伝子の発現制御機構の解析

elf3 変異体は、花成が促進されるほか、徒長形質を示す。徒長形質は GA 生合成阻害剤によって抑制されることから ***elf3*** の徒長の主な原因は、GA 内生量の増加であると考えられた。これまでに、ELF3 が転写抑制能を示すこと、ELF3 は、複数の DNA 結合型転写因子と複合体を形成し標的遺伝子の転写を抑制することを明らかにしている。ELF3 複合体による GA 生合成遺伝子の発現制御機構を明らかにする（研究代表者）。

実験方法 2：*elf3* 変異体が放出する揮発性植物ホルモン様分子（GA-X）の同定

elf3 変異体は、近隣の GA 生合成変異体の矮性を回復することから GA 中間体、又は類縁の揮発性分子を放出していると考えられた。各 GA 生合成酵素の変異体を用いたバイオアッセイ系により ***elf3*** から放出される GA 中間体を推定する（研究代表者）。化学研究所の GC-MS を用いて、***elf3*** が放出する揮発性植物ホルモン様分子（GA 中間体または、類縁の揮発性分子を想定）を同定する（共同研究者、研究協力者）。

実験結果&考察

elf3 変異体と野生型における、主な GA 生合成遺伝子の発現量を比較した結果、***GA20ox*** の発現量が、野生型よりも顕著に増加しており、ELF3 が ***GA20ox*** 遺伝子の発現を直接制御する可能性が考えられた。ELF3 は、DNA 結合型転写因子と複合体を形成し転写を制御することが知られている。シロイヌナズナの培養細胞を用いてトランジェント解析により、ELF3 複合体が、***GA20ox*** の転写を抑制することを明らかにした。また、複数の GA 生合成遺伝子の変異体を用いたバイオアッセイの結果より、***elf3*** 変異体は、GA 生合成変異体 ***ga1, ga2*** の矮性は回復するが、***ga3*** の矮性は回復しないことを明らかにした。これらの結果から、***elf3*** が放出する揮発性分子として特定の GA 中間体が予想された。今後、GC-MS を用いた質量分析により同定を試みる。

高分子複合材料における多分岐高分子の挙動

田上秀一　福井大学

１．緒　言

直鎖高分子のレオロジー特性や力学特性は、分子鎖の絡み合いに大きく影響される。これらの特性を制御する目的で可塑剤などの低分子添加材をブレンドすることができるが、その場合にはブリードアウトなどの問題が生じる。近年開発された手法により合成される、構造の制御された多分岐高分子（HBP）[1]は、こうした問題を回避すると同時に、低分子添加材とは異なる分子機構で、既存高分子材料の物性をチューニングできる材料として期待できる。本研究では、構造制御されたHBP を汎用高分子に少量添加することにより、どのような物性の変化が起こるかを探索する。

２．実験方法

今回はマトリックスとなる汎用ポリマーとしてポリスチレン（PS）、ポリメチルメタクリレート（PMMA）、ポリ-L-乳酸(PLLA)を選んだ。枝の長さと分岐の密度が制御された数種類の HBP は、京都大学化学研究所の山子研究室より提供された。この HBP には構造の分布があるものの、設計通りの構造が主成分となっている[2]。PS はトルエンに、PMMA と PLLA はジクロロメタンに溶解した後、2wt%の HBP を加えて溶液中でブレンドした。溶媒を蒸発させた後、試料を加熱ローラーで成形してフィルムとした。そこから試験片を切り出し、一軸伸長試験を行った。

３．結果と考察

PS と PMMA には、コアが多分岐ポリブチルアクリレート（HBPBA）、末端に直鎖の PS あるいは PMMA をブロック共重合した HBP 試料をブレンドした。これらの試料では末端にマトリックスと同じ種類の高分子をブロックすることにより相溶化することを期待していた。しかし、今回はフィルム成形の段階で白色のブリードが生じており、また、伸長強度も低下したことから、相溶性が不足していたことが示唆された。

一方、PLA には多分岐ポリオクタデシルアクリレート（HBPOdA）、HBPBA および末端に POdA をブロック共重合した HBPBA（HBPBA-b-POdA）をブレンドした。無添加の PLA はネッキングしながら大きく延伸されたが、同様な挙動が HBPBA をブレンドした試料にもみられた。一方、HBPOdA をブレンドした試料はネッキングせずに破断した。これらの結果は、PLA と HBPBA はある程度相溶する一方で HBPOdA の相溶性が低いことを示す。さらに、HBPBA の末端に直鎖の POdA をブロックした試料を PLA にブレンドした場合にも、ネッキングしながら延伸するという挙動が示された。今後、マトリックスポリマーと HBP の組み合わせについて、さらに検討を進める予定である。

[1]　Lu, Y.; Nemoto, T.; Tosaka, M.; Yamago, S. Nature Commun. 8, Article 1863 (2017).

[2]　Tosaka, M.; Takeuchi, H.; Kibune, M.; Tong, T.; Zhu, N.; Yamago, S. Angew. Chem. Int. Ed. 62

超分岐構造高分子の滑剤作用の解明と最適化

高橋裕　東北大学

【目的】高分子は潤滑油添加剤として用いられてきたが、その分子構造は直鎖状のものに限定されていた。多数の末端基を有する超分岐構造高分子 (HBP) は、分岐構造と基材との相互作用により、特に境界潤滑領域 (低速度・高荷重) において潤滑性能を大幅に向上させると期待されている。しかし、精密な構造特性を有する HBP の制御合成は依然として課題であった。化学研究所の山子教授らは、制御された構造を持つ HBP の合成に向けた新規手法の開発に成功した。本研究では、HBP を用いて、分岐構造が潤滑性能に及ぼす影響を解明することである。得られた測定結果を活用して HBP の構造を再設計し、境界潤滑用途に最適化された HBP 潤滑剤の開発基盤を築く。

【方法】HBP は制御されたラジカル重合により合成された。潤滑油の基油である PAO を用いて、HBP の 5 mg/mL 溶液を調製した。雲母表面の間に閉じ込められた潤滑油の特性は，共振ずり測定によって評価した。

【結果】これまでの検討により、モノマーに Octadecyl acrylate (C18) を用いた HBP (HBP_C18) は、潤滑油添加剤として使用した際に境界潤滑領域で優れた潤滑性を示した［研究成果 (1), (2)］。しかし、HBP_C18 は室温で完全に溶解せず、約 40 °C 以上で溶解した。HBP の潤滑油添加剤としての実用化に向けて、約 40 °C 以下における PAO への溶解性に課題がある。この課題に対して、モノマーを Decyl acrylate (C10) とした HBP (HBP_C10) を合成した。HBP_C10 は、室温下でも PAO に完全に溶解した。境界潤滑に相関するナノスケールの潤滑特性を共振ずり測定によって評価した。共振ピーク強度 (U_{out}/U_{in}) は試料の摩擦に相関する。それぞれの高分子溶液の摩擦を比較するため、共振ピーク強度を固体接触 (SC, 摺動しない状態) の共振ピーク強度で規格化した。様々な荷重 (L) に対する規格化した共振ピーク強度 (U_{out}/U_{out_SC}) を **Fig. 1** に示した。L = 4.0 mN における U_{out}/U_{out_SC} は、HBP_C18 (0.12) ≈ HBP_C10 (0.13) < PAO (0.35) であり、本研究にて新たに合成した HBP_C10 溶液は、これまでに検討した HBP_C18 と同様に、境界潤滑領域において低摩擦で高い潤滑性を示すことが分かった。

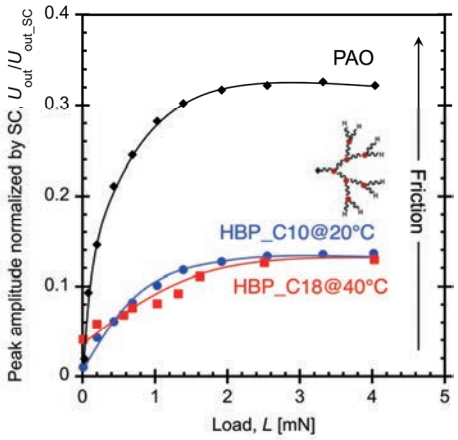


Fig. 1 Resonance peak amplitude normalized to the SC peak amplitude under various normal applied loads (L). The solid lines are visual guides.

【研究成果】

(1)（論文）Takahashi, Y.; He, Y.; Jiang, Y.; Tosaka, M.; Mizukami, M.; Yamago, S. *; Kurihara, K.* *Langmuir*, **42**(1), 509-516 (2026)

(2)（学会発表）高橋　裕、He Yuzhong、Jiang Yuhan、登阪雅聡、水上雅史、山子　茂、栗原和枝、“潤滑油添加剤としての多分岐ポリマーの特性”、第 76 回コロイドおよび界面化学討論会、3G01

Regulatory mechanisms of vegetative reproduction in response to environmental cues

Shiori S Aki　Yamato University

Background: The generation of clonal progeny from somatic cells is referred to as vegetative reproduction. Vegetative reproduction is widespread across plant lineages and plays a crucial role in global agriculture. In recent decades, climate warming has been widely recognized as a critical constraint on agricultural productivity, with vegetatively propagated plants likewise being affected. However, the mechanisms underlying the formation of vegetative reproductive organs and their responses to environmental cues remain largely unexplored due to the lack of genetic tools in many vegetatively propagated plant species. We have previously focused on 'gemma cup' of the liverwort *Marchantia polymorpha* as a model vegetative reproductive organ and have elucidated key aspects of its molecular basis mediated by phytohormones. The present work aims to clarify the regulatory mechanisms governing how environmental cues regulate vegetative reproductive organ formation, with particular emphasis on phytohormone crosstalk under elevated temperature conditions and the molecular framework underlying this crosstalk.

Results: Previously, we demonstrated that gemma cup formation is suppressed under elevated temperature conditions. In this study, we quantitatively validated this phenomenon and further investigated its molecular basis. Our analyses revealed that the number of gemma cup is reduced in a temperature-dependent manner under elevated temperature conditions. Moreover, in transgenic plants exhibiting elevated levels of a specific phytohormone, the suppression of gemma cup formation under elevated temperature conditions was fully rescued. These results suggest that this phytohormone is involved in the temperature-dependent regulation of gemma cup formation.

Gene expression analyses were subsequently conducted focusing on genes associated with the relevant phytohormone biosynthesis and signaling. Under elevated temperature conditions, the expression levels of several genes were significantly altered. These findings support a link between temperature-dependent modulation of phytohormone signaling and the suppression of gemma cup formation.

In addition, in silico analyses suggested that another phytohormone signaling pathway may negatively regulate the signaling of the relevant phytohormone. Collectively, these findings indicate that multiple hormonal signaling pathways interact under elevated temperature conditions to appropriately regulate gemma cup formation.

Biochemical characterization of aldehyde dehydrogenases involved in the biosynthesis of plant volatile benzenoids

Takao Koeduka　Yamaguchi University

【Research aims】Aromatic compounds, particularly volatile benzenoids, derived from natural resources, including rare plants, serve as functional components with health-promoting properties and as signaling molecules mediating ecological interactions. Accordingly, elucidating the biosynthetic and regulatory mechanisms has attracted considerable interest in plant biochemistry. In this study, we used petunia flowers as a model system for floral scent formation to investigate the molecular mechanisms underlying the production and regulation of diverse aromatic compounds, focusing on aldehyde dehydrogenases that convert benzaldehyde, a key intermediate in volatile benzenoid biosynthesis, into benzoic acid.

【Method and results】To identify candidate genes, we performed tBLASTx searches using aldehyde dehydrogenase (HcBD and AmBALDH) from *Hypericum calycinum* and *Antirrhinum majus* as queries against a petunia transcriptome dataset. Four candidate genes (*PhBALDH-1* to *-4*) showing more than 60% amino acid identity were identified. Among them, *PhBALDH-1* and *PhBALDH-2* were co-expressed with known volatile benzenoid biosynthetic genes and were highly expressed in post-anthesis flowers. Recombinant PhBALDH-1 and PhBALDH-2 were expressed in *E. coli*, purified and biochemically characterized. Both enzymes catalyzed the oxidation of benzaldehyde with NAD^+, with apparent K_m values of 92.7±6.0 (PhBALDH-1) and 51.0±12.7 μM (PhBALDH-2). While PhBALDH-2 showed strict specificity for NAD^+, PhBALDH-1 was able to utilize both NAD^+ and $NADP^+$. Sequence comparison, site-directed mutagenesis, and homology modeling revealed that Ala195 in PhBALDH-1 plays a critical role in determining cofactor specificity by providing sufficient space to accommodate NAD^+ and $NADP^+$, whereas substitution with Glu restricts $NADP^+$ binding.

【Summary】These results suggest that, following gene duplication in the petunia genome, PhBALDH-1 evolved to utilize both NAD^+ and $NADP^+$ through a single amino acid substitution, in contrast to the more restricted specificity of PhBALDH-2. Given the distinct physiological roles and intracellular ratios of NAD(H) and NADP(H) in plants, this flexibility may enable petunia flowers to maintain a stable and efficient supply of precursors for volatile benzenoid production under varying metabolic conditions. Overall, this study advances our understanding of key enzymes involved in volatile benzenoid biosynthesis and provides new insights into its regulatory mechanisms in *Petunia hybrida*.

【Publication】The results of this study have been published as an original article:

Biochemical characterization of benzaldehyde dehydrogenases from petunia. Koeduka T, Ito K, Yamamoto S, Ozaki S, Tsuge T, Kitajima S. *Plant Mol Biol*, 115, 70-80. (2025)

The 18th International Workshop for East Asian Young Rheologists

Tadashi Inoue University of Osaka

Purpose of project

The ICR budget was used to support the organization of the 18th International Workshop for East Asian Young Rheologists (IWEAYR-18), held in Kobe, Japan. IWEAYR is a long-running international workshop designed to promote scientific exchange and personal networking among young researchers, especially graduate students, in rheology and related fields of polymer science, soft matter, and materials science across East Asia. The present project was adopted as Project code 2025-132 under the Promotion of Collaborative and Multidisciplinary Research category. The adopted budget was 700,000 JPY, with 70,000 JPY for meeting expenses and 630,000 JPY for travel expenses. In the original proposal, support for student travel was a central objective, and the ICR support was intended to facilitate participation by young researchers and enhance the educational and scientific impact of the workshop.

Place and schedule of workshop

IWEAYR-18 was held at Kobe University, Convention Hall, Kobe, Japan, from July 25 to 27, 2025. The workshop was chaired by Prof. Hiroshi Suzuki (Kobe University), and the organizing committee included faculty members from Kobe University, the University of Osaka, Kyoto University, and Nagoya University. The program included registration and poster preparation, long-oral sessions, short-oral sessions, poster presentations, group presentations, a banquet, and associated faculty and student activities. The meeting was organized in connection with the broader 2025 rheology community gathering in Japan, which further strengthened its visibility and regional impact.

Purpose and background of the workshop

IWEAYR has been organized annually since 2006, except during the interruption caused by the COVID-19 pandemic, in a rotating order among Korea, Japan, China, and Thailand. Since its inception, the workshop has served as a place where faculty members and graduate students can engage in close discussion, scientific exchange, and international collaboration in an informal and highly interactive atmosphere. Many former student participants later became faculty members and continued to contribute to the IWEAYR network in their home countries. In this sense, IWEAYR is not merely a one-time meeting, but a long-term framework for cultivating international academic relationships and future collaborative research in rheology.

Participants

The workshop attracted approximately 140 participants in total, including 43 faculty members and 95 students based on the accommodation arrangements, together with organizers and related staff. Participants came primarily from Japan, Korea, China, and Thailand, reflecting the established international framework of IWEAYR. The actual turnout appears to have exceeded the scale anticipated at the proposal stage. The scientific program itself also confirms active participation from these four countries through the affiliations of speakers, session chairs, and organizers.

Overview of IWEAYR-18

According to the final program, the scientific program consisted of 12 long oral presentations, 36 short oral presentations, and 51 poster presentations, including one cancelled poster listed in the program. These numbers indicate a highly active meeting with substantial contributions, especially from students and young researchers. The topics covered a wide range of current interests in rheology and related soft-matter science, including polymer dynamics, battery slurries, gels, nanocomposites, extensional flow, machine-learning-assisted rheological analysis, and processing-related phenomena. The workshop therefore functioned both as an educational forum for young researchers and as a scientifically relevant venue covering fundamental and applied aspects of contemporary rheology.

Summary

IWEAYR-18 successfully achieved its original purpose. The workshop provided an active and friendly environment in which students and faculty members from Japan, Korea, China, and Thailand could present their research, exchange ideas, and strengthen personal and academic connections. The large number of student contributions demonstrates that the workshop effectively served its primary mission of supporting young rheologists in East Asia. At the same time, the continued participation of senior faculty members and long-term collaborators confirmed the stability and maturity of the IWEAYR network. The ICR budget was effectively used to support travel and local organization, thereby promoting broad participation and helping maintain the long-standing international framework of the workshop. In conclusion, IWEAYR-18 made a meaningful contribution to the development of scientific exchange, friendship, and future international collaboration in rheology and related soft-matter research in East Asia.

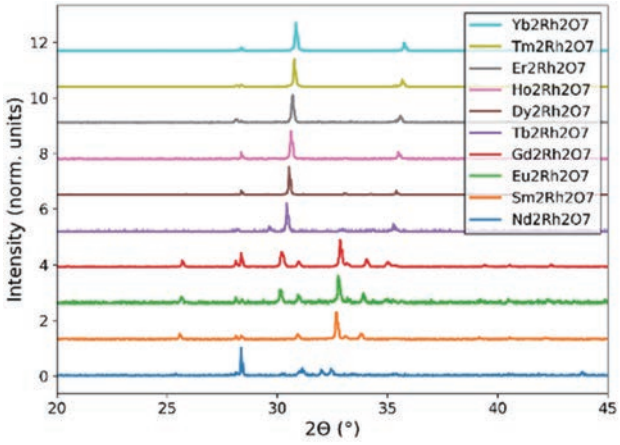
High pressure synthesis of new Rh based quantum materials

Sean Injac　University of Edinburgh

Objectives: This project sought to synthesise and characterise a number of new Rh based quantum materials. Initially two compounds $Ho_2Rh_2O_7$ and $PbRhO_3$ were targeted for synthesis using high pressure, high temperature (HPHT) techniques. These materials were expected to show highly correlated electron behaviour giving rise to quantum properties due to the geometrically frustrated nature of the two crystal structures and the itinerant nature of Rh^{4+} 4*d* electrons.

Experimental Methods: Synthesis of these targeted compounds was undertaken using the Infinite large volume press available at the Advanced Solid State Laboratory in collaboration with Professor Yuichi Shimakawa. Synthesis was undertaken at between 6 and 8 GPa at a number of temperatures between 1000 °C and 1400 °C. Phase formation and sample purity was confirmed via X-ray diffraction measurements using a D8 powder diffractometer using Cu Kα radiation. Temperature and field dependent magnetisation measurements were undertaken using a Quantum Design MPMS3 SQUID.

Experimental Results: Over the course of the approximately six-week research project the synthesis of 10 compounds of the form $Ln_2Rh_2O_7$ (*Ln* = Pr ~ Yb) was attempted. Synthesis was undertaken by treating precursor mixtures of Ln_2O_3 (or similar), Rh_2O_3 and $KClO_4$ powders at elevated pressures and temperatures for up to 1 hour. Synthesis attempts were initially undertaken on $Ho_2Rh_2O_7$ in order to determine the ideal combination of pressure, temperature, heating time, and oxygen stoichiometry. Of the 10 compositions attempted six compounds were recovered to high purity as new pyrochlore materials (*Ln* = Tb, Dy, Ho, Er, Tm, Yb). X-ray diffraction patterns of all attempted compounds is shown.



Discussion: All pure pyrochlore samples crystallised in the *Fd*-3*m* pyrochlore structure, trace amounts of Ln_2O_3 oxides were present for several samples, for *Ln* = Tb, Dy trace $LnRhO_3$ perovskite, which contains diamagnetic Rh^{3+} was present. Initial magnetic analysis consisting of zero-field cooled (ZFC) and field cooled (FC) temperature dependent magnetisation measurements between 2 K and 300 K and field dependent magnetisation measurements were collected. For $Tm_2Rh_2O_7$ a feature suggesting antiferromagnetic (AFM) order below approximately 40 K was observed in temperature dependent magnetisation. Field dependent magnetisation at 2 K is also consistent with AFM order. No other sample showed clear evidence of magnetic order above 2 K. For *Ln* = Dy, Ho, enhanced field dependent magnetisation was observed at 2 K, suggesting nearness to ferromagnetic order or a spin-ice state below 2 K. The remaining samples for *Ln* = Tb, Yb and Er show deviation from Curie-Weiss type paramagnetism at low temperature and negative Weiss constants suggest nearness to AFM order below 2 K, field dependent measurements for $Er_2Rh_2O_7$ further suggest metamagnetic behaviour.

Outcomes: In order to better understand the formation of these pyrochlores at HPHT conditions in-situ X-ray diffraction data were collected at the ID06 LVP beamline of the European Synchrotron Radiation Facility (ESRF) for = Nd, Gd, and Er. These experiments replicated the synthesis pressure and temperature conditions. Analysis of these data is underway. A proposal for neutron powder diffraction (NPD) measurements using the WISH instrument of the ISIS spallation source, UK has been submitted to investigate the magnetic properties of these compounds. The results of this proposal are pending as of writing. The synthesis of these compounds will produce at least one publication in a reputable journal. Should NPD measurements indicate quantum behaviours further impactful publications are expected

Atomic Structure Investigation by Advanced Transmission Electron Microscopy of AlxCrFeNiCu Alloys

Natthaphol CHOMSAENG　Burapha University

Objectives

We have investigated and characterized AlxCrFeNiCu alloys in collaboration with Associate Prof. Dr. Mitsutaka HARUTA, Division of Electron Microscopy and Crystal Chemistry. For advanced ARM-TEM was used to study phase of AlxCrFeNiCu alloys, and TEM-EDS was used to confirm their chemical composition. This work was supported by the Collaborative Research Program of Institute for Chemical Research, Kyoto University (Grant No. 2025-134).

Experiment Results

TEM analysis shows that ordered phase distribution changes systematically with aluminum content . In $Al_{0.5}$ alloy, the $L1_2$ ordered matrix contains cuboidal B2 precipitates with size close to 1 μm shown as Figure 1. FFT analysis confirms $L1_2$ ordering in the Cu-Al-Ni rich matrix regions through ½{110} superlattice reflections characteristic of Cu_3Au-type structure. SAED from the Fe-Cr rich cuboidal precipitates along [001] zone axis shows {010} superlattice reflections, indicating B2 (CsCl-type) ordering rather than disordered BCC. The presence of Al in the precipitates, evident from EDS mapping, enables Fe-Al pair ordering. Dark-field imaging using superlattice reflections reveals precipitate morphology and distribution in the ordered $L1_2$ matrix.

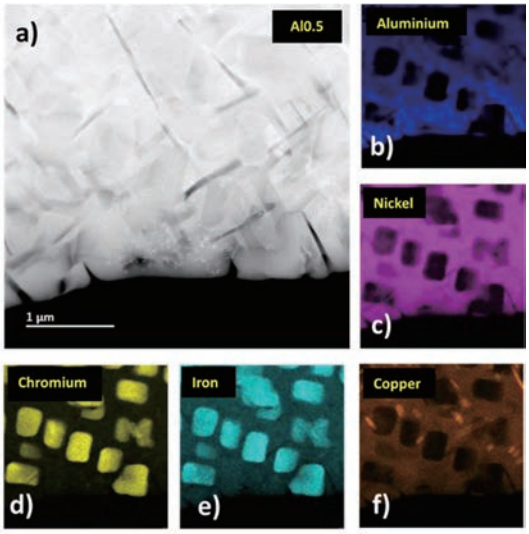


Figure 1. STEM-EDS elemental maps for $Al_{0.5}CrFeNiCu$: (a) Annular dark field image, (b-f) Elemental mapping for Al, Ni, Cr, Fe, and, Cu, respectively

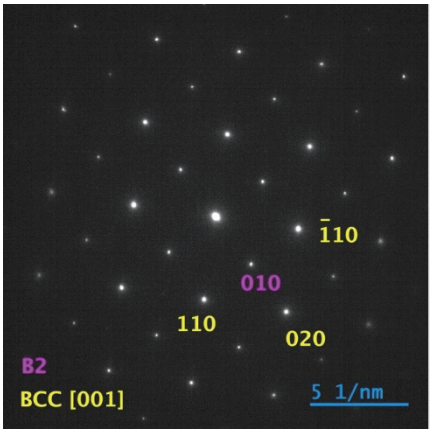


Figure 2. SAED pattern of $Al_{0.5}CrFeNiCu$ (a) from precipitates along [001] zone axis with {010} superlattice reflections.

Tackling Plasmon Dispersions in Quantum Matters by Momentum-Resolved Electron-Energy Loss Spectroscopy

Ming-Wen Chu　National Taiwan University

This project focuses on experimentally exploring the plasmon-dispersion behaviors in 2D materials. Unlike the 3D plasmon is under q^2 dispersion, the 2D plasmon disperses by $\sqrt{q}$. Here below are the 2D plasmon-dispersion functions of gapless and gapped electrons, where n_{2D} is the 2D charge density, e is the electron charge, m^* is the effective mass, ε_∞ is the non-local screen dielectric constant, and ω_c is the correction term of plasmon crossover the light line in the gapped case. The difference between these two functions sketch the plasmon behavior near the light line under different conditions: gapless and gapped.

$$\text{Gapless: } \omega_p^{2D} = \sqrt{\frac{2\pi n_{2D} e^2}{m^* \varepsilon_\infty}}\sqrt{q}$$

$$\text{Gapped: } \omega_p^{2D} = \omega_c + \sqrt{\frac{2\pi n_{2D} e^2}{m^* \varepsilon_\infty}}\sqrt{q}$$

Due to their novel physical properties, 2D materials have been a hotly debated research topic in recent years. Advances in sample fabrication techniques have enabled the design of more precise and complex systems. In this highly competitive field, we believe there is still room for experimental clarification of the physical properties of 2D materials. We stacked ML MoS_2 and ML WSe_2 into a heterostructure to observe how the plasmon behavior of the stacked heterostructure changes, further understanding the alterations in its electronic structure and other physical properties. To achieve this, we used the momentum-resolved, high-resolution electron energy loss spectroscopy (q-EELS) of Prof. M. Haruta. We measured along the Gamma point at the Brillouin-zone center towards the boundary in the reciprocal space. The results were very exciting; the spectrum clearly showed plasmon and exciton peaks in the low-energy region, and the results were consistent along both the MoS_2 and WSe_2 directions, indicating a redistribution of electrons in the stacked heterostructure. This is a preliminary result, and further research discussions and experimental progress are needed in the future. It is expected that this collaboration will yield very good results.

Nano-structural and Atomic-resolution Characterization on the Local Structure of Novel Functional Energy Materials by Advanced Transmission Electron Microscopy

Thapanee Sarakonsri Chiang Mai University

1. Sn/Si-based nanocomposite anode materials for lithium-ion batteries

Fig. 1(a-e) showed electron energy loss spectroscopy (EELS) mapping of Si, Sn, O and C retrieved from the Sn/Si-based nanocomposite. C was found to surround other elements. The EEL spectrum of C (Fig. 1(f)) exhibited a weak π* (~284 eV) and a broad σ* feature (290–300 eV) without a pre-peak, characteristic of amorphous C. These results confirm the successful C coating on the Sn/Si-based nanocomposite.

2. Biomass-derived thin-layer carbon anode materials

Fig. 2 exhibited the morphology of biomass-derived thin-layer carbon material (Fig. 2(a)), showing the absence of lattice fringes, indicating the formation of amorphous carbon. The EEL spectrum (Fig. 2(b)) revealed a weak π* peak along with a broad σ* features which were also indicative of amorphous carbon.

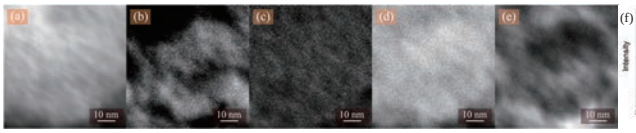


Fig. 1 (a) TEM image and EELS mapping of (b) Si, (c) Sn, (d) O and (e) C; (f) EEL spectrum of C

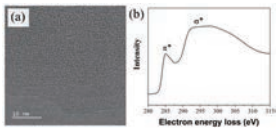


Fig. 2. (a) TEM image, (b) EEL spectrum

3. Biomass-derived porous hard carbon for next-generation sodium-ion batteries

Peanut shell–derived porous carbons (PC) were characterized by EELS (Fig. 3(a)). More pronounced π* and σ* features were detected after treatment, indicating increased sp^2 carbon and graphitic-like domains. TEM image (Fig. 3(b)) revealed irregular carbon sheets with abundant nanoscale pores, while HRTEM (Fig. 3(c)) confirmed fringes typical of turbostratic carbon with interlayer spacing of ~0.36 nm.

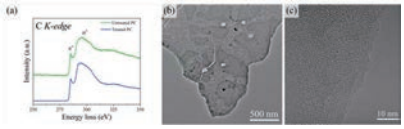


Fig. 3. (a) EELS spectra of untreated PC and microwave-assisted KOH-treated PC, (b) TEM image, (c) HRTEM image of treated PC

4. Anthraquinone-based Porous Organic Polymers (POP-AQ) composited with TiO_2(B)

AQ-POP with sheet-like morphology was achieved via nano-interfacial synthesis (AQ-POP-NI). Fig. 4(a) shows AQ-POP appears in a bright area. The TEM and HRTEM images of AQ-POP are shown in Fig. 4(b-c), indicating amorphous nature. EELS mapping (Fig. 5) showed C, O, and N distributed in AQ-POP-NI. After composite with TiO_2(B), AQ-POP-NI (Fig. 6) displayed as nanoparticles on TiO_2(B) nanorod.

5. Novel Metal-Organic Frameworks (MOFs) as anode in LIBs

MOFs offer tunable molecular architectures with controllable porosity, coordination environment, and electronic properties, making them promising anode materials. Advanced characterization using STEM-HAADF, and TEM-EELS enables detailed investigation of metal centers, bonding environments, and oxidation states. However, TEM measurements of MIL-53(Al) (Fig. 7) did not show diffraction spots, indicating poor crystallinity or amorphous character, preventing acquisition of HRTEM images.

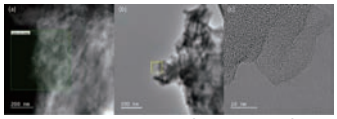


Fig. 4. (a) Annular dark-field image of AQ-POP and (b-c) HRTEM image of AQ-POP

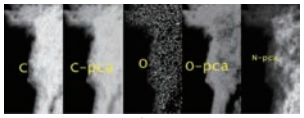


Fig. 5. EELS map of (a) C and C-pca, (b) O and O-pca and (c) N-pca of AQ-POP-NI

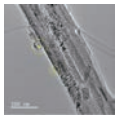


Fig. 6.TEM image of AQ-POP-NI

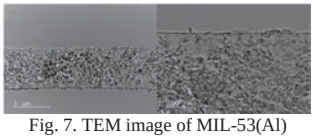


Fig. 7. TEM image of MIL-53(Al)

6. Investigation of novel hierarchical carbon materials and mix-phase Titanium dioxide for Wastewater treatment

Hierarchical PC spheres functionalized with Ni-Fe nanoparticles were characterized (Fig. 8(a-c)). Results confirmed a core-shell structure consisting of a metallic Ni-Fe core and oxidized Fe shell, encapsulated by graphitic C. Residual N signals indicated adsorption of dye molecules. EELS of Au-doped mixed-phase TiO_2 distinguished anatase and B phases and revealed defect structures, confirming its suitability for photocatalytic wastewater treatment.

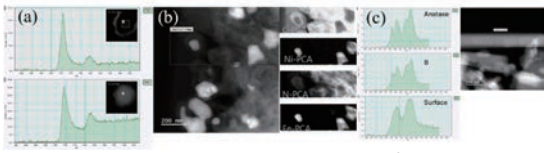


Fig. 8. (a) EELS spectrum at the core and shell of the Ni-Fe particles, (b) EELS maps for C, Ni, N and Fe (c) EELS spectrum at the TiO_2 nanorod

Publications

1. O. Namsar, T. Autthawong, C. Yodbunork, W. Yodying, N. Mahamai, K. Kunniyom, M. Haruta, T. Sarakonsri, Radiation Physics and Chemistry 235 (2025).
2. W. Punyaarthansakun, T.-N. Pham-Truong, T.-T. Bui, P.-H. Aubert, M. Haruta, T. Sarakonsri, N. Semakul, Efficient Synthesis of Dual Redox-Active Disulfide Polymers for High-Performance Lithium-Sulfur Batteries (submitted manuscript)

レーザー駆動イオン加速機構による
高品質なイオンビーム生成のためのレーザー照射条件の最適化

小島完興　量子科学技術研究開発機構

【目的及びねらい】

本研究の目的は、室温で気体状態にある重イオン（ヘリウム、ネオン、酸素、窒素、アルゴンなど）をレーザー駆動により高効率で加速する技術を開発することである。これにより、多様なイオン種を活用したがん治療の可能性を拡大し、従来の放射線治療では効果が低いがんへの対応や、正常組織へのダメージ低減を実現する新たな治療法の確立を目指す。

【実験方法、実験結果、考察】

現在の重粒子線がん治療では主に炭素イオンが用いられているが、放射線治療の効果が低いがん（例：すい臓がん）に対しては、酸素やネオンなど質量の大きいイオンを用いた治療の有効性が指摘されている。また、正常組織へのダメージ低減を目的として、ヘリウムなどの軽イオンを利用する治療法も提案されており、腫瘍特性に応じたマルチイオン照射の実現が期待されている。しかし、これらのイオン種は室温で気体状態にあるため、従来手法では標的作製が困難であり、レーザー駆動加速の適用が制限されていた。

本研究では、気体原子を固体標的中に高密度で保持するため、半導体製造に用いられるイオン注入装置を用いた標的作製手法を採用した。具体的には、固体密度の 10 at.%を超える高密度で窒素イオンをニッケル箔中に人工的に注入し、レーザー加速に適した被加速粒子層を形成した。その後、CW レーザー照射によって標的薄膜を加熱し、表面汚染層の除去を行った。最終的に、高強度・超短パルスレーザーを照射してイオン加速実験を実施した。

実験結果の解析にはトムソンパラボラ分光器を用いた。標的を非加熱状態で照射した場合には主として陽子線が観測された一方、CW レーザー加熱後には窒素イオンの検出が確認された。これは、レーザー加熱によって表面汚染由来の軽元素成分が低減され、標的内部に注入された窒素が優先的に加速されたことを示唆している。

以上の結果から、イオン注入技術とレーザー加熱技術を組み合わせることで、室温で気体状態にある原子をレーザー駆動により効率的に加速可能であることを実証した。本手法は、多様なイオン種に対して適用可能な新しい標的設計指針を提供するものである。

【専門分野における位置付け】

本研究は、がん治療における多イオン種利用の可能性を拡張し、放射線治療の新たな展開に寄与するものである。特に、従来治療では効果が限定的であったがんへの対応や、正常組織の保護を目的としたマルチイオン照射治療において、今後重要な役割を担うことが期待される。本技術の発展により、より柔軟かつ高精度な重粒子線治療の実現が促進され、がん治療のさらなる高度化に貢献すると考えられる。

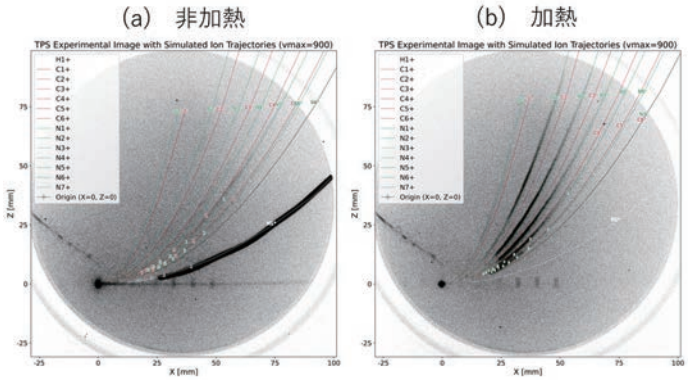


図 1　窒素を人工的に注入した
ニッケル標的から加速したイオン信号
(a)非加熱時　(b)加熱時

スギ木質組織構造の効率的化学分解過程から先端化学物質生産をめざした質量分析解析

秦野修　奈良県立医科大学

目的：

本研究は再生可能資源である森林バイオマスに着目し、木質細胞壁の主成分であるセルロースやリグニン等を、先端化学材料（CNF など）を含む有用化学物質への効率的変換/利用法の開発を目的とする。化学研究所・中村研究室では、種々の触媒と過酸化水素水を用いて、新奇な木材の効率的分解/合成/利用法の開発を行っている。この際、有機酸触媒等を木粉や木材チップに直接作用させ、軽量で高剛性を実現できる新規材料として注目されるセルロースナノファイバー（CNF）様の構造物が容易に得られることを見出している。

申請者は、スギ木幹部の薄い切片を作成して、形態学的側面から、これらの触媒反応による組織構造の前後変化を可視化（Imaging）する系を構築した。この際、光学顕微鏡と SEM を併用して、リグニン、セルロース等の存在部位を可視化し（光学顕微鏡）、SEM を用いて電顕レベルの形態学的変化を追跡する系を構築した（CLEM 法: 光学・電子顕微鏡相関法）。

本研究は、過酸化水素水と触媒等による木材分解過程を、薄い光学顕微鏡用切片を用いた効率的な分解系を用いて、組織形態学的変化と、FT-ICR MS 分析を用いた分解産物の解析に重点を置き、木材から先端化学材料等の有用化学物質への効率的分解/合成/利用法の開発・解析を行うことを目的とする。

実験方法、実験結果、考察：

申請者は、薄いスギ木幹部切片（0.009 mm 厚）を用いることにより、触媒を用いず、過酸化水素水のみで、効率的に木質切片を分解できることを明らかにした。本実験系は、薄い切片とごく微量の反応液(0.04 ml 可）を用いて、簡便に触媒のスクリーニングが可能である。R6 年度は、スギ木幹部の薄い切片等を、過酸化水素水（30%）溶液で分解したのち、カルボン酸、アルデヒド／ケトンを誘導体化・検出する誘導体化法(主に 3-NPH 試薬)を用いて、FT-ICR MS を用いて、H_2O_2 単独/+触媒添加分解産物中に存在する低分子領域のカルボン酸、アルデヒド／ケトンの化合物（分子式）を網羅的に同定した。しかしながら、3-NPH はカルボン酸以外にもアルデヒド／ケトンとも反応するため、本年度は、カルボン酸を誘導体化するが、アルデヒド／ケトンを、ほぼ誘導化しない試薬として、2022 年に開発されたカルボン酸を高効率に誘導体化するピリジニウム誘導体化試薬：TPP-AEP (J. Am. Soc. Mass Spectrom. 33(2022):1492)を合成し、スギ木質 H_2O_2 分解産物を基質として誘導体化を行ない、FT-ICR MS を用いて、分解産物の網羅的な解析を行っている。その結果、3-NPH 試薬において強く誘導体化/検出された 6 種の化合物は、TPP-AEP を用いた場合においても、強く誘導体化/検出され、カルボン酸構造をもつものと推定された。

一方、同定されたこれらのカルボン酸化合物（分子式）は、異性体をもつものと、持たない化合物が存在するため、今後、異性体を判別する目的で、ion-mobility MS, CE-MS, LC-MS 等を用いて、異性体の同定を行っていきたい。又、異性体構造を含めて同定された分子を新たな基質として経時的に H_2O_2 分解を行い、より低分子への分解経路と、最終分解産物の同定を FT-ICR MS を用いて明らかにしていきたい。

謝辞：

TPP-AEP 合成法を御教授いただきました、福岡大学薬学部・吉田秀幸教授に感謝致します。

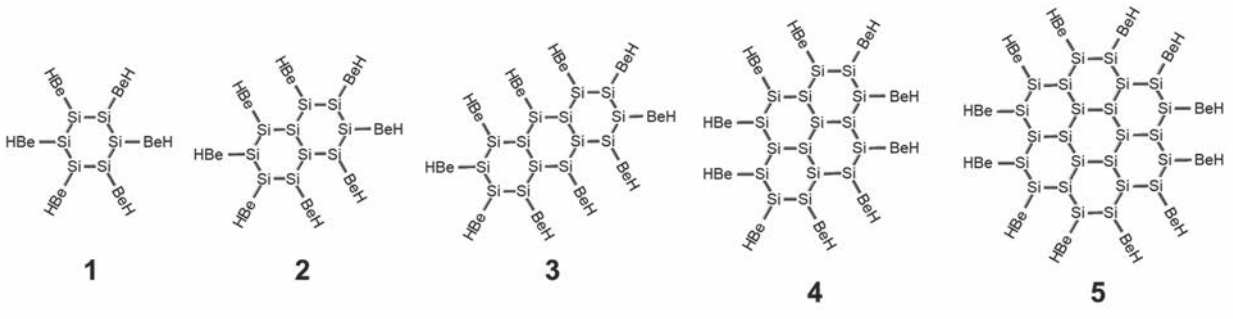
Theoretical design of low-dimensional silicon material embedded in a flat two-dimensional sheet and exploration for operating principles

Masae Takahashi　Tohoku University

【Objectives】The advent of flat two-dimensional (2D) materials such as graphene has rapidly advanced nanotechnology. Silicene, the silicon counterpart of graphene, promises seamless integration with existing silicon-based nanotechnologies. However, silicene faces significant challenges, including instability in air due to its non-planar, buckled structure. Additionally, silicene is typically synthesized via epitaxial growth on a substrate, which significantly disrupts its π-conjugated system. The fabrication of free-standing, planar silicene has long been a highly sought-after goal. We report here the computational design of five planar silicon-rich 2D alloys consisting of silicon and beryllium, structurally derived from our previously designed molecular building blocks with planar configurations (**1**–**5**) (M. Takahashi, Sci. Rep. 2017, 7, 10855).

【Computational Details】We performed structural and electronic calculations within the density functional theory (DFT) framework, as implemented in the CASTEP code (ver. 2024). Total-energy calculations were based on the plane-wave DFT method within a generalized gradient approximation. The Perdew–Burke–Ernzerhof exchange–correlation functional was employed as implemented in the CASTEP code. Norm-conserving pseudopotentials were used to describe the electron–ion interactions.

【Results and Discussion】We have investigated the structural flatness, dynamical and thermal stability, electronic and mechanical properties. Four of the five alloys exhibit planar geometries as local minima without imaginary frequency at the Γ point, a key factor for air stability. Notably, we achieved direct band gaps in these materials, contrasting with the indirect gap of bulk silicon and the zero-gap nature of silicene. Phonon dispersion and ab initio molecular dynamics simulations confirm the dynamical and thermal stability of the direct-gap semiconductor. Additionally, their reduced in-plane Young's modulus and comparable minimum thermal conductivity compared to graphene suggest high mechanical flexibility and efficient heat dissipation.



【Publications】[1] M. Takahashi, Discover NANO 2026, 21, 50. [2] M. Takahashi, Chem. Phys. Impact 2025, 11, 100977. [3] M. Takahashi, Molecules 2025, 30, 1158. [4] M. Takahashi, OMCOS XXII, September 1–5, 2025, Kyoto, Japan.

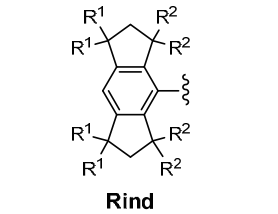
13 族元素水素化物の合成と分子構造の解明

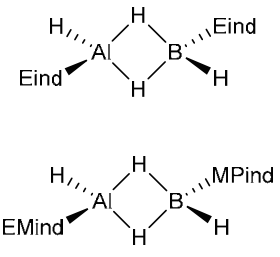
松尾司　近畿大学

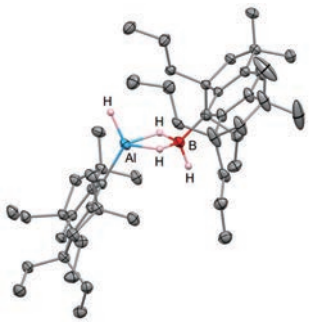
13 族元素であるホウ素やアルミニウムに水素が置換した「水素化ホウ素化合物」や「水素化アルミニウム化合物」は、その高い反応性から有機化合物や無機化合物の還元剤や水素化剤として幅広く利用されている。異なる 13 族元素から構成される「13 族元素混合型水素化物」は、「アルマボラン(6)」などが知られており、理論計算による研究が古くから行われてきた（Lammertsma, *J. Chem. Phys.* 1991 など)。しかし、異なる 13 族元素の間に２つの水素が二重架橋した化合物の合成例は限られており（*J. Chem. Soc., Dalton Trans.* 1997, *Eur. J. Inorg. Chem.* 1998 など)、「13 族元素混合型水素化物」の合成や反応性については未知の部分が多く残されている。

これまでの共同研究により、汎用性の高い「縮環型立体保護基（Rind 基)」を導入することで、「ジアルマン(6)」を合成し、分子構造を単結晶 X 線構造解析により決定した（*Angew. Chem. Int. Ed.* 2016)。また、ピリジン類のヒドロアルミニウム化の反応機構を「重水素化ジアルマン(6)」を用いて明らかにした（*Inorganics* 2019)。今回の共同研究では、「アルマボラン(6)」に着目し、化学研究所所有の単結晶 X 線構造解析装置を利用して、分子構造や化学結合を解明することを目的とした。また、合成した「アルマボラン(6)」の反応性について明らかにすることを目指した。

ホウ素とアルミニウムともにかさ高い Eind 基が置換した「アルマボラン(6)」、および、ホウ素にはよりかさ高い MPind 基、アルミニウムにはよりかさの小さな EMind 基が置換した「アルマボラン(6)」を合成した。後者の分子構造を単結晶 X 線構造解析により決定し、ホウ素とアルミニウムとの間に「非対称な三中心二電子結合」が存在することを明らかにした。また、理論計算により、ホウ素がマイナス、アルミニウムがプラスに電荷分離した極限構造式の寄与が示唆された。アルマボラン(6)と強いルイス塩基である「*N*–ヘテロ環状カルベン（NHC)」との反応では、「ボラン・NHC 付加体」と「アルマン・NHC 付加体」が生成した。このうち、「アルマン・NHC 付加体」の分子構造を単結晶 X 線構造解析により明らかにした。







成果報告

1. 前谷 一颯、石本 翔真、松尾 司、アルマボラン(6)の理論的研究、日本化学会第 106 春季年会、2026 年 3 月 17－20 日、日本大学、発表予定
2. T. Moriya, T. Kuroda, K. Kubo, T. Oshiki, Y Nishina, Y. Mizuhata, R. Inoue, T. Agou, Air-Stable 2,2′-Azobispyridine Radical–Boron Complexes and Their Near-Infrared Absorption Properties, *Chemistry–A European Journal, in press.* DOI: 10.1002/chem.202503525.

Cs_4PbBr_6 薄膜への電子線照射による $CsPbBr_3$ ナノ光源生成

斉藤光　九州大学

ハライドペロブスカイトは優れたオプトエレクトロニクス材料であり、中でも $CsPbBr_3$ は高効率の緑色発光や短い発光寿命から発光デバイスへの応用が期待されている。さらに、$CsPbBr_3$ ナノ粒子は、その励起子のボーア半径程度(＜10 nm)まで小さくすると、室温でも単一光子源として機能することも見出されている[1]。$CsPbBr_3$ ナノ粒子をデバイス中に自在に配置することができれば、光電変換インターフェースの集積化や量子光学デバイスの基盤技術となりうる。そこで本研究では、電子線照射により、局所的に材料中の構造を変化させる方法[2]で、$CsPbBr_3$ ナノ粒子を自在に配置する技術開発に取り組んだ。膜厚 160 nm の Cs_4PbBr_6 薄膜(微量の CsBr を含む)を含む多層膜 SiO_2 (10 nm)/Cs_4PbBr_6 (160 nm)/SiO_2 (5 nm)/Si_3N_4 (20 nm)を作製し、Cs_4PbBr_6 相への高電流電子線照射によって Cs_4PbBr_6 母相中に緑色発光を示す $CsPbBr_3$ ナノ光源が形成されるかどうか検証した。カソードルミネセンス(CL)測定系を装備した走査透過電子顕微鏡(STEM)装置[3]にて、nA オーダーの電子線を 3×3 の正方格子状に順次滞留させた後、低電流条件で同視野の CL 強度マップを取得したところ、図 1 (a)に示すように、正方格子状にナノ光源が生成されたことが明瞭に確認された。輝点分布幅は 100 nm を大きく下回り、輝点中心は高電流照射中心から 10 nm 以内に位置する。また、図 1 (b)に示すように、高電流照射位置を含む視野で取得した電子エネルギー損失分光(EELS)スペクトルには、$CsPbBr_3$ のバンドギャップに相当する 2.4 eV の立ち上がりが観測され、生成された光源が $CsPbBr_3$ ナノ粒子であることが確認された。さらに、EELS マッピングより、$CsPbBr_3$ ナノ粒子のサイズが~25 nm であると評価された。エネルギー分散 X 線分光分析により、高電流照射位置の Cs と Br の濃度が低下することがわかった。すなわち、電子線の高電流照射により、化学組成(Cs:Pb:Br)が局所的に 4:1:6 から 1:1:3 へ近づくことで、$CsPbBr_3$ ナノ粒子が生成することが示唆された[4]。

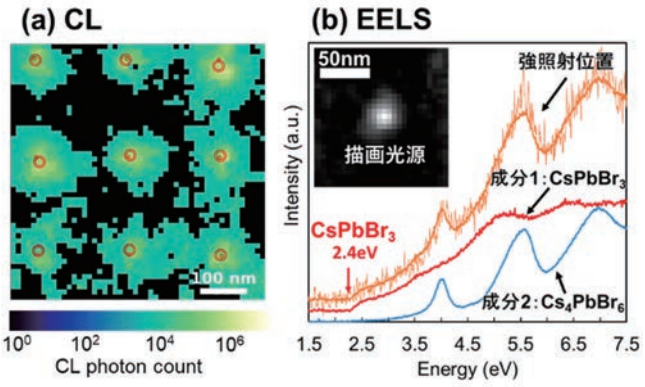


図 1　Cs_4PbBr_6 薄膜への電子線照射による $CsPbBr_3$ ナノ光源の描画。(a) 3×3 格子状に描画されたナノ光源の CL マップ。(b)照射位置の EELS 解析。$CsPbBr_3$ と Cs_4PbBr_6 から得た EELS スペクトルの線形結合によりフィッティングした。左上は $CsPbBr_3$ の割合のマップ。

[1] F. Hu et al., ACS Nano 9, 12410 (2015)

[2] H. Saito et al., Appl. Phys. Lett. 127, 261102 (2025)

[3] T. Fujimaru et al., ACS Photonics 12, 3073 (2025)

[4] T. Fujimaru et al., arXiv:2601.14898 (2026)

2. 国際会議、シンポジウム・研究会報告

赤外ラマンセミナー「振動分光学の研究最前線」

主　催：(公社) 日本分光学会・赤外ラマン分光部会
共　催：京都大学化学研究所共同利用・共同研究拠点
協　賛：日本化学会，応用物理学会，日本分析化学会，分子科学会
日　時：2025 年 11 月 28 日（金）　13:00〜17:00
場　所：京都大学化学研究所・共同研究棟 大セミナー室，および Zoom 配信によるハイブリッド形式

2016 年からシリーズ化して開催している，赤外分科会企画の部会イベントである“MAIRS ワークショップ”の第 8 回を当初企画していたが，ラマン分科会の学習院大・齊藤結花教授からの提案で，今年は赤外とラマンの分科会が初の合同で「振動分光学の研究最前線」と題してのセミナーを開催した．趣旨が変わったものの，参加者は例年通り集まり，対面に 31 名，オンラインが 33 名で，合計 64 名であった．学生の参加者が 24 名と，若手の参加者がとくに今年は多めだった．

今年も日本化学会，日本分析化学会，分子科学会，応用物理学会の 4 学協会の協賛を得て実施し，これら協賛学会からの参加者は分光学会員と同額の参加費とした．学生は例年通り無料とした．

2021 年から始めたハイブリッド開催は毎年好評であるため，今年も継続した．運営をスムーズに実現するため，専門業者にマイクなどの設定を任せ，最終的に 60,247 円の黒字で終了した．

対面式の会場は京大化研で，プログラムは次のとおりである．

1.　In-situ IR 測定による固体触媒のキャラクタリゼーション（大須賀遼太（北海道大））
2.　波長変換を駆使した中赤外タイムストレッチ分光法（橋本和樹（東京大））
3.　有機半導体を用いた光エネルギー変換（玉井 康成（東京大））
4.　電気化学探針増強ラマン分光の現状と周辺技術の開発（横田泰之（理研））
5.　コヒーレントラマン顕微鏡を用いた薬剤イメージング（伊藤輝将（東京農工大））
6.　顕微ラマン分光法と培養系を用いたヒト感染性ウイルスの検出技術開発（岩崎啓太（関学大））



大須賀先生は，赤外分光法の基本的な長所を活かした，触媒化学での利用法を示した．すなわち，これまで詳細が不明だった液相中での固体触媒の表面が持つ酸塩基の性質を，赤外分光法で明らかにする挑戦をしており，定量的な再現性の良さも十分に活かした検討を行っていた．

橋本先生は，パラメトリックなレーザー分光技術の最先端をいく研究として，長短パルスレーザーの時間ストレッチによる，ガス試料を中心とした波数分解が高く精度が極めて高い測定への挑戦事例を示した．基本技術の紹介も大変に分かりやすかった．

玉井先生は，緑の光を吸って青の光を出すアップコンバージョンの研究を，その分子科学的な仕組みから大変わかりやすく説明し，実際の NIR 光に対しての取り組みの事例

を詳しく解説した.

横田先生は, 電気化学 TERS の最前線を, 基本から詳しく解説し, チュートリアル的にも優れた講演であった. 電気化学での TERS を広く実用化に向けて必要な研究はなにか, という問いからわかりやすく, 非常に勉強になった.

伊藤先生は, コヒーレントラマン顕微鏡を用いて, x, y だけでなく z 方向にもイメージング可能な技術を紹介し, 皮膚に塗りこんだ薬剤が具体的に皮下組織に浸みこんで行く様子が可視化できることを示し, 印象的であった.

最後の岩崎先生は, 実験用の細胞培地のウィルス感染の有無を, ラマン分光法でどのように識別するかという課題に取り組んでいる様子を, 多数のアプローチで提示し, 多くの関心を集めた.

このように, 今年の講演会は, 赤外とラマンをまとめて扱うことで, 本来あるべき振動分光法の基礎と応用を俯瞰できる良い機会となった.

会のスムーズな運営を可能にしてくれた, 国際共共拠点にこの場をお借りして, 厚く御礼を申し上げる.

長谷川健（分子環境解析化学研究領域）

NIMS Award 2025 Satellite Symposium at Kyoto University
実施報告書

日　時：20245 年 11 月 13 日（木）
場　所：京都大学化学研究所　宇治キャンパス　きはだホール
参加者：60 名（海外 15 名　国内 45 名）

2025 年 11 月 13 日、京都大学宇治キャンパスきはだホールにおいて、「NIMS Award 2025 サテライトシンポジウム」が開催されました。本講演会は、材料科学分野で国際的に高い評価を受ける研究者の講演を一度に聴講できる貴重な機会として、多くの研究者および学生が参加しました。

本シンポジウムでは、宮坂力教授（桐蔭横浜大学）、Henry J. Snaith 教授（オックスフォード大学）、Nam-Gyu Park 教授（成均館大学）の 3 名が登壇され、主にペロブスカイト太陽電池を中心とした最先端研究の進展についてご講演が行われました。宮坂教授からはペロブスカイト材料の基礎および実用化に向けた展開について、Snaith 教授からはデバイス物理および高効率化の戦略について、Park 教授からは材料開発および安定性向上に関する取り組みについてご説明があり、それぞれの視点から同分野の発展を俯瞰的に理解することができました。

いずれの講演も最新の研究成果に基づいており、学術的意義に加え、産業応用への展望が示された点が大変印象的でした。また、講演後には講演者および参加者との交流の機会が設けられ、活発な質疑応答や意見交換が行われました。

本シンポジウムは、国際的な研究動向を把握する上で非常に有意義な場であり、今後の研究活動に多くの示唆を与える機会となりました。参加者全員が高い研究の質と密な交流に満足し、大変盛会でありました。国際共同利用共同研究拠点の支援に感謝します。

NIMS Award 2025 Satellite Symposium at Kyoto University
参加者の集合写真



分子集合化学研究領域

International Symposium on Atomic Level Characterizations for New Materials and Devices in Winter 2026(ALC-W’26)
実施報告書

主　催：ALC-W’26 実行委員会
共　催：京都大学化学研究所　国際共同利用・共同研究拠点
日　時：2026 年 1 月 20 日（火）～24 日（土）
場　所：新富良野プリンスホテル

International Symposium on Atomic Level Characterizations for New Materials and Devices in Winter 2026（ALC-W’26）が，2026 年 1 月 20 日（火）～24 日（土）の日程で，新富良野プリンスホテルで開催されました。本シンポジウム ALC-W は，日本表面真空学会のマイクロビームアナリシス（MBA）技術部会が主催する国際会議 International Symposium on Atomic Level Characterizations for New Materials and Devices（ALC）の冬季版国際会議として企画されました。本シンポジウムは，ヨーロッパで開催されている Symposium on Surface Science（通称 3S）や，日本では応用物理学会 薄膜・表面物理分科会の特別研究会として開催されてきた表面・ナノ科学シンポジウム（SSNS）の形式にならい，合宿スタイルで交流を深めながら最新の科学技術の情報交換をするシンポジウムです。3S も SSNS も COVID-19 のため 3 年間にわたって中断されていました。しかし，COVID-19 の終息とともに 3S が再開されたのをきっかけに，日本では装いも新たに ALC-W として昨年から再出発することとなりました。

ALC-W 第 3 回目の本シンポジウムには，国内外から 39 名が参加しました。このうち，招待講演者 19 名を含む 23 名が海外からの参加者であり，本シンポジウムが国際的にも広く認知されていることが示されました。人数を限った合宿スタイルによる本シンポジウムでは，熱心な討論が昼夜に渡って繰り広げられました。非常に質の高い最先端の研究成果の共有のみならず，国際的な人のつながりが強化され，表面・ナノ科学の新しい展開へとつながる機会になったと感じます。

最後になりましたが，本シンポジウムを開催するにあたりご支援をいただいた MBA 技術部会，京都大学化学研究所国際共同利用・共同研究拠点，日本物理学会，応用物理学会，韓国 IBS-CALDES，SPECS 様に厚く御礼を申し上げます。

文責：小野　輝男

3. 成果発表論文

紙数の都合により、目次に記載した論文の一部についてのみ、別刷りを次頁以降に掲載する。

Reprinted from *Nat. Commun.*, 17, 2660 (2026)

nature communications

Article

https://doi.org/10.1038/s41467-026-70593-y

Direct observation of cation-dependent polarisation switching dynamics in fluorite ferroelectrics

Received: 17 September 2025

Accepted: 26 February 2026

Published online: 30 March 2026

Check for updates

Kousuke Ooe[1,2] ✉, Yufan Shen[3], Kazuki Shitara[2], Rintaro Maki[3], Shunsuke Kobayashi[2], Yuichi Shimakawa[3], Daisuke Kan[3,5] & Joanne Etheridge[1,4]

Fluorite ferroelectrics are exciting candidates for next-generation non-volatile memory devices because their unique ferroelectric mechanism, which arises from unconventional oxygen displacements, permits ferroelectricity with minimal thickness constraints. However, the polarisation switching mechanism remains the subject of intense debate due to a limited understanding of the atomic-scale dynamics which are extremely challenging to detect and measure. Here, we observe directly the polarisation switching pathways by visualising oxygen site dynamics in ZrO_2 and $Hf_{0.5}Zr_{0.5}O_2$ freestanding membranes using an advanced atomic-column imaging technique—optimum bright-field scanning transmission electron microscopy. We observe that the 180° and 90° polarisation pathways involve different nonpolar intermediate states with distinct spatial scales. Coupled with density functional theory, we also reveal how different cation species in fluorite oxides impact the accessible polarisation switching pathways. Our atomic-level insights into the polarisation switching dynamics open new avenues for the advanced engineering of fluorite ferroelectric materials and resulting memory devices.

Ferroelectric materials, characterised by a spontaneous polarisation that can be reversed by an external electric field, have long been a focus of research in materials science[1]. Their unique ability to switch polarisation provides a wide range of applications, including non-volatile memory devices[2]. Traditionally, perovskite oxides such as $BaTiO_3$ and $Pb(Zr,Ti)O_3$ have been known as typical ferroelectric materials[3]. However, these materials face intrinsic limitations when scaled to nanometre dimensions; for instance, the ferroelectric properties in perovskites generally degrade at film thicknesses of tens of nanometres, which hampers further miniaturisation of memory devices[4]. In addition, the growth techniques for these materials are less compatible with complementary metal-oxide-semiconductor (CMOS) processes, due to the high temperatures required and lattice-mismatched substrates[5,6]. To overcome the limitations imposed by film thicknesses, recent studies have reported an inverse size-scaling ferroelectric transition in centrosymmetric $DyScO_3$ occurring below a critical thickness of ~5 nm, driven by surface charge transfer and symmetry breaking, as well as switchable multistate ferroelectricity in NH_3-based topotactically transformed $La_{0.7}Sr_{0.3}MnO_{3-\delta}$ with quasi two-dimensional ferroelectric layers thinner than 2 nm[7,8].

A breakthrough in the field came with the discovery of ferroelectricity in fluorite-type oxides such as HfO_2, ZrO_2, and $Hf_{0.5}Zr_{0.5}O_2$ (HZO)[9]. Unlike conventional perovskites, ferroelectricity in these materials arises from shifts of oxygen anions rather than from the displacement of cations within a crystalline structure. HfO_2, already a standard high-κ material in CMOS processes[10], demonstrated robust

[1]School of Physics and Astronomy, Monash University, Clayton, VIC, Australia. [2]Nanostructures Research Laboratory, Japan Fine Ceramics Center, Nagoya, Japan. [3]Institute for Chemical Research, Kyoto University, Uji, Kyoto, Japan. [4]Monash Centre for Electron Microscopy, Monash University, Clayton, VIC, Australia. [5]Present address: Division of Applied Chemistry, Graduate School of Engineering, The University of Osaka, Suita, Osaka, Japan.
✉e-mail: kousuke.ooe@monash.edu

ferroelectric switching in Si-doped films, as first reported by Böscke et al[11]. This discovery not only spurred extensive investigations into the fundamental mechanisms governing ferroelectricity in these systems but also highlighted their potential for enabling devices with ultrathin active layers—down to nanometre or even just a few atomic layers—thus overcoming the critical thickness limitations inherent to perovskite ferroelectrics[12].

In fluorite-type oxides, the ferroelectric phase is typically associated with a non-centrosymmetric orthorhombic structure (space group $Pca2_1$), in which displacements of oxygen ions with respect to the heavy cations (e.g., Hf and Zr) produce a net dipole moment[11]. Notably, these materials often exhibit polycrystalline structures, i.e., a texture of nanometre-sized grains with different crystalline phases, even if fabricated by an epitaxial-film growth technique such as pulsed laser deposition (PLD)[13–16], including metastable polar and nonpolar phases due to the near-degeneracy of these phases. Consequently, unveiling these crystalline structure characteristics and their transitions, and engineering polarisation switching in the ferroelectric phase of fluorite oxides is critical not only for advancing fundamental understanding but also for optimising their performance in memory applications because these dynamics are inevitably related to the wake-up and/or fatigue phenomena[12].

Scanning transmission electron microscopy (STEM) has been emerging as a powerful tool in this regard. Modern aberration-corrected STEM techniques enable direct imaging of individual atomic columns with sub-Ångström resolution, thereby providing detailed insights into the local atomic structure[17]. High-angle annular dark-field (HAADF) STEM is a common STEM imaging technique for materials characterisation that excels in visualising heavy elements such as cations, and hence is useful for detecting the cation-induced polarisation structures[18]. As for the oxygen sites, which plays a pivotal role for the fluorite-type ferroelectrics, phase-contrast-based techniques can be applied to visualise them. By means of these, recent STEM analysis of fluorite ferroelectric materials not only identified crystalline phase of individual nano-sized grains[15] but also observed polarisation structures, some of which visualised the structure evolution such as polar-nonpolar phase transition and polarisation switching triggered by an electron irradiation or electric-field biasing[19–21]. In these STEM observations, it was reported that a nonpolar tetragonal phase plays an important role as an intermediate or interfacial structure during the switching, which has also been observed by in-situ grazing incidence X-ray diffraction measurements[22,23]. However, the detailed atomic structures and dynamics of these transition pathways, including intermediate states, remain unclear, and consequently the means to selectively facilitate or suppress specific pathways to obtain the desired ferroelectric phase and polarisation switching paths remain unknown.

In this study, we unveil the atomistic pathways of 180° and 90° polarisation switching and their intermediate structures involved in the fluorite ferroelectrics. Critically, we reveal the accessible pathways to be cation-species-dependent, by comparing the atomic-structure dynamics of freestanding ZrO_2 and HZO membranes. To investigate the detailed polarisation structures and switching pathways, we employ an optimum bright-field (OBF) STEM technique[24], which can visualise both oxygen and cation sites simultaneously with high sensitivity. Our approach first demonstrates that OBF STEM can effectively visualise the local atomic structure within these membranes, resolving both the polar and nonpolar phases. Building on this static analysis, we then explore the dynamic behaviour of these atomic structures under high beam-current electron irradiation. In particular, our observations in ZrO_2 membranes reveal the 180° and 90° polarisation switching within the ferroelectric structure is mediated by reversible phase transitions between polar and nonpolar states. Furthermore, we perform a higher-speed OBF STEM data acquisition, which allows us to capture two different nonpolar intermediate structures along the 180° and 90° polarisation switching pathways, providing unprecedented insight into the transient states that occur during the switching process. We also perform the observation of an HZO membrane, shedding light on how the different atomic species of cation sites impacts the dynamic behaviour regarding the phase transition and polarisation switching. The energetic landscape governing these transitions and switching processes is elucidated by the density functional theory (DFT) calculations, complementing our experimental findings. In addition to the detailed structure evolution analysis during the phase transition and polarisation switching of ZrO_2 and HZO, our approach offers a critical guideline to engineer these dynamics and realise the advanced fluorite ferroelectrics.

Results

Visualisation of the static polarisation structure at the atomic scale

The projected atomic-structure models along the [001] zone-axis of nonpolar tetragonal (space group $P4_2/nmc$), polar orthorhombic (space group $Pca2_1$), and anti-polar orthorhombic (space group $Pbca$) phases in the fluorite ZrO_2 and HZO are shown in Fig. 1a. In the tetragonal phase, cation (Hf/Zr) sites form a cubic-like lattice along this projection and oxygen sites are located in the centre of this cation lattice, giving a nonpolar structure as shown in Fig. 1a. In the orthorhombic phase, on the other hand, the distance in the [100] direction between the tetragonal (100) and (200) cation planes alternates from narrow (2.36 Å) to wide (2.69 Å), in this projection. Moreover, in the wide layer, the oxygen site shifts off-centre within the wide cation lattice in the [010] direction, while the oxygen sites in the narrow layer remain centred. This polarisation due to oxygen shifts causes the ferroelectricity in (H)ZO (where we use (H)ZO as shorthand to refer to both ZrO_2 and HZO). These fluorite-type oxides have distinct polarised atomic layers in between oxygen-centred nonpolar spacers, making the polar domain stable even down to a single atomic layer in width[25]. In the anti-polar orthorhombic phase, the direction of the oxygen shift alternates as shown in Fig. 1a, resulting in the anti-polar behaviour.

We first analysed these features inside the (H)ZO membranes using OBF STEM. The OBF STEM technique can visualise atomic structures including both heavy and light elements with high sensitivity, making it powerful for probing the oxygen-induced polarisation structures described above. For the structure analysis of ZrO_2 and HZO, nanometre-thickness membranes were fabricated using the pulsed laser deposition (PLD) method and then transferred onto TEM specimen grids, with details described in the Method section. Figure 1b–d show the resulting experimental OBF images of each phase inside the ZrO_2 (5 and 10 nm thicknesses) and HZO (5 nm thickness) membranes, visualising both the Hf/Zr and O atomic sites. As shown in Fig. 1b, in the nonpolar tetragonal phase observed in the 5 nm ZrO_2 membrane, the higher intensity spots, which correspond to the Hf/Zr sites, are arranged in a square lattice in projection, and lower intensity spots, corresponding to the oxygen sites, are located in the centre of this square cation lattice. On the other hand, in the orthorhombic phases, the oxygen sites show a dumbbell-like elongated intensity distribution compared with the tetragonal phase and are located in the off-centred position inside the wider-spaced layers of the cation lattice as shown in Fig. 1c, d. It is also evident that the oxygen shift is aligned along one direction in the polar orthorhombic phase (Fig. 1c), which was observed in the 5 nm thick HZO membrane, whereas the oxygen shift direction alternates 180-degree in the anti-polar phase observed in the 10 nm ZrO_2 membrane (Fig. 1d). These results show that the OBF STEM technique is promising for probing the atomic-scale oxygen-triggered polarisation structures in the fluorite oxides. It is noted that recent atomic-structure investigations have revealed that perovskite oxides can also exhibit ferroelectricity due to the oxygen displacements relative to the cation sublattice despite the traditional picture of cation-induced polarisation[26], indicating that observations of the

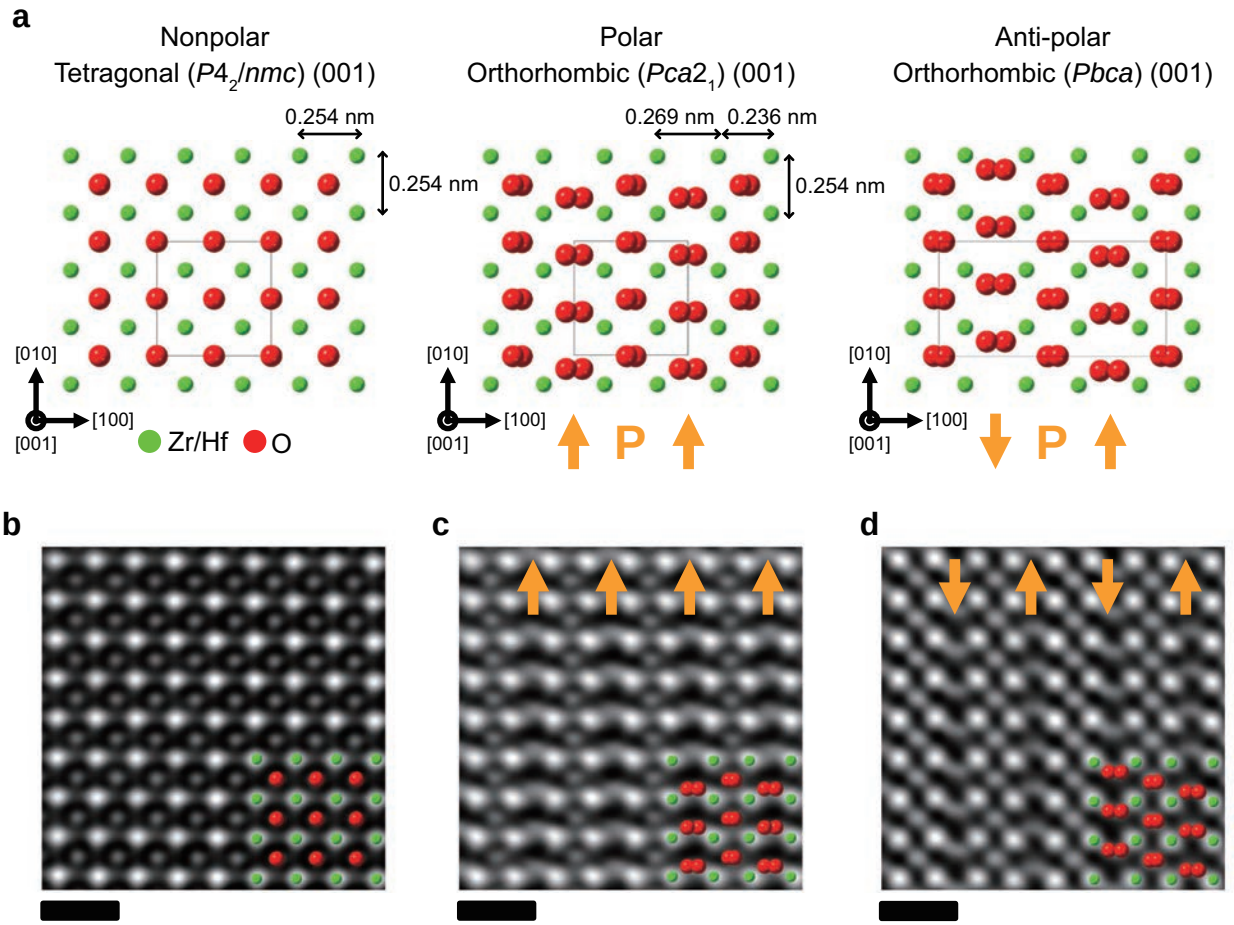


Fig. 1 | Atomic-structure model and atomic-resolution OBF STEM images of polar/non-polar phases in (H)ZO membranes. a Atomic-structure models of nonpolar tetragonal, polar orthorhombic, and anti-polar orthorhombic phases along the projection perpendicular to the (001) plane. Cation (Zr/Hf) and oxygen sites are shown as green and red spheres, respectively. The projected cation lattice distances are also shown, using values obtained from DFT calculations. Experimental OBF STEM images of (**b**) tetragonal in a ZrO_2 membrane (5 nm thick), (**c**) polar orthorhombic in a HZO membrane (5 nm thick), and (**d**) anti-polar orthorhombic phases in a ZrO_2 membrane (10 nm thick). Yellow arrows indicate the polarisation direction of each atomic layer in the orthorhombic phases. The atomic-structure models are also overlaid. Scale bar: 1 nm.

atomic displacements of both cations and anions are essential for analysing the ferroelectricity.

Reversible phase transition and polarisation switching under high electron dose illumination

In electron microscopy, electron illumination can cause dynamic structure changes inside materials such as phase transitions[27,28], grain boundary migration[29], and polarisation switching[30]. In the case of fluorite ferroelectric materials such as (H)ZO, it is reported that electron irradiation can trigger the phase transition and/or polarisation switching[19]. Observing these structure evolutions and their transition pathway at the atomic scale is critical for understanding the ferroelectric mechanism and how it might be manipulated and optimised for practical applications. Here, we use OBF STEM with a high illumination beam current to capture the dynamic behaviour of our ferroelectric membrane sample at the atomic-scale, where a mechanism to induce these dynamic events via the electron beams is discussed in the Supplementary Note 4. In typical STEM measurements, such as shown in Fig. 1, the electron beam current is around 10-20 pA. Here, we deliberately use a 100 pA probe current to stimulate the phase transition and record as a movie, a sequence of images from the same field-of-view (FOV). We have confirmed a clear threshold of the beam current to trigger the dynamics, providing a strategy to choose the proper current for the experiments performed in the present study as shown in Supplementary Note 6.

To establish a baseline, we first use a relatively low probe current of 15 pA. Figure 2a, b shows the corresponding OBF STEM image of the nonpolar tetragonal grain of the 5 nm thickness ZrO_2 membrane, as discussed in Fig. 1. We obtained thirty images sequentially with a scanning speed of 500 ns/pixel with a 2048 × 2048 pixels scan (equivalent to three seconds per frame or 0.33 frames per second) from the same field-of-view, resulting in 2.7×10^3 $e^-/Å^2$/frame as a total dose per area. We then averaged these images after aligning them to correct for stage drift. During the sequential acquisition, the tetragonal grain retained its original atomic arrangement as shown in Supplementary Movie S1, indicating that the electron irradiation at 15 pA did not change the atomic structure.

We then increased the probe current to a high current of 100 pA by changing monochromator focus value only (while keeping all other electron-optical parameters and resultant observation condition the same) and obtained another image sequence from the same initially tetragonal grain observed above, with results shown in Fig. 2c–e. Here, the electron dose per area was also increased to 1.8×10^4 $e^-/Å^2$/frame. At 69 s, the tetragonal grain changed into the orthorhombic phase that has polarised oxygen shifting off centre relative to the cation lattice along the tetragonal [010] direction,

https://doi.org/10.1038/s41467-026-70593-y

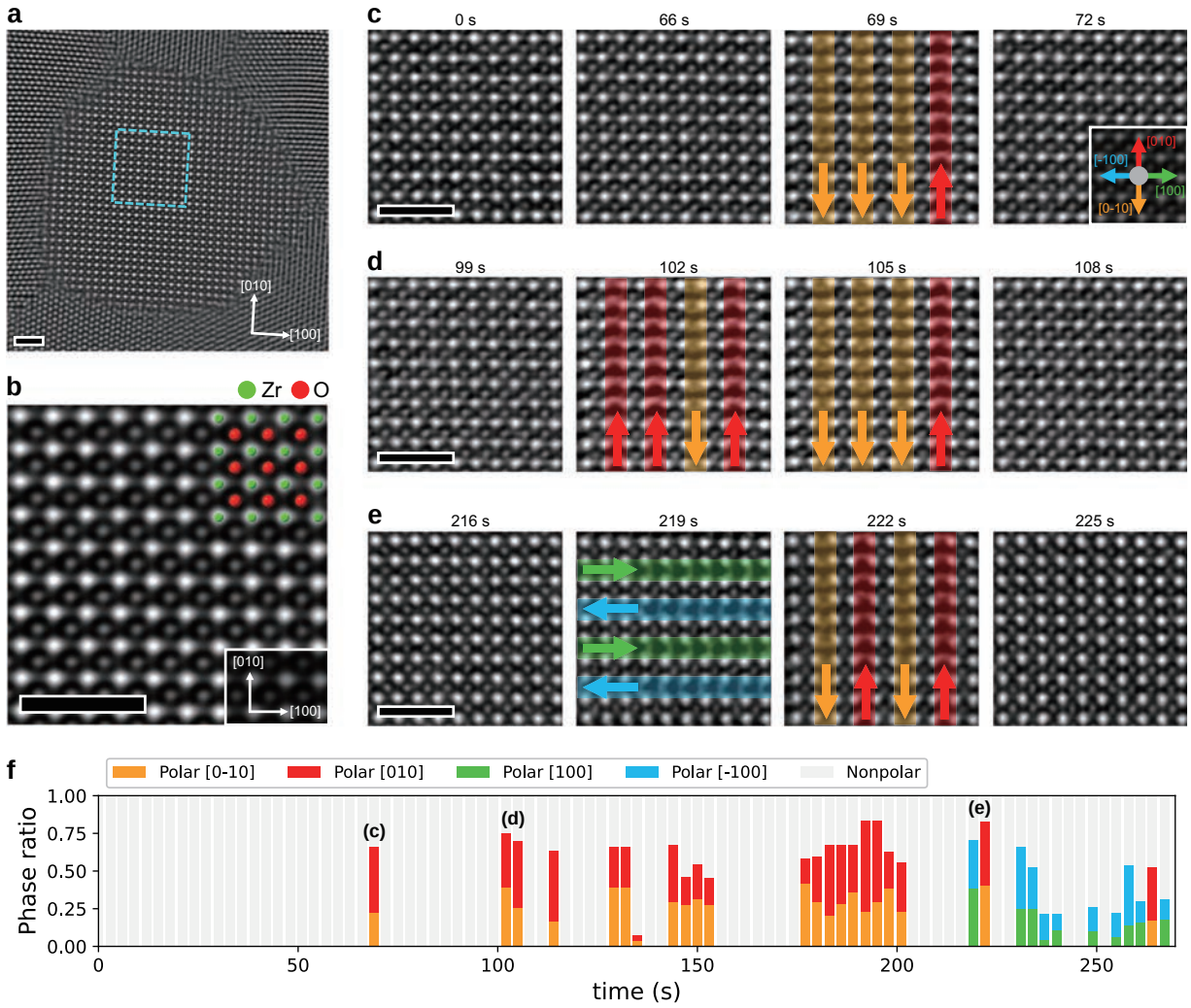


Fig. 2 | Direct observation of reversible phase transition and polarisation switching in ZrO_2. a OBF STEM image of a tetragonal grain in the ZrO_2 membrane. Scale bar: 1 nm. **b** OBF STEM image obtained by cropping and magnifying the cyan-dotted rectangular region shown in (**a**). The atomic-structure model is overlaid. Scale bar: 1 nm. Sequentially obtained OBF STEM images which show (**c**) (0–72 s) the phase transition between tetragonal and orthorhombic phases, (**d**) (99–108 s) 180-degree polarisation switching, and (**e**) (216–225 s) 90-degree polarisation switching. The time count is set so that the first image acquisition is 0 s just after increasing the probe current to 100 pA. Scale bar: 1 nm. **f** Time-series showing the ratio of the nonpolar and polar phases in the whole nanocrystal. Yellow, red, green and blue bars indicate the ratio of the phase polarised along [0–10], [010], [100], and [–100] directions, respectively. The relationship between the colours and the directions are also indicated in the right-hand side panel of (**c**). The nonpolar tetragonal phase is shown as grey bars. The events shown in (**c**–**e**) are highlighted on this timeline.

which is evident in the OBF STEM image (see also Supplementary Movie S2). After an extra scan, this structure changed back to the original tetragonal structure reversibly.

After several scans taking a further ~30 s, the tetragonal grain changed back to an orthorhombic phase (at 102 seconds), however, this time the polarisation structure is still along tetragonal [010] direction but has different polarisation ordering from what was observed in Fig. 2c. After a further beam exposure (at 105 s), this grain remained in the orthorhombic phase but a 180-degree polarisation switching occurred in the two leftmost atomic layers shown in Fig. 2d. Before and after this polarisation switching, the arrangement of the cation lattice remained unchanged, but the oxygen sites are shifted locally relative to the Zr cation lattice. After an additional scan, this orthorhombic phase changed back to the tetragonal phase reversibly, with the oxygen located at the centre of the cation lattice. As shown in the Supplementary Movie S3, the 180-degree polarisation switching and phase transition between tetragonal and orthorhombic phases were observed multiple times and were reversed in the subsequent scans.

After additional electron exposure, 90-degree polarisation switching also started to be triggered as shown in Fig. 2e and Supplementary Movie S4. The grain had a tetragonal atomic structure at 216 s and then, after a single scan, became a polarised orthorhombic structure where the oxygen sites are shifted in the tetragonal [100] direction with reference to the cation sites (horizontal direction in the figure orientation). At 222 s, the orthorhombic structure has changed into an orthorhombic structure polarised along tetragonal [010] direction, showing a different type of switching path from previous results. As discussed in Fig. 1, the polar orthorhombic structure has a uniform cation-cation distance along the polarisation direction and alternately wide and narrow distances perpendicular to it. During this 90-degree switching process, not only the oxygen sites but also the cation sites change their positions, requiring a larger shift of the atomic positions than that required in the 180-degree switching. The

distinct change of cation lattice spacing and resulting lattice strain are also confirmed by the lattice strain measurement based on the simultaneously obtained ADF images as described in Supplementary Note 2. Here it is clearly visualised that the orthorhombic phase has two different sublattices strained alternately perpendicularly to the polarisation direction, while the tetragonal phase has uniform strain distributions. Furthermore, it is visualised that the grain contains the tetragonal phase near the perimeter of the grain despite the bulk area having transformed to the orthorhombic phase in ZrO_2. This is confirmed via the oxygen position determined approximately from OBF STEM images and strain distribution determined from the ADF STEM images, as shown in Supplementary Figs. S3 and S5.

From the time-series of OBF STEM images, a ratio of the volume of polar and nonpolar phases within the whole ZrO_2 nanocrystal was also counted as a function of time, as shown in Fig. 2f. It can be seen that the initially tetragonal nanocrystal takes some time, (i.e. accumulated electron dose), before the first reversible phase transition between tetragonal and orthorhombic phases occurs (Fig. 2c) and further time/dose for the first 180-degree switching event to occur (Fig. 2d) and even further time/dose for the 90-degree switching events to occur, as discussed above. This suggests qualitatively that the activation energy required is lowest for the tetragonal to orthorhombic phase transition, higher for the 180-degree switching event and highest for the 90-degree switching event.

We also performed this (non)polar-phase-ratio statistical analysis under higher-dose electron illumination over several ZrO_2 grains, as shown in Supplementary Fig. S8, and find the dynamic behaviour and frequency of the switching events are consistent with what was shown in Fig. 2 (see Supplementary Note 5 for details). It has been observed by Lomenzo et al using band-excitation piezoresponse force microscopy (BE-PFM), that the nano-sized grains in ZrO_2 independently undergo the reversible tetragonal-orthorhombic phase transition under applied electric field, which is responsible for the anti-ferroelectric nature of ZrO_2 such as the double hysteresis loop in the P-E measurement[31]. Given the switching observed in the present study is also driven by an electric field induced by electron irradiation (see the Supplementary Note 4), it can be said that the reversible phase-transition and switching events visualised here at the atomic-level, provide a direct atomic-scale counterpart to the electric-field-driven dynamics reported in the literature using BE-PFM. We also demonstrate how the switching dynamics can be manipulated via different electron-probe scanning strategies as discussed in Supplementary Note 6. Unconventional scan patterns and/or electron dose modulation using a high-speed electrostatic beam-blanker, beyond the uniform raster scan of the STEM probe, may allow for the further manipulation of switching dynamics[32–34].

Intermediate structures during the polarisation switching

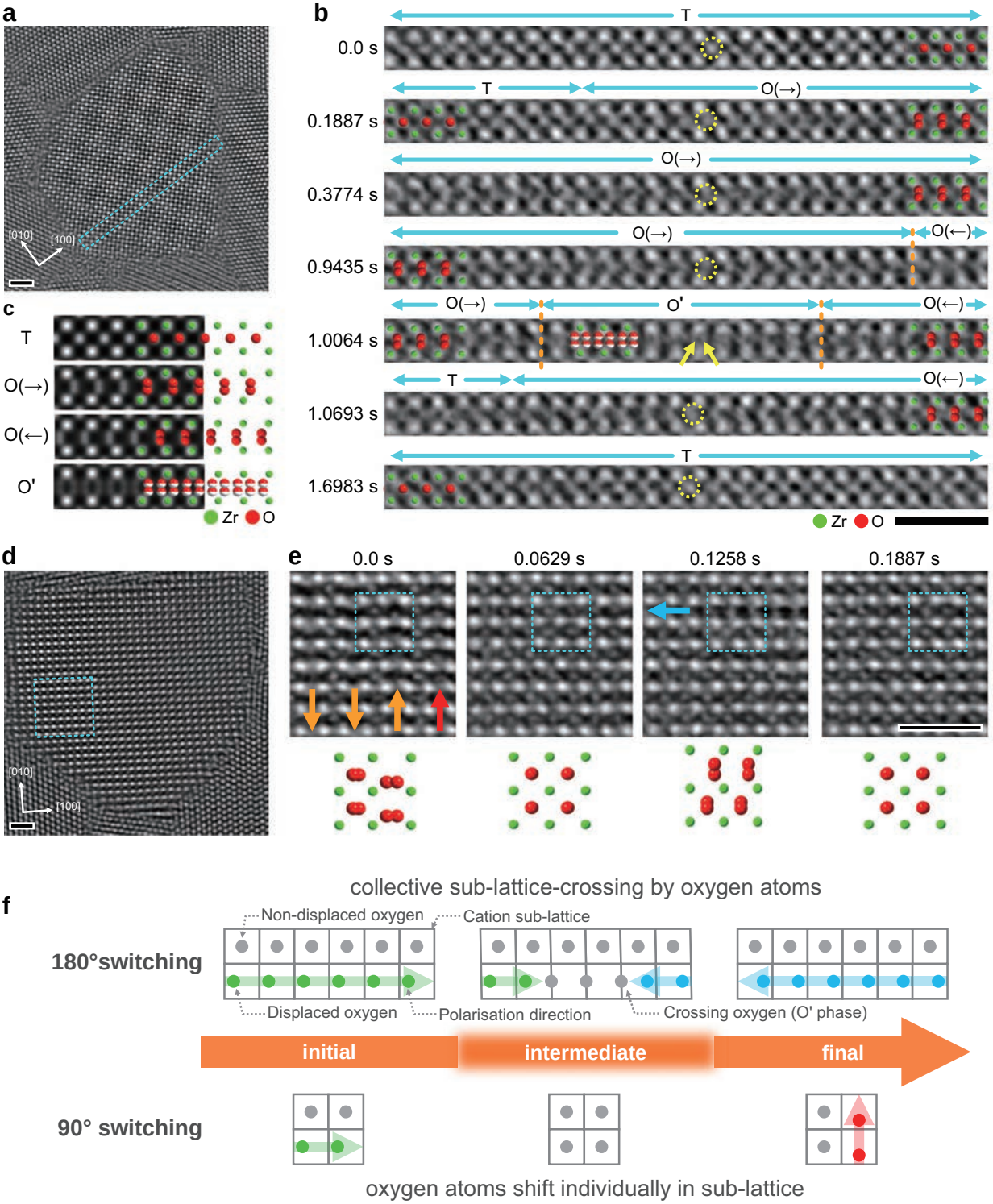
In the previous section, we observed reversible phase transitions and polarisation switching in the ZrO_2 membrane by means of OBF STEM with a high probe current. To provide a detailed understanding of the polarisation switching pathway, we performed OBF STEM measurements with a higher-speed scan. With a scan speed of 200 ns/pixel and sampling of 512 × 512 pixels, we obtained sequential OBF images at 0.0629 seconds/frame or 16 frames-per-second. Figure 3a shows the tetragonal grain observed under an initial 15 pA probe current illumination (5.5×10^2 $e^-/Å^2$/frame), which shows the nonpolar oxygen-centred atomic configuration consistent with the result shown in Fig. 2a. We focus on the single atomic layer along the tetragonal [100] direction as highlighted by the cyan dotted rectangular in Fig. 3a.

Following the initial low current OBF STEM image of the tetragonal grain, we increased the illumination current to 150 pA (5.5×10^3 $e^-/Å^2$/frame) and took a higher-speed time-series OBF STEM images. Figure 3b and Supplementary Movie S5 show the sequence of OBF STEM images, focusing on the single atomic layer inside the grain, where a more extended field-of-view is shown in the Supplementary Note 10. As observed in the lower probe current (15 pA) condition, the layer shows the tetragonal structure at 0.0 s. At 0.1887 s, while the atomic layer mostly has the tetragonal structure, it can be seen that some of the oxygen sites in the right-hand side have started to shift away from the centre of the cation lattice, showing a mixture of the two phases (see Supplementary Fig. S12 for details). It is noted that the oxygen-site displacements with respect to the Zr sites can be clearly observed by intensity line profiles of the OBF images as discussed in Supplementary Note 7. At 0.3774 s, the oxygen sites have shifted completely in one direction parallel to tetragonal [100] and the atomic layer has changed to the polarised orthorhombic structure as observed in previous sections. After nine scans (at 0.9435 s), the oxygen sites on the right-hand side of the layer started to shift in another direction along tetragonal [−100] whereas the left-hand side of the layer still shows the polarisation toward the [100] direction. After a further scan (at 1.0064 s) the left polarised domain propagated into the left-hand direction. Here, the area between the right- (O(→)) and left- (O(←)) polarised domains has a transient atomic structure (O′) during the 180-degree polarisation switching, where the image intensity at the oxygen site is lower than that of the polar orthorhombic phase and distributed either side of the vertical tetragonal (100) and (200) planes of the cation lattice.

During the 180-degree domain switching in the fluorite oxide materials such as (H)ZO, it has been suggested that the domain wall has a nonpolar interlayer between two oppositely polarised domains, which has orthorhombic *Pbcm* structure for the head-to-head boundary and tetragonal $P4_2/nmc$ structure for the tail-to-tail boundary[35]. To investigate this, we compare our experimental OBF STEM images with simulated images of nonpolar tetragonal, polar orthorhombic (polarised to right and left directions respectively), and non-polar orthorhombic phase (space group *Pbcm*) within single layers, where the polarised oxygen shift occurs when the structure has polar phase, as shown in Fig. 3c. In the crystallography literature, the nonpolar orthorhombic *Pbcm* structure in fluorite-type materials is considered as a mixture of disordered domains of ferroelectric $Pca2_1$ phase with two opposite polarisation directions, providing a centrosymmetric and nonpolar phase as an average whose oxygen sites are split into two half-occupied sites distributed either side of the cation planes, as shown in Fig. 3c[36,37]. In some theoretical calculations of the switching pathway, the *Pbcm* structure is assumed to have non-split oxygen sites located in a straight line with the cation planes[35,38]. Instead, we employ the former *Pbcm* structure due to its better description of what was observed in the OBF image. Here, in contrast to the tetragonal and polar orthorhombic phases, in the nonpolar orthorhombic *Pbcm* structure, the oxygen site splits into two sites with a half occupancy (shown as half-red and half-white spheres in the structure model)[39], appearing as even lower intensity spots in the simulated OBF image. The experimental OBF image at 1.0064 s shown in Fig. 3b corresponds approximately to the simulated intensity distribution for the nonpolar orthorhombic phase around the head-to-head domain boundary region. After another scan (at 1.0693 s) the left-polarised domain extends into the left-hand side of the layer and a few oxygen sites at the left edge of FOV show diffuse but centred intensity, which is interpreted as the mixture of T and O phases similar to what was observed at 0.1887 seconds. At 1.6983 seconds this atomic layer turns back completely to the tetragonal phase, where the oxygen sites are located in the centre of the cation lattice. This result shows that the oxygen site is bridging across the cation lattice plane for the 180-degree switching via the nonpolar orthorhombic *Pbcm* phase.

We next show higher-speed OBF STEM imaging of 90-degree polarisation switching. Figure 3d shows another tetragonal grain in the same ZrO_2 membrane, whose atomic structure was identified by low probe current OBF STEM imaging. This grain first showed 180-degree domain switching after increasing the probe current and then started

https://doi.org/10.1038/s41467-026-70593-y



90-degree switching subsequently as also shown in Fig. 2e. Figure 3e shows the time-series of 90-degree switching, starting from the vertically polarised structure, whose time is counted as the 0.0 second frame (see also Supplementary Movie S6). In this image, the oxygen sites are shifted along the tetragonal [010] direction (vertically with respect to the cation sites). In the next scan (0.0629 s), these oxygen sites are shifted to the centre of cation lattice, showing the tetragonal phase. At 0.1258 seconds, the oxygen site within a single layer has shifted to the [100] direction (right-hand side), showing the locally left-polarised orthorhombic phase within that monolayer. After another scan at 0.1887 seconds, oxygen sites within the same layer shifted back to the centre of the cation lattice, corresponding to the tetragonal phase again. We illustrate this sequential structure evolution as a series of atomic-structure models below each OBF STEM image, corresponding to the region in the cyan dotted box as highlighted in Fig. 3e. This result shows that the oxygen sites are moving around inside the cation sublattice during the 90-degree polarisation switching: the shifted oxygen sites within the polar orthorhombic phase move to the

Fig. 3 | Observations of intermediate structures during the 180- and 90-degree polarisation switching in ZrO_2. **a** OBF STEM image of a tetragonal grain obtained under the initial lower probe current (15 pA). Scale bar: 1 nm. **b** Time-series of OBF STEM images taken with higher probe current (150 pA), probing the 180-degree switching (16 fps or 0.0629 seconds/image). Each frame is cropped from the region indicated in (**a**). The assigned phases are tetragonal (T), right-polarised orthorhombic (O(→)), left-polarised orthorhombic (O(←)), and nonpolar orthorhombic (O'), respectively. The domain wall between O(→) and O(←) is highlighted by dotted orange lines. Structure models are overlaid, and one of the oxygen sites is highlighted with yellow-dotted circles or arrows. Scale bar: 1 nm. **c** Simulated OBF STEM images of each phase observed in (**b**) with overlaid structure models, where green and red spheres represent Zr and O sites, respectively. The half-red and half-white spheres indicate the O sites with a half occupancy. **d** OBF STEM image of another tetragonal grain obtained under the initial lower probe current (15 pA). Scale bar: 1 nm. **e** Time-series of OBF STEM images, probing the 90-degree polarisation switching. Frame rate and probe current illumination are the same as (**b**) and each frame is cropped from the area highlighted in (**d**). The polarisation directions are indicated by coloured arrows. Schematics of atomic structures are also shown for each frame, corresponding to the area featured in (**e**). Scale bar: 1 nm. **f** Schematic of the structure evolution for 180- and 90-degree switching, which is divided into initial, intermediate, and final structures, showing the different intermediate phases. Grey boxes indicate cation sublattices of the orthorhombic and tetragonal phases. Coloured dots and arrows specify the displaced oxygen sites and their polarisation direction. Nonpolar oxygen sites are denoted with grey dots, which indicate the nonpolar phase with oxygen sites centred in the cation lattice (e.g., tetragonal phase and nonpolar spacer layer in orthorhombic phase) and the nonpolar O' phase observed in (**b**).

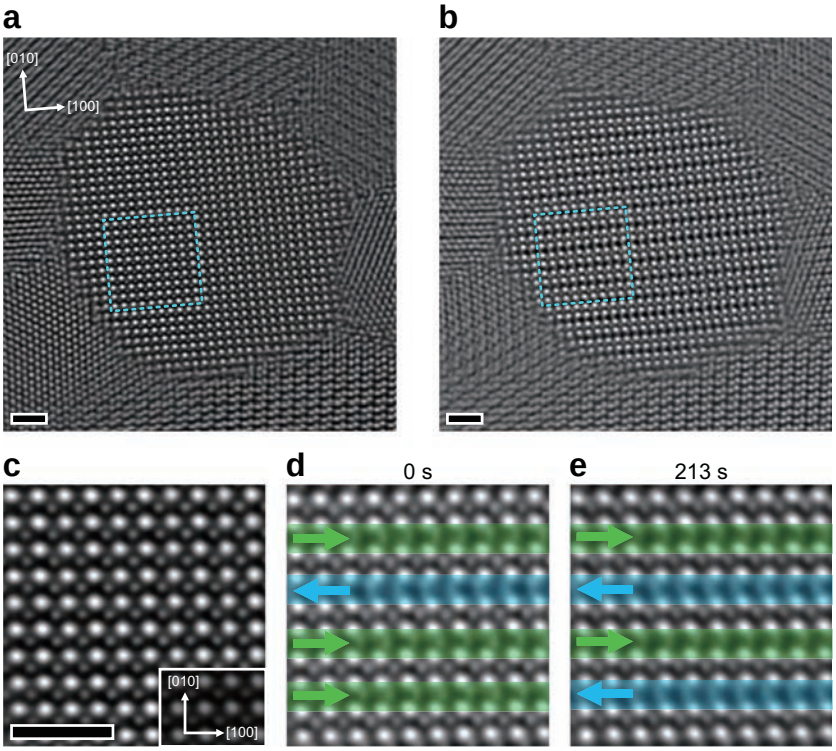


Fig. 4 | Observation of non-reversible phase transition and polarisation switching in an HZO membrane. **a** OBF STEM image of a tetragonal grain in the HZO membrane. **b** OBF STEM image of the polar orthorhombic phase observed in the same grain as (**a**) just after increasing the probe current into 100 pA. **c**, **d** Cropped and magnified OBF STEM images obtained from the cyan dotted area in (**a**, **b**), respectively. Polarisation directions are indicated by coloured arrows. **e** OBF STEM image cropped from the same area as (**c**, **d**) after 213 s electron illumination with the 100 pA probe current. Scale bars: 1 nm.

centre, and then shift perpendicularly to the other side, indicating that the 90-degree switching occurs via the nonpolar oxygen-centred tetragonal phase.

From these results, our OBF STEM observations show that the oxygen site behaves differently between the 180- and 90-degree domain switching via distinct nonpolar intermediate states, as shown schematically in Fig. 3f. In the case of 180-degree switching, several oxygen sites collectively cross the cation lattice plane and form the nonpolar intermediate phase which extends across a few nanometres. In contrast, in the case of the 90-degree switching, each oxygen site is confined and moves locally within the individual cation sublattice.

Effect of different cation species

We observed the polarisation switching pathways in the pure ZrO_2 membrane in the previous sections. In addition to the ZrO_2, ferroelectric fluorite oxides with other cation species are of significant interest because the other cation species may modify the ferroelectric properties[11,40], with the potential to engineer advanced ferroelectric devices. Here we compare ZrO_2 with a HZO membrane, which is a well-known and promising ferroelectric material. In this material, the Hf and Zr are occupying cation sites, which can be considered as a binary of ZrO_2 and HfO_2, exhibiting robust ferroelectricity with a stable orthorhombic phase[41].

We first obtained an OBF STEM image of a tetragonal grain in the HZO membrane with a lower probe current of 15 pA, which is shown in Fig. 4a. As well as the ZrO_2 membrane, the oxygen sites are located at the centre of the cation lattice, showing the nonpolar structure. We then repeated the higher probe current experiments using the same approach and experimental conditions used for the ZrO_2 membrane. However, after increasing the probe current to 100 pA, the tetragonal grain immediately changed into the polar orthorhombic phase with just a single scan (denoted as 0 second). Furthermore, unlike the ZrO_2

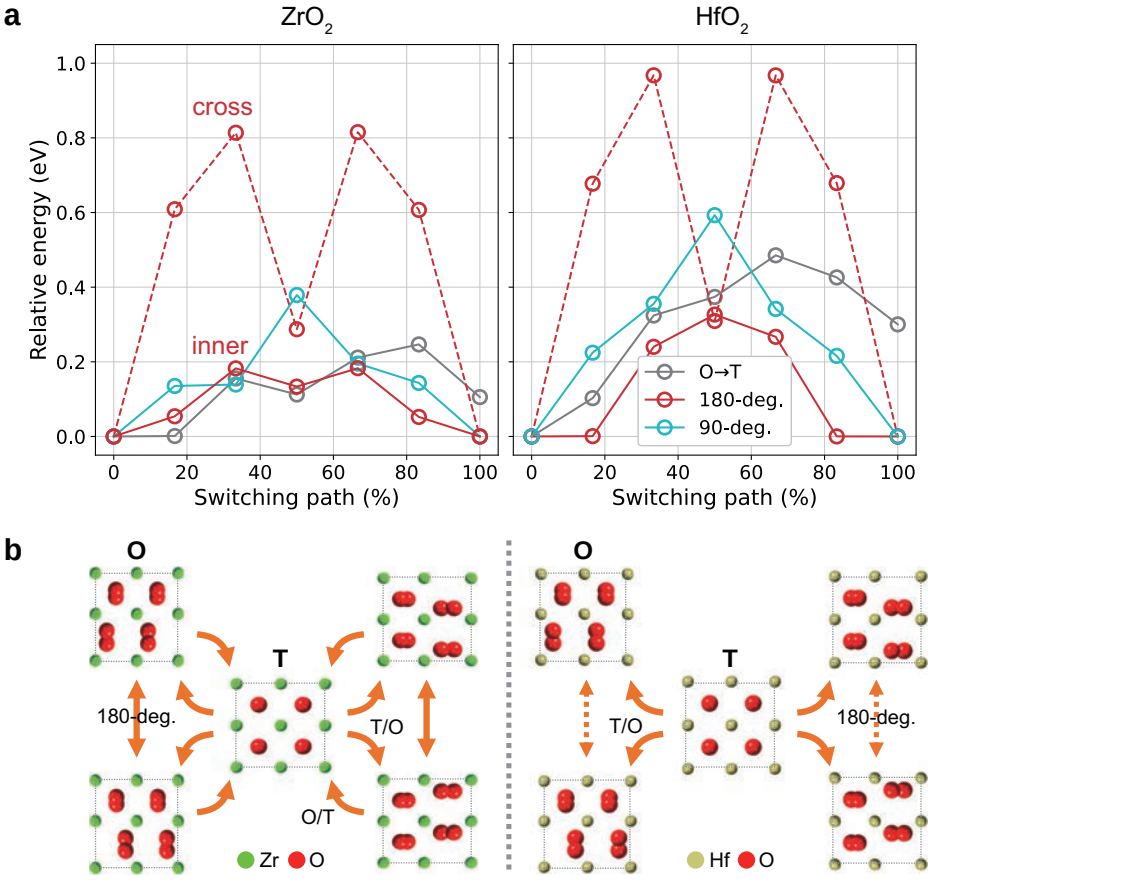


Fig. 5 | DFT-calculated energy landscapes of phase transition and polarisation switching in ZrO_2 and HfO_2. a Energy diagrams of O → T phase transition, 180-degree polarisation switching, and 90-degree polarisation switching in ZrO_2 and HfO_2. Two types of pathways are calculated for 180-degree switching, namely cross-type and inner-type. **b** Schematic diagram showing the possible transition pathways between nonpolar tetragonal phase and polar orthorhombic phases along four different polarisation directions. The dotted arrows in HfO_2 indicate the possible but relatively rare pathway.

membrane, the orthorhombic phase did not change back to the tetragonal phase, nor was 180-degree polarisation switching observed even after more than 200 s of irradiation with 100 pA probe current. At 213 seconds, we observed a 180-degree switching of just a single atomic layer. However, phase transitions back to the tetragonal phase and 90-degree switching were not observed. This result indicates that the reversible nature of the phase transition between nonpolar tetragonal and polar orthorhombic phases is absent in the HZO membrane (at least under this illumination condition). In terms of the polarisation switching, the 180-degree type can still occur but even this is rare compared with the pure ZrO_2 membrane, and the 90-degree switching and the phase transition to tetragonal phase did not occur at all. This switching property was consistent over multiple grains as discussed in Supplementary Note 8, showing the robustness of the ferroelectric phase in HZO.

In addition to the HZO, we also performed observations of a Y-doped HfO_2 ($Hf_{0.93}Y_{0.07}O_2$; HYO) membrane. To a tetragonal grain in the HYO specimen, we illuminated with electron beams following the same procedure as the ZrO_2 and HZO. However, despite a much longer exposure time of 810 s with the 100 pA beam current, the tetragonal phase did not show a phase transition, nor did it change with a beam current of 200 pA, as described in Supplementary Note 9. This demonstrates a higher phase stability of the tetragonal phase in HYO compared with ZrO_2 and HZO.

Energetic landscape of structural transitions

Transition between nonpolar tetragonal and polar orthorhombic phases. To clarify the different structural behaviour of the two membranes, ZrO_2 and HZO, under electron irradiation, we performed density functional theory (DFT) calculations. As summarised in Fig. 5a and Table 1, we calculated the relative energy of the tetragonal phase with respect to the orthorhombic phase in ZrO_2 and HfO_2, and the energy barrier to polarisation switching and phase transitions in both materials. It is technically difficult to evaluate the energy landscape of HZO with DFT calculations due to the likely random arrangement of Hf and Zr on the cation site and the periodicity constraints of the calculation. Hence, we calculated energies for pure ZrO_2 and HfO_2 to obtain insights into HZO, which can be considered as a mixture of ZrO_2 and HfO_2[41]. As shown in Fig. 5b, we also schematically summarise the transition/switching pathways accessible in the ZrO_2 and HfO_2 membranes by indicating which path can be triggered in each material as per the following discussion. As shown in Table 1, the relative energy of the tetragonal phase with respect to the orthorhombic phase of HfO_2 is higher than that of ZrO_2, indicating that the tetragonal phase is more unstable in HfO_2. As shown in Fig. 5a and Table 1, whereas the energy barrier of the phase transition from tetragonal to orthorhombic is comparable between ZrO_2 and HfO_2, the barrier from orthorhombic to tetragonal shows a much higher value for HfO_2 than for ZrO_2. These results agree well with the experimental OBF STEM observations: the phase transition between these two phases was observed to be reversible in ZrO_2 but irreversible in HZO, that is, in HZO the tetragonal phase can transition to the orthorhombic phase but not vice versa. The difference in the phase stability is also manifested by the distinct lattice-strain distributions of ZrO_2 and HZO as discussed in the Supplementary Note 2. This result corresponds to

Table 1 | DFT-calculated energy barriers of phase transition and polarisation switching in ZrO_2 and HfO_2

	Energy (eV)	
	ZrO_2	HfO_2
Relative energy of T phase w.r.t. O phase	0.11	0.30
T → O phase transition barrier	0.14	0.19
O → T phase transition barrier	0.25	0.49
180-degree switching barrier	0.18 (inner) 0.82 (cross)	0.34 (inner) 0.97 (cross)
90-degree switching barrier	0.37	0.59

Relative energy of T phase to O phase, energy barrier of 180-/90-degree polarisation switching and O → T/T → O phase transition in ZrO_2 and HfO_2 evaluated by NEB method in DFT calculations.

our previous findings that the HZO membrane with a 5 nm thickness mostly has orthorhombic grains while the ZrO_2 membrane mainly has tetragonal grains, even though both films have approximately the same thickness[13,14].

While a polar-nonpolar phase transition between the tetragonal and orthorhombic phases is investigated in the present study, a phase transition from the orthorhombic to a nonpolar monoclinic phase has been reported in the ZrO_2 during electron irradiation in the literature[20]. In that case, a lattice-deformation process and ferroelasticity play a critical role in attaining the reversible polar-nonpolar phase transition. It is also observed that the monoclinic structure in the HfO_2 can have a polarised structure in the presence of twin defects without breaking centrosymmetry[42].

180-degree polarisation switching. For the 180-degree polarisation switching, we observed that the oxygen sites shifted by crossing the cation lattice planes. In the literature describing DFT calculations, two mechanisms are suggested for the 180-degree switching, namely the crossing pathway and the inner pathway[43]. We therefore also calculated the energy diagram of these two paths using the nudged elastic band (NEB) method, which is able to evaluate the ferroelectric transition pathway[44]. In the crossing pathway, the oxygen sites cross between the cation atoms in the (100) and (200) cation lattice planes. Whereas in the inner pathway, the oxygen sites pass through the centre of the cation lattice. From the energy diagram and barrier of the two 180-degree switching mechanisms shown in Fig. 5a, though the minimum energy levels in the middle (50%) of switching paths are comparable for both types, the energy barrier of the crossing pathway is much higher than that of the inner pathway in both ZrO_2 and HfO_2. Our calculations are based on the bulk model, where the calculated structure is periodic and atomic shifting occurs everywhere simultaneously in the bulk. On the other hand, calculations in the literature using the domain wall model, where the large atomic cell is prepared and polarisation switching occurs locally within a single atomic layer, show that the crossing pathway has a lower energy barrier than that for the bulk model[35,43]. It can be said that the energy barrier can be lowered by taking an aperiodic structure locally around the domain wall to initiate the polarisation switching.

In our bulk-model based calculations, we also made a comparison between the two crossing-type pathways with and without a symmetry constraint, as shown in Suppl Figure S6, where the one without symmetry has been employed for Table 1. In the presence of a symmetry constraint, the two oxygen sites, which are visible along the projection direction along [001] in the polarised layer, pass through the cation lattice at the same time, whereas without the symmetry constraint, the oxygen sites pass through one-by-one as seen in the NEB calculation. This indicates that the transient structures during the switching can relax by taking lower-symmetry structures, particularly regarding switching oxygen sites. According to the above discussion, the experimentally observed 180-degree switching shown in Fig. 3b can be interpreted as follows; the oxygen sites passed through the cation lattice one-by-one to lower the energy barrier and this oxygen configuration may be non-uniform along the [001] (film thickness) direction as the oxygen sites are distributed in a disordered manner in the nonpolar *Pbcm* structure[36], making the depth-projected oxygen sites look similar to the O' phase with half-occupied oxygen sites as shown in Fig. 3c. It is noted that there is likely to be native oxygen vacancies in the specimen observed in our study. Recent quantitative analysis via multislice electron ptychography reported that the oxygen sites near the 180-degree domain wall in ferroelectric ZrO_2 may have a non-stoichiometric (i.e., excess or deficient) occupancy to compensate for bound polarisation charges at the domain wall[45], suggesting that the switching and domain wall propagation can promote a migration of oxygen ions.

90-degree polarisation switching. For the 90-degree polarisation switching in ZrO_2, the energy barrier and whole energy diagram show higher values than those of the O → T transition, indicating that the direct 90-degree switching is not energetically preferred and this switching occurs via the O → T transition as observed in the OBF STEM experiment (Fig. 3e), which is also consistent with the STEM observation and DFT calculation in the literature[46]. In the presence of Hf, 180-degree switching has a higher energy barrier than that of ZrO_2 for both inner- and cross-types as shown in Fig. 5 and Table 1. Moreover, 90-degree switching also has a higher barrier as well as the O → T phase transition, which makes the 90-degree switching less favourable even via the tetragonal phase in HfO_2. These DFT results are consistent with the experimental results which show that the HZO membrane has less frequent 180-degree switching than that in ZrO_2, and the 90-degree switching was not observed at all.

Effect of different cations in fluorite ferroelectrics. Our results indicate that different cation species and/or dopants may substantially affect the switching behaviour and stability of the ferroelectric phases in fluorite oxide materials. In the case of (H)ZO, DFT calculations suggest that the ionic radius of Hf and Zr cations, and the bonding between them and oxygen, may be an important factor: Hf (76 pm) has a smaller ionic radius than Zr (78 pm)[47], resulting in smaller lattice constants of HfO_2 compared with ZrO_2[48], which is also confirmed in our DFT calculations (Supplementary Table S1). In addition, it is evaluated that the Hf-O bonding is stronger than that of Zr-O by the difference of their cohesive energy[49], whereby the oxygen sites are less constrained by a softer bonding within a larger cation lattice in ZrO_2 compared with HfO_2, making it easier for oxygen ions to shift when switching in ZrO_2[38]. In the same way, other species of dopant such as Si, Y, and La at cation sites may also alter the stability of each phase and corresponding switching behaviour as the switching barrier is engineered by the strength of chemical bonds in molecular-type ferroelectrics[50].

In the case of Y doping, for example, we have observed that a tetragonal phase is very stable and the switching events are not triggered despite applying significantly higher beam currents for a longer time than for the ZrO_2 and HZO, as shown in Figure S14. This is a significant difference when compared with the reversible phase transition between tetragonal and orthorhombic phases observed in ZrO_2 and the irreversible and immediate phase transition from tetragonal to orthorhombic phases observed in HZO. When comparing the behaviour of HYO, ZO and HZO, we must consider the cation valency. Whereas Hf^{4+} and Zr^{4+} ions are both tetravalent, Y^{3+} is a trivalent cation and is accompanied with an oxygen vacancy when doped into HfO_2 or ZrO_2. In the field of structural materials that need better hardness

properties, it is well known that Y-doping and resulting oxygen vacancies stabilise the high-temperature phases such as tetragonal and cubic structures in the fluorite ceramics[51]. On the other hand, it has also been reported that the charged oxygen defects stabilise not only these nonpolar phases[52] but also the ferroelectric orthorhombic phase[53,54]. Which crystalline phase can be stabilised sensitively depends on the concentration of the dopant and oxygen vacancies[40,55,56], where the available dopant concentration window is much narrower than that in the HZO[41]. It is also noted that acceptor-donor co-doping via trivalent and pentavalent cations (such as La^{3+} and Ta^{5+}) is also reported to be able to balance robustness of the ferroelectricity and the switching speed[57]. Our experimental result regarding the HYO specimen, which are quite different from ZrO_2 and HZO, suggests that the valency and oxygen vacancy also play a crucial role in modifying the accessible phase and dynamics.

Our results highlight the pivotal role of the cation species in tuning the hardness of ferroelectricity in fluorite oxides, whereby targeted doping and/or cationic composition may realise a more desirable (e.g., more energy-efficient yet durable) switching response critical for next-generation ferroelectric devices.

Discussion

Using the OBF STEM technique, we observed directly the evolution of atomic structures during electron illumination in nanometre-thick ZrO_2 and $Hf_{0.5}Zr_{0.5}O_2$ (HZO) freestanding membranes, revealing at the atomic level the dynamics of polar-nonpolar phase transitions and polarisation switching. Importantly, we find this to be cation dependent. In the ZrO_2 membrane, it was observed that the nonpolar tetragonal phase can be reversibly transformed into the polar orthorhombic phase, where the time-series OBF STEM datasets allowed us to visualise reversible 180- and 90-degree polarisation switching. Furthermore, we clarified the detailed switching pathways by combining higher-speed scanning with OBF STEM: 180-degree polarisation switching occurs via a nonpolar orthorhombic domain wall, while 90-degree switching is facilitated by the nonpolar tetragonal phase, where the dynamic displacement of the oxygen site plays a critical role. Applying the same observation scheme to a $Hf_{0.5}Zr_{0.5}O_2$ (HZO) membrane and complementing the experiments with density functional theory (DFT) calculations, it was revealed that the presence of Hf cation impacts the stability of polar/nonpolar phases and the energy barriers to the phase transition and polarisation switching—rendering the polar orthorhombic phase more energetically favourable in HZO because of the presence of Hf. We note that the tetragonal-phase-mediated 90-degree polarisation switching has been reported in a previous STEM study of ZrO_2[46]. In the present work, together with the 90-degree polarisation switching, we also reveal dynamic 180-degree polarisation switching. Moreover, we uncover the distinct intermediate atomic structures involved in the 180- and 90-degree switching transitions and show how they differ, both structurally and energetically, at the atomic scale. We demonstrate qualitative control over the frequency and prevalence of these transitions by adjusting electron dose. Furthermore, we show this can be controlled by varying spatial and temporal application of the electron beam and hence the electric field. This suggests avenues for manipulating switching behaviour by atomic-scale application of electric fields. Importantly, we also show how different cation compositions affect the strain associated with the different phases and the probability of these transitions occurring, providing broad insights into the atomic-level mechanisms controlling the behaviour of fluorite ferroelectrics and opening pathways for compositional engineering of the switching behaviour. These findings provide fundamental insights into the atomic scale pathways of polarisation dynamics and phase transition phenomena in ferroelectric fluorite-type materials and the role of the cation, thereby enhancing their potential for advanced ferroelectric device applications.

Methods

Fabrication of freestanding (H)ZO membranes

For the (H)ZO membrane fabrication, we firstly obtained an epitaxially grown (H)ZO/$La_{0.7}Sr_{0.3}MnO_3$ (LSMO)/$SrTiO_3$ (STO) (001) thin film, at which the (H)ZO and LSMO films are fabricated on an STO (001) substrate by the pulsed laser deposition (PLD) method with the Coherent COMPex Pro 205 KrF excimer laser (wavelength was 248 nm). The LSMO layer was first deposited at 650–700 °C under an oxygen partial pressure of 100 mTorr. During the deposition, the LSMO ceramic target was ablated with a laser density of 1.2 J/cm^2 and at a repetition frequency of 5 Hz. (H)ZO film was subsequently deposited on the LSMO layer without breaking the vacuum of the PLD chamber. The (H)ZO layer was deposited at 800 °C and under an oxygen partial pressure of 75 mTorr, where the target was pulsed with a laser density of 1.4 J/cm^2 at 2 Hz. After the deposition, the specimen was cooled down to room temperature under an oxygen partial pressure of 75 mTorr. The thickness of (H)ZO layer was evaluated by X-ray reflectivity (XRR) measurements. The freestanding (H)ZO membrane was obtained by etching the LSMO layer in 5 wt.% hydrochloric acid (HCl) and solution with 0.05 M potassium iodide (KI). After the etching and exfoliation, the membranes were transferred onto the TEM grids, which have a holey carbon supporting film. We fabricated freestanding five- and ten-nanometre-thick ZrO_2 membranes and five-nanometre-thick HZO membrane, respectively, where the detailed fabrication process can be found elsewhere[13,14].

Atomic-resolution structure analysis of (H)ZO membranes

Atomic-resolution STEM datasets were acquired using a Thermo Fisher Scientific Spectra φ FEG TEM equipped with a monochromator and probe and image aberration correctors. All images were collected at an accelerating voltage of 300 kV and probe forming semi-angle of 25 mrad. During the experimental observation, the probe current was adjusted by changing the focus of the monochromator, which is performed by a lens underneath the electron gun and can modulate the flux of electrons going through the optical system with all other parameters staying the same. For the OBF STEM imaging, we acquired four quadrant segmented detector datasets using the Panther detector and then reconstructed OBF images via an algorithm that can be referred to in the literature[24]. The ADF images were obtained with an ADF detector simultaneously with the Panther detector datasets. The camera length was set to be 115 mm, resulting in a collection angle of 11-43 mrad for the Panther detector and 48-200 mrad for the ADF detector. A second order Butterworth low-pass filter[58] was applied to the experimental OBF and ADF images. For the OBF STEM image simulation, firstly the quadrant segmented detector images were calculated by the MuSTEM package[59], being subsequently reconstructed into the OBF image via the same procedure as the experiments. The MuSTEM calculation is based on the multislice algorithm, where the full dynamical scattering effect is incorporated. The crystalline structures used in the image simulation were referred to from the DFT-relaxed crystalline structure files used in our present study (tetragonal and polar orthorhombic phases) and from the literature (anti-polar orthorhombic phase)[60].

DFT calculation

The DFT calculations were performed to optimise the crystal structures and investigate the energy landscape using the projector augmented-wave (PAW) method implemented in the VASP code. The exchange-correlation term was treated with GGA-PBE. For the PAW potentials, 2 s and 2p electrons for O, 4 s, 4p, 4 d, and 5 s electrons for Zr, and 5p, 5 d, and 6 s electrons for Hf were explicitly treated as valence electrons. The plane-wave cutoff energy was set to 550 eV. Integration in reciprocal space was performed with a grid spacing of 0.3 Å^{-1}. Structure optimisation was conducted until all residual forces acting on each atom were less than 0.01 eV/Å. The energy barriers of

phase transitions were calculated using the nudged elastic band (NEB) method with five images between initial and final states, where the intermediate structures may be biased according to the symmetry of the initial and final ones. For the calculation without symmetry constraint, all atoms in the intermediate structures were displaced by 0 to 0.1 Å in random directions to reduce the symmetry to *P*1 before performing the structure optimisation, which can mitigate the bias to the intermediate states.

Data availability

The experimental STEM data presented in this study have been deposited in Zenodo (https://doi.org/10.5281/zenodo.18686323).

References

1. Martin, L. W. & Rappe, A. M. Thin-film ferroelectric materials and their applications. *Nat. Rev. Mater.* **2**, 16087 (2016).
2. Hwang, C. S. Prospective of semiconductor memory devices: from memory system to materials. *Adv. Electron. Mater.* **1**, 1–30 (2015).
3. Dawber, M., Rabe, K. M. & Scott, J. F. Physics of thin-film ferroelectric oxides. *Rev. Mod. Phys.* **77**, 1083–1130 (2005).
4. Ihlefeld, J. F. et al. Scaling effects in perovskite ferroelectrics: fundamental limits and process-structure-property relations. *J. Am. Ceram. Soc.* **99**, 2537–2557 (2016).
5. Mikolajick, T. et al. Next generation ferroelectric materials for semiconductor process integration and their applications. *J. Appl. Phys.* **129**, 100901 (2021).
6. Kim, I. J. & Lee, J. S. Ferroelectric transistors for memory and neuromorphic device applications. *Adv. Mater.* **35**, 1–20 (2023).
7. Chen, L. et al. Inverse size-scaling ferroelectricity in centrosymmetric insulating perovskite Oxide $DyScO_3$. *Adv. Mater.* **37**, 1–10 (2025).
8. Wei, X.-K. et al. Quasi–two-dimensional ferroelectricity with multiple switchable polarization states in N-H coinjected perovskite manganites. *Sci. Adv.* **11**, 1–8 (2025).
9. Schroeder, U., Park, M. H., Mikolajick, T. & Hwang, C. S. The fundamentals and applications of ferroelectric HfO_2. *Nat. Rev. Mater.* **7**, 653–669 (2022).
10. Bohr, M., Chau, R., Ghani, T. & Mistry, K. The high-k solution. *IEEE Spectr.* **44**, 29–35 (2007).
11. Böscke, T. S., Müller, J., Bräuhaus, D., Schröder, U. & Böttger, U. Ferroelectricity in hafnium oxide thin films. *Appl. Phys. Lett.* **99**, 2–4 (2011).
12. Park, M. H., Lee, Y. H., Mikolajick, T., Schroeder, U. & Hwang, C. S. Review and perspective on ferroelectric HfO_2-based thin films for memory applications. *MRS Commun.* **8**, 795–808 (2018).
13. Shen, Y. et al. Ferroelectric freestanding hafnia membranes with metastable rhombohedral structure down to 1-nm-thick. *Nat. Commun.* **15**, 1–9 (2024).
14. Shen, Y. et al. Ultrathin freestanding membranes of ZrO_2 with metastable structures and strain-dependent electrical properties. *Phys. Rev. Mater.* **9**, 024411 (2025).
15. Zhong, H. et al. Large-scale $Hf_{0.5}Zr_{0.5}O_2$ membranes with robust ferroelectricity. *Adv. Mater.* **34**, 2109889 (2022).
16. Wei, Y. et al. A rhombohedral ferroelectric phase in epitaxially strained $Hf_{0.5}Zr_{0.5}O_2$ thin films. *Nat. Mater.* **17**, 1095–1100 (2018).
17. Liu, J. J. Advances and applications of atomic-resolution scanning transmission electron microscopy. *Microsc. Microanal.* **27**, 943–995 (2021).
18. Kobayashi, S., Inoue, K., Kato, T., Ikuhara, Y. & Yamamoto, T. Multiphase nanodomains in a strained $BaTiO_3$ film on a $GdScO_3$ substrate. *J. Appl. Phys.* **123**, 064102 (2018).
19. Li, X. et al. Polarization switching and correlated phase transitions in fluorite-structure ZrO_2 nanocrystals. *Adv. Mater.* **35**, 1–9 (2023).
20. Li, X. et al. Ferroelastically protected reversible orthorhombic to monoclinic-like phase transition in ZrO_2 nanocrystals. *Nat. Mater.* **23**, 1077–1084 (2024).
21. Cheng, Y. et al. Reversible transition between the polar and antipolar phases and its implications for wake-up and fatigue in HfO_2-based ferroelectric thin film. *Nat. Commun.* **13**, 645 (2022).
22. Chen, D. et al. Unveiling the polarization switching pathway through tetragonal phase as a metastable intermediate state in ferroelectric $Hf_xZr_{1-x}O_2$ thin film. *Nat. Commun.* **16**, 8188 (2025).
23. Lee, S. et al. Field-induced structural dynamics of polarization switching in $Hf_xZr_{1-x}O_2$ thin films. *Adv. Mater.* **10930**, e10930 (2025).
24. Ooe, K., Seki, T., Ikuhara, Y. & Shibata, N. Ultra-high contrast STEM imaging for segmented/pixelated detectors by maximizing the signal-to-noise ratio. *Ultramicroscopy* **220**, 113133 (2021).
25. Lee, H. J. et al. Scale-free ferroelectricity induced by flat phonon bands in HfO_2. *Science* **369**, 1343–1347 (2020).
26. KP, H. et al. Electron ptychography reveals a ferroelectricity dominated by anion displacements. *Nat. Mater.* **24**, 1433–1440 (2025).
27. Anada, S., Nagase, T., Yasuda, H. & Mori, H. Electron-irradiation-induced phase transition in Cr_2M (M = Ti and Al) intermetallic compounds. *J. Alloys Compd.* **579**, 646–653 (2013).
28. Huang, C. W., Kuo, S. S. & Hsin, C. L. Electron-beam-induced phase transition in the transmission electron microscope: The case of VO_2(B). *CrystEngComm* **20**, 6857–6860 (2018).
29. Wei, J. et al. Direct imaging of atomistic grain boundary migration. *Nat. Mater.* **20**, 951–955 (2021).
30. Jiang, R.-J. et al. Atomic insight into the successive antiferroelectric–ferroelectric phase transition in antiferroelectric oxides. *Nano Lett.* **23**, 1522–1529 (2023).
31. Lomenzo, P. D. et al. Discovery of nanoscale electric field-induced phase transitions in ZrO_2. *Adv. Funct. Mater.* **33**, 2303636 (2023).
32. Velazco, A., Béché, A., Jannis, D. & Verbeeck, J. Reducing electron beam damage through alternative STEM scanning strategies, part I: experimental findings. *Ultramicroscopy* **232**, 113398 (2022).
33. Ortega, E., Nicholls, D., Browning, N. D. & de Jonge, N. High temporal-resolution scanning transmission electron microscopy using sparse-serpentine scan pathways. *Sci. Rep.* **11**, 22722 (2021).
34. Peters, J. J. P. et al. Event-responsive scanning transmission electron microscopy. *Science* **385**, 549–553 (2024).
35. Noor, M. et al. Nearly barrierless polarization switching mechanisms in ZrO_2 having perpendicular in-plane domain walls. *ACS Appl. Mater. Interfaces* **16**, 62282–62291 (2024).
36. Kudoh, Y., Takeda, H. & Arashi, H. In situ determination of crystal structure for high pressure phase of ZrO_2 using a diamond anvil and single crystal X-ray diffraction method. *Phys. Chem. Miner.* **13**, 233–237 (1986).
37. Trolliard, G., Mercurio, D. & Perez-Mato, J. M. Martensitic phase transition in pure zirconia: a crystal chemistry viewpoint. *Z. Krist.* **226**, 264–290 (2011).
38. Dou, X. et al. Polarization switching pathways of ferroelectric Zr-doped HfO_2 based on the first-principles calculation. *Appl. Phys. Lett.* **124**, 092901 (2024).
39. Bendeliani, N.A., Popova, S.V. & VERESCHA. LP, New high pressure modifications of ZrO_2 and HfO_2. *Geochem. Int.* **4**, 557 (1967).
40. Müller, J. et al. Ferroelectricity in yttrium-doped hafnium oxide. *J. Appl. Phys.* **110**, 1–5 (2011).
41. Müller, J. et al. Ferroelectricity in simple binary ZrO_2 and HfO_2. *Nano Lett* **12**, 4318–4323 (2012).
42. Du, H. et al. Multiple polarization orders in individual twinned colloidal nanocrystals of centrosymmetric HfO_2. *Matter* **4**, 986–1000 (2021).
43. Wu, Y. et al. Unconventional polarization-switching mechanism in (Hf, Zr)O_2 ferroelectrics and its implications. *Phys. Rev. Lett.* **131**, 226802 (2023).
44. Li, X. Y. et al. Domain wall motion in perovskite ferroelectrics studied by the nudged elastic band method. *J. Phys. Chem. C* **122**, 3091–3100 (2018).

45. Zhong, H. et al. Observation of one-dimensional, charged domain walls in ferroelectric ZrO_2. *Science* **391**, 407–411 (2026).
46. Wang, S. et al. Unconventional ferroelectric-ferroelastic switching mediated by non-polar phase in fluorite oxides. *Adv. Mater.* **37**, 2415131 (2025).
47. Shannon, R. D. Revised effective ionic radii and systematic studies of interatomic distances in halides and chalcogenides. *Acta Crystallogr. Sect. A* **32**, 751–767 (1976).
48. Reyes-Lillo, S. E., Garrity, K. F. & Rabe, K. M. Antiferroelectricity in thin-film ZrO_2 from first principles. *Phys. Rev. B* **90**, 140103 (2014).
49. Medvedeva, N. I., Zhukov, V. P., Khodos, M. Y. & Gubanov, V. A. The Electronic Structure and Cohesive Energy of HfO_2, ZrO_2, TiO_2, and SnO_2 Crystals. *Phys. Status Solidi* **160**, 517–527 (1990).
50. Hu, Y. et al. Bond engineering of molecular ferroelectrics renders soft and high-performance piezoelectric energy harvesting materials. *Nat. Commun.* **13**, 1–10 (2022).
51. Chevalier, J., Gremillard, L., Virkar, A. V. & Clarke, D. R. The tetragonal-monoclinic transformation in zirconia: lessons learned and future trends. *J. Am. Ceram. Soc.* **92**, 1901–1920 (2009).
52. Lee, C.-K., Cho, E., Lee, H.-S., Hwang, C. S. & Han, S. First-principles study on doping and phase stability of HfO_2. *Phys. Rev. B* **78**, 1–4 (2008).
53. He, R., Wu, H., Liu, S., Liu, H. & Zhong, Z. Ferroelectric structural transition in hafnium oxide induced by charged oxygen vacancies. *Phys. Rev. B* **104**, 1–6 (2021).
54. Ma, L. Y. & Liu, S. Structural polymorphism kinetics promoted by charged oxygen vacancies in HfO2. *Phys. Rev. Lett.* **130**, 96801 (2023).
55. Kita, K., Kyuno, K. & Toriumi, A. Permittivity increase of yttrium-doped HfO_2 through structural phase transformation. *Appl. Phys. Lett.* **86**, 1–3 (2005).
56. Xu, X. et al. Kinetically stabilized ferroelectricity in bulk single-crystalline HfO_2:Y. *Nat. Mater.* **20**, 826–832 (2021).
57. Zhou, C. et al. Enhanced polarization switching characteristics of HfO_2 ultrathin films via acceptor-donor co-doping. *Nat. Commun.* **15**, 2893 (2024).
58. Butterworth, S. On the theory of filter amplifiers. *Wirel. Eng.* **7**, 536–541 (1930).
59. Allen, L. J., D'Alfonso, A. J. & Findlay, S. D. Modelling the inelastic scattering of fast electrons. *Ultramicroscopy* **151**, 11–22 (2015).
60. Kersch, A. & Falkowski, M. New low-energy crystal structures in ZrO_2 and HfO_2. *Phys. Status Solidi-Rapid Res. Lett.* **15**, 10–13 (2021).

Acknowledgements

This research was supported under Japan Society for the Promotion of Science (JSPS) KAKENHI (Grant No. 22KJ3209 and 23K13553 (K.O.), 21H01810 (D.K.), 23KJ1239 (YF.S.), 23H05457 (YU.S.), 24H01190 (D.K.), 23H00241 (S.K.)) and grants for the Integrated Research Consortium on Chemical Sciences and the International Collaborative Research Program of the Institute for Chemical Research in Kyoto University from the Ministry of Education, Culture, Sports, Science, and Technology (MEXT) of Japan. The work was also supported by the Japan Science and Technology Agency (JST) as part of PRESTO, Grant No. JPMJPR24H3 (D.K.), and Adopting Sustainable Partnerships for Innovative Research Ecosystem (ASPIRE), Grants No. JPMJAP2312 (D.K.) and No. JPMJAP2314 (YU.S.). This work was also partly supported by The Samco Foundation, Iketani Science and Technology Foundation, and Murata Science and Education Foundation. J.E. acknowledges fellowship support from the Australian Research Council (ARC) grant FL220100202. The authors acknowledge the use of instruments and scientific and technical assistance at the Monash Centre for Electron Microscopy (MCEM), Monash University, a node of Microscopy Australia (ROR: 042mm0k03) supported by NCRIS. This research used equipment funded by ARC grants LE0454166 and LE17010118. This work was partially supported by MEXT projects for data-driven materials research (JPMXP1122683430) and Program for Promoting Researches on the Supercomputer Fugaku (JPMXP1020230327 and JPMXP1020230325) (K.S.). Computational resources were partially provided by the supercomputer Fugaku at the RIKEN Center for Computational Science (Project IDs: hp230205, hp240212, hp240223).

Author contributions

K.O. and J.E. conceived, designed, and supervised the project under helpful discussions with S.K. and D.K. K.O. performed electron microscopy experiments and simulations, and analysed the data. YF.S. and R.M. fabricated membrane samples with help from D.K. and YU.S. K.S. performed the density functional theory calculations. K.O. and J.E. prepared the manuscript. All authors contributed to the discussion of the results and revision of the manuscript.

Competing interests

The authors declare no competing interests.

Additional information

Supplementary information The online version contains supplementary material available at https://doi.org/10.1038/s41467-026-70593-y.

Correspondence and requests for materials should be addressed to Kousuke Ooe.

Peer review information *Nature Communications* thanks Piush Behera, Mengjiao Han, Anton Ievlev and the other anonymous reviewer(s) for their contribution to the peer review of this work. A peer review file is available.

Reprints and permissions information is available at http://www.nature.com/reprints

Publisher's note Springer Nature remains neutral with regard to jurisdictional claims in published maps and institutional affiliations.

Open Access This article is licensed under a Creative Commons Attribution-NonCommercial-NoDerivatives 4.0 International License, which permits any non-commercial use, sharing, distribution and reproduction in any medium or format, as long as you give appropriate credit to the original author(s) and the source, provide a link to the Creative Commons licence, and indicate if you modified the licensed material. You do not have permission under this licence to share adapted material derived from this article or parts of it. The images or other third party material in this article are included in the article's Creative Commons licence, unless indicated otherwise in a credit line to the material. If material is not included in the article's Creative Commons licence and your intended use is not permitted by statutory regulation or exceeds the permitted use, you will need to obtain permission directly from the copyright holder. To view a copy of this licence, visit http://creativecommons.org/licenses/by-nc-nd/4.0/.

© The Author(s) 2026

Reprinted from *Nat. Microbiol.*, 11, 584–596 (2026)

nature microbiology

Article

https://doi.org/10.1038/s41564-025-02234-x

A giant virus forms a specialized subcellular environment within its amoeba host for efficient translation

Received: 31 October 2024

Accepted: 8 December 2025

Published online: 9 January 2026

Check for updates

Ruixuan Zhang[1,7], Lotte Mayer[2,7], Hiroyuki Hikida[1,6], Yuichi Shichino[3,4], Mari Mito[3], Anouk Willemsen[2], Shintaro Iwasaki[3,5] ✉ & Hiroyuki Ogata[1] ✉

Many eukaryotic viruses, including amoeba-infecting mimiviruses, have codon usage that deviates from their hosts. However, codon usage patterns that align with the cellular tRNA pool enable efficient translation. How these viruses cope with the mismatch between tRNA supply and demand is unclear. Here we show that Acanthamoeba polyphaga mimivirus (APMV) generates a subcellular area to translate viral mRNAs. tRNA sequencing showed that the tRNA pool was not substantially altered during the infection, even though the virus encodes tRNA genes. Using in situ labelling, we found that viral mRNAs and newly synthesized proteins were localized in the periphery of the viral factory, suggesting that APMV creates a discrete subcellular environment to facilitate translation. Frequently used codons in viral mRNAs had higher tRNA accessibility than the same type of codons in amoeba mRNAs. Our data show how local translation assists the virus in overcoming the mismatch between tRNA supply and demand.

Codon usage in genes is unique in each genome. Even for synonymous codons that encode the same amino acid, the codon usage frequency varies. Preferentially used codons are associated with high tRNA copy numbers in fast-growing microorganisms such as *Escherichia coli*[1]. Recent studies highlighted the importance of synonymous codon usage in mRNA stability[2,3]. Therefore, the concordance of tRNA supply and demand is crucial for ensuring efficient gene expression.

Giant viruses are characterized by huge genomes, a large number of genes for reprogramming host cell metabolism and large virions[4–7]. Infection by giant viruses induces a rapid shift in the host cell transcriptome, characterized by large occupancy of viral mRNAs[8–10]. However, the codon usage of some giant viruses is poorly adapted to the tRNA pool of the host[11,12]. For example, APMV—the first virus isolate of family *Mimiviridae*—has an AT-rich genome (G+C content of 28%), whereas the genome of its host *Acanthamoeba castellanii* is GC-rich (G+C content 58%)[13,14]. Consequently, the APMV codon usage varies extensively from the codon usage of *A. castellanii*[11,13]. This raises the question of whether translation of APMV mRNAs is negatively impacted by the codon usage or whether APMV alleviates the unfavourable translation condition during infection.

Several observations and hypotheses have been made related to the codon usage discrepancy. Genomic analysis found that members of the *Mimiviridae* encode more translation-related genes, including translation factors, tRNAs and aminoacyl-tRNA synthetases[4–7], than other clades of giant viruses. A transcriptomic study reported that the late-expressed genes of APMV exhibit a slight adaptation to the host

[1]Bioinformatics Center, Institute for Chemical Research, Kyoto University, Uji, Japan. [2]Centre for Microbiology and Environmental Systems Science, Division of Microbial Ecology, University of Vienna, Vienna, Austria. [3]RNA Systems Biochemistry Laboratory, Pioneering Research Institute, RIKEN, Wako, Japan. [4]Department of RNA Biochemistry, Institute of Medicine, University of Tsukuba, Tsukuba, Japan. [5]Department of Computational Biology and Medical Sciences, Graduate School of Frontier Sciences, The University of Tokyo, Kashiwa, Japan. [6]Present address: Research Center for Biosafety, Laboratory Animal and Pathogen Bank, National Institute of Infectious Diseases, Japan Institute for Health Security, Shinjuku, Japan. [7]These authors contributed equally: Ruixuan Zhang, Lotte Mayer. ✉e-mail: shintaro.iwasaki@riken.jp; ogata@kuicr.kyoto-u.ac.jp

https://doi.org/10.1038/s41564-025-02234-x

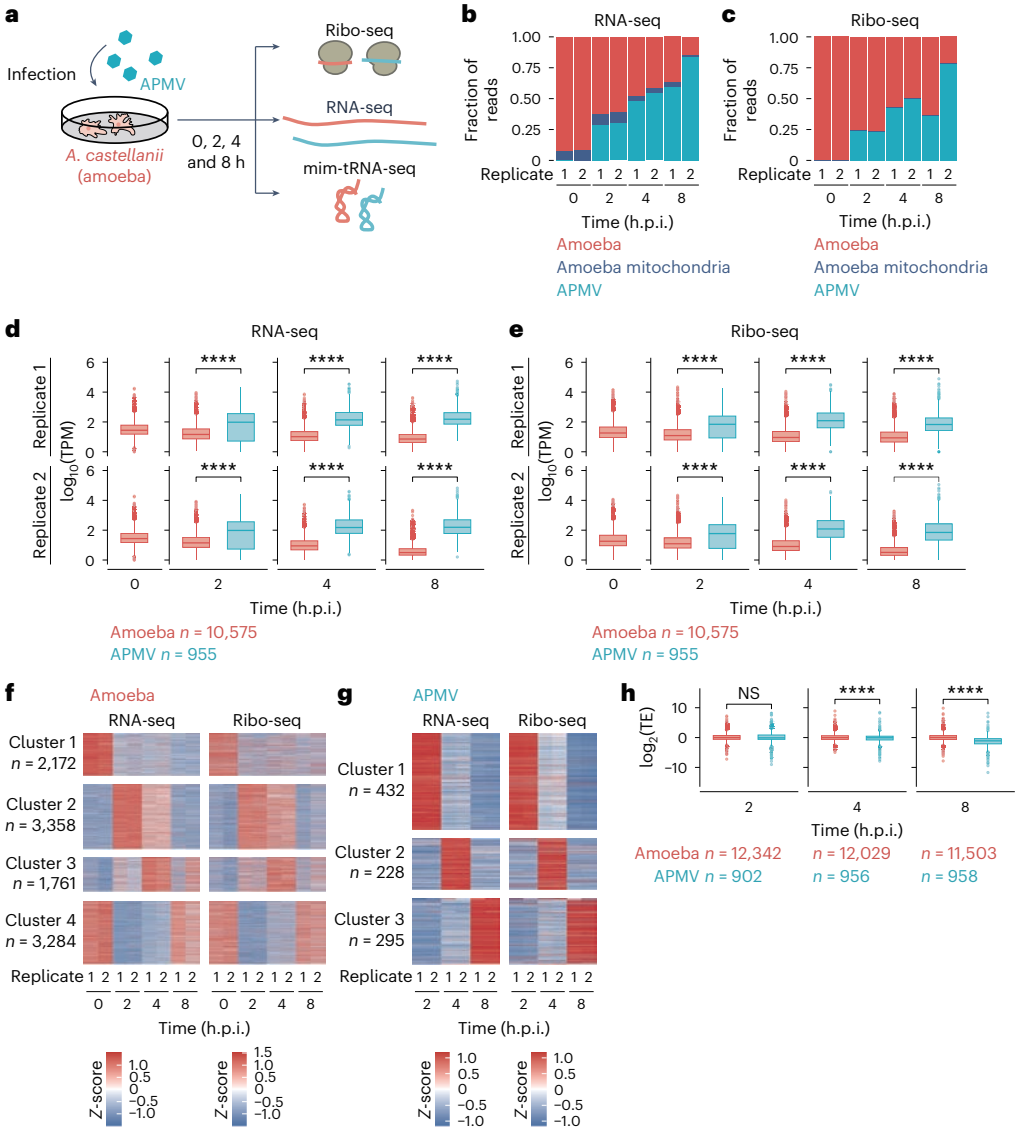


Fig. 1 | Global impacts of APMV infection on RNA abundance and translation. **a**, Schematic diagram of the experimental design. Cells were infected with APMV for 0 (mock infection), 2, 4 or 8 h and used for RNA-seq, Ribo-seq and mim-tRNA-seq. **b**,**c**, Fraction of reads that aligned to indicated genomes by RNA-seq (**b**) and Ribo-seq (**c**) analyses at different infection stages. **d**,**e**, Box plots of transcripts per kilobase million (TPM) for amoeba and APMV mRNAs in the RNA-seq (**d**) and Ribo-seq (**e**) data. **f**,**g**, Heat maps of the *Z*-score normalized TPM in the RNA-seq and Ribo-seq data for amoeba (**f**) and APMV (**g**) mRNAs at different infection stages. Colour scales indicate the *Z*-scores. **h**, Box plots of translation efficiency (TE) of amoeba and APMV mRNAs at different infection stages. In all box plots, the median (centre line), upper/lower quartiles (box limits), 1.5× interquartile range (whiskers) and outliers (points) are shown. The *P* values were calculated using one-sided Wilcoxon rank sum test. NS, not significant; *$P < 0.05$; **$P < 0.01$; ***$P < 0.001$; ****$P < 0.0001$.

tRNA pool[11]. These findings suggest that translation-related fitness has shaped viral genes and genome evolution. However, the actual translation dynamics in infected cells have never been explored so far. Moreover, APMV forms an organelle-like structure known as a viral factory upon infection for viral DNA replication and transcription[15,16]. Ribosomes and some translation factors have been observed to localize around the viral factory[17,18]. How this spatial organization within infected cells relates to the observed patterns of genome evolution is still unknown.

To characterize the translation landscape of mimiviruses, we monitored changes in the transcriptome, tRNAs and translatome during viral infection by RNA sequencing (RNA-seq), optimized tRNA-seq[19] and ribosome profiling (Ribo-seq)[20,21]. Ribo-seq captures ribosome-protected fragments of mRNA, so-called 'ribosome footprints', generated by RNase treatment, enabling high-resolution measurements of translation dynamics. Our results indicate that the overall composition of the global tRNA pool was not significantly altered during APMV infection, with limited contribution of tRNAs encoded in the viral genome. At the early infection stage, the translation efficiency of the viral mRNAs was comparable to that of the host mRNAs despite using rare codons. Even at the later infection stages, the rare codons did not cause the ribosome to pause on viral mRNAs; rather, the accessibility to tRNAs for codons ending with A or U was different between viral and host mRNAs. The microscopic analysis using fluorescence in situ hybridization (FISH) and fluorescent non-canonical amino acid tagging (FUNCAT)[21] showed that the spatial organization within infected cells indicated co-localization of viral mRNAs, host ribosomal RNAs and newly synthesized proteins around the viral factory. Our results

suggest that APMV created a subcellular heterogeneity for efficient translation of the viral genes.

Results

Imbalance of codon usage between APMV and the amoeba host

We characterized the dissimilarity in codon usage between APMV and the host *A. castellanii* (hereafter referred to as amoeba). Consistent with previous genome analyses[13,14], the host and viral genes had distinct G+C content (Extended Data Fig. 1a) and codon usage (Extended Data Fig. 1b). APMV mRNAs predominantly use AU-rich codons, such as AAA, AAU and AUU, whereas AU-rich codons were much less common in amoeba mRNAs. The tRNA gene copy number of amoeba was positively correlated with the amoeba codon usage (Extended Data Fig. 1c), whereas it showed no such correlation with the APMV codon usage (Extended Data Fig. 1d).

Impact of APMV infection on RNA abundance and translation

To investigate the dynamics of transcription and translation of viral and host genes, we performed RNA-seq and Ribo-seq in APMV-infected amoeba cells at 0, 2, 4 and 8 h post-infection (h.p.i.) (Fig. 1a and Supplementary Table 1). We avoided pre-treatment with cycloheximide in the media, as it may induce bias through aberrant ribosome pausing in a context-dependent manner[22–25]. Instead, the post-lysis approach (that is, cycloheximide in cell lysis buffer), which is a current standard[26–28], was used. Consistent with an earlier report[29], the footprints showed two length peaks at 21–22 and 29–30 nucleotides (nt) (Extended Data Fig. 2a,b). The footprint counts along genes showed a clear 3 nt periodicity for both long (29–30 nt) (Extended Data Fig. 2c–f) and short (21–22 nt) footprints (Extended Data Fig. 2g–j). Discrete Fourier transform analysis further ensured the periodicity (Extended Data Fig. 3a). Our data had high reproducibility for read mapping for both the host and viral genes (Extended Data Fig. 3b–e). These features indicate the robust detection of footprints generated by ribosomes translating mRNAs for both host and virus.

The RNA-seq reads from viral mRNAs increased incrementally along with the viral infection time and were dominant at the late time points (up to approximately 62% and 85% for each replicate at 8 h.p.i.) (Fig. 1b). Footprints from viral mRNAs also increased and occupied a large proportion of the library at 8 h.p.i. (approximately 40% and 81% for each replicate) (Fig. 1c). We also observed a general increase of short footprints during virus infection (Extended Data Fig. 3f,g; see Methods for definition).

The average expression levels of viral mRNAs were higher than those of amoeba mRNAs at all time points (Fig. 1d). The expression levels of individual viral mRNAs increased gradually, whereas those of host mRNAs decreased throughout infection (Fig. 1d). Translation activity, evaluated by Ribo-seq, followed the same trends as that obtained by RNA-seq (Fig. 1e).

The host genes were classified into four clusters based on their mRNA levels from RNA-seq (Fig. 1f). To characterize the functions of genes in each cluster, we selected host genes that had high variance in their expression and performed a functional enrichment analysis using the Kyoto Encyclopedia of Genes and Genomes (KEGG) (Extended Data Fig. 3h and Supplementary Table 2). Genes in cluster 1, which showed an expression shutdown by 2 h.p.i., were enriched in energy metabolism, amino acid metabolism and motor proteins. Ribosomal genes had various expression patterns and were enriched in clusters 1, 3 and 4. tRNA and protein processing functions were enriched in clusters 2 and 3. Viral mRNAs were classified into three expression clusters (Fig. 1g), which largely correspond to the early, intermediate and late genes reported previously[8]. The translation levels of host and viral mRNAs in individual clusters showed dynamics consistent with the transcription patterns, suggesting that the abundance of mRNAs is a major determinant of the level of translation (Fig. 1f, g).

To assess the density of ribosomes on mRNAs, we calculated the translation efficiency as the ratio of the amounts of footprints to the amounts of mRNAs. At 0 and 2 h.p.i., the median translation efficiency values were 0.991 and 0.992 for host mRNAs, respectively, and 0.935 (2 h.p.i.) for viral mRNAs, indicating no significant difference between the translation efficiency of host and viral mRNAs (Fig. 1h). However, viral translation efficiency dropped and was significantly lower than that of host translation efficiency at later time points; at 4 and 8 h.p.i., the median translation efficiency values were 0.989 and 1.010 for host mRNAs, and 0.956 and 0.468 for viral mRNAs (Fig. 1h). This result suggests that host mRNAs were twice as likely to bind to ribosomes as viral mRNAs at 8 h.p.i., indicating the reduced accessibility to ribosomes for viral mRNAs at later time points.

Translation of viral mRNAs is not associated with ribosome pausing

Given the deviated codon usage of APMV mRNAs, we investigated whether the rare codons on viral mRNAs hampered virus mRNA translation. As APMV genes are biased to codons ending with A or U (hereafter AU3 codons) and host genes are biased to codons ending with G or C (hereafter GC3 codons) (Extended Data Fig. 1a), we investigated the translation elongation speed on codons from viral and host mRNAs by calculating the A-site ribosome occupancy. No significant difference was found in ribosome occupancy at the A-site between AU3 and GC3 codons for amoeba (Fig. 2a), and this balanced elongation was maintained in viral mRNAs (Fig. 2b).

Next, we focused on individual codon positions to determine whether ribosomes tended to pause on either viral or host mRNAs. Codon positions with relatively high ribosome occupancy were defined as pause sites (Fig. 2c and Methods). We found that viral mRNAs had a lower tendency of ribosome pausing than host mRNAs did (Fig. 2d), indicating that ribosome traversal on viral mRNAs was smooth, even with the obvious codon usage conflict (Extended Data Fig. 1). This result is robust under different cut-offs for putative pausing site prediction (Extended Data Fig. 4a).

The tRNA pool was stable during viral infection

Because APMV encodes tRNA genes (three Leu (two TTAs, one TTG), Trp (TGG), Cys (TGC) and His (CAC))[13], we hypothesized that alteration of the cellular tRNA pool facilitated ribosome traversal along viral mRNAs. To assess the abundance of tRNA species, we applied modification-induced misincorporation tRNA sequencing (mim-tRNA-seq)[19]. As tested in an earlier study[19], we also evaluated the salt concentration, pH, temperature and reverse transcription enzymes for optimal cDNA synthesis (Extended Data Fig. 5a,b). Ultimately, we selected the most efficient condition (with the thermostable group II intron reverse transcriptase, TGIRT-III, at 49 °C for 16 h) for downstream tRNA-seq. The tRNA supply (*W*-score; see Methods) showed a significant negative correlation with ribosome occupancy on codons in growing amoeba (Extended Data Fig. 5c), further ensuring that our Ribo-seq reflects ribosome traversal speed in cells.

The mim-tRNA-seq showed that the expression of tRNAs encoded in the amoeba genome remained at a high level (>87% in every library), whereas the expression of the six tRNAs encoded by APMV was only 1.8%, even at the late infection stage (8 h.p.i.) (Fig. 3a), suggesting that the contribution of viral tRNA to the cellular tRNA pool may be limited. In addition, the codons decoded by the APMV-encoded tRNAs did not show significantly different ribosome occupancy (that is, elongation speed) compared to other codons in viral mRNAs (Extended Data Fig. 6a).

To investigate whether the virus infection altered the tRNA pool composition to favour viral mRNA translation, we calculated the proportion of each tRNA type in the tRNA pool (including amoeba nuclear and APMV tRNAs). We used *W*-score to quantify the tRNA supply level. For a given codon type, *W*-score was calculated by summing the

https://doi.org/10.1038/s41564-025-02234-x

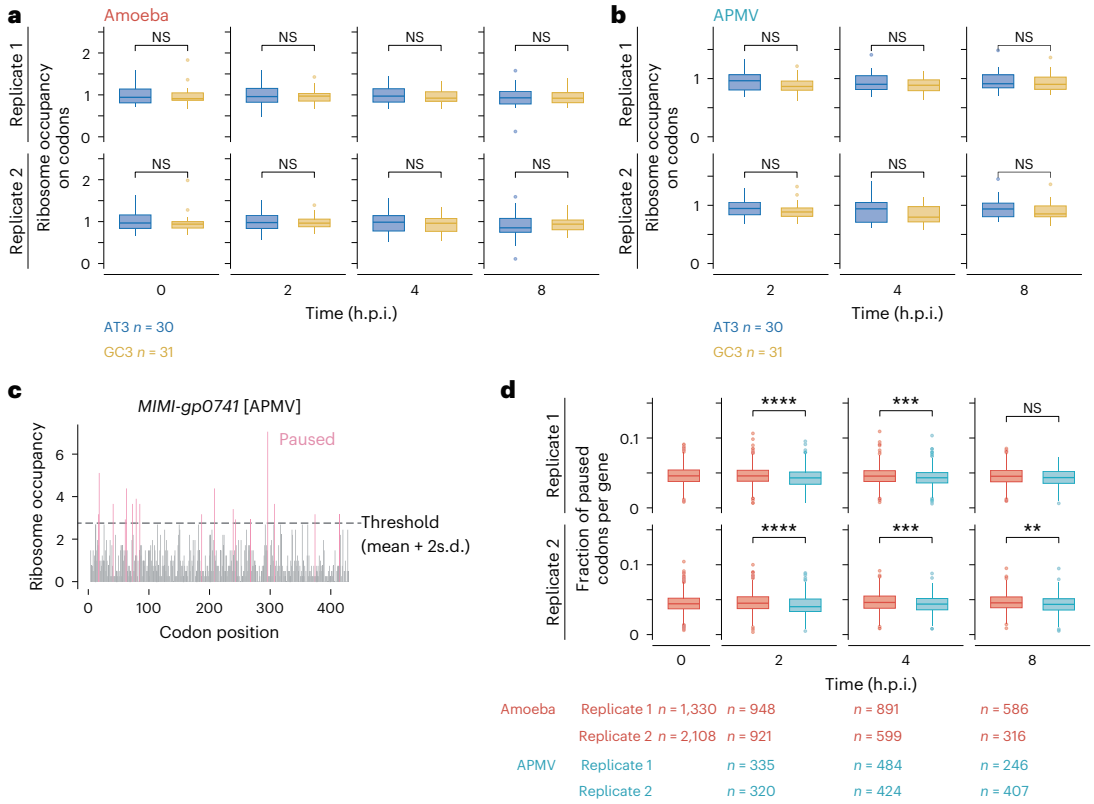


Fig. 2 | Smooth ribosome traversal on APMV mRNAs. a,**b**, Box plots of ribosome occupancy on AU3 and GC3 codons in amoeba (**a**) and APMV (**b**) mRNAs at different infection stages. AU3, codons ending with A or U; GC3, codons ending with G or C. **c**, Distribution of ribosome footprints along the open reading frames of *MIMI-gp0741* (locus tag of an APMV gene) in the APMV genome for replicate 1 at 2 h.p.i. The A-site position of the ribosomes is shown. The first four codons and stop codons were not included and are not plotted. The grey horizontal line (Threshold) indicates the cut-off of pausing (mean + two standard deviations (2 s.d.)). Pause sites are shown in pink. **d**, Box plots of the fraction of paused codons per gene in the amoeba and APMV genomes at different infection stages. Box plots as in Fig. 1. The *P* values were calculated using one-sided Wilcoxon rank sum test. **P* < 0.05; ***P* < 0.01; ****P* < 0.001; *****P* < 0.0001.

proportions of cognate and wobble-paired tRNAs (see Methods)[30]. Essentially, *W*-scores were stable during the APMV infection; high correlation of the *W*-scores was observed between time points (Fig. 3b). In naive amoeba (that is, 0 h.p.i.), the *W*-scores were higher for GC3 than they were for AU3 codons (Fig. 3c and Extended Data Table 1). This finding corresponds with codon usage in the amoeba genome, which is biased to GC3 codons (Extended Data Fig. 1) and probably contributed to the smooth elongation of GC3 codons (Fig. 2a) with no shortage of tRNA supply. The high tRNA supply for GC3 codons was maintained throughout the infection, indicating that viral infection did not largely change the composition of the global tRNA pool.

To quantitatively assess the imbalance of tRNA supply and demand during APMV infection, we calculated the balance score, which borrowed the idea of the normalized translation efficiency index[31]. In brief, we calculated the ratio between tRNA supply and codon usage, considering the mRNA abundance (see Methods). In naive amoeba, the AU3 codons generally had a higher balance score than the GC3 codons (Fig. 3d), indicating that tRNAs for AU3 codons are 'excessive' despite their concentration being lower than that for GC3 codons. During APMV infection, the high expression of viral mRNAs led to a decrease in the balance score for AU3 codons, whereas the balance score for GC3 increased (Fig. 3d and Extended Data Table 2). Together, these findings indicate that the tRNA supply and demands inside the cell seemed unsuitable for the translation of AU3-rich viral mRNAs (Fig. 3), even though protein synthesis from viral mRNAs was rather smooth (Fig. 2d).

Distinct ribosome elongation environment for viral mRNAs

The conflict between tRNA supply and demand for viral mRNA translation is based on our assumption that cellular resources, such as tRNAs, are equally available for host and viral mRNAs. Thus, our results suggest that the translation environment for viral mRNAs was not the same as that for host mRNAs. Consistent with this scenario, we observed differences in tRNA accessibility in host and viral mRNAs. Given that long (29–30 nt) and short (21–22 nt) footprints represent ribosomes with or without tRNA at the A-site[29], we defined the short footprint ratio as the ratio of short footprints to total footprints for a given codon type at the A-site to represent tRNA accessibility. The short footprint ratio was higher (that is, lower tRNA accessibility) on AU3 codons than it was on GC3 codons in amoeba mRNAs, irrespective of the viral infection stage (Fig. 4a). This finding is consistent with the lower tRNA supply for AU3 codons compared with the tRNA supply for GC3 codons (Fig. 3c). There was no such difference in the short footprint ratio for viral mRNAs (Fig. 4b). The same results were obtained when the ratio of short footprint over long footprints was considered (Extended Data Fig. 7a,b). The correlation between viral codon occupancy and host codon occupancy decreased at the late infection stage (8 h.p.i.) (Extended Data Fig. 6a), indicating divergence in codon-specific elongation speed between viral and host mRNAs. These data suggest that the translation environment of viral mRNAs differed from that of amoeba mRNAs.

To further investigate the cytosolic translation situation during viral infection, we set out a reporter assay to monitor the effects of AT-rich and GC-rich sequences in amoeba with or without APMV infection (Extended Data Fig. 8a). We used an established reporter system,

https://doi.org/10.1038/s41564-025-02234-x

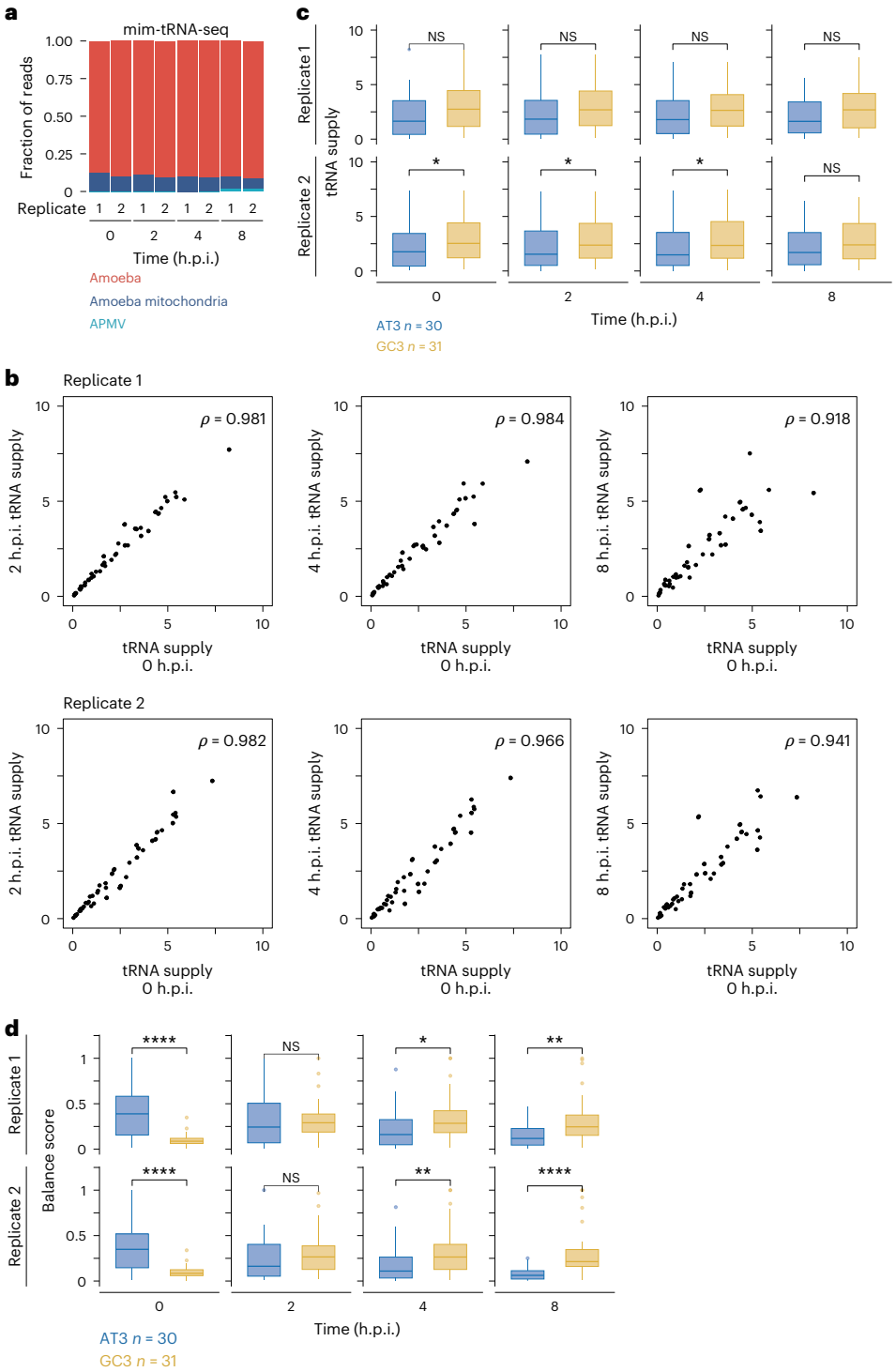


Fig. 3 | Stable tRNA pool during infection conflicts with translation elongation on APMV mRNAs. a, Fraction of reads that aligned to the indicated genomes in the mim-tRNA-seq analysis at different infection stages. **b**, Correlation of tRNA supply evaluated by *W*-score among the different infection stages. ρ, Spearman's correlation coefficient (two-tailed). **c**, Box plots of *W*-scores for AU3 and GC3 codons at different infection stages. **d**, Box plots of balance scores for tRNA for AU3 and GC3 codons at different infection stages. Box plots as in Fig. 1. The *P* values were calculated using one-sided Wilcoxon rank sum test. $^{*}P < 0.05$; $^{**}P < 0.01$; $^{***}P < 0.001$; $^{****}P < 0.0001$.

which is sensitive to translation elongation effects[32–35]. This reporter consists of an N-terminal *Renilla* luciferase (Rluc) and a C-terminal firefly luciferase (Fluc) in frame, with the open reading frame (ORF) region of the test in the middle. Viral 2A sequences, which induce self-cleavage of peptide bonds during translation[36], were inserted in the middle (Extended Data Fig. 8a). The ratio of the two individual luciferase proteins allows measurement of protein synthesis rate in the region between luciferases. Here, we investigated the effects of AT-rich

https://doi.org/10.1038/s41564-025-02234-x

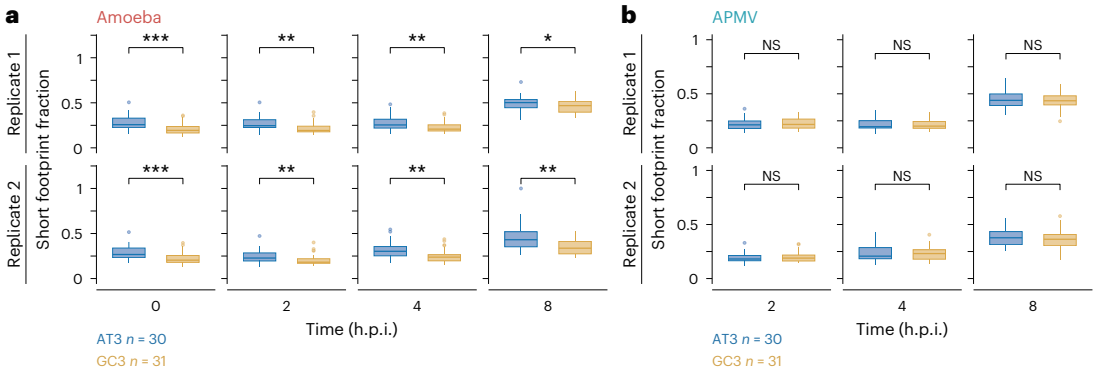


Fig. 4 | Difference in tRNA accessibility between amoeba and APMV mRNAs. a,**b**, Box plots of the short footprint fraction on AU3 and GC3 codons in amoeba (**a**) and APMV (**b**) mRNAs at different infection stages. Box plots as in Fig. 1. The *P* values were calculated using one-sided Wilcoxon rank sum test. **P* < 0.05; ***P* < 0.01; ****P* < 0.001; *****P* < 0.0001.

ORF originating from TATA-box binding protein (TBP) gene of APMV and GC-rich ORF from actin gene of amoeba (Extended Data Fig. 8a).

Consistent with genomic sequences, the GC-rich region of the reporter resulted in a higher Fluc/Rluc ratio than the AT-rich region, suggesting a smoother elongation for GC-rich mRNAs (Extended Data Fig. 8b). The slow elongation of the AT-rich region was not improved, while a smoother elongation of the GC-rich region was maintained upon viral infection (Extended Data Fig. 8b). These observations suggest that the cytosolic environment performs a smoother translation of GC-rich mRNAs, further supporting the requirement of a unique environment for viral protein synthesis.

Viral mRNAs are locally translated

As ribosomes were found to localize around the viral factory[17,18], we hypothesized that viral mRNA translation may occur in a distinct subcellular location near the viral factory. To investigate this hypothesis, we combined 4′,6-diamidino-2-phenylindole (DAPI) staining, FISH and FUNCAT[16,21] to determine the location of the viral factory, viral mRNAs, amoeba ribosomes and newly synthesized proteins. The FUNCAT signal was enriched around the periphery of the viral factory (Fig. 5a). Similarly, FISH for amoeba rRNA showed that a sub-population of ribosomes was also enriched in this region (Fig. 5a), which is consistent with previous tomography results[18], suggesting that protein synthesis occurred at the viral factory periphery. Moreover, this local translation milieu contained the APMV-encoded *mcp* mRNAs, probed by single-molecule mRNA fluorescence in situ hybridization (sm-mRNA FISH) (Fig. 5b). Thus, our data suggest that APMV created a unique environment tailored for viral mRNA translation at the periphery of the viral factory.

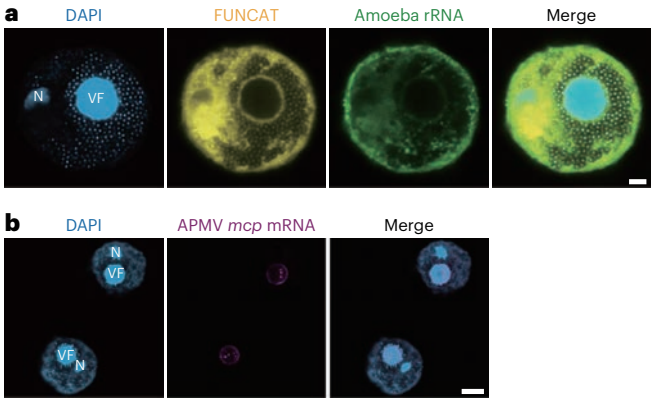


Fig. 5 | Local translation at the peripheral region of the viral factory during APMV infection. a, Microscopy images for DAPI (light blue), FUNCAT (yellow) and rRNA FISH (green) of APMV-infected amoeba cells at 12 h.p.i. **b**, Microscopy images for DAPI (light blue) and sm-mRNA FISH for APMV *mcp* mRNA of APMV-infected amoeba cells at 18 h.p.i. N, amoeba nucleus; VF, viral factory. Scale bars, 3 μm (**a**) and 8 μm (**b**).

Discussion

A consonant pattern between codon usage and tRNA concentration was thought to be important for translation[2,3]. However, APMV has a codon usage pattern that deviates from its host, suggesting potential problems in viral gene translation. The deep sequencing-based techniques (RNA-seq, Ribo-seq and mim-tRNA-seq) showed that APMV genes were smoothly translated without reduced accessibility to tRNAs for frequently used codons. The cell biology methods (FUNCAT and FISH) showed that viral mRNAs, host rRNA and protein synthesis were co-localized at the periphery of the viral factory. These findings suggest that APMV mitigates the codon usage conflict by creating a local translation milieu for its mRNAs.

Viral mRNAs dominated the mRNA pool at the late stages of infection, which is consistent with a previous study[8]. However, this increase was not perfectly reflected in the footprint proportion (Fig. 1b,c), leading to a decline in translation efficiency of viral mRNAs (Fig. 1h). A low translation efficiency during viral infection has been reported for influenza A virus and SARS-CoV-2 (refs. 37,38). It suggests that overwhelming the host's translation machinery through massive mRNA synthesis might be a common strategy shared by diverse viral taxa. Consistently, we found a general increase of A-site empty ribosomes, represented by short footprints along the viral infection stages (Extended Data Fig. 3f,g), probably because of the global tRNA or amino acid shortage.

In terms of translation dynamics and tRNA pool, we found that APMV genes were smoothly translated without significantly altering the tRNA composition in the host cell (Figs. 2d and 3). This unaltered cellular tRNA pool aligns with the previous report on vaccinia virus and influenza A virus[39]. One possible explanation is that AU-rich mRNAs form fewer secondary structures than GC-rich mRNAs, facilitating a smooth translation. However, this cannot explain the observed higher tRNA accessibility for AU3-codons on viral mRNAs than that on host mRNAs (Fig. 4). These observations suggest that a local tRNA pool could be selectively used for viral mRNAs. APMV may achieve smooth translation by generating a local translation environment within the cell.

In terms of the subcellular organization within the infected cells, the viral factory is a unique intracellular structure that is formed by many large DNA viruses during infection. For APMV, DNA replication

and transcription occur in the viral factory[15,39], whereas endoplasmic reticulum, ribosomes and the viral translation initiation factor SUI1 have been observed outside the viral factory[15,17,18]. In this study, we showed that viral mRNAs surrounded the viral factory (Fig. 5b), and protein synthesis occurred in the same region (Fig. 5a). Other translation-related proteins and tRNAs may also be recruited to the same place, which would further increase the local concentration of translation machineries. Other viruses might also use similar translation strategies. For example, poxviruses, asfarviruses and iridoviruses have been reported to induce changes in cytoskeleton[40,41], recruitment and local enrichment of proteins[42] and even re-localization of organelles such as mitochondria[40,43]. Moreover, endoplasmic reticulum membrane recruitment and protein re-localization have been observed for RNA viruses[44–46], indicating that subcellular remodelling is a common feature of viral infections across diverse virus families.

APMV likely uses a local translation environment to overcome the codon–tRNA mismatch. However, the reason for the mismatch (that is, AT-rich genomic feature) still needs an explanation. One hypothesis is that the AT-rich genome arises from mutational biases due to the lack of DNA repair genes, as proposed for many AT-rich viruses and intracellular microorganisms[47,48]. However, this scenario might not apply to APMV, which has a large set of DNA repair genes[49]. Instead, our results brought another possibility for the origin of the genomic feature. The AT-rich genome might be selectively advantageous by allowing access to the excessive tRNAs for AU3 codons at the early stage of infection (Fig. 3d). This possibility may apply to other viruses, as APMV is not the only virus that has a deviated codon usage with its host[50–52]. In the case of APMV, this advantage is likely to cease at later infection stages with high viral mRNA load (Fig. 3d). The viral mRNA load at later infection stages appears to cause a translation-associated bottleneck, which may be alleviated through the acquisition of translation-related genes by APMV and related viruses to build favourable translation environments. Viruses in the order *Imitervirales* are atypical among viruses by encoding abundant tRNA genes and translation-related proteins such as aminoacyl-tRNA synthetases[53,54]. It was also noted that viral aminoacyl-tRNA synthetases were found to be frequently associated with AT-rich codons[53]. Similar hypotheses have been proposed for the incorporation of tRNA genes into other viral genomes[55–57].

In this study, we proposed that the creation of a subcellular translation environment is a key strategy for APMV to overcome the discrepancy between host and viral codon usages. Virus-induced subcellular structures have been observed across a wide range of viruses, from prokaryotic to eukaryotic and from RNA to DNA viruses[17,58,59]. Although the spatial association between these viral subcellular structures and translation is largely unknown for other viruses, they may also form a local environment for viral mRNA translation.

Methods

Cells and viruses

A. castellanii, strain Neff (American Type Culture Collection (ATCC), 30010) was cultured in peptone–yeast–glucose (PYG) medium at 28 °C. Although a recent study proposed a reclassification of this strain[60], it has not yet been recognized by the National Center for Biotechnology Information (NCBI). We used the original naming for consistency with the NCBI database. APMV was used as a prototype of mimiviruses[61]. The virus titre was determined by the 50% tissue culture infectious dose ($TCID_{50}$) assay using *A. castellanii* cells.

Lysate preparation

Lysate for Ribo-seq, RNA-seq and mim-tRNA-seq was prepared as described previously[28]. In brief, *A. castellanii* cells were seeded on 10 cm plates at 3×10^6 cells per ml supplemented with 10 ml of PYG medium. Amoeba cells were infected with APMV at a multiplicity of infection of 10. The plates were incubated for 1 h at room temperature to allow viral absorption, then the medium was replaced with fresh PYG medium. The medium replacement timing was set to 0 h.p.i., and APMV-infected cells were collected at 2, 4 and 8 h.p.i. For mock treatment, PYG medium was used and collected at 0 h.p.i. Two independent replicates were prepared for each time point.

Cells were treated with 100 μg ml^{-1} cycloheximide for 1 min, then scraped down and pelleted at 300*g* at 4 °C for 3 min, washed with 1 ml of PBS containing 100 μg of cycloheximide (Sigma–Aldrich) and 100 μg of chloramphenicol (Wako Pure Chemical Industries) and pelleted again at 300*g* at 4 °C for 2 min. The cell pellets were resuspended with 600 μl lysis buffer (20 mM Tris pH 7.5, 150 mM NaCl, 5 mM $MgCl_2$, 1 mM dithiothreitol, 1% Triton X-100, 100 μg ml^{-1} cycloheximide and 100 μg ml^{-1} chloramphenicol), treated with 5 μl of TURBO DNase (2 U μl^{-1}, Thermo Fisher Scientific) on ice for 10 min, then centrifuged at 20,000*g* at 4 °C for 10 min. The supernatant was stored at −80 °C before library construction. RNA concentration of cell lysates was measured with a Qubit RNA BR Assay Kit (Thermo Fisher Scientific).

Preparation of Ribo-seq library

Ribo-seq was performed as described previously[28]. The cell lysate containing 10 μg total RNA was incubated with 2 U of RNase I (LGC Biosearch Technologies) in a 300 μl reaction mixture at 25 °C for 45 min. The RNase digestion was stopped by adding 10 μl of SUPERase•In (Thermo Fisher Scientific). Ribosomes were isolated by sucrose cushion ultracentrifuged at 100,000 r.p.m. (543,000*g*) for 1 h at 4 °C with a TLA110 rotor and an Optima MAX-TL ultracentrifuge (Beckman Coulter). Subsequently, RNA was purified with TRIzol-LS reagent (Thermo Fisher Scientific) and a Direct-zol RNA Microprep kit (Zymo Research). RNA fragments of 17–35 nt were gel-purified after running polyacrylamide gel electrophoresis. The isolated RNA fragments were ligated to custom-made pre-adenylated linkers containing unique molecular identifiers and barcodes for library pooling using T4 RNA ligase 2, truncated KQ (New England Biolabs). rRNA was depleted using a Ribo-Zero Gold (Human/Mouse/Rat) kit (Illumina), followed by a pull-down using RNAClean XP beads (Beckman Coulter). The rRNA-depleted samples were reverse transcribed with ProtoScript II (New England Biolabs), circularized with CircLigase II (LGC Biosearch Technologies) and PCR-amplified using Phusion polymerase (New England Biolabs). The libraries were sequenced on an Illumina HiSeqX system (Illumina) with the 150 nt paired-end read option (Supplementary Table 1).

Preparation of RNA-seq library

Total RNA was purified from the cell lysate using TRIzol-LS and a Direct-zol RNA Microprep kit (Zymo Research). RNA-seq libraries were prepared with TruSeq Stranded Total RNA Library Prep Gold (Illumina). The library was sequenced on a HiSeqX system (Illumina) with the 150 nt paired-end reads option (Supplementary Table 1).

Preparation of mim-tRNA-seq library

The tRNA fraction was collected from the lysate using a mirVana miRNA Isolation Kit (Thermo Fisher Scientific) and deacylated by incubating at 37 °C for 45 min in 100 mM Tris–HCl pH 9.0. The library preparation scheme was adapted from the method for Ribo-seq[28], using 80 ng of tRNAs. Then, 2 μl of 1.25 μM reverse transcription primer (NI-802)[28] was hybridized to linker-ligated tRNA dissolved in 10 μl of RNase-free water by denaturing at 82 °C for 2 min and cooling at 25 °C for 5 min in a thermocycler. Reverse transcription was conducted in 21.6 mM Tris–HCl pH 7.5, 5.4 mM MgCl2 and 486 mM KCl containing 5.4 mM dithiothreitol, 0.54 U μl^{-1} SUPERase•In (Thermo Fisher Scientific) and 540 nM TGIRT-III (InGex) in an 18.5 μl reaction mixture and pre-incubated at 42 °C for 10 min in a thermocycler. Next, 2.5 μl of 10 mM dNTP was added to the tube to make a 20 μl reaction mixture and incubated at 49 °C for 16 h in a thermocycler. Subsequent circularization and PCR amplification were conducted as in the Ribo-seq[28]. The library was sequenced on a HiSeqX system (Illumina) with the 150 nt paired-end reads option (Supplementary Table 1).

Construction of a non-coding RNA database

We constructed a non-coding RNA (ncRNA) database by collecting annotated sequences from databases and de novo prediction. The annotated ncRNA sequences of *A. castellanii* were downloaded from the RNAcentral database (17 August 2023) and searched by queries '*Acanthamoeba castellanii*', which hit to the following two TAXONOMY levels, 'TAXONOMY 5755' and 'TAXONOMY 1257118' (RNAcentral Consortium, https://rnacentral.org)[62]. The TAXONOMY 5755 search identified 241 ncRNA records: 205 rRNAs, 32 small ncRNAs, 3 RNase P RNAs, 1 RNase MRP RNA and 1 group I intron. The TAXONOMY 1257118 search identified 205 ncRNA records: 44 rRNAs, 149 small non-coding RNAs, 1 RNase P RNA, 1 RNase MRP RNA, 4 SRP RNAs and 2 vault RNAs.

For de novo prediction, the nuclear genome sequence of *A. castellanii* was downloaded from the latest chromosome-scale genome assembly[14]. The mitochondrial (NC_001637.1) and APMV (NC_014649.1) genome sequences were downloaded from the RefSeq database and used for de novo ncRNA prediction. rRNA genes were predicted using RNAmmer (v.1.2)[63], and tRNA genes were predicted using tRNAscan-SE (v.2.0.12; parameters: -HQ for amoeba, -G -HQ for APMV, -mt -Q for mitochondria)[64].

Read mapping

For the Ribo-seq and RNA-seq reads, data were processed as described previously[65]. In brief, adapter trimming was performed with fastp (v.0.21.0)[66]. Reads were mapped to the ncRNA sequences using STAR (v.2.7.0a)[67] to remove reads that originated from rRNA genes and other ncRNA genes in silico. The remaining reads were mapped to the merged genomes of the virus, amoeba nucleus and mitochondria, using STAR (v.2.7.0a). BAM file indexing and read extraction were performed using SAMtools (v.1.10)[68]. Offsets for footprints of different lengths were determined by checking the enrichment of footprints around the start and stop codons of genes (Supplementary Table 3). The quality of ribosomal footprints was checked by mapping status around start and stop codons (Extended Data Figs. 2 and 3a).

The mim-tRNA-seq reads were quality controlled using fastqc (v.0.12.1; http://www.bioinformatics.babraham.ac.uk/projects/fastqc/), and regions after 97 nt (quality ≤ 20) were trimmed using fastx-trimmer (v.0.0.14; http://hannonlab.cshl.edu/fastx_toolkit/). The trimmed reads were mapped to the ncRNA sequences (except for tRNAs) using Bowtie2 to remove other ncRNAs[69]. The unmapped reads were extracted and mapped to the tRNA sequences using Bowtie2.

Gene filtering, quantification and normalization

To quantify gene expression levels, reads per kilobase per million mapped reads (RPKM) values were calculated for protein-coding genes in the amoeba and APMV genomes based on the total number of reads that uniquely aligned to the coding regions of the amoeba or virus, respectively.

Footprints that mapped to the first five codons (including the start codon) or the last five codons (including the stop codon) were not counted. Open reading frames with total RNA and footprint RPKM values < 10 in any replicate were discarded. After filtering, 10,575 and 955 protein-coding genes from the amoeba nuclear genome and APMV genome, respectively, remained for subsequent analyses.

Transcripts per million kilobase (TPM) values were used to compare host and viral gene expression levels. To analyse the gene expression patterns in the host or virus, TPM values were recalculated separately for the host and virus genes. Translation efficiency was calculated using DEseq2 (ref. 70) as a mean fold-change between footprint and read counts, considering replicates.

Gene clustering and enrichment analysis

After filtering lowly expressed genes, *Z*-score normalization was performed on each gene in one replicate. The optimal number of *K*-means clusters was determined based on TPM values using the R package factoextra (v.1.0.7; https://rpkgs.datanovia.com/factoextra/index.html). KEGG pathway and KEGG orthologue groups were assigned using the eggNOG-mapper webserver (v.2.1.1.2)[71] (http://eggnog-mapper.embl.de/) with the following settings: *e*-value < 1×10^{-5}, bit score ≥60, identity ≥60%, query coverage ≥20% and subject coverage ≥20%. The KEGG Pathway database for amoeba was built with the assigned KEGG Orthology terms using a homemade R code. Enrichment analyses were performed for the top 2,000 genes with the highest standard deviation using clusterProfiler (v.4.8.3)[72] (Supplementary Table 2).

Quantification of tRNA expression

For tRNA read mapping, reads that met the following criteria were retained: (1) length ≥20 bp; (2) uniquely mapped to tRNA genes that encode the same anticodons; (3) anticodon of mapped tRNA was not 'NNN', 'TTA' (that is, tRNA suppressor) or 'TCA' (that is, tRNA for selenocysteine); and (4) reads mapped to the same genome. These criteria ensured that reads with unique mapping and reads that mapped to multiple genes but encoded the same type of anticodon were kept for quantification.

The composition of the cellular tRNA pool was calculated as the proportion of tRNA species in each sample. Because tRNA and a codon can pair by wobble pairing, we used absolute adaptiveness (*W*) to measure the tRNA supply to each type of codon[30]. The *W*-score of a codon was computed as the weighted sum of the selection constraint (s_{ij}) and tRNA ratio (tRNA_j), considering both Crick's rules and wobble pairing. The selective constraint (s_{ij}) represents the difficulty of the pairing between codon *i* and anticodon *j*.

$$W_i = \sum_{j=1}^{n_i} (1 - s_{ij}) \mathrm{tRNA}_j \tag{1}$$

In brief, to infer s_{ij}, we performed Nelder–Mead optimization on Spearman's correlation between the expression level and computed tRNA adaptation index (tAI) of corresponding genes using the Python package scipy[73]. The tAI is a measure of the tRNA usage by coding sequences[30]. For a gene *g*, tAI_g was computed as the geometric mean of the relative adaptiveness w_i of its codons. If $\mathrm{tAI}_g = 1$, it indicates the gene *g* is well supported by the tRNA pool, whereas tAI_g close to 0 indicates that the gene is poorly supported.

$$\mathrm{tAI}_g = \left(\prod_{k=1}^{l_g} w_{i_{kg}} \right)^{\frac{1}{l_g}} \tag{2}$$

Here, i_{kg} is the codon at the *k*th position in the gene *g*, and l_g is the length of the gene in codons (excluding the stop codon). Consequently, tAI_g estimates the amount of adaptation of a gene *g* to its genomic tRNA pool.

In equation (2), the relative adaptiveness w_i is the normalized absolute adaptiveness (*W*-score). The relative adaptiveness w_i was calculated as the ratio between the W_i for each codon and the maximum *W*. Thus, $w_i = 1$ indicates that the codon *i* is the most adapted codon to the tRNA pool, and w_i close to 0 indicates that the codon is very poorly adapted.

Originally, the maximum *W* was set as the highest *W* among all codons. To avoid making this value biased to being much higher than other values, we used the geometric mean of the three highest *W* values (W_N) as the maximum *W* value for computation. W_N was used to calculate the relative adaptiveness of each codon.

$$W_N = \sqrt[3]{\prod_{i \in \mathrm{top3}} W_i} \tag{3}$$

$$w_i = \min\left(1, \frac{W_i}{W_N}\right) \tag{4}$$

After calculating tAI for each gene, we performed parameter optimization for s_{ij} using the top 2,000, 3,000, 4,000 and 5,000 amoeba genes based on the ranking of the footprint TPM separately and initialized the parameter set from [0, 0, 0, 0, 0], [0.25, 0.25, 0.25, 0.25, 0.25], [0.5, 0.5, 0.5, 0.5, 0.5], [0.75, 0.75, 0.75, 0.75, 0.75], [1, 1, 1, 1, 1]. The s_{ij} set was [1, 0, 1, 0.0065956, 0.90832489] ($\rho \approx 0.450$), which represents the wobble pairing between A:I, C:I, G:U, U:G and A:G (for the codon–ATA:tRNA–GAT pair), respectively.

Codon usage and balance score

For codon usage, U_i, the total number of occurrences of codon type i was computed by summing up the occurrences of codon i in the gene g, denoted as c_{ig}, weighted by the mRNA abundance $\mathrm{TPM}_{\mathrm{RNA},g}$.

$$U_i = \sum_{g=1}^{G} \mathrm{TPM}_{\mathrm{RNA},g} \times c_{ig} \tag{5}$$

We defined codon usage cu_i as a relative estimate of how often each codon is used. We computed cu_i by rescaling U_i to have a maximum value of 1. $U_{\max}$ in equation (7) is the geometric mean of U_i of the top three codons.

$$\mathrm{cu}_i = \min\left(1, \frac{U_i}{U_{\max}}\right) \tag{6}$$

$$U_{\max} = \sqrt[3]{\prod_{i \in \mathrm{top3}} U_i} \tag{7}$$

The balance score is defined as the ratio of tRNA availability, the relative adaptiveness of each codon (w_i), and codon usage (cu_i), then linearly rescaled to have a maximum value of 1 (ref. 31).

$$\mathrm{ratio}_i' = \frac{w_i}{\mathrm{cu}_i} \tag{8}$$

$$\mathrm{ratio}_{\max}' = \sqrt[3]{\prod_{i \in \mathrm{top3}} \mathrm{ratio}_i'} \tag{9}$$

$$\text{Balance score}_i = \min\left(1, \frac{\mathrm{ratio}_i'}{\mathrm{ratio}_{\max}'}\right) \tag{10}$$

A codon with ratio′ > 1 was defined as 'excessive tRNAs', indicating that the tRNA supply was higher than the codon usage, and ratio′ < 1 was defined as 'moderate tRNAs', indicating the tRNA supply was lower than the codon usage. The balance score is derived from this score by rescaling the range from 0 to 1.

Codon occupancy

The relative ribosome density at the kth codon of gene g (e_{kg}) was defined as the number of ribosome footprints at position k (RPF_{kg}) to the average number of ribosome footprints per codon of gene g ($\overline{\mathrm{RPF}}_g$).

$$e_{kg} = \frac{\mathrm{RPF}_{kg}}{\overline{\mathrm{RPF}}_g} \tag{11}$$

$$\overline{\mathrm{RPF}}_g = \frac{\mathrm{RPF}_g}{l_g} \tag{12}$$

The ribosome occupancy of a given type of codon i was the mean value of all positions where the corresponding codon is i. Only genes with $\overline{\mathrm{RPF}}_g > 1$ were included in this analysis. The first four codons in each gene were excluded when calculating codon occupancy[74]. Stop codons were also not included in the analysis.

Short footprint ratio

The short footprint ratio of codon type i was defined as the ratio between the number of short footprints (RPF_S) mapped to a codon k and the total number of footprints (RPF_T) mapped to codon type i. Genes that were used in the codon occupancy analysis were used in this study. The start and stop codons were excluded from the calculation. Short footprint ratio was repeated using 21–22 nt and 29–30 nt footprints alone to examine the signal (Extended Data Fig. 7a,b).

$$\text{Short footprint ratio for codon type } i = \frac{\mathrm{RPF}_{S,i}}{\mathrm{RPF}_{T,i}} \tag{13}$$

Identification of a putative pausing site

For each gene, we calculated the mean and standard deviation of the relative ribosome density as $\bar{e}_g$ and sd_g. We considered positions as putative pausing sites when $e_{k,g}$ exceeds the mean ($\bar{e}_g$) plus two standard deviations (s_{dg}) of the gene[34]. The number of putative paused sites was summed based on their codon type and the original gene. These numbers were normalized by the total occurrences of codon types and gene length, excluding the first four codons and the stop codon.

FUNCAT, sm-mRNA FISH, rRNA FISH and DAPI staining

A. castellanii, strain Neff (ATCC 30010) cells were seeded in PYG medium at 10^5 cells per ml in a 24-well plate (Thermo Fisher Scientific) with a final volume of 1 ml per well. The cells were incubated to attach to the dish bottom at 25 °C for at least 30 min. Subsequently, the cells were infected with APMV at a multiplicity of infection of 1. The plates were centrifuged for 30 min at 1,000*g* at room temperature to synchronize the infection. Then, the medium was exchanged for fresh PYG medium to minimize the possibility of re-infections.

For each well, the 1 ml cell solution was collected and transferred into a 1.5 ml tube (Eppendorf) and centrifuged at 5,000*g* for 5 min at room temperature. After removing 80% of the supernatant, the remaining volume was resuspended using a vortex. Then, 50 µl of this concentrated cell suspension was added to each well of a microscopy slide (Marienfeld). The cells were incubated for 1 h to attach to the microscopy slide. The supernatant was removed, and the cells were fixed using 4% paraformaldehyde for 10 min at room temperature. The cells were washed using Milli-Q water and permeabilized with 70% ethanol for 2 h at 4 °C.

FUNCAT, sm-mRNA FISH and rRNA FISH were performed as described previously[16]. FUNCAT was developed from bio-orthogonal noncanonical amino acid tagging[21,75–78]. In brief, homopropargylglycine was added at a concentration of 50 µM at least 30 min before sampling. To identify newly synthesized proteins, an azide-bearing affinity tag was covalently attached by 'click chemistry'. For this, 221 µl Page's amoeba saline buffer (PAS, ATCC medium 1323) was mixed with 12.5 µl of 100 mM sodium ascorbate and 12.5 µl of 100 mM aminoguanidine hydrochloride. Separately, 1.25 µl of 20 µM $CuSO_4$, 1.25 µl of 100 µM Tris[(1-hydroxypropyl-1H-1,2,3-triazol-4-yl)methyl]amine (THPTA) and 0.3 µl of 5 mM Cy3-azide dye were mixed and left to react in the dark for 3 min at room temperature. The two solutions were mixed carefully, and 10 µl was added to each well of the microscope slides. The slides were incubated in the dark for 30 min at room temperature and then washed with PAS.

For the sm-mRNA FISH, 35 20 nt probes were designed to target the *mcp* gene of APMV[16] using the Stellaris RNA FISH Probe Designer of LGC Biosearch Technologies (https://www.biosearchtech.com/support/tools/design-software/stellaris-probe-designer). To each well on the microscopy slides, 10 µl of hybridization buffer (2× SCC, 100 mg ml^{-1} dextran sulfate, 2 mM ribonucleoside-vanadyl complex, 0.2 mg ml^{-1} BSA, 1 mg ml^{-1} *E. coli* tRNA and 20% formamide) containing the probe mix (with each probe labelled with the fluorophore Cy5) was added at a working probe solution of 437.5 nM. The slides were placed

in a moist chamber and incubated at 37 °C for 20 h. The hybridization buffer was washed away with a wash buffer (2× SCC in nuclease-free water) at 39 °C for 10 min. Then, the slides were dipped in ice-cold water and air dried.

For the rRNA FISH, 10 µl of hybridization buffer (0.9 M NaCl, 20 mM Tris–HCl pH 8.0, 0.01% SDS and 25% formamide) and 1 µl of Euk516 probe (5′-GGAGGGCAAGTCTGGT-3′; labelled with the fluorophore Fluos) were added to each well of the microscopy slides. Hybridization was performed in moist chambers at 46 °C for 1.5 h. Subsequently, slides were washed with a wash buffer (20 mM Tris–HCl pH 8.0, 5 mM EDTA and 0.149 M NaCl) and kept in the wash buffer in a 50 ml tube at 48 °C for 10 min. Then, the slides were dipped in ice-cold Milli-Q water and air dried.

After the sm-mRNA FISH or rRNA FISH, DAPI (1 µg ml^{-1}) was added to the wells on the slides, incubated for 3 min and washed off with nuclease-free water and air dried. The slides were observed using a confocal laser-scanning microscope (Leica SP8).

Plasmid construction

The plasmid for exogenous expression (pAcasTBP-GFP) in amoeba cells was constructed as follows. A promoter sequence of the *A. castellanii* TBP gene, a fused ORF of the enhanced green fluorescence gene (GFP) and the neomycin resistance gene (NEO), and the SV40 early polyA sequence were PCR-amplified from *A. castellanii* genomic DNA, a synthetic plasmid (VectorBuilder), and pIZ/GFP[79], respectively, using KOD One PCR Master Mix (Dye-free 2×PCR Master Mix) (TOYOBO). These fragments were cloned into the pBR322 backbone, which was PCR-amplified from pUC19, using the In-Fusion HD Cloning Kit (TaKaRa). Subsequently, the SV40 late polyA sequence and an additional TBP promoter sequence were PCR amplified from the synthetic plasmid and the *A. castellanii* genomic DNA, respectively, and introduced between the GFP and NEO ORFs, using the In-Fusion HD Cloning Kit.

To generate pAcasTBP-Rluc-2A-GC-2A-Fluc and pAcasTBP-Rluc-2A-AT-2A-Fluc, fragments containing *Renilla* luciferase (RLuc) or firefly luciferase (FLuc) with self-cleavage 2 A sequences were PCR-amplified from plasmid psiCHECK2-2A-3xFLAG-SBP-2A[34]. The GC-rich sequence from the amoeba actin gene (BAESF_03529.mRNA.1)[14] and the AT-rich sequence from the APMV TBP ORF (RefSeq GeneID: 9925078, protein ID: YP_003986960.1) were PCR-amplified from *A. castellanii* and APMV genomic DNA, respectively. The amplified DNA was cloned into pAcasTBP-GFP that was linearized by PCR using the In-Fusion Snap Assembly Master Mix (TaKaRa).

APMV genomic DNA was prepared as described previously[80]. *A. castellanii* genomic DNA was prepared using NucleoSpin Tissue XS (TaKaRa).

Reporter assay

Amoeba cells at the growth phase were collected, and 5×10^5 cells were seeded in a 35 cm Nunc EasYDish (Thermo Fisher Scientific) with 2 ml of PYG medium. Then 5 µg of plasmids was transfected with 10 µl of PolyFect Transfection Reagent (Qiagen) in 100 µl of phosphate-buffered saline and 600 µl of PYG. One day after transfection, 1 ml of floating cells was transferred into a 10 cm Nunc EasYDish (Thermo Fisher Scientific) with 9 ml PYG and 10 µg ml^{-1} of G418 (Nacalai Tesque). After 3 days of incubation, the medium was replaced with 10 ml of fresh PYG with 50 µg ml^{-1} of G418 and incubated for 3 days. Subsequently, the cells were scraped with a cell lifter, and 5×10^5 cells were seeded into a 35 cm dish with 2 ml of PYG medium. APMV infection was performed as described above, and cells were collected with a cell lifter at 8 h.p.i. The cell suspension was centrifuged at 500*g* for 5 min at room temperature. The cell pellets were lysed with 200 µl of 1× Passive Lysis Buffer (Promega) and stored at −80 °C until the luciferase-activity measurement. FLuc and RLuc activities were measured using the Dual-Luciferase Reporter Assay System (Promega) and the GloMax-Multi Detection System (Promega). FLuc activity was normalized by RLuc activity. Infection experiments were independently performed twice, and luciferase activity was measured in two technical replicates.

Statistics and reproducibility

All statistical tests were done in R (v.4.3.1; R Core Team, 2023). Significance annotation in boxplots was done using the R package ggpubr (v.0.6.0; https://rpkgs.datanovia.com/ggpubr/). Exact *P* values for each subfigure are saved in Supplementary Tables 2 and 4. Representative images from over three independent biological replicates are shown (Fig. 5). Various conditions were tested once to optimize the tRNA-seq sequencing protocol (Extended Data Fig. 5).

No statistical methods were used to pre-determine sample sizes. The number of biological replicates for experiments were chosen based on previous studies and are similar to those generally used in the field. Data collection and analysis were not performed blind to the conditions of the experiments. Sequencing data were processed using standardized computational pipelines. There is no subjective scoring in our analysis.

Reporting summary

Further information on research design is available in the Nature Portfolio Reporting Summary linked to this article.

Data availability

The RNA-seq, Ribo-seq and mim-tRNA-seq results obtained in this study have been deposited in the NCBI Gene Expression Omnibus (GEO) database under the following accession numbers: RNA-seq, GSE276076; Ribo-seq, GSE276078; and mim-tRNA-seq, GSE276080. Source data are provided with this paper.

Code availability

The key codes for the analyses of RNA-seq, Ribo-seq and mim-tRNA-seq are publicly available via Github (https://github.com/ruixuan-zhang/Zhang_Lotte_GiantVirusRiboSeq) and Zenodo (https://doi.org/10.5281/zenodo.16555392)[81].

References

1. Dong, H., Nilsson, L. & Kurland, C. G. Co-variation of tRNA abundance and codon usage in *Escherichia coli* at different growth rates. *J. Mol. Biol.* **260**, 649–663 (1996).
2. Bae, H. & Coller, J. Codon optimality-mediated mRNA degradation: linking translational elongation to mRNA stability. *Mol. Cell* **82**, 1467–1476 (2022).
3. Hanson, G. & Coller, J. Codon optimality, bias and usage in translation and mRNA decay. *Nat. Rev. Mol. Cell Biol.* **19**, 20–30 (2018).
4. Abrahão, J., Araújo, R., Colson, P. & Scola, B. L. The analysis of translation-related gene set boosts debates around origin and evolution of mimiviruses. *PLoS Genet.* **13**, e1006532 (2017).
5. Schulz, F. et al. Giant viruses with an expanded complement of translation system components. *Science* **356**, 82–85 (2017).
6. Abrahão, J. et al. Tailed giant Tupanvirus possesses the most complete translational apparatus of the known virosphere. *Nat. Commun.* **9**, 749 (2018).
7. Schulz, F., Abergel, C. & Woyke, T. Giant virus biology and diversity in the era of genome-resolved metagenomics. *Nat. Rev. Microbiol.* **20**, 721–736 (2022).
8. Legendre, M. et al. mRNA deep sequencing reveals 75 new genes and a complex transcriptional landscape in *Mimivirus*. *Genome Res.* **20**, 664–674 (2010).
9. Rodrigues, R. A. L. et al. Analysis of a *Marseillevirus* transcriptome reveals temporal gene expression profile and host transcriptional shift. *Front. Microbiol.* **11**, 651 (2020).

10. Zhang, R., Endo, H., Takemura, M. & Ogata, H. RNA sequencing of Medusavirus suggests remodeling of the host nuclear environment at an early infection stage. *Microbiol. Spectr.* **9**, e00064-21 (2021).
11. Colson, P., Fournous, G., Diene, S. M. & Raoult, D. Codon usage, amino acid usage, transfer RNA and amino-acyl-tRNA synthetases in mimiviruses. *Intervirology* **56**, 364–375 (2013).
12. Willemsen, A., Manzano-Marín, A. & Horn, M. Novel high-quality amoeba genomes reveal widespread codon usage mismatch between giant viruses and their hosts. *Genome Biol. Evol.* **17**, evae271 (2025).
13. Raoult, D. et al. The 1.2-megabase genome sequence of *Mimivirus*. *Science* **306**, 1344–1350 (2004).
14. Matthey-Doret, C. et al. Chromosome-scale assemblies of *Acanthamoeba castellanii* genomes provide insights into *Legionella pneumophila* infection-related chromatin reorganization. *Genome Res.* **32**, 1698–1710 (2022).
15. Rigou, S. et al. Evolutionarily conserved grammar rules viral factories of amoeba-infecting members of the hyperdiverse *Nucleocytoviricota* phylum. *Proc. Natl Acad. Sci. USA* **122**, e2515074122 (2025).
16. Mayer, L., Nikolov, G., Kunert, M., Horn, M. & Willemsen, A. Mimivirus transcription and translation occur at well-defined locations within amoeba host cells. *J. Virol.* **99**, e0055425 (2025).
17. Fridmann-Sirkis, Y. et al. Efficiency in complexity: composition and dynamic nature of *Mimivirus* replication factories. *J. Virol.* **90**, 10039–10047 (2016).
18. Mutsafi, Y., Shimoni, E., Shimon, A. & Minsky, A. Membrane assembly during the infection cycle of the Giant Mimivirus. *PLoS Pathog.* **9**, e1003367 (2013).
19. Behrens, A., Rodschinka, G. & Nedialkova, D. D. High-resolution quantitative profiling of tRNA abundance and modification status in eukaryotes by mim-tRNAseq. *Mol. Cell* **81**, 1802–1815.e7 (2021).
20. Ingolia, N. T., Ghaemmaghami, S., Newman, J. R. S. & Weissman, J. S. Genome-wide analysis in vivo of translation with nucleotide resolution using ribosome profiling. *Science* **324**, 218–223 (2009).
21. Iwasaki, S. & Ingolia, N. T. The growing toolbox for protein synthesis studies. *Trends Biochem. Sci* **42**, 612–624 (2017).
22. Hussmann, J. A., Patchett, S., Johnson, A., Sawyer, S. & Press, W. H. Understanding biases in ribosome profiling experiments reveals signatures of translation dynamics in yeast. *PLoS Genet.* **11**, e1005732 (2015).
23. Santos, D. A., Shi, L., Tu, B. P. & Weissman, J. S. Cycloheximide can distort measurements of mRNA levels and translation efficiency. *Nucleic Acids Res.* **47**, 4974–4985 (2019).
24. Duncan, C. D. S. & Mata, J. Effects of cycloheximide on the interpretation of ribosome profiling experiments in *Schizosaccharomyces pombe*. *Sci. Rep.* **7**, 10331 (2017).
25. Sharma, P., Wu, J., Nilges, B. S. & Leidel, S. A. Humans and other commonly used model organisms are resistant to cycloheximide-mediated biases in ribosome profiling experiments. *Nat. Commun.* **12**, 5094 (2021).
26. Ingolia, N. T., Brar, G. A., Rouskin, S., McGeachy, A. M. & Weissman, J. S. The ribosome profiling strategy for monitoring translation in vivo by deep sequencing of ribosome-protected mRNA fragments. *Nat. Protoc.* **7**, 1534–1550 (2012).
27. McGlincy, N. J. & Ingolia, N. T. Transcriptome-wide measurement of translation by ribosome profiling. *Methods* **126**, 112–129 (2017).
28. Mito, M., Mishima, Y. & Iwasaki, S. Protocol for disome profiling to survey ribosome collision in humans and zebrafish. *STAR Protoc.* **1**, 100168 (2020).
29. Wu, C. C.-C., Zinshteyn, B., Wehner, K. A. & Green, R. High-resolution ribosome profiling defines discrete ribosome elongation states and translational regulation during cellular stress. *Mol. Cell* **73**, 959–970.e5 (2019).
30. dos Reis, M., Savva, R. & Wernisch, L. Solving the riddle of codon usage preferences: a test for translational selection. *Nucleic Acids Res.* **32**, 5036–5044 (2004).
31. Pechmann, S. & Frydman, J. Evolutionary conservation of codon optimality reveals hidden signatures of cotranslational folding. *Nat. Struct. Mol. Biol.* **20**, 237–243 (2013).
32. Juszkiewicz, S. & Hegde, R. S. Initiation of quality control during poly(A) translation requires site-specific ribosome ubiquitination. *Mol. Cell* **65**, 743–750.e4 (2017).
33. Sundaramoorthy, E. et al. ZNF598 and RACK1 regulate mammalian ribosome-associated quality control function by mediating regulatory 40s ribosomal ubiquitylation. *Mol. Cell* **65**, 751–760.e4 (2017).
34. Han, P. et al. Genome-wide survey of ribosome collision. *Cell Rep.* **31**, 107610 (2020).
35. Ishibashi, K. et al. Translation of zinc finger domains induces ribosome collision and Znf598-dependent mRNA decay in zebrafish. *PLoS Biol.* **22**, e3002887 (2024).
36. De Felipe, P. et al. E unum pluribus: multiple proteins from a self-processing polyprotein. *Trends Biotechnol.* **24**, 68–75 (2006).
37. Finkel, Y. et al. SARS-CoV-2 uses a multipronged strategy to impede host protein synthesis. *Nature* **594**, 240–245 (2021).
38. Bercovich-Kinori, A. et al. A systematic view on influenza induced host shutoff. *eLife* **5**, e18311 (2016).
39. Mutsafi, Y., Zauberman, N., Sabanay, I. & Minsky, A. Vaccinia-like cytoplasmic replication of the giant Mimivirus. *Proc. Natl Acad. Sci. USA* **107**, 5978–5982 (2010).
40. Heath, C. M., Windsor, M. & Wileman, T. Aggresomes resemble sites specialized for virus assembly. *J. Cell Biol.* **153**, 449–456 (2001).
41. Chen, M., Goorha, R. & Murti, K. G. Interaction of frog virus 3 with the cytomatrix. IV. Phosphorylation of vimentin precedes the reorganization of intermediate filaments around the virus assembly sites. *J. Gen. Virol.* **67**, 915–922 (1986).
42. Katsafanas, G. C. & Moss, B. Colocalization of transcription and translation within cytoplasmic poxvirus factories coordinates viral expression and subjugates host functions. *Cell Host Microbe* **2**, 221–228 (2007).
43. Schepis, A., Schramm, B., de Haan, C. A. M. & Locker, J. K. Vaccinia virus-induced microtubule-dependent cellular rearrangements. *Traffic* **7**, 308–323 (2006).
44. Novoa, R. R. et al. Virus factories: associations of cell organelles for viral replication and morphogenesis. *Biol. Cell* **97**, 147–172 (2005).
45. Netherton, C. L. & Wileman, T. Virus factories, double membrane vesicles and viroplasm generated in animal cells. *Curr. Opin. Virol.* **1**, 381–387 (2011).
46. Hein, M. Y. et al. Global organelle profiling reveals subcellular localization and remodeling at proteome scale. *Cell* **188**, 1137–1155.e20 (2025).
47. Serrano-Solís, V., Toscano Soares, P. E. & de Farías, S. T. Genomic signatures among *Acanthamoeba polyphaga* entoorganisms unveil evidence of coevolution. *J. Mol. Evol.* **87**, 7–15 (2019).
48. Sau, K., Gupta, S. K., Sau, S., Mandal, S. C. & Ghosh, T. C. Factors influencing synonymous codon and amino acid usage biases in Mimivirus. *Biosystems* **85**, 107–113 (2006).
49. Blanc-Mathieu, R. & Ogata, H. DNA repair genes in the Megavirales pangenome. *Curr. Opin. Microbiol.* **31**, 94–100 (2016).
50. Mihara, T. et al. Linking virus genomes with host taxonomy. *Viruses* **8**, 66 (2016).
51. Pavon-Eternod, M. et al. Vaccinia and influenza A viruses select rather than adjust tRNAs to optimize translation. *Nucleic Acids Res.* **41**, 1914–1921 (2013).
52. Monier, A., Claverie, J.-M. & Ogata, H. Horizontal gene transfer and nucleotide compositional anomaly in large DNA viruses. *BMC Genomics* **8**, 456 (2007).

53. Kijima, S., Hikida, H., Delmont, T. O., Gaïa, M. & Ogata, H. Complex genomes of early nucleocytoviruses revealed by ancient origins of viral aminoacyl-tRNA synthetases. *Mol. Biol. Evol.* **41**, msae149 (2024).
54. Koonin, E. V. & Yutin, N. Multiple evolutionary origins of giant viruses. *F1000Res.* **7**, 1840 (2018).
55. Michely, S. et al. Evolution of codon usage in the smallest photosynthetic eukaryotes and their giant viruses. *Genome Biol. Evol.* **5**, 848–859 (2013).
56. Bailly-Bechet, M., Vergassola, M. & Rocha, E. Causes for the intriguing presence of tRNAs in phages. *Genome Res.* **17**, 1486–1495 (2007).
57. Yang, J. Y. et al. Degradation of host translational machinery drives tRNA acquisition in viruses. *Cell Systems* **12**, 771–779.e5 (2021).
58. Chaikeeratisak, V. et al. Subcellular organization of viral particles during maturation of nucleus-forming jumbo phage. *Sci. Adv.* **8**, eabj9670 (2022).
59. den Boon, J. A. & Ahlquist, P. Organelle-like membrane compartmentalization of positive-strand RNA virus replication factories. *Annu. Rev. Microbiol.* **64**, 241–256 (2010).
60. Corsaro, D., Mrva, M., Colson, P. & Walochnik, J. Validation and redescription of *Acanthamoeba terricola* Pussard, 1964 (Amoebozoa: Acanthamoebidae). *Eur. J. Protistol.* **94**, 126091 (2024).
61. La Scola, B. et al. A giant virus in amoebae. *Science* **299**, 2033 (2003).
62. RNAcentral Consortium. RNAcentral 2021: secondary structure integration, improved sequence search and new member databases. *Nucleic Acids Res.* **49**, D212–D220 (2021).
63. Lagesen, K. et al. RNAmmer: consistent and rapid annotation of ribosomal RNA genes. *Nucleic Acids Res.* **35**, 3100–3108 (2007).
64. Chan, P. P., Lin, B. Y., Mak, A. J. & Lowe, T. M. tRNAscan-SE 2.0: improved detection and functional classification of transfer RNA genes. *Nucleic Acids Res.* **49**, 9077–9096 (2021).
65. Kashiwagi, K. et al. eIF2B-capturing viral protein NSs suppresses the integrated stress response. *Nat. Commun.* **12**, 7102 (2021).
66. Chen, S., Zhou, Y., Chen, Y. & Gu, J. fastp: an ultra-fast all-in-one FASTQ preprocessor. *Bioinformatics* **34**, i884–i890 (2018).
67. Dobin, A. et al. STAR: ultrafast universal RNA-seq aligner. *Bioinformatics* **29**, 15–21 (2013).
68. Li, H. et al. The Sequence Alignment/Map format and SAMtools. *Bioinformatics* **25**, 2078–2079 (2009).
69. Langmead, B. & Salzberg, S. L. Fast gapped-read alignment with Bowtie 2. *Nat. Methods* **9**, 357–359 (2012).
70. Love, M. I., Huber, W. & Anders, S. Moderated estimation of fold change and dispersion for RNA-seq data with DESeq2. *Genome Biol.* **15**, 550 (2014).
71. Cantalapiedra, C. P., Hernández-Plaza, A., Letunic, I., Bork, P. & Huerta-Cepas, J. eggNOG-mapper v2: functional annotation, orthology assignments, and domain prediction at the metagenomic scale. *Mol. Biol. Evol.* **38**, 5825–5829 (2021).
72. Wu, T. et al. clusterProfiler 4.0: a universal enrichment tool for interpreting omics data. *Innovation* **2**, 100141 (2021).
73. Virtanen, P. et al. SciPy 1.0: fundamental algorithms for scientific computing in Python. *Nat. Methods* **17**, 261–272 (2020).
74. Weinberg, D. E. et al. Improved ribosome-footprint and mRNA measurements provide insights into dynamics and regulation of yeast translation. *Cell Rep.* **14**, 1787–1799 (2016).
75. Landgraf, P., Antileo, E. R., Schuman, E. M. & Dieterich, D. C. BONCAT: metabolic labeling, click chemistry, and affinity purification of newly synthesized proteomes. *Methods Mol. Biol.* **1266**, 199–215 (2015).
76. Hatzenpichler, R. & Orphan, V. J. in *Hydrocarbon and Lipid Microbiology Protocols: Single-Cell and Single-Molecule Methods* (eds McGenity, T. J. et al.) 145–157 (Springer, 2016).
77. Dieterich, D. C., Link, A. J., Graumann, J., Tirrell, D. A. & Schuman, E. M. Selective identification of newly synthesized proteins in mammalian cells using bioorthogonal noncanonical amino acid tagging (BONCAT). *Proc. Natl Acad. Sci. USA* **103**, 9482–9487 (2006).
78. Dieterich, D. C. et al. In situ visualization and dynamics of newly synthesized proteins in rat hippocampal neurons. *Nat. Neurosci.* **13**, 897–905 (2010).
79. Kawaoka, S. et al. A role for transcription from a piRNA cluster in de novo piRNA production. *RNA* **18**, 265–273 (2012).
80. Hikida, H., Okazaki, Y., Zhang, R., Nguyen, T. T. & Ogata, H. A rapid genome-wide analysis of isolated giant viruses using MinION sequencing. *Environ. Microbiol.* **25**, 2621–2635 (2023).
81. Zhang, R. Giant virus creates subcellular environment to overcome codon–tRNA mismatch (including review). *Zenodo* https://doi.org/10.5281/zenodo.16555392 (2025).

Acknowledgements

Computation time was provided by the Supercomputer System, Institute for Chemical Research, Kyoto University, and the HOKUSAI SailingShip supercomputer facility at RIKEN. This study was supported by the Japan Society for the Promotion of Science (JP23KJ1258 (to R.Z.), JP18H02279 (to H.O.), JP22H00384 (to H.O.) and JP24H02307 (to S.I.)), The Japan Science Society (Sasakawa Scientific Research Grant 2022-4103 (to R.Z.)), RIKEN (TRIP initiative 'TRIP-AGIS' to S.I.) and the Japan Science and Technology Agency (JPMJFS2123 (to R.Z.)). A.W. acknowledges funding from the European Union's Horizon 2020 research and innovation programme under the Marie Sklodowska-Curie grant agreement number 891572 and the European Union (European Research Council, CHIMERA, 101039843). Views and opinions expressed are, however, those of the author(s) only and do not necessarily reflect those of the European Union or the European Research Council Executive Agency. Neither the European Union nor the granting authority can be held responsible for them. APMV was provided by B. La Scola, Aix-Marseille Université, Marseille, France. R.Z. was a recipient of a fellowship from Japan Society for the Promotion of Science (DC2) and was supported by International Short-term Exchange Program for Young Researchers by the ICR-iJURC Kyoto University. We thank M. Biswas for editing a draft of this manuscript. We thank M. Imanishi for technical assistance on the reporter assay.

Author contributions

Conceptualization, R.Z., L.M., H.H., A.W., S.I. and H.O.; methodology, M.M., A.W., Y.S. and S.I.; formal analysis, R.Z. and L.M.; investigation, R.Z., L.M., H.H., Y.S. and M.M.; writing—original draft, R.Z., L.M., S.I. and H.O.; writing—review and editing, R.Z., L.M., H.H., Y.S., M.M., A.W., S.I. and H.O.; visualization, R.Z. and L.M.; supervision, H.H., Y.S., A.W., S.I. and H.O.; project administration, S.I. and H.O.; funding acquisition, R.Z., A.W., S.I. and H.O.

Competing interests

S.I. is a member of the *Scientific Reports* editorial board. The other authors declare no competing interests.

Additional information

Extended data is available for this paper at https://doi.org/10.1038/s41564-025-02234-x.

Supplementary information The online version contains supplementary material available at https://doi.org/10.1038/s41564-025-02234-x.

Correspondence and requests for materials should be addressed to Shintaro Iwasaki or Hiroyuki Ogata.

Peer review information *Nature Microbiology* thanks Athanasios Zervas and the other, anonymous, reviewer(s) for their contribution to the peer review of this work. Peer reviewer reports are available.

Reprints and permissions information is available at www.nature.com/reprints.

Publisher's note Springer Nature remains neutral with regard to jurisdictional claims in published maps and institutional affiliations.

Open Access This article is licensed under a Creative Commons Attribution 4.0 International License, which permits use, sharing, adaptation, distribution and reproduction in any medium or format, as long as you give appropriate credit to the original author(s) and the source, provide a link to the Creative Commons licence, and indicate if changes were made. The images or other third party material in this article are included in the article's Creative Commons licence, unless indicated otherwise in a credit line to the material. If material is not included in the article's Creative Commons licence and your intended use is not permitted by statutory regulation or exceeds the permitted use, you will need to obtain permission directly from the copyright holder. To view a copy of this licence, visit http://creativecommons.org/licenses/by/4.0/.

© The Author(s) 2026

https://doi.org/10.1038/s41564-025-02234-x

Extended Data Table 1 | Average tRNA supply (*W* score) for AU3 and GC3 codons in each sample and *p* value from Wilcoxon rank sum test (one-sided)

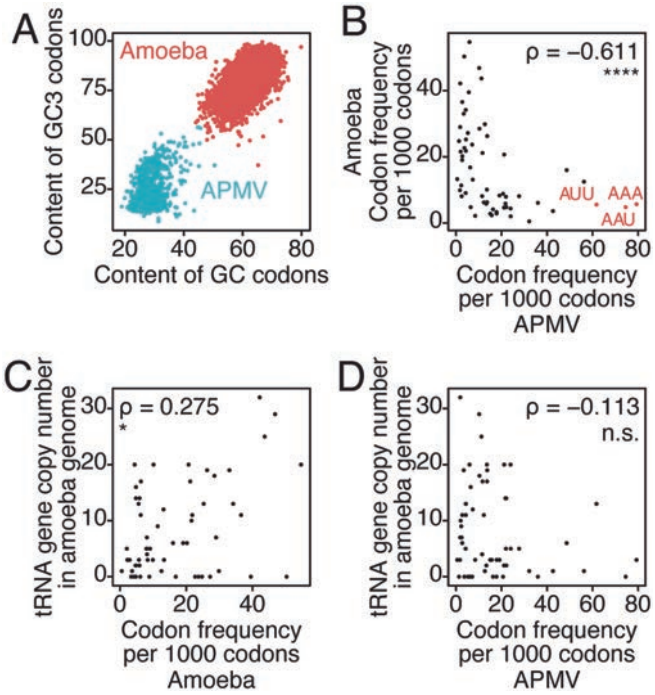
Sample	Codon type		*p* value	
	AU3	GC3	AU3<GC3	AU3>GC3
R1 0 hpi	2.1672	2.8443	0.0587	0.9429
R2 0 hpi	2.1429	2.8509	0.0450	0.9563
R1 2 hpi	2.1709	2.8497	0.0587	0.9429
R2 2 hpi	2.1463	2.8408	0.0457	0.9557
R1 4 hpi	2.1051	2.8212	0.0587	0.9429
R2 4 hpi	2.0956	2.8264	0.0464	0.9550
R1 8 hpi	2.1713	2.8126	0.0696	0.9323
R2 8 hpi	2.1598	2.8240	0.0580	0.9437

https://doi.org/10.1038/s41564-025-02234-x

Extended Data Table 2 | Average balance score for AU3 and GC3 codons in each sample and *p* value from Wilcoxon rank sum test (one-sided)

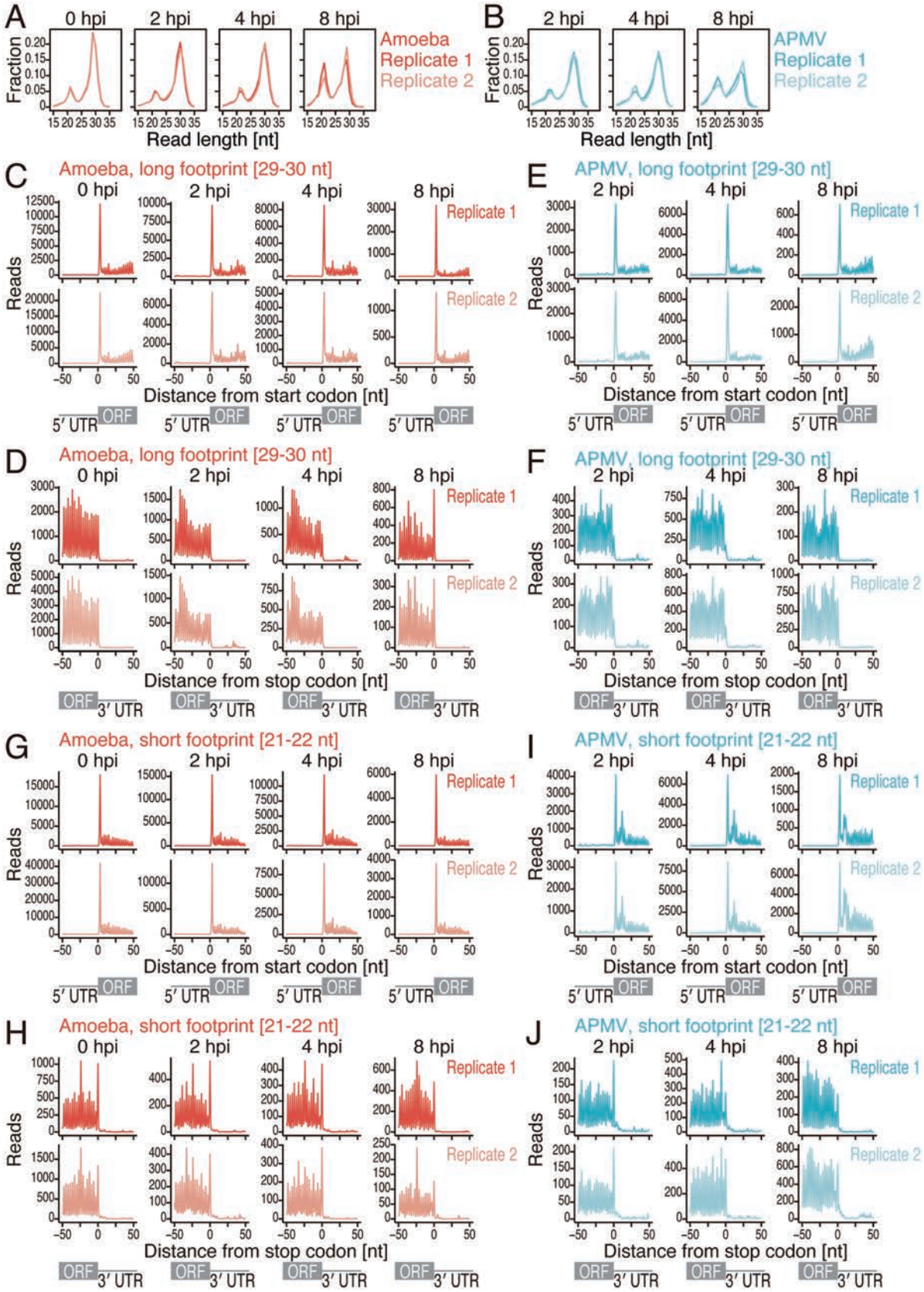
Sample	Codon type		*p* value	
	AU3	GC3	AU3<GC3	AU3>GC3
R1 0 hpi	0.3858	0.0991	1.0000	1.2017e-06
R2 0 hpi	0.3656	0.0979	1.0000	1.2017e-06
R1 2 hpi	0.3024	0.3227	2.5347e-01	7.5113e-01
R2 2 hpi	0.2568	0.3004	1.8112e-01	8.2265e-01
R1 4 hpi	0.2116	0.3451	9.1690e-03	9.9118e-01
R2 4 hpi	0.1773	0.3326	3.7242e-03	9.9643e-01
R1 8 hpi	0.1445	0.3236	5.2970e-04	9.9950e-01
R2 8 hpi	0.0796	0.3099	1.5285e-06	1.0000

https://doi.org/10.1038/s41564-025-02234-x



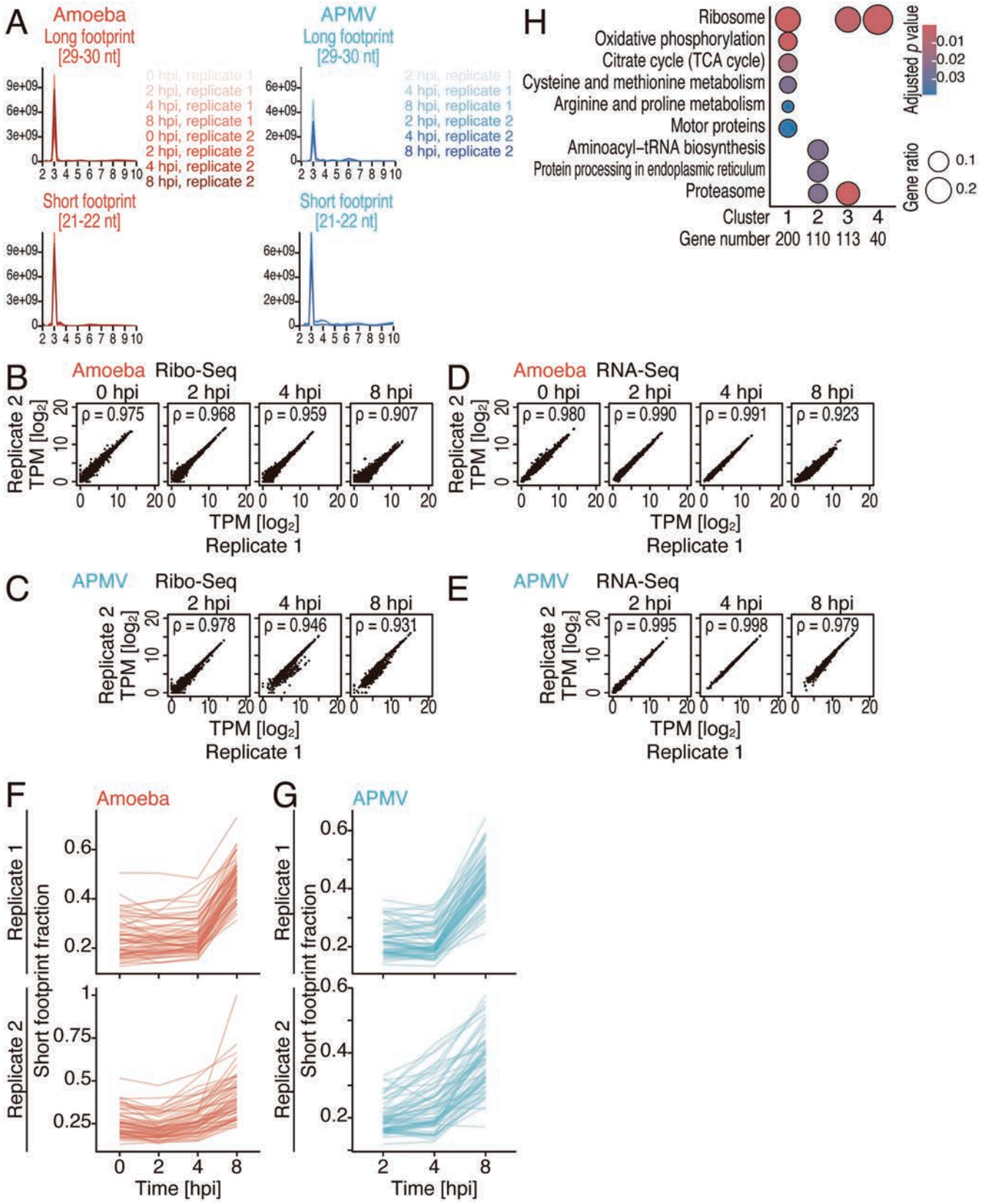
Extended Data Fig. 1 | Codon usage difference between amoeba and APMV genomes. (**a**) Correlation between G + C content of codons and G + C content of the 3rd position of codons in amoeba (red) and APMV (light blue) mRNAs. (**b**) Correlation between codon frequency per 1000 codons in amoeba and APMV mRNAs. (**c**) Correlation between codon frequency per 1000 codons of amoeba mRNAs and corresponding tRNA copy number in the amoeba genome. (**d**) Correlation between codon frequency per 1000 codons of APMV mRNAs and corresponding tRNA copy number in the amoeba genome. ρ, Spearman's correlation coefficient (two-tailed). ns, not significant; *, $p < 0.05$; **, $p < 0.01$; ***, $p < 0.001$; ****, $p < 0.0001$.

https://doi.org/10.1038/s41564-025-02234-x



Extended Data Fig. 2 | Ribosome footprints mapping around start and stop codon. (**a, b**) Distribution of ribosome footprint length at different infection stages. Reads originating from amoeba and APMV mRNAs were analysed separately. hpi, hours post-infection. (**c**–**j**) Metagene plots of the relative footprint distribution around start codons (**c, e, g**, and **i**) and stop codons (**d, f, h**, and **j**) at different infection stages. Long (29-30 nt, **c**–**f**) and short (21-22 nt, **g**–**j**) footprints were analyzed separately. Reads originating from amoeba (**c, d, g**, and **h**) and APMV (**e, f, i**, and **j**) mRNAs were analysed separately.

https://doi.org/10.1038/s41564-025-02234-x

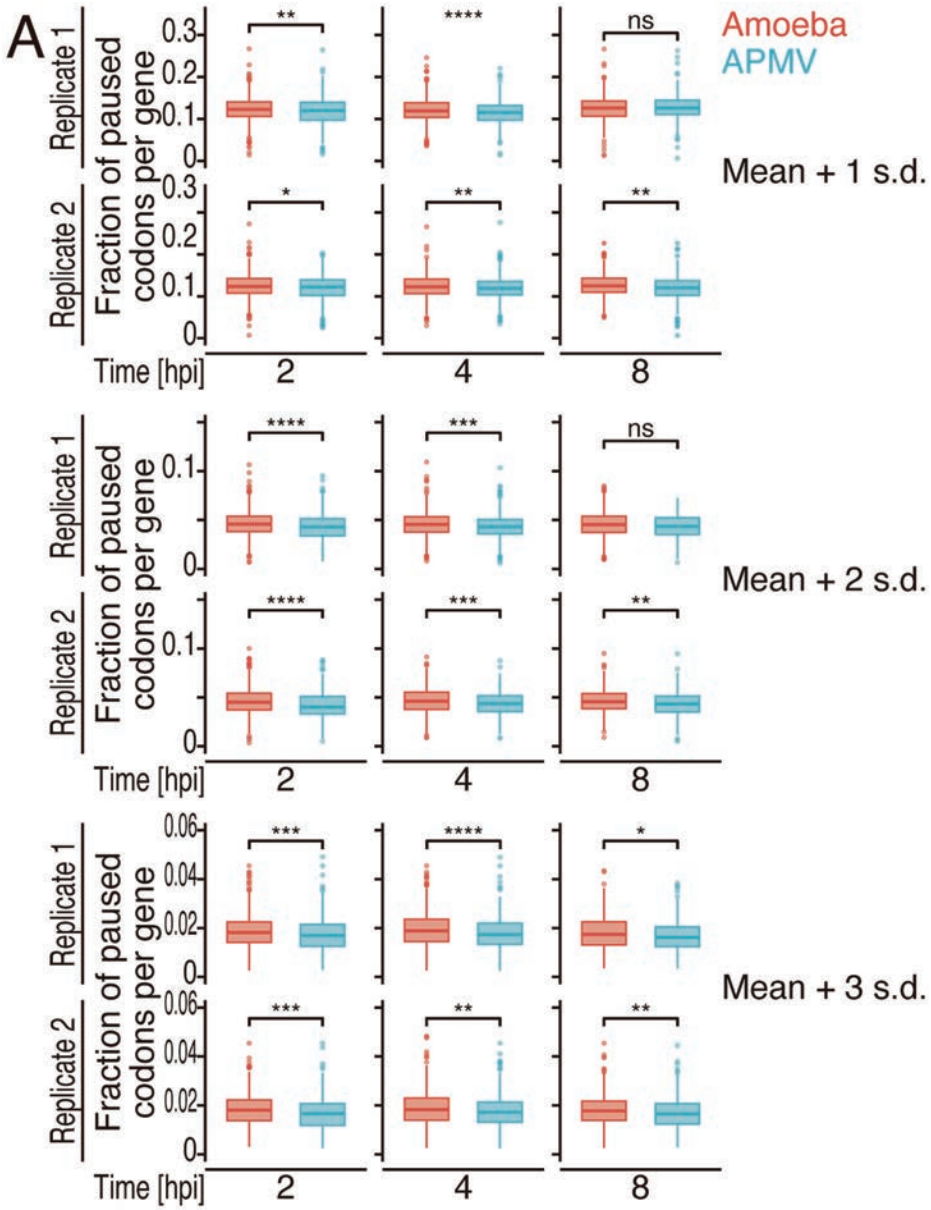


Extended Data Fig. 3 | See next page for caption.

https://doi.org/10.1038/s41564-025-02234-x

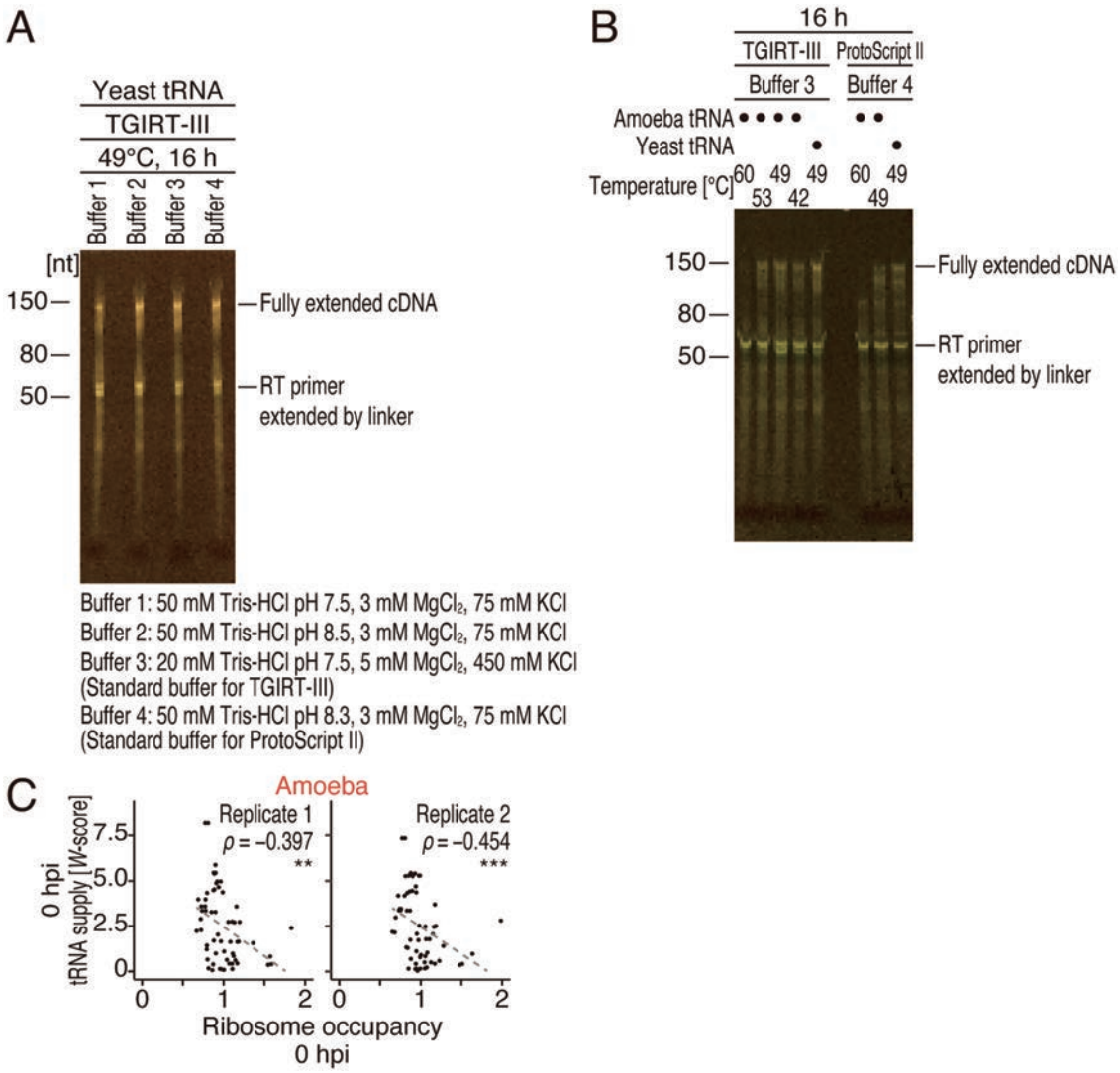
Extended Data Fig. 3 | Characterization of Ribo-Seq and RNA-Seq data. (**a**) Discrete Fourier transform of long (29-30 nt, top) and short (21-22 nt, bottom) footprints downstream of the start codon of the amoeba (left) and APMV (right) at different infection stages. (**b-e**) Scatter plots of the transcripts per kilobase million (TPM) values from two independent biological replicates for ribosomal footprints (**b, c**) and mRNAs (**d, e**) at different infection stages. (**f, g**) Short footprint accumulation during viral infection. Short footprint ratios on each codon type in amoeba (**f**) and APMV (**g**) mRNAs at different infection stages. (**h**) Enriched KEGG pathways in each host gene cluster. The colour scale for significance and the size scale for the gene ratio in each category are shown. The *p* values were calculated by the hypergeometric distribution implemented in the enrichGO function in clusterProfiler. The Benjamini–Hochberg method was used to control the false discovery rate. The cutoffs for the *p* value and *q*-value were both 0.05.

https://doi.org/10.1038/s41564-025-02234-x



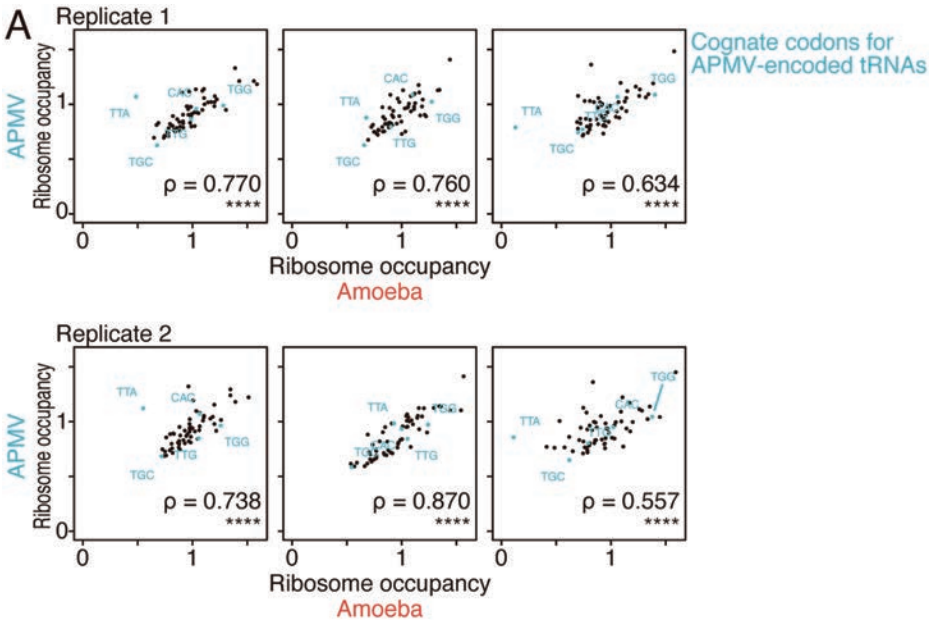
Extended Data Fig. 4 | Detection of paused codons per gene. (**a**) Box plots of the fraction of paused codons per gene in the amoeba and APMV genomes at different infection stages with different cutoffs for the paused codons. Note that the middle panels are the same plot as Fig. 2d. The median (centre line), upper/lower quartiles (box limits), 1.5× interquartile range (whiskers), and outliers (points) are shown. The p values were calculated by the one-sided Wilcoxon rank sum test. ns, not significant; *, $p < 0.05$; **, $p < 0.01$; ***, $p < 0.001$; ****, $p < 0.0001$.

https://doi.org/10.1038/s41564-025-02234-x



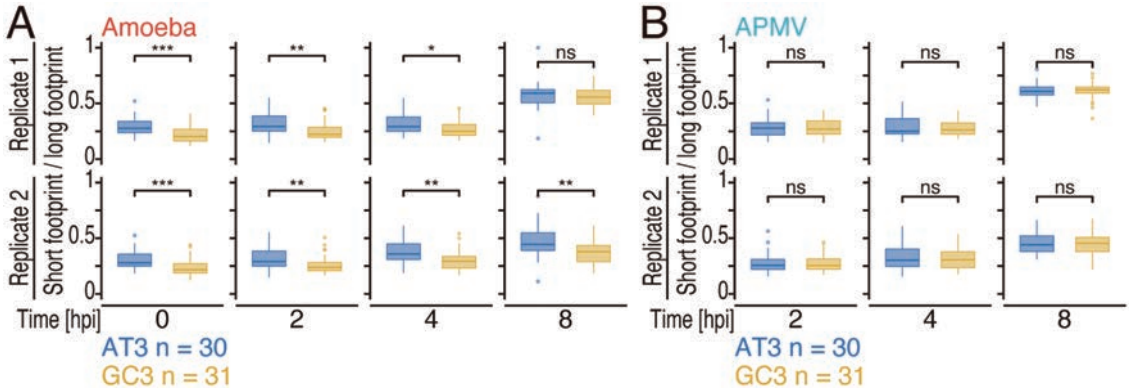
Extended Data Fig. 5 | Optimization of library preparation for mim-tRNA-Seq. (**a, b**) Optimization of the reverse transcription condition was conducted using titrating buffers, the reverse transcriptases TGIRT-III and ProtoScript II, and temperatures. Linker-ligated tRNAs (from yeasts or amoebae) at the 3′ end were used for the experiments. (**c**) Comparison of tRNA supply (W-score) and ribosome occupancy for amoeba mRNAs in the growing condition. ρ, Spearman's correlation coefficient (two-tailed). **, $p < 0.01$; ***, $p < 0.001$.

https://doi.org/10.1038/s41564-025-02234-x



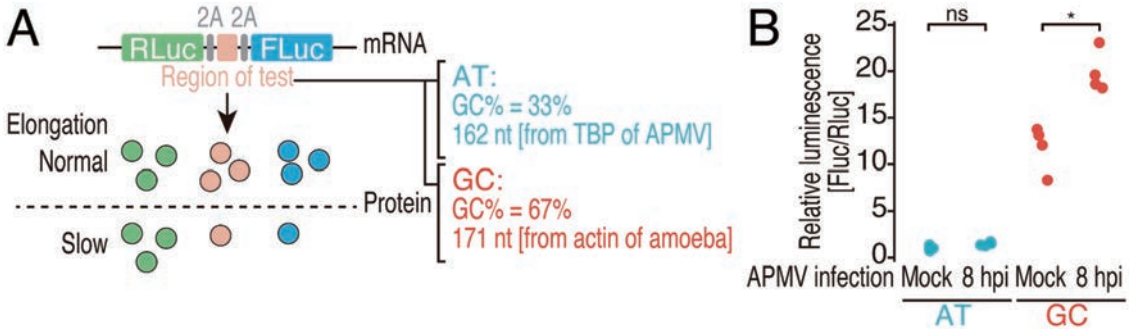
Extended Data Fig. 6 | Correlationbetween amoeba and APMV ribosome occupancy. (**a**) Scatter plots of the codon-specific ribosome occupancy on amoeba (horizontal axis) and APMV (vertical axis) mRNAs at different infection stages. Cognate codons of APMV-encoded tRNAs were coloured in pink. hpi, hours post-infection; ρ, Spearman's correlation coefficients (two-tailed); ****, $p < 0.0001$.

https://doi.org/10.1038/s41564-025-02234-x



Extended Data Fig. 7 | The short footprint/long footprint ratio at different infection stages. (**a**, **b**) Box plots of the short footprint/long footprint ratio on AU3 and GC3 codons in amoeba (**a**) and APMV (**b**) mRNAs at different infection stages. AU3, codons ending with A or U; GC3, codons ending with G or C; hpi, hours post-infection. The median (centre line), upper/lower quartiles (box limits), 1.5× interquartile range (whiskers), and outliers (points) are shown. The p values were calculated by the one-sided Wilcoxon rank sum test. ns, not significant; *, $p < 0.05$; **, $p < 0.01$; ***, $p < 0.001$; ****, $p < 0.0001$.

https://doi.org/10.1038/s41564-025-02234-x



Extended Data Fig. 8 | Reporter assay to monitor ribosome pausing during infection. (**a**) Schematic of reporter mRNAs used in this study. Rluc, Renilla luciferase; Fluc, firefly luciferase. (**b**) Relative Fluc/Rluc luminescence (the average values of the AT repoter with mock infection was set as 1). Individual data points (n = 4) are shown. The p values were calculated by the one-sided Wilcoxon rank sum test. ns, not significant; *, $p < 0.05$.

nature portfolio

Corresponding author(s): Hiroyuki Ogata

Last updated by author(s): Nov 17, 2025

Reporting Summary

Nature Portfolio wishes to improve the reproducibility of the work that we publish. This form provides structure for consistency and transparency in reporting. For further information on Nature Portfolio policies, see our Editorial Policies and the Editorial Policy Checklist.

Statistics

For all statistical analyses, confirm that the following items are present in the figure legend, table legend, main text, or Methods section.

n/a	Confirmed	
☐	☒	The exact sample size (*n*) for each experimental group/condition, given as a discrete number and unit of measurement
☐	☒	A statement on whether measurements were taken from distinct samples or whether the same sample was measured repeatedly
☐	☒	The statistical test(s) used AND whether they are one- or two-sided *Only common tests should be described solely by name; describe more complex techniques in the Methods section.*
☒	☐	A description of all covariates tested
☐	☒	A description of any assumptions or corrections, such as tests of normality and adjustment for multiple comparisons
☐	☒	A full description of the statistical parameters including central tendency (e.g. means) or other basic estimates (e.g. regression coefficient) AND variation (e.g. standard deviation) or associated estimates of uncertainty (e.g. confidence intervals)
☐	☒	For null hypothesis testing, the test statistic (e.g. *F*, *t*, *r*) with confidence intervals, effect sizes, degrees of freedom and *P* value noted *Give P values as exact values whenever suitable.*
☒	☐	For Bayesian analysis, information on the choice of priors and Markov chain Monte Carlo settings
☒	☐	For hierarchical and complex designs, identification of the appropriate level for tests and full reporting of outcomes
☒	☐	Estimates of effect sizes (e.g. Cohen's *d*, Pearson's *r*), indicating how they were calculated

Our web collection on statistics for biologists contains articles on many of the points above.

Software and code

Policy information about availability of computer code

Data collection	Ribosome profiling, RNA-Seq, and tRNA-Seq data were collected using HiSeq X (Illumina)
Data analysis	fastp v.0.21.0, STAR v.2.7.0a, SAMtools v.1.10, fastqc v.0.12.1, fastx-trimmer v.0.0.14, Bowtie2, RNAmmer v.1.2, tRNAscan-SE v.2.0.12, factoextra v.1.0.7, eggNOG-mapper webserver v.2.1.1.2, clusterProfiler v.4.8.3, ggpubr v.0.6.0, R v.4.3.1. For quantification of ribosomal footprints and RNA-Seq reads, a custom script was used (https://github.com/ingolia-lab/RiboSeq) Scripts for analysis and figures of high-resolution have been uploaded to zenodo under doi: 10.5281/zenodo.16555392

For manuscripts utilizing custom algorithms or software that are central to the research but not yet described in published literature, software must be made available to editors and reviewers. We strongly encourage code deposition in a community repository (e.g. GitHub). See the Nature Portfolio guidelines for submitting code & software for further information.

Data

Policy information about availability of data

All manuscripts must include a data availability statement. This statement should provide the following information, where applicable:

- Accession codes, unique identifiers, or web links for publicly available datasets
- A description of any restrictions on data availability
- For clinical datasets or third party data, please ensure that the statement adheres to our policy

The RNA-Seq, Ribo-Seq, and mim-tRNA-Seq results obtained in this study have been deposited in the National Centre for Biotechnology Information (NCBI) database under following accession numbers.

RNA-Seq: GSE276076 (https://www.ncbi.nlm.nih.gov/geo/query/acc.cgi?acc=GSE276076)
Ribo-Seq: GSE276078 (https://www.ncbi.nlm.nih.gov/geo/query/acc.cgi?acc=GSE276078)
tRNA-Seq: GSE276080 (https://www.ncbi.nlm.nih.gov/geo/query/acc.cgi?acc=GSE276080)

Research involving human participants, their data, or biological material

Policy information about studies with human participants or human data. See also policy information about sex, gender (identity/presentation), and sexual orientation and race, ethnicity and racism.

Reporting on sex and gender	Not applicable
Reporting on race, ethnicity, or other socially relevant groupings	Not applicable
Population characteristics	Not applicable
Recruitment	Not applicable
Ethics oversight	Note applicable

Note that full information on the approval of the study protocol must also be provided in the manuscript.

Field-specific reporting

Please select the one below that is the best fit for your research. If you are not sure, read the appropriate sections before making your selection.

☒ Life sciences ☐ Behavioural & social sciences ☐ Ecological, evolutionary & environmental sciences

For a reference copy of the document with all sections, see nature.com/documents/nr-reporting-summary-flat.pdf

Life sciences study design

All studies must disclose on these points even when the disclosure is negative.

Sample size	The study focuses on investigating the translation dynamics during the infection course of acanthamoeba castellanii mimivirus. We conducted a time-course virus infection experiments and collected samples at 0 (for mock infection), 2, 4, and 8 hours post infection. For each time point, two independent biological replicates were prepared. When conducting statistical test at gene level, all genes with enough reads were used. For codon-wise comparison, all codons except stop codon were used. Detailed information about the sample numbers is provided in the manuscript. These samples were used for ribosome profiling, RNA-Seq and tRNA-Seq, in line with the standard protocols in the field. No statistical methods were employed to predetermine the sample size. The sample size is similar to those generally employed in the field.
Data exclusions	No data were excluded from the analysis.
Replication	The reproducibility of our experiments was confirmed with two replicates tested for deep sequencing experiments. All experiments were repeatable. Results can be reproduced with the parameters and program provided in the methods section.
Randomization	Randomization is not relevant to this study.
Blinding	Blinding is not applicable to this study.

Reporting for specific materials, systems and methods

We require information from authors about some types of materials, experimental systems and methods used in many studies. Here, indicate whether each material, system or method listed is relevant to your study. If you are not sure if a list item applies to your research, read the appropriate section before selecting a response.

Materials & experimental systems

n/a	Involved in the study
☒	☐ Antibodies
☐	☒ Eukaryotic cell lines
☒	☐ Palaeontology and archaeology
☒	☐ Animals and other organisms
☒	☐ Clinical data
☒	☐ Dual use research of concern
☒	☐ Plants

Methods

n/a	Involved in the study
☒	☐ ChIP-seq
☒	☐ Flow cytometry
☒	☐ MRI-based neuroimaging

Eukaryotic cell lines

Policy information about cell lines and Sex and Gender in Research

Cell line source(s)	Acanthamoeba castellanii, strain Neff [American Type Culture Collection (ATCC), 30010]
Authentication	n.a
Mycoplasma contamination	n.a
Commonly misidentified lines (See ICLAC register)	n.a

Plants

Seed stocks	n.a
Novel plant genotypes	n.a
Authentication	n.a

4. 参考資料

京都大学化学研究所
化学関連分野の深化・連携を基軸とする先端・学際グローバル研究拠点
令和７年度国際共同利用・共同研究公募要領

京都大学化学研究所は、「化学に関する特殊事項の学理及び応用の研究を掌る」ために、化学を中心とする分野で基礎研究に重点を置いた先端研究に邁進して参りました。平成 22 年度より国立大学共同利用・共同研究拠点としての活動を始め、平成３０年にはそのグローバルな事業展開が評価され、文部科学大臣から国際共同利用・共同研究拠点として認定されました。これを受けて平成３１年度からは第１期、さらに令和３年の再認定を受けて同４年度からは第２期の国際共同利用・共同研究拠点活動を実施し、多様でグローバルな化学分野の共同研究を一層強力に推進すべく、さらなる事業展開を図っております。

つきましては、化学が関わる分野でご活躍の皆様のご意見・ご要望を尊重しつつ、世界の化学の基礎・応用研究を皆様とともに一層推進することを念頭に置き、下記の要領で令和７年度の拠点共同利用・共同研究の課題公募をさせて頂きたく存じます。

この公募に当たりましては、分野選択型（計画研究型）、課題提案型、連携・融合促進型および施設・機器利用型の四つに分けて研究課題を募集いたします。令和４年度から、分野選択型には従来の【基幹分野】の他に、化学研究所が重要分野と考える【特定分野】を設けました。これらの課題の実施に際しては当研究所の専任教員または客員教員との共同研究を基調といたしますが、いずれの課題でも後述の共通設備・機器・資料等のご利用が可能です。なお、各課題とも、海外研究者を研究代表者あるいは研究協力者とする国際共同研究（この場合、英語フォームで申請下さい）と、国内研究者を研究代表者とする国内共同研究を実施致します。これらの点も勘案いただき、本公募要領の詳細について十分ご確認の上、期日までにご申請下さいますようお願いいたします。

京都大学化学研究所長　　島川祐一
共同研究ステーション長　小野輝男

1. 研究期間

１年間（令和７年４月１日から令和８年３月３１日まで）。

2. 研究課題分類

下記のような分類（型）ごとに研究課題を募集いたします。いずれの課題についても、分類ないし分野の担当者もしくは当研究所で対応する共同研究者にご一報の上、ご申請下さい。

2-1. 分野選択型（計画研究型）研究課題

分野選択型（計画研究型）研究課題は、あらかじめ設定された分野に関して化学研究所内の研究者と共同で遂行する課題です。令和７年度は下記の基幹５分野および特定２分野について課題を公募いたします。７分野を合わせて、萌芽的な課題と発展的な課題をそれぞれ２５件程度、採択の予定です。

2-1-1. 分野選択型【基幹分野】研究課題

ビーム科学分野（担当者：若杉 昌徳；wakasugi.masanori.8z@kyoto-u.ac.jp）
基本テーマ：先進量子ビームの開発と新奇診断分析手法の創出
趣旨：レーザー、X 線、電子線、イオンビームなどの量子ビームの高度化とその先端的診断分析法への応用を進めます。また、これらの量子ビームを複合的に用いて、極微細領域での超高速化学・物理現象の解明を目指します。

元素科学分野（担当者：大木 靖弘; ohki@scl.kyoto-u.ac.jp）
基本テーマ：元素科学に基づく物質創製・機能創出
趣旨：元素の新たな特性を引き出し、この特性をもとに優れた機能を有する新物質を創製します。元素と社会との関わりを俯瞰した元素戦略研究も推進します。物質の機能は、構成元素の特性を相乗的に反映

して発現します。この発現機構を明らかとし、望みの機能を意のままに創出することを目指します。

バイオ情報学分野（担当者：阿久津 達也; takutsu@kuicr.kyoto-u.ac.jp）
基本テーマ：バイオ情報を含む複合情報の融合解析
趣旨：ゲノムやメタゲノムに代表される最新バイオ情報に立脚して、バイオ情報がいかに生体内や自然環境における化学現象と関わっているかを明らかにし、生命システムについての化学的理解の深化を図ります。さらに、その成果を応用して、ゲノム創薬やパーソナライズド医療などへの展開も目指します。

物質合成分野（担当者：村田 靖次郎; yasujiro@scl.kyoto-u.ac.jp）
基本テーマ：複合機能材料の戦略的創製
趣旨：異種材料のハイブリッド化・複合化ならびにナノサイズ化に重点を置き、新規な機能をもつ新世代材料や分子システムの創製を目指すとともに、生体の認識、応答、反応などの諸機能を担う例えば生体膜等も複合機能材料と捉え、機能物質と生命現象の化学的相関の解明も目指します。

現象解析分野（担当者：長谷川 健; htakeshi@scl.kyoto-u.ac.jp）
基本テーマ：複合測定に基づく物質解析
趣旨：化学を基盤とする多種の分光学的手法・解析的手法を複合的に駆使して、天然および人工物質の構造・性質を分子レベルから巨視的レベルまで階層的に理解・記述することを目指し、一方、その結果を還元することによって新たな物質科学の枠組みを構築する取組みも目指します。

2-1-2. 分野選択型【特定分野】研究課題

量子情報・スピントロニクス分野（担当者：小野 輝男; ono@scl.kyoto-u.ac.jp）
基本テーマ： 量子情報・スピントロニクス分野
趣旨：物理学、応用物理学、電子工学、磁気工学、材料科学、化学、情報科学および境界領域の新しい科学技術の創造により、古典情報と量子情報技術を融合・発展させ、Society 5.0 とポストコロナ社会で必要とされる将来情報技術の基盤構築を目指します。

スピン生命フロンティア分野（担当者：山子茂；yamago@scl.kyoto-u.ac.jp）
基本テーマ：MR 計測における新たなスピンプローブの開発
趣旨：新たなスピンプローブ（新規特性を持つプローブ、強いシグナルを生じるプローブ、特定の細胞や生体組織に局在するプローブなど）、およびその周辺技術の開発を行うことにより、MR 計測における新規原理・手法の創出へとつなげるとともに、分子科学・生命科学・生理科学が融合した新たな分野の開拓を目指します。

2-2. 課題提案型研究課題（担当者：寺西 利治; teranisi@scl.kyoto-u.ac.jp）
課題提案型研究課題は、前項１で設定した一つの分野に留まらない分野、あるいはそれ以外の分野について、化学関連分野の研究者から自由にご提案いただく課題です。萌芽的な課題と発展的な課題を、それぞれ２０件程度、採択の予定です。新分野の開拓につながるような課題を特に歓迎いたします。なお、緊急性・重要性が極めて高いと判断した課題については、前記の応募期日にかかわらず、直ちに採択することもあります。

2-3. 連携・融合促進型研究課題（担当者：栗原 達夫; kurihara@scl.kyoto-u.ac.jp）
連携・融合促進型研究課題は、化学関連分野における国内外の研究連携の強化を主目的とする共同研究課題です。国外も念頭に置く場合は、化学研究所の部局間国際学術交流締結先 (http://www.kuicr.kyoto-u.ac.jp/sites/international_exchange/agreement/ 参照)との共同研究を開始する場を求めていただくことも可能です。また、この目的に沿った研究集会の開催も本課題として応募いただけます。５件程度を採択する予定です。

2-4. 施設・機器利用型研究課題（担当者：二木 史朗; futaki@scl.kyoto-u.ac.jp）
施設・機器利用型研究課題は、拠点ホームページに記載の共通設備・機器・資料等（https://www.icr-

ijurc.jp/equipment/）の利用を主とする共同研究課題です。１５件程度を採択する予定です。

令和７年度国際共同利用・共同研究経費概算値

	経費上限／件*（千円）	
	国際共同研究	国内共同研究
分野選択型萌芽的研究	1,000	800
分野選択型発展的研究	2,000	1,500
課題提案型萌芽的研究	1,000	800
課題提案型発展的研究	2,000	1,500
連携・融合促進型研究	1,000	800
施設・機器利用型研究	1,000	800

*表中の金額は目安です。予算の状況に応じた減額もありえますことをご了解下さい。
経費内での備品費、消耗品費、旅費の配分は、申請者と化学研究所の共同研究者
が協議して決定下さい。特に、旅費については、地域性を勘案してご決定下さい。

3. 共同研究応募方法

3-1. 申請資格

国公私立大学、国公私立研究機関、独立行政法人等の専任研究者、または、これに準ずる者。

3-2. 申請書記入要領

申請に当たっては、該当する募集分類・分野の担当者もしくは当研究所で対応する共同研究者と、事前に研究課題、研究内容、研究経費に関して、必ずご協議下さい。対応する共同研究者は、当研究所の専任教員または令和７年度客員教員からお選び下さい。なお、教員のリストは下記の化学研究所ホームページをご参照下さい。

教員リスト　http://www.kuicr.kyoto-u.ac.jp/sites/research_activities/chemist/

また、対応する共同研究者をお決めになれない場合は、各分類・分野の担当者に、まず、ご相談ください。上記の表の経費上限は目安です。特に、経費内での備品費、消耗品費、旅費の配分については、当研究所で対応する共同研究者と十分にご協議の上で申請下さい。特に、旅費については、地域性を勘案してご申請下さい。

課題申請は、本要領に添付の分野選択型共同利用・共同研究申請書（様式１）、課題提案型共同利用・共同研究申請書（様式２）、連携・融合促進型共同利用・共同研究申請書（様式３）、施設・機器利用型共同利用・共同研究申請書（様式４）に必要事項を記入し、下記の要領で、化学研究所共同研究推進室にご提出下さい。

なお、各課題とも、海外研究者を研究代表者あるいは研究協力者とする国際共同研究も実施可能です。この場合、英語フォーム（Forms 1~4）の左肩の欄にチェックを入れて、当研究所の共同研究者に提出をご依頼下さい。

<記入上の注意事項>

1. ※を付した事項は当研究所で記入します。
2. 当研究所で対応する共同研究者は必ずご記入下さい。
3. 申請者（研究代表者）と共同研究者の役割分担を明記して下さい。事前に共同研究者の承諾を得ていただくことが必要です。
4. 申請書は３頁以内にまとめて下さい。

3-3. 提出期限および提出先

応募に当たっては、前記の申請書にご記入の上、令和７年１月１７日（金）までに、下記宛に電子メール添付書類（Word 書類）としてお送り下さい。

問い合わせ先
京都大学化学研究所 共同研究推進室
E-mail: icr-hub@scl.kyoto-u.ac.jp, 電話: (0774)38-3107

4. 課題選考と採択通知

応募課題の採否は、当研究所の共同研究委員会で審査し、運営評議会の承認を経て決定されます。審査に際しては、共同研究の申請内容だけでなく、予算枠や、共通設備・機器・資料の使用時間等も考慮いたします。採否の結果（内定）については、令和７年３月に当研究所の所長から研究代表者に通知いたします。

5. 研究の実施および研究成果報告

5-1. 研究経費等

研究代表者と当研究所で対応する共同研究者には、予算の範囲内で、研究経費（備品費および消耗品費）と旅費が支給されます。また、研究協力者（学生も含めることが可能です*）にも予算の範囲内で旅費が支給されます。共同研究の実施に当たっては、まず対応する共同研究者にご連絡下さい。なお、当研究所には、共同研究者のための宿泊施設はありません。

＊研究協力者について、学生の場合は原則として大学院生といたします。なお、傷害保険等に加入していることが必要です。

5-2. 研究成果報告

採択された研究課題については、研究成果報告書を次に記す作成要領に従って記載・提出していただきます。その報告書は、まとめて当研究所の国際共同利用・共同研究報告書集として公開させていただく予定です。また、その内容を研究成果報告会でご報告いただくことがあります。なお、報告会についての詳細は、採択課題の研究代表者に後日お知らせいたします。

5-3. 研究成果報告書の作成要領

分野選択型研究、課題提案型研究、施設・機器利用型研究については１頁、連携・融合促進型研究については２頁の報告書を（様式５）を用いて作成下さい。Ａ４版の用紙には１頁あたり１，２００字程度が記載できます。図表などカラーを用いても構いませんが、報告書集刊行の際はモノクロ印刷になることもありますので、その点をお含み置き下さい。

１頁の１行目の中央に研究課題名、３行目に右詰めで研究代表者の氏名と所属、５行目から本文を記載して下さい。なお、当研究所で対応した共同研究者は報告書の共著者とはせず、必要に応じて本文中に明記して下さい。また、国際共同研究の場合、報告書は英文でご作成ください。

5-4. 報告書の内容

形式は自由ですが、例えば、実験的研究では、目的、実験方法、実験結果、考察、成果報告（論文、学会発表等）をお書き下さい。なお、連携・融合促進型研究で研究集会を開催した場合には、研究集会のプログラム、参加者名簿（所属機関・部局・職名を明記）、および、作成された場合は要旨集またはプロシーディングスを添付して下さい。

5-5. 報告書の提出

提出締切日は、令和８年２月末日とします。電子ファイル（Word ファイルと PDF ファイル）を、下記宛にお送り下さい。なお、ファイル名は「課題番号＋代表者名（姓）」として下さい（例：2025-1 田中.doc、2025-1 田中.pdf）。

問い合わせ先
京都大学化学研究所 共同研究推進室
E-mail: icr-hub@scl.kyoto-u.ac.jp, 電話: (0774)38-3104

5-6. 研究成果の公開

学術論文などによる研究成果の公開に際しては、京都大学化学研究所の国際共同利用・共同研究として行われたことを明記して下さい。英文での謝辞例を次に示します。

謝辞例: This work was supported by the International Collaborative Research Program of Institute for Chemical Research, Kyoto University (grant # XXXX).
日本語での謝辞は、この英文表記に準ずるものとして下さい。

化学研究所　国際共共拠点 R7年度採択課題（応募 237件，採択 141件，採択率 59% 国際共同研究割合53%）

課題番号	研究代表者	研究代表者所属	化研内 研究協力者	型	選択 分野	実施 状況	国際	課題名（和文・英文）
2025-1	Michel Koenig	Laboratoire LULI, Ecole Polytechnique, CNRS Research Director	時田 茂樹	分野選択型	1	萌芽的	国際	マイクロキャピラリーを組み合わせた高感度X線分光器の開発 Development of high sensitive x-ray spectrometer using microcapillary
2025-2	Ma, Yue	RIKEN, Few-body Systems in Physics Laboratory, Senior Research Scientist	塚田 暁	分野選択型	1	発展的	国際	エネルギー敏感型ミュオンスピン回転（muSR）分光計の開発 III Development of energy sensitive muon spin rotation (muSR) spectrometer III
2025-3	Sohtaro KANDA	KEK	塚田 暁	分野選択型	1	発展的	国際	 Multi-particle Imager for Next-Generation Exotic Atom Spectroscopy
2025-4	Tamon KUSUMOTO	QST, Radiation Measurements Research	若杉 昌徳	分野選択型	1	萌芽的	国際	金ナノ粒子による放射線増感効果の線量率依存性 Clarification of the mechanism of dose rate dependence on the enhancement of biological effectiveness by gold nanoparticles
2025-5	石川 正純	北海道大学・大学院保健科学研究院・教授	若杉 昌徳	分野選択型	1	萌芽的		超高線量率照射（FLASH）のためのリアルタイム線量計の開発 Development of real-time dosimeter for ultra-high dose-rate irradiation (FLASH)
2025-6	木河 達也	京都大学・大学院理学研究科・助教	若杉 昌徳	分野選択型	1	萌芽的		水ベース液体シンチレータの開発と電子ビームを用いた性能評価 Development of the water-based liquid scintillator and performance evaluation using an electron beam
2025-7	井川 和代	岡山大学・中性子医療研究センター	若杉 昌徳	分野選択型	1	発展的		三次元培養口腔がんモデルに対するFLASH照射の生物化学的現象の解明 Biochemical Phenomena of FLASH Irradiation of Three-Dimensional Oral Cancer Models
2025-8	W. M. C. Sameera	Department of Chemistry and Molecular Biology, University of Gothenburg, Sweden, Researcher	大木 靖弘	分野選択型	2	発展的	国際	四核ニッケルヒドリドクラスター錯体によるC-H結合活性化の反応機構研究 On the mechanism of the C-H bond activation of hydrocarbons catalyzed by a $[Ni_4H_4(P^tBu_3)_4]$ cluster
2025-9	Yilin Hu	Professor at Department of Molecular Biology and Biochemistry, Department of Chemistry, University of California, Irvine	谷藤 一樹	分野選択型	2	発展的	国際	$[Mo_3S_4Fe]$クラスターによるCO_2からCH_4への変換機構解析 Mechanistic investigations into CO_2 to CH_4 conversion catalyzed by a $[Mo_3S_4Fe]$ clusters
2025-10	Mohamad Shazwan Shah Jamil	Department of Chemistry, Faculty of Science, Universiti Teknologi Malaysia, Senior Lecturer	伊豆 仁	分野選択型	2	萌芽的	国際	不活性炭化水素のホウ素化反応を志向した嵩高いハーフサンドイッチ型Rh錯体触媒の開発 Half-sandwich Rh Complexes Having Bulky Cp Ligand toward Borylation Catalyst of Inert Hydrocarbons
2025-11	Susana García Martín	Departamento de Química Inorgánica, Facultad de Ciencias Químicas, Universidad Complutense; Professor	島川 祐一	分野選択型	2	発展的	国際	 High-performance Fe-perovskites as oxygen electrodes for solid oxide fuel cells (SOFCs)
2025-12	Haichuan Guo	China Spallation Neutron Source Science Center (CSNS), Institute of High Energy Physics, Chinese Academy of Sciences, Assistant researcher	島川 祐一	分野選択型	2	発展的	国際	新規遷移金属複合アニオン化合物の合成と物性研究 Synthesis and physical properties research of new transition metal compounds with mixed-anions
2025-13	ALAKANANDA HAJRA	DEPARTMENT OF CHEMISTRY, VISVA-BHARATI UNIVERSITY, SANTINIKETAN-731235, INDIA; Associate Prof.	中村 正治	分野選択型	2	発展的	国際	 Photocatalytic C-H Silylation under visible-light enabled Fe-catalysis
2025-14	W. M. C. Sameera	Department of Chemistry and Molecular Biology, University of Gothenburg, Sweden, Researcher	中村 正治	分野選択型	2	発展的	国際	木本植物細胞壁中のリグニン分解反応の理論研究 Computational Study on Lignin Degradation Reaction in Woody Plant Cell Walls
2025-15	Silver-Hamill Turren-Cruz	Institute of Materials Science (ICMUV), University of Valencia, Principal investigator	若宮 淳志	分野選択型	2	発展的	国際	Sn-Pb混合型高性能ペロブスカイト太陽電池の開発 Development of Efficient Mixed Sn and Pb-based Perovskite Photovoltaics
2025-16	Kenichiro Kamei	New York University Abu Dhabi (NYUAD), Programs of Biology and Bioengineering, Associate Professor	廣理 英基	分野選択型	2	萌芽的	国際	テレヘルツ波を用いたヒト多能性幹細胞由来肝臓オルガノイドの高機能化 Functionalization of liver organoids from human pluripotent stem cells by using THz waves
2025-17	Taketo Handa	Columbia University, Department of Chemistry, Postdoctoral research scientist	廣理 英基	分野選択型	2	発展的	国際	高強度テラヘルツ磁場パルスによるファンデルワールス磁性半導体のスピン波励起 Spin-wave excitation of van der Waals magnetic semiconductors by intense terahertz magnetic field pulses

2025-18	近藤 美欧	東京科学大学・理学院化学系・教授	谷藤 一樹	分野選択型	2	発展的		電子移動制御を利用したナノ金属クラスター触媒の高活性化 Development of highly active metal cluster catalysts by using electron Transfer network
2025-19	小笠原 正道	徳島大学・大学院社会産業理工学研究部・教授	大木 靖弘	分野選択型	2	発展的		Cp-Fe-Cp軸の回転阻害に基づく「面不斉フェロセニルホスフィン配位子」の開発（2） Development of Novel Planar-Chiral Ferrocenylphosphine Ligands Based on the Restricted Cp-Fe-Cp Rotation: phase 2
2025-20	藤井 達生	岡山大学・環境生命自然科学学域・教授	後藤 真人	分野選択型	2	萌芽的		六方晶フェライトの磁気異方性を制御による広帯域ミリ波用電波吸収体の開発 Wideband millimeter wave absorber based on huge anisotropic hexagonal ferrites
2025-21	竹歳 絢子	横浜国立大学・大学院工学研究院・助教	中村 正治	分野選択型	2	発展的		高選択的官能基変換のためのニッケルクラスター触媒の開発 Development of nickel cluster catalysts for highly selective functionalization
2025-22	渡邊 浩	大阪大学・生命機能研究科・准教授	廣理 英基	分野選択型	2	萌芽的		オルソフェライトにおける高強度THz電場を用いたスピン制御 Spin control by high-power THz pulse in orthoferrite
2025-23	佐藤 駿丞	東北大学・理学研究科・准教授	廣理 英基	分野選択型	2	萌芽的		光誘起異常Hall効果の微視的機構に関する研究 Investigation on microscopic mechanism of light-induced anomalous Hall effects
2025-24	小布施 秀明	北海道大学・工学研究院・准教授	廣理 英基	分野選択型	2	萌芽的		トポロジカル・エッジ状態によるマグノン高次高調波発生 High-harmonic generation in magnonic systems with topological edge states
2025-25	Jinn-Moon Yang	National Yang Ming Chiao Tung University, Department of Biological Science and Technology/Institute of Bioinformatics & Systems Biology, Professor	阿久津 達也	分野選択型	3	発展的	国際	深層学習を用いたオミクスデータとモジュールに基づくネットワークデータの統合解析による腫瘍細胞分類 Integrating omics data and module-based network with deep learning to develop cancer type predictive models
2025-26	Jiangning Song	Monash University, Biomedicine Discovery Institute, Professor	阿久津 達也	分野選択型	3	発展的	国際	タンパク質のミスセンス突然変異による安定性の変化予測のための機械学習方式の開発 Developing machine learning approaches for prediction of protein stability changes upon missense mutations
2025-27	Eric Pelletier	CEA/Genoscope, UMR8030, Research Director	緒方 博之	分野選択型	3	発展的	国際	海洋巨大ウイルスの遺伝子機能プロファイリング Marine giant viruses functional profiling
2025-28	David Demory	CNRS, UMR7231, Sorbone Université, USR3579 Laboratoire de Biodiversité et Biotechnologies Microbiennes (LBBM), Chargé de recherche	遠藤 寿	分野選択型	3	発展的	国際	野外観測と数理モデルを融合した海洋プランクトン細胞溶解動態の解明 Dynamics of marine plankton cell lysis as revealed by field observation and mathematical modeling
2025-29	DAI HAI NGUYEN	Hokkaido University, Graduate School of Information Science and Technology, Associate Professor	馬見塚 拓	分野選択型	3	萌芽的	国際	グラフ構造データを用いた学習のための最適輸送に関する研究 A Study on Optimal Transport for Learning with Graph Structured Data
2025-30	高坂 智之	山口大学・中高温微生物研究センター・准教授	田村 武幸	分野選択型	3	萌芽的		遺伝子破壊株における発現量データとシミュレーション結果の比較解析 Comparison and analysis of expression data and simulation results in gene knockout strains
2025-31	Jose Nacher	東邦大学・理学部情報科学科・教授	阿久津 達也	分野選択型	3	萌芽的		確率的最小支配集合による複雑ネットワークの制御と解析 Control and Analysis of Complex Networks via Probabilistic Minimum Dominating Sets
2025-32	西村 陽介	海洋研究開発機構・生命理工学センター・特任研究員	緒方 博之	分野選択型	3	萌芽的		環境ウイルス情報を統合した次世代ウイルス分類ツールの開発 Development of a next generation tool for virus classification that integrates environmental viral information.
2025-33	武村 政春	東京理科大学・教養教育研究院・教授	緒方 博之	分野選択型	3	発展的		巨大ウイルス感染アメーバのトランスクリプトーム解析による宿主・巨大ウイルス相互作用の解明 Elucidation of host-giant virus interaction using transcriptomics of giant virus-infected acanthamoeba cells
2025-34	高尾 祥丈	福井県立大学・海洋生物資源学部・准教授	緒方 博之	分野選択型	3	萌芽的		海産原生生物ラビリンチュラゲノムに潜む新奇ウイルス「ミルスウイルス」の探索 Comprehensive search for the novel virus “Mirusivirus” hidden in the genome of marine protist Labyrinthulids
2025-35	大西 一光	帯広畜産大学・環境農学研究部門・教授	馬見塚 拓	分野選択型	3	発展的		機械学習による作物根の微生物叢の比較解析 Comparative analysis of microbiome in crop root using machine learning
2025-36	Steve Eichhorn	Bristol Composites Institute, University of Bristol, Professor	石田 紘一朗	分野選択型	4	発展的	国際	三次元セル構造を有するセルロースナノファイバー/ポリマーモノリス複合材料の創生 Fabrication of cellulose nanofiber/polymer monolith composite materials with 3D cell structures

2025-37	CHAOLUMEN	Inner Mongolia University (IMU), College of Chemistry and Chemical Engineering, Lecturer, Ph.D.	村田 靖次郎	分野選択型	4	発展的	国際	巨大分子ナノカーボンの合成 Synthesis of Wide-Surface Molecular Nanocarbons
2025-38	MARGETIC, Davor	Rudjer Boskovic Institute, Division of Organic Chemistry and Biochemistry, Laboratory for Physical Organic Chemistry, Prof. PhD, head of Laboratory	村田 靖次郎	分野選択型	4	発展的	国際	グアニジン官能基を有するベンゾ[c]フランの芳香族環同族体の探索 Exploration of aromatic-ring homologue of benzo[c]furan with guanidine functionality
2025-39	IL JEON	Sungkyunkwan University (SKKU), Department of Nano Engineering, Associate Professor	村田 靖次郎	分野選択型	4	発展的	国際	新しい分子手術法の開発を通じた内包フラーレンの拡張および新しい現象や応用先の探索 Advancing Molecular-Surgery Method for Expansion of Endohedral Fullerenes towards Novel Applications
2025-40	Chi-How Peng	National Taiwan University, Department of Chemistry, Professor	山子 茂	分野選択型	4	発展的	国際	 Elucidation of the mechanism of troponoid-mediated controlled radical polymerization
2025-41	Hyunjung Shin	Department of Energy Science, Sungkyunkwan University, Professor	若宮 淳志	分野選択型	4	発展的	国際	ペロブスカイト太陽電池の材料開発：デバイス特性と基礎特性の関係性 Exploration of perovskite solar cell composition: Correlating device performance and fundamental property
2025-42	JOSHY JOSEPH	CSIR-National Institute for Interdisciplinary Science and Technology, Thiruvananthapuram	若宮 淳志	分野選択型	4	発展的	国際	クロスリンク可能な正孔輸送材料を用いたペロブスカイト半導体デバイスの開発 Perovskite Device Engineering with Cross-linkable Hole Transport Materials
2025-43	若林 成知	鈴鹿医療科学大学・保健衛生学部医療栄養学科・教授	大木 靖弘	分野選択型	4	萌芽的		ホウ素の特性を活かした自己集合性アズレン誘導体の合成と会合状態・色調の関連 Synthesis of borane-functionalized azulene derivative, and the relationship between the aggregation state and color
2025-44	細川 三郎	京都工芸繊維大学・材料化学・准教授	島川 祐一	分野選択型	4	萌芽的		酸素吸蔵材料の開発 Exploration of oxygen insertion materials
2025-45	平井 智康	大阪工業大学・応用化学科・准教授	竹中 幹人	分野選択型	4	萌芽的		階層構造を基盤とする新規キラルシリカの開発 Development of novel chiral silica based on controlling of hierarchical structure
2025-46	岡 弘樹	東北大学・多元物質科学研究所・講師	竹中 幹人	分野選択型	4	萌芽的		有機高分子材料の重水素化技術の確立と中性子散乱による高次構造の解明 Establishment of deuteration technology for polymer materials and elucidation of higher-order structures by neutron scattering
2025-47	横田 慎吾	九州大学・大学院農学研究院・准教授	石田 紘一朗	分野選択型	4	萌芽的		液体界面におけるセルロースナノファイバー膜の粘弾性測定 Viscoelastic measurements of cellulose nanofiber films at fluid interface
2025-48	田原 弘量	横浜国立大学・工学研究院・准教授	猿山 雅亮	分野選択型	4	萌芽的		ナノ粒子超構造体における量子協同過程の超高速光電流計測 Ultrafast photocurrent measurement of quantum cooperative processes in nanocrystal superlattices
2025-49	鈴木 充朗	大阪大学・大学院工学研究科・准教授	村田 靖次郎	分野選択型	4	発展的		塗布重合による2次元共有結合性有機構造体の精密成膜 Controlled in situ polymerization for preparing thin films of two-dimensional covalent organic frameworks (2D COFs)
2025-50	村田 理尚	大阪工業大学・工学部・准教授	村田 靖次郎	分野選択型	4	発展的		高い電気伝導率を指向したn型有機金属半導体の開発 Development of Organometallic n-Type Semiconductors with Improved Conductivity
2025-51	Gurumurthy GP	Scientist-C, Geochemistry Research Lab, Birbal Sahni Institute of Palaeosciences, Lucknow, India	宗林 由樹	分野選択型	5	発展的	国際	ダルワール・クラトン堆積岩のMoおよびW同位体分析による古原生代海洋におけるGOE前の酸素発生とGOE後の酸化還元状態の解明 Resolving Pre-GOE Oxygen Whiffs and Post-GOE Redox State of Paleoproterozoic Oceans through Mo and W isotope Analyses of Sedimentary Rocks of the Dharwar Craton
2025-52	HO, Tung-Yuan	Academia Sinica, Research Center for Environmental Changes, Research Fellow	宗林 由樹	分野選択型	5	発展的	国際	北太平洋における微量金属の元素・同位体組成：エアロゾル沈着の役割 Trace metal elemental and isotopic composition in the North Pacific Ocean: the roles of aerosol deposition
2025-53	Chi Wang	National Cheng Kung University (NCKU), Chemical Engineering Department, Professor	竹中 幹人	分野選択型	5	萌芽的	国際	 Chain orientation in single electrospun fibers: diameter dependence and correlation with mechanical properties
2025-54	Byeongdu Lee	Argonne National Laboratory, X-ray Science Diviosn, Group Leader	竹中 幹人	分野選択型	5	萌芽的	国際	 Imaging of block copolymer morphology with small angle x-ray scattering

2025-55	Yasuhiro Tachibana	RMIT University, School of Engineering, Professor	寺西 利治	分野選択型	5	発展的	国際	ハロゲン化鉛ペロブスカイトの発光スペクトルのアンチストークスシフト化の解明 Elucidation of anti-stokes shifted photoluminescence from lead-based halide perovskite
2025-56	Wei-Ssu Liao	National Taiwan University, Chemistry, Professor	長谷川 健	分野選択型	5	萌芽的	国際	 Investigation of molecule arrangements in artificially abrupted self-assembled monolayers with surface specific spectroscopy techniques.
2025-57	Quan Chen	Chinese Academy of Sciences, Changchun Institute of Applied Chemistry, Professor	松宮 由実	分野選択型	5	発展的	国際	会合性イオノマーの非線形レオロジー Nonlinear Rheology of Dynamically Associative Ionomers
2025-58	中口 譲	近畿大学・理工学部・教授	宗林 由樹	分野選択型	5	萌芽的		大阪湾およびその流入河川水中の生物活性微量金属の化学量論(3) Stoichiometry of biologically active trace metals in Osaka Bay and its inflowing rivers (3)
2025-59	向井 浩	京都教育大学・教育学部理学科・教授	宗林 由樹	分野選択型	5	萌芽的		イオン液体を用いた液膜輸送法によるレアメタルの分離濃縮 Separation and concentration of rare metals by a liquid membrane transport method using ionic liquid
2025-60	西辻 祥太郎	山形大学・大学院有機材料システム研究科・准教授	竹中 幹人	分野選択型	5	発展的		時分割超小角・小角・広角X線散乱法によるゴム中フィラーの分散に関する研究 Time-resolved ultra-small-, small-, and wide-angle X-ray scattering study on the dispersion of filler in rubber
2025-61	飯田 健二	北海道大学・触媒科学研究所・准教授	寺西 利治	分野選択型	5	発展的		プラズモニック合金ナノ粒子を設計するための理論的指針の構築 Construction of Theoretical Guidelines for Designing Plasmonic Nanoalloys
2025-62	丸山 伸伍	東北大学・大学院工学研究科・准教授	長谷川 健	分野選択型	5	萌芽的		液晶性有機薄膜の構造解析 Structure analysis of liquid crystalline organic thin films
2025-63	飯野 裕明	東京科学大学・総合研究院・准教授	長谷川 健	分野選択型	5	萌芽的		液晶性有機半導体における結晶構造とトランジスタ特性の研究 Study on crystalline structure and transistor characteristics of liquid crystalline organic semiconductors
2025-64	下赤 卓史	群馬大学・大学院理工学府・准教授	長谷川 健	分野選択型	5	萌芽的		新規部分フッ素化リン脂質の化学構造と膜物性・構造の関係の解明 Relationship between primary structure of partially fluorinated phospholipids and membrane properties
2025-65	吉竹 良洋	京都大学・生命科学研究科・助教	山口 信次郎	分野選択型	5	発展的		基部陸上植物苔類ゼニゴケにおける活性型ジベレリンの単離と同定 Identification of bioactive gibberellins in the liverwort *Marchantia polymorpha*
2025-66	佐藤 健	金沢大学・設計製造技術研究所・助教	松宮 由実	分野選択型	5	萌芽的		実験およびシミュレーションによる非絡み合い高分子のダイナミクスの統一的解析 A unified analysis of dynamics of unentangled polymers through collaboration of experiments and simulations
2025-67	Kab-Jin Kim	Korea Advanced Institute of Science and Technology, Department of Physics, Associate Professor	小野 輝男	分野選択型	特定1	発展的	国際	スピン波ダイナミクスの探究:ドップラー効果からマグノンブラックホール類似体まで Exploring Spin Wave Dynamics: From Doppler Effects to Magnonic Black-Hole Analogues
2025-68	Satoru Emori	Virginia Tech, Physics, Associate Professor	小野 輝男	分野選択型	特定1	発展的	国際	 Possible Quantum Origin of Unusual Magnetoresistance in Thin-Film Magnetic Metals
2025-69	Sanghoon Kim	University of Ulsan, Department of Physics, Associated professor	小野 輝男	分野選択型	特定1	発展的	国際	 Research on Magnetic Octupoles in Non-Collinear Antiferromagnets
2025-70	Jörg Wrachtrup	3rd Physics Institute, Stuttgart University, Professor	水落 憲和	分野選択型	特定1	発展的	国際	高品質ダイヤモンドを用いた高感度量子センサーの研究 Research on high-sensitive quantum sensor with high quality diamond
2025-71	山田 貴大	東京科学大学・理学院物理学系・助教	小野 輝男	分野選択型	特定1	発展的		熱磁気効果・磁気光学効果を利用した磁化ベクトルの可視化 Visualization of magnetization vector using magneto-thermo and magneto-optical effects
2025-72	田中 雅章	名古屋工業大学・大学院工学研究科・准教授	小野 輝男	分野選択型	特定1	発展的		絶縁性フェライト薄膜によるスピン偏極電流の生成に関する研究 Study on generation of spin-polarized current using insulating ferrite films
2025-73	後藤 穣	東京理科大学・先進工学部・准教授	小野 輝男	分野選択型	特定1	発展的		MgO	Co-Fe-B構造の熱輸送機構に関する研究 Research on heat transport mechanism of MgO	Co-Fe-B structure

2025-74	徳田 規夫	金沢大学・ナノマテリアル研究所・教授	水落 憲和	分野選択型	特定1	発展的		量子スピントロニクスのためのダイヤモンド半導体材料研究 Research of diamond semiconductors for diamond quantum spintronics
2025-75	牧野 俊晴	産業技術総合研究所・先進パワーエレクトロニクス研究センター・研究チーム長	水落 憲和	分野選択型	特定1	発展的		量子センサの高感度化のためのリンドープダイヤモンド合成研究 Research of diamond synthesis for higher sensitivity of NV quantum sensor
2025-76	Takuya F. Segawa	Institute of Molecular Physical Science, ETH Zürich	水落 憲和	分野選択型	特定2	発展的	国際	生命科学応用に向けたナノダイヤモンド中の発光中心の効率的作製研究 Research on the efficient color centers creation in nanodiamond for bio-application
2025-77	Graham J. Bodwell	Memorial University of Newfoundland, Department of Chemistry, University Research Professor	山子 茂	分野選択型	特定2	発展的	国際	 Synthesis of Pyrene-based Materials with Diradical Character
2025-78	Wei-Tin Chen	National Taiwan University, Center for Condensed Matter Sciences, Assistant Research Fellow	島川 祐一	分野選択型	特定2	発展的	国際	 Investigation of geometric magnetic frustrated materials with structure design and high-pressure synthesis
2025-79	Eli Zysman-Colman	University of St Andrews, Organic Semiconductor Centre, EaStCHEM School of Chemistry, Professor of Optoelectronic Materials	梶 弘典	分野選択型	特定2	発展的	国際	塗布製膜可能な多重共鳴型熱活性遅延蛍光材料の開発 Development of solution-processable multi-resonant TADF emitters
2025-80	Francesco Di Maiolo	University of Parma, Department of Chemistry, Life Science and Environmental Sustainability, Prof.	梶 弘典	分野選択型	特定2	発展的	国際	高効率有機ELのための新規有機発光材料の設計：理論と合成の融合 Design of novel organic emitters for highly efficient OLED: Theory meets Synthesis
2025-81	Andrej Jancarik	Centre de Recherche Paul Pascal (CRPP-CNRS and Université de Bordeaux-UBx Joint research unit-UMR Bordeaux Univ.)	山田 容子	分野選択型	特定2	発展的	国際	高次アセン誘導体の合成とシングレットフィッション特性評価 Synthesis of higher acene derivatives and the evaluation of their singlet-fission properties
2025-82	Dang Khoa Andrea Phan Huu	University of Parma, Department of Mathematical, Physical and Computer Sciences, Assistant Professor	梶 弘典	分野選択型	特定2	発展的	国際	CISSおよびCPLを志向したキラル発光分子のモデリング、設計および合成 Modelling, design and synthesis of chiral dyes for CISS and CPL
2025-83	Malte Gather	Humboldt Centre for Nano- and Biophotonics, Department of Chemistry, University of Cologne	梶 弘典	分野選択型	特定2	発展的	国際	エキシマ形成による高性能溶液発光デバイス High-Performance Solution-State Light-Emitting Devices through Excimer-Formation
2025-84	五十嵐 龍治	量子科学技術研究開発機構・量子生命科学研究所・チームリーダー	水落 憲和	分野選択型	特定2	萌芽的		生命科学分野への応用に向けたナノダイヤモンド高感度化研究 Research of high-sensitive nanodiamond for quantum life science application
2025-85	茅原 栄一	広島大学・大学院先進理工系科学研究科・准教授	山子 茂	分野選択型	特定2	発展的		ビスホモ面内芳香族分子の電子状態の解明 Elucidation of electronic state for bis-homo in-plane aromatic molecules
2025-86	奥島 鉄雄	愛媛大学・大学院理工学研究科・准教授	山田 容子	分野選択型	特定2	発展的		熱変換型π電子系有機材料の合成と半導体素子の作製 Synthesis of thermally convertible pi-electronic organic materials and fabrication of the organic semiconducting devices
2025-87	森下 弘樹	東北大学・先端スピントロニクス研究開発センター・准教授	梶 弘典	分野選択型	特定2	発展的		固体NMRとEDMR・ODMRの連携による電子・正孔対の挙動解析
2025-88	菊地 和也	大阪大学・大学院工学研究科・教授	上杉 志成	分野選択型	特定2	発展的		細胞内相分離タンパク質の可視化解析 Visualization and Analysis of Cellular Phase-Separating Proteins
2025-89	服部 鮎奈	京都大学・医生物学研究所・准教授	梶 弘典	分野選択型	特定2	萌芽的		HR-MAS法を用いた悪性腫瘍の代謝プロファイリング Metabolic Profiling of Malignant Tumors Using HR-MAS
2025-90	Lu Zhou	Fudan University, School of Pharmacy, Professor	上杉 志成	課題提案型		発展的	国際	XZA-1の化学遺伝学 Chemical Genetics of XZA-1
2025-91	Young-Tae Chang	Professor, Department of Chemistry, POSTECH	上杉 志成	課題提案型		発展的	国際	生体分子凝縮体の蛍光プローブの探索と解析 Exploration and Analysis of Fluorescent Probes for Biomolecular Condensates
2025-92	Xiaoguang Lei	Peking University	上杉 志成	課題提案型		発展的	国際	アルベニンIの合成と機能解析 Synthetic and Functional Investigation of Arvenin I

2025-93	Wei Yunlin	Kunming University of Science and Technology, Faculty of Life Science and Technology, Professor	栗原 達夫	課題提案型		萌芽的	国際	細菌細胞外膜小胞の形成・機能・応用に関する研究 Biogenesis, functions, and application of bacterial extracellular membrane vesicles
2025-94	Maria Michela Corsaro	University of Naples Federico II, Department of Chemical Sciences, Professor	栗原 達夫	課題提案型		発展的	国際	細菌が放出する外膜小胞の表層多糖の構造機能解析 Structural and functional analysis of the surface polysaccharides of outer membrane vesicles released by bacteria
2025-95	Douglas Bartlett	Scripps Institution of Oceanography, UC San Diego	川本 純	課題提案型		発展的	国際	ナノバイオテクノロジーに資する有用細菌の探索 Exploration of useful bacteria for nanobiotechnology
2025-96	Maya Endoh	Stony Brook University, Department of Material Science and Chemical Engineering, Research Professor	竹中 幹人	課題提案型		発展的	国際	亜・超臨界水を用いた高分子系複合材料のリサイクル II Recycling of polymer-matrix composites by subcritical/supercritical water II
2025-97	Kohji Ohno	Osaka Metropolitan University, Graduate School of Engineering, Professor	辻井 敬亘	課題提案型		発展的	国際	ポリエーテルブラシ被覆粒子の合成とトライボロジー応用 Synthesis and Tribological Applications of Polyether-Brush-Coated Particles
2025-98	Oh-Hoon Kwon	Professor, Department of Chemistry, Ulsan National Institute of Science and Technology (UNIST)	寺西 利治	課題提案型		発展的	国際	 Real-time observation of self-assembly and phase transformation of nanocrystals
2025-99	Masato Ota	National Institute for Fusion Science (NIFS), Assistant Professor	時田 茂樹	課題提案型		発展的	国際	相対論的レーザー生成プラズマの超高速計測 Ultrafast measurement of relativistic laser-generated plasma
2025-100	Kensuke Homma	Hiroshima University, Physics, Associate professor	時田 茂樹	課題提案型		発展的	国際	宇宙暗黒成分解明へ向けた真空内四光波混合の探索 Search for four-wave-mixing in the vacuum – Unveiling dark components in the Universe –
2025-101	Thomas Wirth	Cardiff University, School of Chemistry, Professor	中村 正治	課題提案型		発展的	国際	 Flow Chemistry for the investigation of sustainable cyclisation conditions
2025-102	Ilaria BONADUCE	University of Pisa, Dept. of Chemistry, Associate Prof.	PINCELLA Francesca	課題提案型		発展的	国際	アジアの生漆・重合漆サンプルの合成と特性評価：材料科学・文化遺産保全学のための包括的漆ライブラリーの開発に向けて Synthesis and characterization of raw and polymerized Asian lacquer samples: towards the development of a comprehensive collection of lacquer reference samples for materials science and conservations studies.
2025-103	Fabienne Burlina	Sorbonne Université – CNRS –ENS, CPCV Laboratory – UMR 8228, Directrice de recherche CNRS, PhD	今西 未来	課題提案型		発展的	国際	化学修飾したホメオタンパク質のDNA結合性 DNA-binding properties of chemically modified homeoproteins
2025-104	Sílvia PUJALS	Institute for Advanced Chemistry of Catalonia (IQAC), Supramolecular chemistry group, Biological Chemistry department. CSIC Tenured Scientist	川口 祥正	課題提案型		発展的	国際	ナノ医薬の細胞内移行機構の解析 Analysis of intracellular delivery mechanism of nanomedicine
2025-105	Tim Stasevich	Colorado State University, Dept. of Biochemistry and Molecular Biology, Associate Professor	今西 未来	課題提案型		発展的	国際	生細胞でのRNA編集の可視化：1分子レベルでの技術開発 Visualizing RNA Editing in Action: Developing Single-Molecule Resolution Techniques for Live Cells
2025-106	Zuhua He	Chinese Academy of Sciences, CAS Center for Excellence in Molecular Plant Sciences, Institute of Plant Physiology and Ecology, Professor	山口 信次郎	課題提案型		発展的	国際	イネの成長ホルモンの不活性化機構の解析 Molecular mechanisms for the inactivation of a growth hormone in rice
2025-107	David C. Nelson	University of California, Riverside, Department of Botany and Plant Sciences, Professor of Genetics	山口 信次郎	課題提案型		萌芽的	国際	植物の成長を調節する新奇シグナル分子の生合成遺伝子の同定 Identification of biosynthetic genes for a novel signaling molecule that modulates plant development
2025-108	Yunde Zhao	University of California San Diego, Division of Biological Sciences, Department of Cell and Developmental Biology, Professor	増口 潔	課題提案型		萌芽的	国際	新規ストリゴラクトン輸送体タンパク質の解析 Analysis of novel transporters for strigolactones or their biosynthetic intermediates
2025-109	Matthew J. Fuchter	Univeristy of Oxford, Chemistry, Professor	山子 茂	課題提案型		発展的	国際	 Cycloparaphenylene/Fullerenes Supramolecular Complexes in Chiroptical Applications
2025-110	Songlin Xue	Jiangsu University, School of Chemistry and Chemical Engineering, Special-Term Prof. Dr.	山田 容子	課題提案型		発展的	国際	ヘテロ金属ポルフィリン（2.1.2.1）アレイの合成と電気触媒 Synthesis and Electrocatalysis of Hetero-Metal Porphyrin(2.1.2.1) Arrays

2025-111	Hao-Wu Lin	Department of Materials Science and Engineering, National Tsing Hua University, Taiwan, Professor	若宮 淳志	課題提案型		発展的	国際	真空蒸着型ペロブスカイト光電子デバイス：先進的な正孔選択材料を用いて Vacuum-deposited Perovskite Optoelectronic Devices with Advanced Hole-selection Materials
2025-112	NAMBARA, Eiji	Department of Cell & Systems Biology, University of Toronto, Professor	柘植 知彦	課題提案型		萌芽的	国際	シロイヌナズナの光に応答した形態形成の可塑性における植物ホルモンの作用に関する研究 Elucidating molecular functions of plant hormones in light-responsive morphological plasticity in *Arabidopsis thaliana*
2025-113	KAWACHI-REUSCHER, Miki	Georg-August-Universität Göttingen, Division of Crop Plant Genetics, Scientist	加藤 真理子	課題提案型		発展的	国際	亜鉛トランスポーターと脂質キナーゼが関与する花粉の小胞輸送のイメージング解析 Imaging analysis of zinc transporter and lipid kinase-associated pollen vesicle transport
2025-114	RUBIO, Vicente	National Center of Biotechnology (CNB-CSIC), Plant Molecular Genetics Department, Associate Professor	柘植 知彦	課題提案型		発展的	国際	植物光形態形成モデルにおけるタンパク質分解とmRNAプロセシングの協調的制御機構 Crossroads of proteostasis and RNA processing in Arabidopsis photomorphogenesis
2025-115	竹本 操	福島県立医科大学・医学部・助教	上杉 志成	課題提案型		萌芽的		T細胞の免疫機能を賦活化する共有結合性小分子化合物の開発 Development of Covalent Small Molecules That Potentiates Antitumor Immunity
2025-116	Daniel Packwood	Associate Professor, iCeMS, Kyoto University	上杉 志成	課題提案型		萌芽的		機械学習による自己集合化合物の予測 Machine-Learning Prediction of Self-Assembly Compounds
2025-117	山崎 思乃	関西大学・化学生命工学部・准教授	栗原 達夫	課題提案型		発展的		腸内細菌が分泌する細胞外膜小胞の生理機能の解析とその応用 Analysis and application of the physiological functions of extracellular vesicles secreted by intestinal bacteria
2025-118	豊竹 洋佑	立命館大学・生命科学部生物工学科・助教	小川 拓哉	課題提案型		萌芽的		酢酸菌における膜脂質依存的な発酵ストレス応答の解析 Analysis of membrane lipid-dependent fermentation stress response in acetic acid bacteria
2025-119	倉橋 健介	大阪公立大学工業高等専門学校・プロダクトデザインコース・准教授	宗林 由樹	課題提案型		萌芽的		溶媒含浸樹脂を用いた連続的分離法による希土類元素分離の最適化 Optimization of continuous separation of rare earth element method with solvent impregnated resins
2025-120	村瀬 浩貴	共立女子大学・家政学部被服学科・教授	辻井 敬亘	課題提案型		発展的		3Dプリンティング技術を用いた3次元構造化モノリス造形 3D Structured Monolith Moulding using 3D Printing Technology
2025-121	真島 豊	東京科学大学・フロンティア材料研究所・教授	寺西 利治	課題提案型		発展的		カチオン交換非平衡単一半導体ナノプレートのエネルギー準位の解明 Band diagram of single nonequilibrium semiconductor nanoplate by cation exchange
2025-122	内田 裕之	京都大学・大学院理学研究科物理学第二教室・助教	時田 茂樹	課題提案型		萌芽的		大型レーザー装置を利用した電荷交換反応の地上再現実験と天体放射モデルの構築 Ground-based experiment of charge exchange reactions using a large laser device and construction of an astronomical radiation model
2025-123	岸本 泰明	京都大学大学院・エネルギー科学研究科・名誉教授、京都大学エネルギー理工学研究所・特任教授、京都大学学際融合教育研究推進センター／非線形・非平衡プラズマ科学研究ユニット・構成員	時田 茂樹	課題提案型		発展的		高強度レーザーと構造性ターゲットとの相互作用による水素・ホウ素核融合等価プラズマ生成と緩和・閉込め過程の検証 Verification of hydrogen-boron fusion equivalent plasma generation and relaxation/confinement process by the interaction between high-intensity laser and structured target
2025-124	遠藤 玉樹	甲南大学・フロンティアサイエンス研究科・准教授	今西 未来	課題提案型		発展的		RNA構造を標的とした相互作用ペプチドのオンデマンド設計 On demand design of peptides targeting RNA structures
2025-125	中瀬 生彦	大阪公立大学・大学院理学研究科・教授	川口 祥正	課題提案型		発展的		インクジェットプリンターによる細胞内への機能性ペプチド送達研究 Study of intracellular peptide delivery by inkjet printer
2025-126	瀬戸 義哉	明治大学・農学部・准教授	山口 信次郎	課題提案型		発展的		新規ストリゴラクトン生合成阻害剤の探索 Identification of novel strigolactone biosynthetic inhibitors
2025-127	深澤 壽太郎	広島大学・統合生命科学研究科・准教授	山口 信次郎	課題提案型		萌芽的		揮発性植物ホルモン様分子による生長制御機構の解析 Analysis of growth regulation mechanisms by volatile plant hormone-like molecules
2025-128	田上 秀一	福井大学 ・繊維・マテリアル研究センター・教授	山子 茂	課題提案型		萌芽的		高分子複合材料における多分岐高分子の挙動 Behavior of Hyperbranched Polymers in Polymer Composites

2025-129	髙橋 裕	東北大学・未来科学技術共同研究センター・特任助教	山子 茂	課題提案型		発展的		超分岐構造高分子の滑剤作用の解明と最適化 Elucidation of the lubrication properties of hyperbranched polymers and their optimization
2025-130	安喜 史織	大和大学・理工学部・准教授	柘植 知彦	課題提案型		萌芽的		環境に応答した植物の栄養繁殖制御メカニズムの解析 Regulatory mechanisms of vegetative reproduction in response to environmental cues
2025-131	肥塚 崇男	山口大学・大学院創成科学研究科・准教授	柘植 知彦	課題提案型		発展的		植物揮発性ベンゼノイド生合成に関わるアルデヒド脱水素酵素の機能解析 Biochemical characterization of aldehyde dehydrogenases involved in the biosynthesis of plant volatile benzenoids
2025-132	Tadashi Inoue	Osaka University, Department of Macromolecular Science, Professor	松宮 由実	連携・融合促進型			国際	東アジア圏の若手レオロジストのための第18回ワークショップ The 18th International Workshop for East Asian Young Rheologists
2025-133	Sean Dusan Alexander Injac	University of Edinburgh, Centre for Science at Extreme Conditions (CSEC), Postdoctoral Research Associate	島川 祐一	施設・機器利用型			国際	 High pressure synthesis of new Rh based quantum materials
2025-134	Natthaphol CHOMSAENG	Burapha University, Advanced Materials Engineering, Assist. Prof.	治田 充貴	施設・機器利用型			国際	AlxCrFeNiCu合金の電子顕微鏡による原子構造解析 Atomic Structure Investigation by Advanced Transmission Electron Microscopy of AlxCrFeNiCu Alloys
2025-135	Ming-Wen Chu	National Taiwan University, Center for Condensed Matter Sciences, Distinguished Research Fellow	治田 充貴	施設・機器利用型			国際	角度分解電子エネルギー損失分光法による量子物質におけるプラズモン分散の解明 Tackling Plasmon Dispersions in Quantum Matters by Momentum-Resolved Electron-Energy Loss Spectroscopy
2025-136	Thapanee SARAKONSRI	Chiang Mai University, Chemistry, Assoc. Prof. Dr.	治田 充貴	施設・機器利用型			国際	 Nano-structural and Atomic-resolution Characterization on the Local Structure of Novel Functional Energy Materials by Advanced Transmission Electron Microscopy
2025-137	小島 完興	量子科学技術研究開発機構・量子応用光学研究部・主任研究員	時田 茂樹	施設・機器利用型				レーザー駆動イオン加速機構による高品質なイオンビーム生成のためのレーザー照射条件の最適化 Optimization of laser irradiation conditions for high-quality ion beam generation by laser-driven ion acceleration mechanism
2025-138	秦野 修	奈良県立医科大学・医学部・博士研究員	中村 正治	施設・機器利用型				スギ木質組織構造の効率的化学分解過程から先端化学物質生産をめざした質量分析解析 Mass spectrometry analysis for the production of advanced chemical materials from the efficient chemical decomposition process of cedar wood tissue structure
2025-139	髙橋 まさえ	東北大学・大学院理学研究科・特任研究員	水畑 吉行	施設・機器利用型				平面二次元シートに埋め込まれた低次元ケイ素材料の理論設計と動作原理の探求 Theoretical design of low-dimensional silicon material embedded in a flat two-dimensional sheet and exploration for operating principles
2025-140	松尾 司	近畿大学・理工学部・教授	水畑 吉行	施設・機器利用型				13族元素水素化物の合成と分子構造の解明 Synthesis and Structural Characterization of Hydrides of Group 13 Elements
2025-141	斉藤 光	九州大学・先導物質化学研究所・准教授	治田 充貴	施設・機器利用型				Cs_4PbBr_6薄膜への電子線照射による$CsPbBr_3$ナノ光源生成 $CsPbBr_3$ nano-light source generation by electron beam irradiation on Cs_4PbBr_6 thin film

